Solar fusion III: New data and theory for hydrogen-burning stars

B. Acharya
Oak Ridge National Laboratory, Oak Ridge, Tennessee 37831, USA

M. Aliotta
SUPA, School of Physics and Astronomy, University of Edinburgh, Edinburgh EH9 3FD, United Kingdom

A. B. Balantekin
Department of Physics, University of Wisconsin–Madison, Madison, Wisconsin 53706, USA

D. Bemmerer
Helmholtz-Zentrum Dresden-Rossendorf, 01328 Dresden, Germany

C. A. Bertulani
Department of Physics and Astronomy, Texas A&M University–Commerce, Commerce, Texas 75429-3011, USA

A. Best
University of Napoli Federico II, 80126 Napoli, Italy and Istituto Nazionale di Fisica Nucleare–Napoli, 80126 Napoli, Italy

C. R. Brune
Edwards Accelerator Laboratory, Department of Physics and Astronomy, Ohio University, Athens, Ohio 45701, USA

R. Buompane and L. Gialanella
Dipartimento di Matematica e Fisica, Università degli Studi della Campania "Luigi Vanvitelli," 81100 Caserta, Italy and Istituto Nazionale di Fisica Nucleare–Napoli, 80126 Napoli, Italy

F. Cavanna
Istituto Nazionale di Fisica Nucleare–Torino, 10125 Torino, Italy

J. W. Chen
Department of Physics and Center for Theoretical Physics, National Taiwan University, Taipei 10617, Taiwan and Physics Division, National Center for Theoretical Sciences, Taipei 10617, Taiwan

J. Colgan
Los Alamos National Laboratory, Los Alamos, New Mexico 87545, USA

A. Czarnecki
Department of Physics, University of Alberta, Edmonton, Alberta T6G 2E1, Canada

B. Davids
TRIUMF, Vancouver, British Columbia V6T 2A3, Canada and Department of Physics, Simon Fraser University, Burnaby, British Columbia V5A 1S6, Canada

R. J. deBoer

Department of Physics and Astronomy and the Joint Institute for Nuclear Astrophysics, University of Notre Dame, Notre Dame, Indiana 46556, USA

F. Delahaye

Observatoire de Paris–PSL, Sorbonne Université, 5 Place Jules Janssen, 92195 Meudon Cedex, France

R. Depalo and A. Guglielmetti

Università degli Studi di Milano, 20133 Milano, Italy and Istituto Nazionale di Fisica Nucleare-Milano, 20133 Milano, Italy

A. García and R. G. H. Robertson

Department of Physics and Center for Experimental Nuclear Physics and Astrophysics, University of Washington, Seattle, Washington 98195, USA

M. Gatu Johnson

Massachusetts Institute of Technology, Cambridge, Massachusetts 02139, USA

D. Gazit

Racah Institute of Physics, The Hebrew University, The Edmond J. Safra Campus, Givat Ram, Jerusalem 9190401, Israel

U. Greife

Colorado School of Mines, Golden, Colorado 80401, USA

D. Guffanti

Dipartimento di Fisica, Università degli Studi e INFN Milano-Bicocca, 20126 Milano, Italy

K. Hambleton

Department of Physics, University of California, Berkeley, California 94720, USA

W. C. Haxton*

Department of Physics, University of California, Berkeley, California 94720, USA and Lawrence Berkeley National Laboratory, Berkeley, California 94720, USA

Y. Herrera and A. Serenelli

Institute of Space Sciences, 08193 Cerdanyola del Vallès, Barcelona, Spain and Institut d'Estudis Espacials de Catalunya, 08034 Barcelona, Spain

M. Huang

Department of Physics and Astronomy, Iowa State University, Ames, Iowa 50011, USA and Lawrence Livermore National Laboratory, P.O. Box 808, L-414, Livermore, California 94551, USA

C. Iliadis

Department of Physics and Astronomy, University of North Carolina at Chapel Hill, Chapel Hill, North Carolina 27599-3255, USA and Triangle Universities Nuclear Laboratory (TUNL), Duke University, Durham, North Carolina 27708, USA

K. Kravvaris

Lawrence Livermore National Laboratory,
P.O. Box 808, L-414, Livermore, California 94551, USA

M. La Cognata

Istituto Nazionale di Fisica Nucleare, Laboratori Nazionali del Sud, 95123 Catania, Italy

K. Langanke

GSI Helmholtzzentrum für Schwerionenforschung, Darmstadt, Germany
and Institut für Kernphysik, Technical University Darmstadt, Darmstadt, Germany

L. E. Marcucci

Department of Physics "E. Fermi," University of Pisa, 56127 Pisa, Italy
and Istituto Nazionale di Fisica Nucleare–Pisa, 56127 Pisa, Italy

T. Nagayama

Sandia National Laboratories, Albuquerque, New Mexico 87123, USA

K. M. Nollett

Department of Physics, San Diego State University, San Diego, California 92182, USA

D. Odell

Department of Physics and Astronomy, Ohio University, Athens, Ohio 45701, USA

G. D. Orebi Gann

University of California, Berkeley, California 94720, USA
and Lawrence Berkeley National Laboratory, Berkeley, California 94720, USA

D. Piatti

Università degli Studi di Padova, Via Francesco Marzolo 8, 35131 Padova, Italy
and INFN, Sezione di Padova, Via Francesco Marzolo 8, 35131 Padova, Italy

M. Pinsonneault

Department of Astronomy, The Ohio State University,
140 West 18th Avenue, Columbus, Ohio 43210, USA
and Center for Cosmology and AstroParticle Physics, The Ohio State University,
191 West Woodruff Avenue, Columbus, Ohio 43210, USA

L. Platter

Department of Physics and Astronomy, University of Tennessee,
Knoxville, Tennessee 37996, USA
and Physics Division, Oak Ridge National Laboratory, Oak Ridge, Tennessee 37831, USA

G. Rupak

Department of Physics and Astronomy and HPC2 Center for Computational Sciences,
Mississippi State University, Mississippi State, Mississippi 39762, USA

M. Sferrazza

Université Libre de Bruxelles, Bruxelles, Belgium

T. Szücs

HUN-REN Institute for Nuclear Research (HUN-REN ATOMKI), 4026 Debrecen, Hungary

X. Tang

IMP Chinese Academy of Science, Lanzhou, China

A. Tumino

Dipartimento di Ingegneria e Architettura, Università degli Studi di Enna "Kore," Enna, Italy and Istituto Nazionale di Fisica Nucleare, Laboratori Nazionali del Sud, 95123 Catania, Italy

F. L. Villante

Dipartimento di Scienze Fisiche e Chimiche, Università dell'Aquila, 67100 L'Aquila, Italy and Istituto Nazionale di Fisica Nucleare, Laboratori Nazionali del Gran Sasso, 67100 Assergi (AQ), Italy

A. Walker-Loud

Nuclear Science Division, Lawrence Berkeley National Laboratory, Berkeley, California 94720, USA

X. Zhang

Facility for Rare Isotope Beams, Michigan State University, East Lansing, Michigan 48824, USA

K. Zuber

Institute for Nuclear and Particle Physics, Technical University of Dresden, 01062 Dresden, Germany

(published 4 September 2025)

In stars that lie on the main sequence in the Hertzsprung-Russell diagram, like our Sun, hydrogen is fused to helium in a number of nuclear reaction chains and series, such as the proton-proton chain and the carbon-nitrogen-oxygen cycles. Precisely determined thermonuclear rates of these reactions lie at the foundation of the standard solar model. This review, the third decadal evaluation of the nuclear physics of hydrogen-burning stars, is motivated by the great advances made in recent years by solar neutrino observatories, putting experimental knowledge of the proton-proton (pp)-chain neutrino fluxes in the few-percent precision range. The basis of the review is a one-week community meeting held in July 2022 in Berkeley, California, and many subsequent digital meetings and exchanges. The relevant reactions of solar and stellar hydrogen burning are reviewed here from both theoretical and experimental perspectives. Recommendations for the state of the art of the astrophysical S factor and its uncertainty are formulated for each of them. Several other topics of paramount importance for the solar model are reviewed as well: recent and future neutrino experiments, electron screening, radiative opacities, and current and upcoming experimental facilities. In addition to reaction-specific recommendations, general recommendations are also formed.

DOI: 10.1103/8lm7-gs18

CONTENTS

I. Introduction 5
A. Purpose 5
B. Terminology used 6
C. Scope and structure 8
II. Solar Neutrino Observations 9
A. Open questions 9
1. The solar composition problem 10
2. The gallium anomaly 11
3. The ^{8}B neutrino spectrum 12
B. Experimental program on solar neutrinos 13
1. Super-Kamiokande and Hyper-Kamiokande 13
2. Sudbury Neutrino Observatory and SNO+ 13
3. Borexino 14
4. JUNO 14
5. DUNE 15
6. Future prospects 15
III. The ^{1}H$(p, e^+\nu)^2$H Reaction (S_{11}) 15
A. Introduction and terminology 15
B. Adopted parameters for this review 16
C. Experimental progress on muon capture of the deuteron 17
D. Progress in $S_{11}(0)$ calculations since SF II 17
1. χEFT 17
2. $\not\pi$EFT 18

*Contact author: haxton@berkeley.edu

3. Lattice QCD and lattice EFT 18
4. Final recommendation of $S_{11}(0)$ 19
E. Progress in $S'_{11}(0)$ and $S''_{11}(0)$ 19
IV. The ^{2}H$(p,\gamma)^3$He Reaction (S_{12}) 20
A. Introduction 20
B. Datasets used in this review 20
C. Theoretical studies 21
D. Phenomenological and Bayesian analyses 21
E. Summary and recommendations 22
V. The ^{3}He$(^3$He$, 2p)^4$He Reaction (S_{33}) 22
A. Shape of the particle spectrum 22
B. Recommendation 24
VI. The ^{3}He$(\alpha,\gamma)^7$Be Reaction (S_{34}) 24
A. Previous S_{34} recommendation in SF II 24
B. Theory progress on S_{34} 24
C. Experimental progress on S_{34} 26
D. Data fitting 26
E. Recommended S_{34} value 28
F. Recommendations for future work on S_{34} 29
VII. The hep Reaction ($S_{\rm hep}$) 29
VIII. Electron Capture by $p+p$ and ^{7}Be 30
IX. The ^{7}Be$(p,\gamma)^8$B Reaction (S_{17}) 31
A. Introduction 31
B. Experimental data 31
1. Direct measurements 31
2. Indirect measurements 32
C. Theory 32
D. Fitting procedures 33
E. Data analysis and S_{17} determination 34
F. Theoretical uncertainty 35
G. Conclusions and recommendation for S_{17} 36
X. The ^{14}N$(p,\gamma)^{15}$O Reaction (S_{114}) 36
A. Current status and results 36
B. Absolute strength of the 259 keV resonance 36
C. Indirect studies 37
D. R-matrix considerations 37
E. Partial S factors 37
1. Ground-state transition 38
2. 6.79 MeV transition 39
3. Other transitions 39
F. Total S factor and conclusions 39
XI. Other CNO, Ne-Na Reactions 39
A. Reactions of the CNO-I cycle 40
1. ^{12}C$(p,\gamma)^{13}$N 40
2. ^{13}C$(p,\gamma)^{14}$N 41
3. ^{15}N$(p,\alpha)^{12}$C 41
B. Reactions of the NO or CNO-II cycle 43
1. ^{15}N$(p,\gamma)^{16}$O 43
2. ^{16}O$(p,\gamma)^{17}$F 43
3. ^{17}O$(p,\gamma)^{18}$F 44
4. ^{17}O$(p,\alpha)^{14}$N 44
C. Reactions of the CNO-III cycle 45
1. ^{18}O$(p,\gamma)^{19}$F 45
2. ^{18}O$(p,\alpha)^{15}$N 45
3. ^{19}F$(p,\gamma)^{20}$Ne 45
4. ^{19}F$(p,\alpha)^{16}$O 46
D. Reactions of the neon-sodium (NeNa) cycle 47
1. ^{20}Ne$(p,\gamma)^{21}$Na 47
2. ^{21}Ne$(p,\gamma)^{22}$Na 47
3. ^{22}Ne$(p,\gamma)^{23}$Na 47
4. ^{23}Na$(p,\gamma)^{24}$Mg 48
5. ^{23}Na$(p,\alpha)^{20}$Ne 48
XII. Electron Screening of Nuclear Reactions 48
A. Screening in laboratory experiments 48
B. Screening in the solar core 50
XIII. Radiative Opacities 50
A. Introduction 50
B. Opacity models 52
C. Production of tables 53
D. Experimental testing of calculated iron opacity 54
E. Future opacity work 55
XIV. Experimental Facilities for Solar Fusion Studies 56
A. Aboveground facilities 56
1. LENA 56
2. NSL 56
B. Underground facilities 56
1. Bellotti Ion Beam Facility 57
2. JUNA 57
3. CASPAR 57
4. Felsenkeller 57
C. Indirect methods 58
D. Plasma facilities 58
1. NIF and OMEGA 58
2. PANDORA 58
3. Sandia Z 59
E. Storage rings for nuclear astrophysics studies 59
1. CRYRING 59
XV. Closing Remarks 60
A. Summary 60
B. Recommended values for S factors and their derivatives 60
C. General recommendations for future work 60
D. Outlook 61
List of Symbols and Abbreviations 62
Acknowledgments 62
Appendix A: Gallium Neutrino Source Cross Sections 63
Appendix B: Bayesian Methods 64
References 65

I. INTRODUCTION

This review summarizes the state of our understanding, in the third decade of the 21st century, of the nuclear reactions and decays taking place in solar and stellar hydrogen burning. It also addresses related issues, including solar neutrino detection, radiative opacities, electron screening of nuclear reactions, and the status of the current facilities for measuring cross sections and opacities. As was the case in two previous decadal reviews (Adelberger *et al.*, 1998, 2011), this review summarizes the progress made over the past decade in advancing the nuclear physics of main-sequence stars and makes recommendations for future work.

A. Purpose

Davis's measurements of the flux of solar neutrinos (Davis, Harmer, and Hoffman, 1968; Davis, 2003) showed a significant deficit with respect to the predictions of the standard solar model (SSM) (Bahcall, 1966). This discrepancy became known as the solar neutrino problem. An intense debate ensued about possible explanations for this discrepancy, summarized in the review by Bahcall *et al.* (1988). Suggestions included plausible flaws in the SSM that might produce a cooler solar core

(Schatzman *et al.*, 1981; Cumming and Haxton, 1996), new particle physics such as neutrino oscillations (Gribov and Pontecorvo, 1969; Wolfenstein, 1978), changes in the nuclear physics governing He synthesis, such as an unidentified low-energy resonance in the $^3\mathrm{He} + {}^3\mathrm{He}$ reaction affecting extrapolations of laboratory cross sections to solar energies (Fetisov and Kopysov, 1972; Fowler, 1972), and the presence of dark matter particles modifying energy transport in the solar core (Spergel and Press, 1985). By the mid-1990s, with new results from the Kamioka II and III (Hirata *et al.*, 1989; Fukuda *et al.*, 1996) and SAGE-GALLEX (Abazov *et al.*, 1991; Anselmann *et al.*, 1992) experiments revealed a pattern of neutrino fluxes that was inconsistent with the expected scaling of those fluxes with the solar core temperature. Attention increasingly turned to neutrino oscillations and other potential particle physics solutions. Concerns about the nuclear physics of the SSM also evolved, focusing more on the uncertainties that might inhibit extraction of any such "new physics."

At that time, during a meeting on the solar neutrino problem hosted by the Institute for Nuclear Theory (INT) at the University of Washington, Seattle, a suggestion was made to convene the community working on solar nuclear reactions in order to reach consensus on the best current values of cross sections and their uncertainties. The INT hosted the proposed workshop in February 1997, drawing representatives from almost every experimental group active in this area, as well as many of the theorists who were engaged in solar neutrino physics. The working groups that formed during this meeting worked over the following year to evaluate past work, determining the needed cross sections and their uncertainties. The results of this evaluation, which came to be known as Solar Fusion I or SF I (Adelberger *et al.*, 1998), became the standard for use in solar modeling over the following decade.

An update of the work of Adelberger *et al.* (1998) was launched with the January 2009 workshop Solar Fusion Cross Sections II, hosted again by the INT in Seattle. Initial results from Super-Kamiokande, the Sudbury Neutrino Observatory, and Borexino were then in hand, and the conversion of approximately two-thirds of solar electron neutrinos into other flavors had been firmly established (Ahmad *et al.*, 2002a). Consequently, the motivation for the study was to ensure that solar model predictions would be based on the most current nuclear physics so that meaningful uncertainties could be placed on neutrino parameters derived from solar neutrino measurements, such as the mixing angle θ_{12}. An additional source of uncertainty had arisen at the time, with the advent of three-dimensional (3D) radiative-hydrodynamic models of the Sun's atmosphere for determining element abundances from photoabsorption lines (Asplund, Grevesse, and Sauval, 2006; Asplund *et al.*, 2009). This improved analysis, though, lowered the inferred metallicities, leading to tension with the Sun's interior sound speed profile determined from helioseismology (Christensen-Dalsgaard, 2002). The discrepancy between higher metallicity models that accurately reproduce the Sun's interior sound speed and lower metallicity models based on the most current treatment of the photosphere was called the solar composition problem. While the neutrino fluxes were not known to the precision needed to distinguish between the competing models, it had been shown that the solar core metallicity could be extracted directly from future carbon-nitrogen (CN) solar neutrino measurements if the precision of associated nuclear cross sections were improved (Haxton and Serenelli, 2008). Reflecting the impact of new experimental work and improved theory, the study of Adelberger *et al.* (2011) significantly revised the Adelberger *et al.* (1998) cross section for the driving reaction of the carbon-nitrogen-oxygen (CNO)-I cycle, and updated key pp-chain cross sections.

The present SF III review began with a four-day workshop, Solar Fusion Cross Sections III, in July 2022. The meeting was hosted by the Physics Frontier Center Network for Neutrinos, Nuclear Astrophysics, and Symmetries (N3AS),[1] a consortium of institutions involved in multimessenger astrophysics whose central hub is the University of California, Berkeley. Sessions were held at the David Brower Center in Berkeley and the physics department at the University of California, Berkeley, with the assistance of N3AS staff. The workshop was organized by the N3AS, by Solar Fusion's long-term sponsor, the INT, and by the European ChETEC-INFRA Starting Community for Nuclear Astrophysics.[2]

The 47 workshop participants represented most of the leading experimental and theoretical research groups that are active in the field. Workshop participants were organized into nine working groups, who were charged with reviewing and evaluating work completed since that of Adelberger *et al.* (2011) to produce updated recommendations. The structure of this review largely follows that of the working groups. The timing of SF III was driven in part by planned large-scale asteroseismic surveys of hydrogen-burning stars such as the European Space Agency's PLATO[3] mission (Rauer *et al.*, 2014), and the expectation that associated data analyses will require large libraries of stellar models in which masses, ages, metallicities, and other parameters are varied. SF III will provide the best current nuclear astrophysics input for such modeling. This review summarizes that input, based on the recommendations of the nine SF III working groups.

B. Terminology used

The terminology used here follows recent practice, as summarized in the Nuclear Astrophysics Compilation of Reaction Rates (NACRE) compilation (Angulo *et al.*, 1999). It is described here to aid the reader.

Nuclear reactions are designated as

$$A(b,c)D, \tag{1}$$

where A is the target nucleus, b is the bombarding particle, and c and D are the reaction products, with D distinguished as the heavier product. Frequently in nuclear astrophysics, the reaction cross section σ is reexpressed in terms of the S factor S_{ij}, with S related to σ as subsequently described, and

[1]See https://n3as.berkeley.edu/.
[2]See https://www.chetec-infra.eu/.
[3]See https://platomission.com/.

with i and j the mass numbers of entrance channel nuclei b and A.

The relation between the nuclear cross section $\sigma(E)$ and the astrophysical S factor is

$$S(E) = \sigma(E)E \exp\left(2\pi \frac{Z_A Z_b \alpha}{\beta}\right), \tag{2}$$

with Z_A and Z_b the charge numbers of the target and projectile, $\alpha \sim 1/137$ the fine-structure constant, $\beta \equiv v/c = \sqrt{2E/\mu c^2}$ the relative velocity of the interacting particles in units of c, μ the reduced mass, and E the center-of-mass energy. (In this review we use energy units of MeV unless otherwise stated.) This removes the sharp energy dependence from the cross section associated with s-wave Coulomb scattering off a point nucleus, thereby accounting for the leading penetration effects associated with the Coulomb barrier. The quantity $Z_A Z_b \alpha/\beta$ is known as the Sommerfeld parameter. Consequently, unless there are resonances, $S(E)$ should be a smooth function that, at low energies, can generally be expressed as a low-order polynomial in E.

The S factor in Eq. (2) is defined in terms of the nuclear (or "bare") cross section, while laboratory experiments are performed with targets consisting of neutral atoms. As electrons shield the nucleus, lowering the Coulomb barrier, their presence enhances the laboratory cross section. The S factors derived from laboratory data must be corrected for this effect. As the energy is lowered, the screening correction becomes increasingly important. Thus, particular care must be taken when extrapolating laboratory cross sections to lower energies, as Fig. 4 of Adelberger *et al.* (2011) illustrates. Unless otherwise noted, the S factors discussed here are those for bare nuclei.

The rapid rise in the nuclear cross section with energy, reflecting the higher probability of penetrating the Coulomb barrier, competes with a rapid decrease in the probability of finding interacting particles with the requisite center-of-mass energy E in the high-energy tail of the Maxwell-Boltzmann distribution. Consequently, the thermonuclear reaction rate $\langle \sigma v \rangle$ for a given stellar temperature T takes the form

$$\langle \sigma v \rangle = \sqrt{\frac{8}{\mu \pi}} (k_B T)^{-3/2} \int_0^\infty S(E) \exp\left[-\frac{b}{\sqrt{E}} - \frac{E}{k_B T}\right] dE, \tag{3}$$

where $b = \pi Z_A Z_b \alpha \sqrt{2\mu c^2}$ is proportional to the Sommerfeld parameter of Eq. (2) and k_B is Boltzmann's constant. The maximum of the integrand defines the Gamow peak—the most probable energy for the interactions—while the $\sim 1\sigma$ range around the peak is frequently called the Gamow window.

For the solar reactions of interest, the energy at the Gamow peak is well below the height of the Coulomb potential. The slowly varying $S(E)$ can be expanded as a power series around $E = 0$, with the leading term being $S(0)$ and with corrections given by derivatives taken at $E = 0$,

$$S(E) \simeq S(0) + S'(0)E + \frac{S''(0)}{2} E^2 + \cdots. \tag{4}$$

Most of the results presented in this review will be given in terms of $S(0)$ and its derivatives.

For most of the nuclear reactions studied here, the notation S_{ij} is adopted, where i and j are the mass numbers of the projectile and the target nuclei, respectively. A summary of SF III reactions and recommended astrophysical S factors is presented in Table I. Finally, we provide a short list of

TABLE I. List of nuclear reactions reviewed in SF III. Denoting the astrophysical S factor by S_{ij}, its value at zero energy $S(0)$ is given along with, where applicable, derivatives parametrized in Eq. (4). See the cited sections for uncertainties, higher precision values, and detailed discussions.

Reaction	S_{ij}	$S(0)$ (MeV b)	$S'(0)$ (b)	$S''(0)$ (MeV^{-1} b)	Section
^{1}H$(p, e^+\nu)^2$H	S_{11}	4.09×10^{-25}	4.5×10^{-24}	9.9×10^{-23}	III
^{2}H$(p,\gamma)^3$He	S_{12}	2.03×10^{-7}	See the text		IV
^{3}He$(^3$He$, 2p)^4$He	S_{33}	5.21	−4.90	22.42	V
^{3}He$(\alpha,\gamma)^7$Be	S_{34}	5.61×10^{-4}	-3.03×10^{-4}	⋯	VI
^{3}He$(p, e^+\nu)^4$He	S_{hep}	8.6×10^{-23}	⋯	⋯	VII
^{7}Be$(p,\gamma)^8$B	S_{17}	2.05×10^{-5}	⋯	⋯	IX
^{14}N$(p,\gamma)^{15}$O	S_{114}	1.68×10^{-3}	⋯	⋯	X F
^{12}C$(p,\gamma)^{13}$N	S_{112}	1.44×10^{-3}	2.71×10^{-3}	3.74×10^{-2}	XI A 1
^{13}C$(p,\gamma)^{14}$N	S_{113}	6.1×10^{-3}	1.04×10^{-2}	9.20×10^{-2}	XI A 2
^{15}N$(p,\gamma)^{16}$O	S^{γ}_{115}	4.0×10^{-2}	1.07×10^{-1}	1.84	XI B 1
^{15}N$(p,\alpha)^{12}$C	S^{α}_{115}	73	3.37×10^{2}	1.32×10^{4}	XI A 3
^{16}O$(p,\gamma)^{17}$F	S_{116}	1.09×10^{-2}	-4.9×10^{-2}	3.11×10^{-1}	XI B 2
^{17}O$(p,\gamma)^{18}$F	S_{117}	4.7×10^{-3}	⋯	⋯	XI B 3
^{18}O$(p,\gamma)^{19}$F	S_{118}	2.30×10^{-2}	⋯	⋯	XI C 1
^{20}Ne$(p,\gamma)^{21}$Na	S_{120}	6.78	⋯	⋯	XI D 1
^{21}Ne$(p,\gamma)^{22}$Na	S_{121}	$\approx 2.0 \times 10^{-2}$	⋯	⋯	XI D 2
^{22}Ne$(p,\gamma)^{23}$Na	S_{122}	0.415	⋯	⋯	XI D 3
^{23}Na$(p,\gamma)^{24}$Mg	S_{123}	1.80×10^{-2}	0	0	XI D 4

abbreviations that are used throughout the review in the List of Symbols and Abbreviations.

C. Scope and structure

In the Sun, the primary mechanism for the conversion of four protons into ^{4}He is the pp chain of Fig. 1, during which two charge-changing weak interactions take place, each converting a proton into a neutron with the emission of a neutrino. The pp chain consists of three main branches, pp I, pp II, and pp III. These branches are distinguished by their dependence on the solar core temperature and by the neutrinos they produce, with the pp, ^{7}Be, and ^{8}B neutrinos serving as "tags" for the pp-I, pp-II, and pp-III chains, respectively. The SSM predicts that the fluxes of pp, ^{7}Be, and ^{8}B neutrinos have an approximate relative temperature scaling of $\sim 1 : T_c^{10} : T_c^{22}$, where T_c is the solar core temperature (Haxton, 1995). By the mid-1990s, solar neutrino experiments had established that the measured fluxes differed significantly from this expected pattern. This contributed to growing expectations that new neutrino physics might be the solution of the solar neutrino problem. It also was an important motivation for Adelberger *et al.* (1998), as errors in the nuclear physics of the pp chain could distort the relationship between the various fluxes.

The pp chain accounts for 99% of solar hydrogen burning and is the main focus of this review. The remaining 1% is generated through the CNO-I cycle; see Fig. 2. Motivated in part by Borexino's recent success in measuring the flux of solar CN neutrinos, this review also considers in more detail than past solar fusion reviews the reactions driving hydrogen burning in stars more massive than the Sun.

The review is structured as follows. Section II begins with a summary of past solar neutrino experiments, highlighting some of the open questions that remain. It discusses the second-generation experiments Super-Kamiokande, the Sudbury Neutrino Observatory, and Borexino that contributed to the resolution of the solar neutrino problem. It also describes Hyper-Kamiokande, SNO+, the Jiangmen Underground Neutrino Observatory (JUNO), and the Deep Underground Neutrino Experiment (DUNE), new detectors at various stages of construction.

The cross section of the driving reaction of the pp chain, $^1\mathrm{H}(p, e^+\nu)^2\mathrm{H}$, is too small to be measured and thus must be taken from theory. This important reaction is reviewed in Sec. III. With the exception of the minor hep branch, all other reactions and decays have been studied in laboratories, with measurements then combined with theory to predict rates under solar conditions. The $^2\mathrm{H}(p,\gamma)^3\mathrm{He}$, $^3\mathrm{He}(^3\mathrm{He}, 2p)^4\mathrm{He}$, and $^3\mathrm{He}(\alpha,\gamma)^7\mathrm{B}$ reactions are reviewed in Secs. IV, V, and VI, respectively. The hep reaction is reviewed in Sec. VII, and the electron-capture reactions on pp and ^{7}Be are discussed in Sec. VIII. The $^7\mathrm{Be}(p,\gamma)^8\mathrm{B}$ reaction responsible for the high-energy neutrinos measured in Super-Kamiokande is treated in Sec. IX.

The CNO-I cycle is a modest contributor to solar energy generation, accounting for about 1% of solar hydrogen burning. It is a potentially important probe of core metallicity, as its hydrogen burning is catalyzed by the Sun's primordial C and N; see Sec. XI.

Higher-temperature pathways, however, are of great importance in more massive stars. The associated nuclear reactions are an increasingly important focus of low-energy nuclear astrophysics facilities. Many of the contributing reactions have been remeasured. That progress is reviewed in Sec. XI.

Charged-particle nuclear reactions occurring at energies below the Coulomb barrier are affected by electron screening, the shielding of the nuclear charge by electrons. Because of their much different atomic environments, laboratory reactions and those occurring in the solar plasma are affected in distinct ways. Section XII describes the current status of efforts to account for these differences when solar cross sections are extracted from laboratory measurements.

The energy transport inside the radiative zone is affected by the metals[4] that were incorporated into the Sun when it first formed. While metals constitute less than 2% of the Sun by mass, they play an outsized role in determining the opacity. Few of the needed radiative opacities have been measured, and the conditions under which measurements are made typically are not identical to those in the Sun. Section XIII describes the current state of the art and discusses connections between opacities and solar composition that have complicated efforts to resolve the solar metallicity problem.

Much of the progress made in constraining the reactions of the pp chain and CNO-I cycles has been possible thanks to new laboratories and the facilities that they host. The underground Laboratory for Underground Nuclear Astrophysics (LUNA) laboratory is a prominent example (Broggini *et al.*, 2018). Section XIV describes the capabilities of selected laboratories involved in the measurements reviewed here.

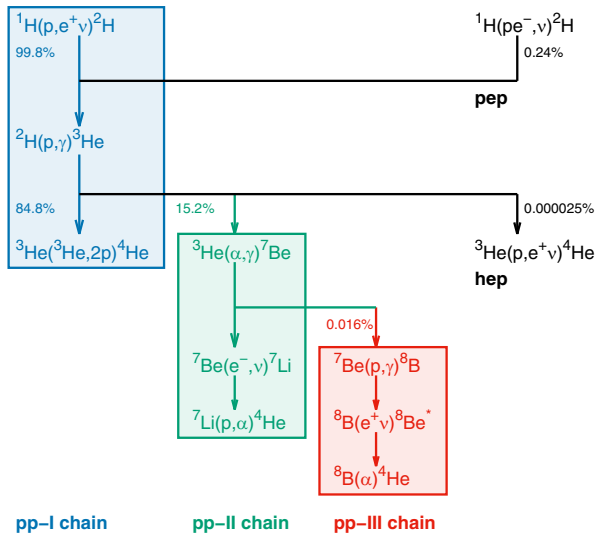

FIG. 1. Nuclear reactions of the proton-proton (pp) chain. The percentage branchings are applicable for the solar composition of Magg *et al.* (2022).

[4]In this review we follow the astrophysical terminology in which *metals* refer to all chemical elements except for the two lightest ones, hydrogen and helium.

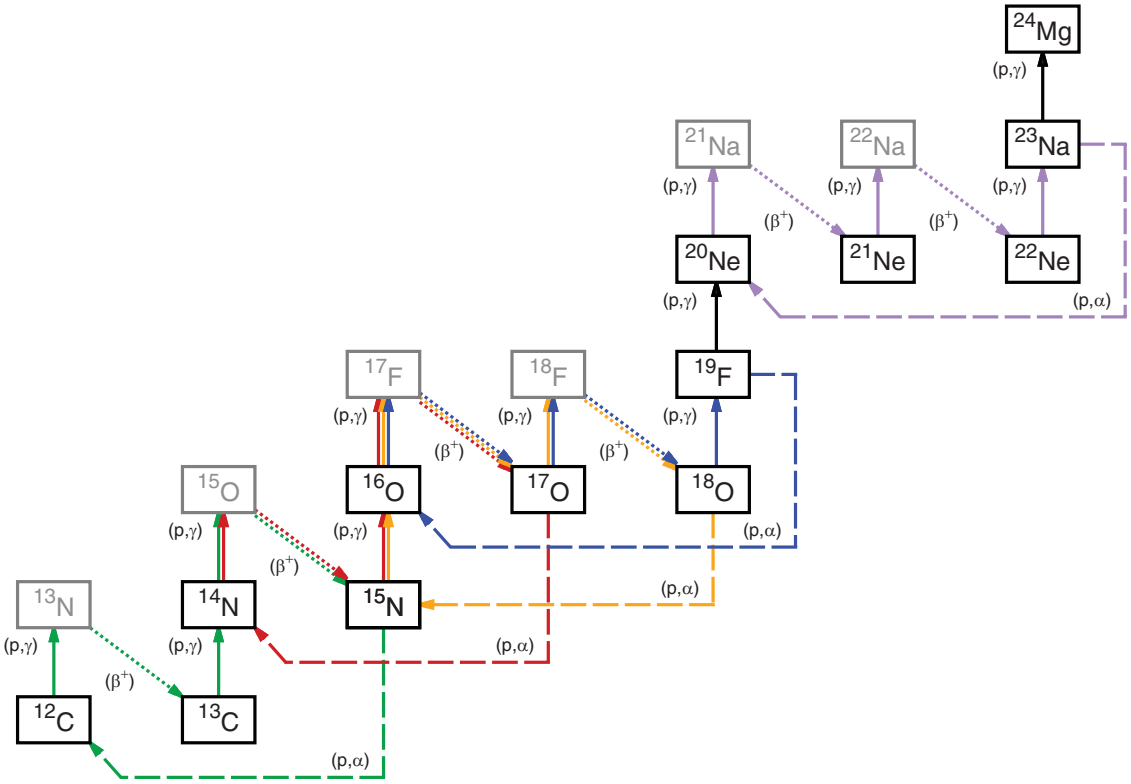

FIG. 2. Nuclear reactions of the CNO-I (green line), CNO-II (red line), CNO-III (orange line), CNO-IV (blue line), and Ne-Na (purple line) cycles. Other reactions reported in this review are also present (in black). For visual aid, (p,γ) reactions are styled using full arrows, while (p,α) reactions use dashed-line arrows. Gray isotopes are short lived and quickly (β^+) decay (dotted arrows), resulting in $e^+ + \nu_e$ emissions.

II. SOLAR NEUTRINO OBSERVATIONS

Solar neutrinos offer a unique toolbox for probing both the fundamental properties of these elusive particles and their interactions with matter, as well as understanding their source: the fusion reactions that power the Sun. The original motivation for observations of solar neutrinos was precisely the hope to probe solar fusion. The first successful experiment beginning in 1967 at the Homestake mine (Cleveland *et al.*, 1998) offered the surprising result of a neutrino flux suppressed to approximately one-third of the expectation. The intervening years have seen a remarkable series of experimental efforts, leading to the resolution of the solar neutrino problem and the confirmation of neutrino oscillations (Fukuda *et al.*, 1998a; Ahmad *et al.*, 2001, 2002a, 2004; Eguchi *et al.*, 2003). These high-precision flux and spectral measurements mapped out the details of solar fusion, probed the structure of the Sun, and demonstrated (together with atmospheric neutrino measurements) that neutrinos have masses and mix. Table II lists the pp-chain and CNO-cycle neutrino sources, their end point (β decay) or line (electron-capture) energies E_ν, and the predicted SSM fluxes.

A. Open questions

The solar neutrino spectrum has been measured for energies above 233 keV, with some fluxes determined to a precision equivalent to or better than theoretical predictions. However, improved measurements can offer further insight on several aspects. For instance, more precise determinations of the fluxes of neutrinos from the CNO cycle (see Fig. 2) could

TABLE II. Solar neutrino sources, energies and SSM flux predictions. All β-decay sources produce continuous spectra, while the pep and ^{7}Be electron-capture sources produce line spectra. The fluxes are taken from the SSM calculations of Herrera and Serenelli (2023), computed with the nuclear reaction rates shown in Table I, for the compositions of GS98 (high Z) (Grevesse and Sauval, 1998), AAG21 (low Z) (Asplund, Amarsi, and Grevesse, 2021), and MB22p (high Z) (Magg *et al.*, 2022), with associated uncertainties indicated.

Source	E_ν (MeV)	GS98	AAG21	MB22p	Units (cm^{-2} s^{-1})
pp	≤ 0.420	5.96 (0.6%)	6.00 (0.6%)	5.95 (0.6%)	10^{10}
pep	1.442	1.43 (1.1%)	1.45 (1.1%)	1.42 (1.3%)	10^{8}
hep	≤ 18.77	7.95 (31%)	8.16 (31%)	7.93 (30%)	10^{3}
^{7}Be	0.862[a] 0.384[b]	4.85 (7.4%)	4.52 (7.3%)	4.88 (8.1%)	10^{9}
^{8}B	≲15	5.03 (13%)	4.31 (13%)	5.07 (15%)	10^{6}
^{13}N	≤ 1.198	2.80 (16%)	2.22 (13%)	3.10 (15%)	10^{8}
^{15}O	≤ 1.732	2.07 (18%)	1.58 (16%)	2.30 (18%)	10^{8}
^{17}F	≤ 1.738	5.35 (20%)	3.40 (16%)	4.70 (17%)	10^{6}

[a]90% of the ^{7}Be neutrino flux.
[b]10% of the ^{7}Be neutrino flux.

determine the contemporary abundances of N and O in the solar core (Castro, Vauclair, and Richard, 2007; Serenelli, Haxton, and Peña-Garay, 2011; Kunitomo, Guillot, and Buldgen, 2022). While these abundances differ significantly from the primordial values that are input into the SSM—the primordial abundances are altered by out-of-equilibrium CNO-cycle burning that occurs in the early Sun (Roxburgh, 1985)—this burning redistributes the C, N, and O but does not alter the net number of such nuclei. Consequently, CNO neutrino flux measurements might allow one to experimentally address the subsequently discussed solar composition problem.

Solar neutrino flux measurements can also constrain physical processes in stars such as chemical mixing. The fluxes are sensitive to solar and stellar model inputs, including the radiative opacities; see Sec. XIII. Measurements of the neutrino fluxes from ^{8}B and ^{7}Be can offer a handle on the temperature of the solar core and other environmental factors (Bahcall and Ulmer, 1996).

A measurement of the pp flux with percent-level precision would provide a test of the luminosity constraint, further probing solar power generation mechanisms (Bahcall, 2002; Vescovi *et al.*, 2021). The one branch of the pp chain that remains undetected, the hep flux, has both the highest energy and also the lowest flux of neutrinos from the Sun. The spectrum extends beyond that of the ^{8}B neutrinos, offering a small window for unequivocal observation. Limits have been placed on this flux (Aharmim *et al.*, 2020), but a definitive observation will likely require a large, next-generation detector such as Hyper-Kamiokande (Hyper-K) (Abe *et al.*, 2018) or DUNE (Capozzi *et al.*, 2019).

Finally, the observation of monochromatic neutrinos produced by electron-capture reactions on ^{13}N, ^{15}O, and ^{17}F (which we refer to as ecCNO neutrinos) (Bahcall, 1990; Stonehill, Formaggio, and Robertson, 2004; Villante, 2015) could be rewarding in terms of physical implications. Indeed, they can be used as probes of the metallicity of the solar core. Moreover, they provide a measure of the electron neutrino survival probability at specific neutrino energies $E_\nu \sim 2.5$ MeV within the broad transition region between vacuum- and matter-enhanced oscillations, where currently we have no constraints. This would constitute a new test of the large-mixing-angle Mikheyev-Smirnov-Wolfenstein (MSW) flavor oscillation solution. The detection of this subdominant component of the CNO cycle is extremely difficult, but it could be within reach of future large ultrapure liquid scintillator detectors (Villante, 2015).

Solar neutrinos provide an opportunity to understand the interaction of neutrinos with matter. The effect of MSW oscillations has a significant impact on the observed solar neutrino spectrum: with vacuum oscillation dominating at low energy, below approximately 1 MeV, where the survival probability is roughly one-half, while matter effects further suppress the flux to a survival probability of roughly one-third above approximately 5 MeV. The transition region between these two regimes offers an extremely sensitive probe of the details of the interactions of neutrinos with matter, including the potential to search for new physics such as sterile neutrinos or nonstandard interactions by looking for distortions to the expected spectral shape (Agarwalla *et al.*, 2020a; Bhupal Dev *et al.*, 2019; Coloma *et al.*, 2023).

The same theory of matter effects predicts a small regeneration of electron neutrinos during the nighttime as they propagate through the bulk of Earth. This so-called day-night effect has been sought after by both Super-Kamiokande (Super-K) and the Sudbury Neutrino Observatory (SNO) (Ahmad *et al.*, 2002b; Renshaw *et al.*, 2014), but a significant observation is still limited by statistics. Future data from Hyper-Kamiokande or DUNE may be needed to confirm our understanding of this prediction of the MSW effect.

The slight tension between measurements of the mass splitting parameters Δm^2_{12} in solar neutrino experiments and terrestrial data sensitive to the same parameter from the KamLAND reactor experiment has now disappeared with the addition of new data on day-night effects and spectral shapes (Capozzi *et al.*, 2018; Esteban *et al.*, 2020). Further tightening of the oscillation parameters can be expected from JUNO, which will obtain highly precise data on both the solar mass splitting and the mixing angle (An *et al.*, 2016).

1. The solar composition problem

Solar photospheric abundances, determined with spectroscopic techniques, are a fundamental input for the construction of SSMs, but they are also used as input to nearly all models in astrophysics, including stellar evolution, protoplanetary disks, and galactic chemical evolution. In the past two decades, the development of three-dimensional radiation hydrodynamic models of the solar atmosphere (Asplund *et al.*, 2000; Ludwig *et al.*, 2009) and of techniques to study line formation under nonlocal thermodynamic conditions (Asplund, 2005), together with improved descriptions of atomic properties [for example, transition strengths (Bergemann *et al.*, 2021; Magg *et al.*, 2022)], have led to a significant revision of solar abundances. Initial results based on these more sophisticated methods favored a markedly lower solar metallicity (Asplund *et al.*, 2009), particularly in the CNO elements, than obtained in the 1990s from older techniques (Grevesse and Noels, 1993; Grevesse and Sauval, 1998).

Recently, two groups have revisited the solar photospheric abundances using modern methods (Asplund, Amarsi, and Grevesse, 2021; Magg *et al.*, 2022). While Asplund, Amarsi, and Grevesse (2021) obtained results consistent with their previous findings, Magg *et al.* (2022) found an O abundance intermediate between that of Asplund's group and those from the 1990s, in agreement with another 3D-based determination by Caffau *et al.* (2011). Magg *et al.* (2022) found higher C and N abundances and, indirectly, a higher Ne abundance due to the larger Ne to O ratio measured in the solar corona (Young, 2018). This leads to a combined metal-to-hydrogen ratio that is by chance comparable to those from Grevesse and Noels (1993) and Grevesse and Sauval (1998), albeit with a different mixture of elements.

Considering that uncertainties in element abundances are difficult to quantify, it has become customary to consider two canonical sets of abundances, which we refer to as high

metallicity (HZ) and low metallicity (LZ) solar admixtures. See Vinyoles *et al.* (2017) for SSM reference values. In this context the new solar abundance determinations by Asplund, Amarsi, and Grevesse (2021) fall into the LZ category, while those from Magg *et al.* (2022) are HZ. Solar models employing the LZ abundances fail to reproduce most helioseismic probes of solar properties. This disagreement constitutes the so-called solar composition problem (Basu and Antia, 2004; Bahcall *et al.*, 2005; Delahaye and Pinsonneault, 2006), which has defied a complete solution. All proposed modifications to physical processes in SSMs offer, at best, only partial improvements in some helioseismic probes; see Guzik, Watson, and Cox (2005), Castro, Vauclair, and Richard (2007), Basu and Antia (2008), Guzik and Mussack (2010), and Serenelli, Haxton, and Peña-Garay (2011). The same conclusions are obtained with SSMs computed with the newest LZ (Asplund, Amarsi, and Grevesse, 2021) and HZ abundances (Magg *et al.*, 2022), as discussed by the researchers. An alternative possibility is to consider modifications to the physical inputs of SSMs at the level of the constitutive physics, radiative opacities in particular. This is possible because most helioseismic probes do not depend directly on the solar composition but instead depend on the radiative opacity profile in the solar interior, i.e., on the combination of solar composition and atomic opacities; see Sec. XIII. The same can be said for solar neutrinos from the pp chain. Early work (Montalbán *et al.*, 2004; Bahcall, Serenelli, and Basu, 2005) had already suggested that a localized increase in opacities could solve—or at least alleviate—the disagreement of low-Z solar models with helioseismology, and Christensen-Dalsgaard *et al.* (2009) and Villante (2010) showed that a tilted increase in radiative opacities with a few-percent increase in the solar core and a larger (15%–20%) increase at the base of the convective envelope could lead to LZ SSMs that would satisfy helioseismic probes equally as well as HZ SSMs.

The degeneracy between solar composition and opacities can be broken using CNO solar neutrinos, for example, following the methodology developed by Haxton and Serenelli (2008). Such a study was recently carried out by the Borexino Collaboration (Agostini *et al.*, 2020c; Appel *et al.*, 2022; Basilico *et al.*, 2023). The Borexino measurement of the CNO-I-cycle neutrino flux (the ^{13}N and ^{15}O fluxes) were used to determine the C + N core abundance. Results show an $\sim 2\sigma$ tension with LZ metallicity determinations, but the results are in better agreement with HZ mixtures. While the error budget is presently dominated by the uncertainty of the Borexino CNO neutrino measurement, a significant contributor to the error ($\sim$10%) is nuclear owing to uncertainties in S_{114}, S_{34}, and S_{17}. The interpretation of future improved CNO neutrino measurements will be impacted unless these nuclear physics uncertainties are reduced.

Recently, Gonzalez-Garcia *et al.* (2024) presented a new global determination of all solar neutrino fluxes using all available experimental data, including the latest phases of Borexino. Results from this global analysis are in line with those from Borexino, although the added ^{13}N and ^{15}O fluxes are about 10% lower than the Borexino result alone. A comparison of the solar fluxes with SSM calculations (Herrera and Serenelli, 2023) shows that HZ SSMs are in better agreement with solar neutrino fluxes than the LZ SSMs, pointing toward a C + N solar core abundance that is consistent with HZ abundances. However, the discrimination that solar neutrino fluxes can offer between solar compositions is, at most, of the order of 2σ. [See Table 2 of Gonzalez-Garcia *et al.* (2024).]

Helioseismology also offers the potential to determine the total solar metallicity, i.e., without disentangling individual element abundances, independent of opacities. This relies on using the so-called adiabatic index Γ_1, which deviates from $5/3$ in regions of partial ionization. The underlying technique has been used widely to determine the helium abundance in the solar envelope and has also been extended to determine solar metallicity. Attempting the latter is difficult because the imprint of partial ionization of metals is subtle. Previous work along these lines (Antia and Basu, 2006) found an overall metallicity consistent with HZ abundances, but new work claims to favor LZ values (Buldgen *et al.*, 2024). While this method depends weakly on radiative opacities, the abundance determination is degenerate with the equation of state. Independent confirmation of these results would be desirable. In short, the controversy related to the solar composition is far from being resolved, with different indicators currently showing contradictory results.

2. The gallium anomaly

With the aid of intense radioactive sources of ^{51}Cr and ^{37}Ar, tests have been made of the rate of production of ^{71}Ge by neutrino interactions on ^{71}Ga, the basis of radiochemical measurements of the low-energy solar neutrino flux. Initial experiments showed lower rates than expected, with interesting but inconclusive statistical precision. The BEST experiment confirmed this anomaly at more than 4σ (Barinov *et al.*, 2018, 2022a, 2022b). Many possible explanations have been explored, but for each one there are contradictions (Akhmedov and Smirnov, 2022; Brdar, Gehrlein, and Kopp, 2023; Giunti *et al.*, 2023; Krueger and Schwetz, 2023). A sterile-neutrino explanation is disfavored (Giunti *et al.*, 2022; Goldhagen *et al.*, 2022), particularly because of conflict with solar neutrino limits (see Fig. 3), as well as cosmological bounds (Hagstotz *et al.*, 2021).

The sterile-neutrino contribution to the solar flux is fundamentally limited by the luminosity constraint, namely, that the Sun's total energy output is the result of nuclear reactions that produce neutrinos, whether active or sterile. If precise neutral-current data were available across the solar spectrum, a completely model-independent limit on a possible sterile component could be determined. The present neutral-current data at low energies (from Borexino) are imprecise but can be supplemented by much more precise charged-current data together with three-flavor oscillation physics. Even better limits, at the cost of some model dependence, can be obtained with fits of experimental data to solar models, as shown in Fig. 3, as well as in Fig. 1 of Goldhagen *et al.* (2022).

The precisely known rate of electron capture on ^{71}Ge to ^{71}Ga, for which the half-life is 11.43(3) d (Hampel and Remsberg, 1985), places an important constraint on the

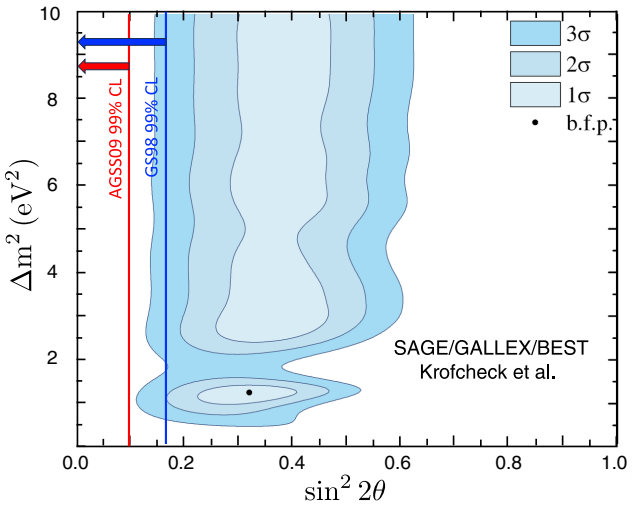

FIG. 3. Contours shown are the sterile-neutrino interpretation of the Ga anomaly of Elliott *et al.* (2023). The limits at the 99% confidence level (CL) on the mixing angle from solar neutrinos of Goldhagen *et al.* (2022) are indicated on the left for two solar models, GS98 and AGSS09, and essentially exclude the indicated sterile-neutrino space.

neutrino absorption rate (Elliott *et al.*, 2023; Giunti *et al.*, 2023). The half-life has now been remeasured by two groups, Norman *et al.* (2024) and Collar and Yoon (2023), whose measurements yielded values of 11.468(8) and 11.46(4) d that are consistent with the previous determination and increase the precision. The allowed matrix element that governs neutrino capture to the ground state of ^{71}Ge can be extracted to a precision of ∼1% from the electron-capture rate. The ground-state transition by itself generates a significant anomaly: inclusion of the excited-state contributions doubles the effect. In Appendix A we describe some of the details of both the 1997 extraction of the allowed (Gamow-Teller) strength by Bahcall (1997) and the recent updates of Elliott *et al.* (2023) and Elliott, Gavrin, and Haxton (2024).

Elliott *et al.* (2023) and Elliott, Gavrin, and Haxton (2024) found the ground-state cross section for absorbing ^{51}Cr neutrinos is 2.5% lower than Bahcall's value. They included the contributions of weak magnetism and radiative corrections, which were shown to be sub-1% effects. An improved extraction of the ∼6% excited-state contribution to neutrino absorption was performed using data from forward-angle (p, n) scattering. This led to a slight increase in that contribution relative to the results of Bahcall (1997), thereby reducing the aforementioned 2.5% difference by about half for the total ^{51}Cr and ^{37}Ar capture cross sections.

The procedures followed by Elliott *et al.* (2023) and Elliott, Gavrin, and Haxton (2024) could be extended to the solar neutrino ^{71}Ga capture cross section, including the contribution from the high-energy ^{8}B neutrinos. That has not been done but, as noted in Appendix A, could help resolve the small discrepancies noted there.

Results from the SAGE and GALLEX/GNO experiments remain part of the solar neutrino database used in various global fits to neutrino parameters. A resolution of the anomaly that emerged from BEST and the four gallium detector calibration experiments is important, as it would increase confidence in these data.

3. The ^{8}B neutrino spectrum

The neutrino spectrum from ^{8}B, extending to approximately 17 MeV, has been the most accessible part of the solar neutrino spectrum (Abe *et al.*, 2016; Aharmim *et al.*, 2020), playing an important role in disclosing the physics of neutrino oscillation and testing the SSM. Knowing it with precision, particularly at the high-energy end, has renewed interest in the context of observing the hep neutrinos (Aharmim *et al.*, 2006, 2020), which could be accessible with future observatories (Askins *et al.*, 2022).

Adelberger *et al.* (2011) decided to recommend the spectrum calculated by Winter *et al.* (2003, 2006) and Winter (2007) based on their measurement of the alpha spectrum from ^{8}B. This spectrum showed excellent agreement with an independent experiment (Bhattacharya, Adelberger, and Swanson, 2006). Both radiative and recoil-order corrections were included by Winter *et al.* The radiative corrections are relatively small owing to a cancellation between the real and virtual contributions (Batkin and Sundaresan, 1995). The recoil-order corrections are dominated by the weak magnetism part, which has been deduced from measurements of the analog electromagnetic decays (de Braeckeleer *et al.*, 1995).

Since then, three additional measurements (Kirsebom *et al.*, 2011; Roger *et al.*, 2012; Longfellow *et al.*, 2023) of the ^{8}B β-decay alpha spectrum have been performed. All three find that the peak of the alpha spectrum appears about 20 keV lower than determined by Winter *et al.* Overall, these new measurements yield differences in the ^{8}B neutrino spectrum of $\lesssim$5% below $E_\nu = 15$ MeV, the energy above which the ^{8}B contribution becomes small compared to the hep component. Figure 4 shows the ^{8}B spectral uncertainties on the scale of the hep spectrum. With resolution effects considered, it will be

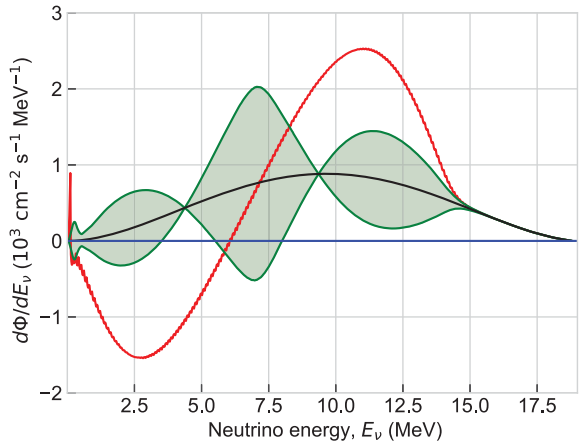

FIG. 4. The hep spectrum is in black, and the uncertainties in ^{8}B from Longfellow *et al.* (2023) span the region between the green lines. The red line indicates the difference between the ^{8}B spectra deduced by Longfellow *et al.* and Winter *et al.* (2006). The hep spectrum is used here as a convenient metric for the size of the uncertainties in the ^{8}B spectrum.

difficult to extract the hep flux from solar neutrino measurements without further reduction in ^{8}B uncertainties.

In producing a recommendation for the ^{8}B neutrino spectrum, we considered the following:

(1) Apparently, the uncertainty estimations for the neutrino spectrum of Roger *et al.* (2012) are not quite correct. Longfellow *et al.* (2023) showed that the uncertainty due only to the weak magnetism part, for which all researchers follow similar prescriptions, is larger in the 0–12 MeV range than the overall uncertainty estimated by Roger *et al.* We estimated the uncertainties due to the weak magnetism term only and found agreement with those of Longfellow *et al.*

(2) All three of the recent efforts (Kirsebom *et al.*, 2011; Roger *et al.*, 2012; Longfellow *et al.*, 2023) used detectors (Si strip) more complicated than those used by Winter *et al.* (a Si surface barrier detector). The strip detectors allow for better position resolution and reduced beta summing. However, for detection from sources external to the detectors (as opposed to detection from sources implanted deep into a detector), the complicated pattern of dead layers needs to be measured and taken into consideration for accurate calibrations. Effects of partial charge collection between strips are also significant. The effects are different for a calibration source than for the emission from ^{8}B trapped as an ion.

Based on these considerations, we recommend the spectrum of Longfellow *et al.* (2023) but suggest that conclusions sensitive to the choice of ^{8}B neutrino spectrum, such as evidence for hep neutrinos, should be evaluated using both the Winter *et al.* and the Longfellow *et al.* spectra.

Given the importance of the weak magnetism contributions, it would be good to have a new experiment with reduced uncertainties that could be compared directly to the results of de Braeckeleer *et al.* (1995). Recoil-order effects in the $A = 8$ system were most recently measured by Sumikama *et al.* (2011), who made use of the alignment-β correlation. Using combinations of their measurements and $\beta - \alpha$ correlation data from McKeown, Garvey, and Gagliardi (1980), they were able to extract some of the recoil-order matrix elements. Calculations of these matrix elements in the symmetry-adapted no-core shell model were recently performed by Sargsyan *et al.* (2022). The comparison to the experimentally derived matrix elements of McKeown, Garvey, and Gagliardi (1980), de Braeckeleer *et al.* (1995), and Sumikama *et al.* (2011) is not straightforward, because the experiments quote averages over the entire β spectrum as opposed to fits for each of the four levels used in the calculation. A more detailed comparison of theory to experiment that takes into account the averaging would be helpful. An additional point of comparison that has been used previously is the β spectrum from ^{8}B (Bahcall *et al.*, 1996). An experiment with improved statistics and systematics that extends over the full range of β energies would be useful. The existing data from Napolitano, Freedman, and Camp (1987) are in good agreement with the α spectrum of Winter *et al.* But, given the apparent 20 keV difference that the newer, previously described α-spectrum experiments report, it would be beneficial to have a modern β-spectrum measurement that is specifically designed to address this difference.

B. Experimental program on solar neutrinos

A broad range of technology can be used to interrogate solar neutrinos. Radiochemical experiments utilizing chlorine and gallium played a crucial role in the early days of the solar neutrino problem. Large monolithic detectors have achieved great success in real-time measurements—from the water Cherenkov detectors such as Kamiokande, SNO, and Super-K, which could use the unique topology of Cherenkov light to point back to the neutrinos' origin, to liquid scintillator detectors such as KamLAND and Borexino, whose high light yield and low threshold allow for precision spectroscopy.

1. Super-Kamiokande and Hyper-Kamiokande

The first real-time detection of solar neutrinos was achieved by the Kamiokande experiment (Hirata *et al.*, 1989), which detected the neutrinos via elastic scattering of electrons, a process in which the outgoing electron's direction is highly correlated to that of the incoming neutrino. This allowed Kamiokande to directly point back to the neutrinos' origin: the Sun. The successor experiment, Super-Kamiokande, is a 50 kton volume of pure water, surrounded by over 10 000 photon detectors, which has achieved an unparalleled program of neutrino observations and other physics over its several decades of operation. This program has included the highest-precision measurement of the elastic-scattering signal from solar neutrino interactions, as well as sensitive searches for the day-night distortions of the spectral shape (Abe *et al.*, 2016). Now filled with a gadolinium additive to enhance neutron capture, Super-K's primary current focus is the search for the diffuse supernova neutrino background (DSNB) via inverse β decay (Harada *et al.*, 2023). It also continues its atmospheric neutrino program: Super-K measurements made 25 years ago demonstrated that the neutrino oscillations were responsible for the puzzling zenith-angle dependence of this flux (Fukuda *et al.*, 1998b).

In parallel to ongoing operation of Super-K, an even larger sister project is under construction. At over 250 kton in total mass and with improved light collection relative to Super-K, Hyper-K will impact statistics-limited searches the involve the higher-energy ^{8}B solar neutrinos, including day-night effects, the search for hep neutrinos, and the shape of the ^{8}B neutrino spectrum. After ten years of operations, Hyper-K will reach a sensitivity to day (night) effects that are greater than or approximately equal to 4σ (8σ) given the oscillation parameters deduced from reactor (solar) experiments. Hyper-K will serve as the far detector for JPARC's long-baseline neutrino program.

2. Sudbury Neutrino Observatory and SNO+

SNO's unique use of heavy water as a target medium offered the ability to detect solar neutrinos via two additional interactions besides elastic scattering. In the charged-current interaction an electron neutrino interacts with the neutron in the deuteron, producing an electron and a proton. This

interaction path is sensitive only to electron-flavor neutrinos at the few-MeV energy scale of solar neutrinos, providing a measurement of the pure ν_e flux. SNO also had access to the neutral-current interaction, in which a neutrino of any flavor interacts with the deuteron, breaking it apart into its constituent nucleons. Being equally sensitive to all active flavors, the neutral-current interaction yields a measurement of the total flavor-blind neutrino flux. It was this capability that allowed SNO to resolve the solar neutrino problem, demonstrating that most of the ν_e's produced by the Sun were arriving at Earth in a different flavor state (Ahmad *et al.*, 2001, 2002a, 2004).

SNO ceased data taking in 2006. Analysis of the dataset has continued and has produced a number of new results, including constraints on nonstandard effects such as Lorentz violation and neutrino decay (Aharmim *et al.*, 2018, 2019a), limits on the fluxes of hep neutrinos and the DSNB (Aharmim *et al.*, 2020), and neutron production from cosmogenic muons and atmospheric neutrino interactions (Aharmim *et al.*, 2019b, 2019c).

After decommissioning the detector was repurposed for the SNO+ experiment, in which the target material was replaced with a pure organic liquid scintillator, linear alkyl benzene, loaded with 2.2 g/l of the secondary fluor, diphenyloxazole (PPO). The high light yield of this scintillator, coupled with the location in SNOLAB—at 6 km water equivalent, one of the deepest underground laboratories in the world—and an extremely well-understood detector, allow for a range of high-precision-measurement programs. In a preliminary water phase, SNO+ demonstrated detection of neutron captures on hydrogen (Anderson *et al.*, 2020), an impressive technical achievement in an unloaded water detector; a low-background measurement of ^{8}B solar neutrinos (Anderson *et al.*, 2019b); several searches for invisible modes of nucleon decay (Anderson *et al.*, 2019a; Allega *et al.*, 2022); and detection of antineutrinos from reactors over 200 km away (Allega *et al.*, 2023). The low backgrounds achieved and the detector's demonstrated technical capabilities set the stage for future measurements. In a "partial-fill" stage in which the upper half of the detector was filled with a liquid scintillator while the lower half still contained water, the first demonstration of event-level direction reconstruction was achieved for ^{8}B neutrinos in a scintillator detector (Allega *et al.*, 2024). This was facilitated by a lower loading of PPO at that time, which results in lower scintillation yield and a slower time profile, effectively enhancing the Cherenkov component, which can be leveraged for directional information.

Now fully filled with a liquid scintillator, SNO+ is the deepest, largest operating liquid scintillator detector in the world. The future program will include measurements of several solar neutrino fluxes, as well as the ^{8}B neutrino energy spectrum.

3. Borexino

Water Cherenkov experiments such as Kamiokande, Super-K, and SNO provided the first real-time measurement of solar neutrinos, but their relatively high-energy threshold made them sensitive only to a small fraction of the solar neutrino flux. To study in real time the bulk of solar neutrino emission, a different detector technology was required. The Borexino experiment, located deep underground at the INFN Laboratori Nazionali del Gran Sasso, used an organic liquid scintillator target made of pseudocumene with 1.5 g/l PPO to detect the elastic scattering of solar neutrinos off electrons. The high light yield of the liquid scintillator made it possible to significantly lower the energy threshold, but, given the small signal rate and the lack of a clear signature to separate it from the background (such as the direction indicated by the emission of Cherenkov radiation), the experiment required a long preparatory phase to develop the most advanced techniques to suppress the background, especially the one due to radioactive contamination of the liquid scintillator itself.

The detector's extreme radiopurity was key to its success, and over its 14 years of data taking, ending in October 2021, Borexino proved itself capable of covering the entire solar neutrino spectrum. At the beginning of its data taking in 2007, the level of ^{238}U and ^{232}Th contamination in Borexino were lower than 2×10^{-17} and 7×10^{-18} g/g, respectively (Arpesella *et al.*, 2008), paving the way for the first measurement of the ^{7}Be sub-MeV solar neutrinos, followed by a low-threshold measurement of the ^{8}B flux and a first indication of the *pep* neutrinos. After a purification campaign that further reduced the liquid scintillator contamination, Borexino aimed at improving the accuracy of its results in the measurement of the *pp*-chain solar neutrinos. The flux of neutrinos produced in the *pp* fusion process was first reported by Bellini *et al.* (2014) and later improved, along with all the other fluxes from the *pp* chain, apart from the hep neutrinos (Agostini *et al.*, 2018, 2019, 2020b). The *pp* flux was determined to an uncertainty of 11%, improving the neutrino-based estimate of solar luminosity, while ^{7}Be neutrinos were measured with an uncertainty of 2.7%, half that of the SSM prediction. Furthermore, using the SSM to constrain the flux of CNO neutrinos, the *pep* neutrino signal was established with a significance exceeding 5σ for the first time, and the ^{8}B flux was measured with a threshold as low as 3 MeV.

After completing the investigation of the *pp*-chain neutrinos, Borexino reported the first detection of solar neutrinos produced in the CNO cycle (Agostini *et al.*, 2020c), demonstrating directly that this mode of hydrogen burning operates in stars. Profiting from a larger exposure and a better understanding of the radioactive backgrounds enabled by the unprecedented thermal stability of the detector, Borexino further improved its measurement of the CNO neutrino flux (Appel *et al.*, 2022; Basilico *et al.*, 2023), where the new CNO result was used in combination with existing solar neutrino results to probe solar composition.

Borexino's physics program was not limited to solar neutrinos: its outstanding radiopurity made it a excellent detector for geoneutrinos (Agostini *et al.*, 2020a) and for searches for various rare processes. Borexino data were used to constrain exotic properties of neutrinos, such as their magnetic moments (Agostini *et al.*, 2017) and nonstandard interactions with matter (Agarwalla *et al.*, 2020a).

4. JUNO

JUNO (Adam *et al.*, 2015) is a large liquid scintillator detector currently under construction in an underground laboratory with a vertical overburden of about 650 m (roughly

1800 m water equivalent) in Jiangmen city in southern China. JUNO is located 52.5 km from two nuclear power plants, a baseline optimized for JUNO's primary goal, the determination of the neutrino mass ordering. To achieve this, JUNO requires a large target mass (20 kton) and excellent energy resolution, attributes also important in solar neutrino detection. The relatively shallow overburden limits the solar neutrino program owing to cosmogenic activity, but the low threshold and large detector mass may allow measurements of the day-night effects, nonstandard neutrino interactions affecting the ^{8}B spectral shape, and ^{7}Be neutrinos, as well as providing a new solar determination of Δm^2_{12}. JUNO's reactor data will constrain Δm^2_{12} to extremely high precision, allowing comparisons between the solar and reactor determinations of this parameter. To the extent that oscillation effects can be treated with greater confidence, the connections between solar neutrino flux measurements and the solar fusion reactions generating those fluxes will be sharpened (An *et al.*, 2016).

5. DUNE

As recommended in the 2023 P5 report (Particle Physics Project Prioritization Panel, 2023), the DUNE Collaboration seeks to construct two 10-kton fiducial liquid argon time projection chambers (LArTPCs) deep underground in the Homestake mine in South Dakota (Acciarri *et al.*, 2016). A third LArTPC will follow in phase II, along with other upgrades. The newly developed Sanford Underground Research Facility (SURF) offers 4800 m water equivalent overburden and will form the far site for a long-baseline neutrino program utilizing a high-energy neutrino beam directed from Fermilab to SURF. The DUNE LArTPC detectors may be sensitive to measurements of the high-energy solar neutrinos via charged-current interactions on argon, which offers good precision on the spectral shape and thus the potential to measure day-night effects (Capozzi *et al.*, 2019). The solar neutrino program at DUNE is limited primarily by backgrounds (the detector is optimized for GeV-scale physics) and energy thresholds. Multiple technologies are under consideration for a fourth detector module, with the motivation of expanding the physics program, including improved sensitivity to solar neutrinos. Use of underground argon, or alternative technologies such as organic or water-based scintillators, could preserve the long-baseline neutrino sensitivity while also opening up a rich program of low-energy physics.

6. Future prospects

A hybrid detector that could utilize both Cherenkov and scintillation light simultaneously could achieve unprecedented levels of particle and event identification and hence background rejection (Alonso *et al.*, 2014). The Cherenkov signature offers directional information, while the high light yield scintillation offers precision energy and vertex reconstruction. A full waveform analysis of detected light offers even more information, based on the pulse shape of the scintillation, which is subject to species-dependent quenching effects, and the impact of the Cherenkov threshold. As a result, both the shape of the waveform and the ratio of the two signals will differ for different particle types. A full-scale detector utilizing novel scintillators along with fast and spectrally sensitive photon detectors, such as the proposed THEIA experiment (Askins *et al.*, 2020) and the Jinping detector (Beacom *et al.*, 2017) could achieve percent-level precision on the CNO neutrino flux and improve precision across the suite of solar neutrino measurements, such as the ^{8}B spectral shape and the hep neutrino flux.

As experiments grow larger and capabilities increase, there are also opportunities to apply detectors designed for purposes other than the detection of solar neutrinos. Noble liquid detectors built primarily for dark matter searches and long-baseline neutrino experiments have now reached sufficient size and background levels to be sensitive to solar neutrinos (Aprile *et al.*, 2024). The detection of neutrinos from the high-energy tail of the ^{8}B spectrum via coherent elastic neutrino-nucleus scattering (CEνNS) is particularly interesting because it is a purely neutral-current process sensitive to the total flux of active neutrinos (above the experimental threshold, about 8 MeV) from the Sun. Only the SNO experiment has had such a capability. Initial results reported by Aprile *et al.* (2024) are in agreement, with limited statistical precision. Solid-state detectors built purposely for observing CEνNS have observed neutrinos from stopped pion decay at the theoretically expected rate (Akimov *et al.*, 2017).

III. THE ^{1}H(p,$e^+\nu$)^{2}H REACTION (S_{11})

The cross section for the initial reaction in the pp chain (see Fig. 1), $p + p \rightarrow d + e^+ + \nu_e$, is too small to be measured in the laboratory. It must be calculated from the standard theory of weak interactions.

A. Introduction and terminology

Near the Gamow peak energy $E \sim 6$ keV for temperatures characteristic of the solar core, the first and second derivatives of the astrophysical S factor at zero energy, $S'_{11}(0)$ and $S''_{11}(0)$, generate ~7% and ~0.5% corrections, respectively, in Taylor's series expansions of $S_{11}(E)$ around $E = 0$. Higher derivative terms are neglected in this review since they contribute only at the 10^{-4} level. The recommended values for $S'_{11}(0)$ and $S''_{11}(0)$ are discussed in Sec. III E. Here we focus on $S_{11}(0)$.

At zero relative energy, $S_{11}(0)$ can be written as (Bahcall and May, 1968, 1969)

$$S_{11}(0) = 6\pi^2 m_p \alpha \ln 2 \frac{\bar{\Lambda}^2}{\gamma^3} \left(\frac{G_A}{G_V}\right)^2 \frac{f^R_{pp}}{(ft)_{0^+\rightarrow 0^+}}, \qquad (5)$$

where $\alpha = 1/137.04$ is the fine-structure constant, $m_p = 938.272$ MeV is the proton mass, $\gamma = (2\mu B_d)^{1/2} = 0.23161$ fm^{-1} is the deuteron binding wave number, μ is the proton-neutron reduced mass, B_d is the deuteron binding energy, and G_V and G_A are the Fermi vector and axial-vector weak coupling constants. Finally, f^R_{pp} is the phase-space factor for the pp reaction with radiative corrections, $(ft)_{0^+\rightarrow 0^+}$ is the ft value for superallowed $0^+ \rightarrow 0^+$ transitions, and $\bar{\Lambda}$ is proportional to the transition matrix element connecting the pp and deuteron states.

B. Adopted parameters for this review

For the phase-space factor f_{pp}^R, we use the same value $f_{pp}^R = 0.144(1 \pm 0.001)$ as Adelberger *et al.* (2011). It comes from the value without radiative corrections, $f_{pp} = 0.142$ (Bahcall and May, 1969), increased by 1.62% to take into account radiative corrections to the cross section (Kurylov, Ramsey-Musolf, and Vogel, 2003). The main source of uncertainty in f_{pp}^R arises from neglected diagrams in which the lepton exchanges a weak boson and a photon with different nucleons. These diagrams are estimated to modify f_{pp}^R by ∼0.1%, based on scaling the similar nucleus-dependent correction in superallowed β decay (Kurylov, Ramsey-Musolf, and Vogel, 2003). Direct computations of these diagrams were recommended in Solar Fusion II. Here we again urge that this computation be carried out.

For G_A/G_V we use the value from the Particle Data Group (PDG) compilation (Workman *et al.*, 2022), 1.2754 ± 0.0013, whose central value is larger than the 2008 PDG value used by Adelberger *et al.* (2011), 1.2695 ± 0.0029, by 0.45% (or 1.9σ). Naively, this would lead to a ∼1% increase in the central value of $S_{11}(0)$ according to Eq. (5). Its effect is discussed later. For $(ft)_{0^+\to 0^+}$ we take 3072.24 ± 1.85 s from the most updated comprehensive analysis of experimental rates with the radiative and Coulomb effects corrected (Hardy and Towner, 2020). This value is consistent with 3071.4 ± 0.8 s (Hardy and Towner, 2009) used by Adelberger *et al.* (2011) with a larger error.

The dominant uncertainty in $S_{11}(0)$ comes from the normalized Gamow-Teller (GT) matrix element $\bar{\Lambda}$. Reducing this uncertainty has been the main focus of theoretical work since Adelberger *et al.* (1998), who wrote $\bar{\Lambda}$ as $\bar{\Lambda} = \Lambda + \delta\Lambda$, i.e., the sum of the one- and two-body current matrix elements, Λ and $\delta\Lambda$, respectively, with their uncertainties estimated independently. In the work of Adelberger *et al.* (2011), two major steps contributed to reducing the uncertainty on $\bar{\Lambda}$. The first was a much deeper understanding of the correlation between the uncertainties in Λ and $\delta\Lambda$: the overall uncertainty in $\bar{\Lambda}$ could be described by a universal parameter that could be fixed by a single measurement. Schiavilla *et al.* (1998) demonstrated this phenomenologically in the context of potential-model approaches, while later analysis via effective field theory (EFT) provided a more formal justification (Butler, Chen, and Kong, 2001; Park *et al.*, 2003). The second step was the use of the precisely known tritium β-decay rate Γ_β^T to fix this universal parameter, as first proposed by Carlson *et al.* (1991). This has been done both in potential models (Schiavilla *et al.*, 1998) and in the hybrid EFT approach (Park *et al.*, 2003), as explained later.

Adelberger *et al.* (2011) determined $\bar{\Lambda}$ with three approaches. The first one was the potential-model approach. In the most elaborate calculation for the pp fusion process, a comparison of the results for five representative modern potentials designed to accurately reproduce nucleon-nucleon scattering data was carried out (Schiavilla *et al.*, 1998). After adjusting the unknown strength of the two-body exchange currents to reproduce Γ_β^T, the variation in $S_{11}(0)$ that otherwise would come from the choice of the phenomenological potential was largely removed. Predictions for five representative high-precision phenomenological potentials fell in a narrow interval $7.03 \lesssim \bar{\Lambda}^2 \lesssim 7.04$. There were additional uncertainties in the three-body potentials and three-body currents in Γ_β^T, of the order of ∼0.8%, and a 0.5% uncertainty due to effective-range parameters for nucleon-nucleon scattering. Hence, the recommended $S_{11}(0)$ value from the potential-model approach was $S_{11}(0) = 4.01(1 \pm 0.009) \times 10^{-25}$ MeV b.

The second and third approaches were both based on EFT. The second one was a hybrid EFT (EFT*), which used the current operators derived from EFT in conjunction with the initial- and final-state wave functions generated by a potential model (Park *et al.*, 2003). For pp fusion the relevant two-body current contained only one unknown low-energy constant (LEC) $\hat{d}^R$ that parametrized the contact axial coupling to two nucleons (Park *et al.*, 2003). A weakness of this approach was the mismatch between the operators and wave functions. However, it was argued that the mismatch only happened for short-distance physics that could be absorbed by the LECs. Hence, when the ultraviolet cutoff was changed over a physically reasonable range, the residual cutoff dependence of physical observables provided a measure of the model dependence of the EFT* calculation. By combining the 0.8% error from changing the cutoff $\Lambda_{\rm NN}$ in the range of 500–800 MeV and the ∼0.4% higher-order correction, obtained by multiplying the 1.8% contribution of the highest calculated order with the small expansion parameter $m_\pi/\Lambda_{\rm NN} \sim 1/4$, Park *et al.* (2003) provided the value $S_{11}(0) = 4.01(1 \pm 0.009) \times 10^{-25}$ MeV b, which was in perfect agreement with the one obtained within the phenomenological approach.

The third study was performed with the pionless EFT ($\not\pi$EFT) approach. It is a framework applicable to processes in which the characteristic momentum p is much smaller than the pion mass m_π, such that the pion field can be "integrated out" and becomes nondynamical (Kaplan, 1996; Bedaque, Hammer, and van Kolck, 1999; Chen, Rupak, and Savage, 1999). In this approach all nucleon-nucleon interactions and two-body currents are described by pointlike contact interactions with a systematic expansion in powers of p/m_π. For all the deuteron weak breakup processes (such as νd and $\bar{\nu} d$ scattering) and their inverse processes, including the pp fusion, only one two-body current (with coupling $L_{1,A}$) is needed up to the next-to-next-to-leading order (N^{2}LO) (Butler, Chen, and Kong, 2001). Therefore, a single measurement will fix $L_{1,A}$ and the rates of all such processes. This feature is shared by the other approaches that we have discussed. The computation of $\bar{\Lambda}$ in $\not\pi$EFT was carried out to the second order in the p/m_π expansion by Kong and Ravndal (2001) and then to the fifth order by Butler and Chen (2001). Constraints on $L_{1,A}$ from two-nucleon systems (Butler, Chen, and Vogel, 2002; Chen, Heeger, and Robertson, 2003) yielded $S_{11}(0) = 3.99(1 \pm 0.030) \times 10^{-25}$ MeV b.

Based on the consistent results of the three aforementioned approaches, Adelberger *et al.* (2011) recommended $S_{11}(0) = 4.01(1 \pm 0.009) \times 10^{-25}$ MeV b. The value $S'_{11}(0) = S_{11}(0)(11.2 \pm 0.1)$ MeV^{-1} of Adelberger *et al.* (1998) from

Bahcall and May (1969) was not recomputed by Adelberger *et al.* (2011). However, with $S_{11}(0)$ reaching a 1% accuracy, new calculations of $S'_{11}(0)$ and $S''_{11}(0)$, together with the full pionful chiral EFT (χEFT) computations to remove the unknown systematics of the hybrid EFT, were called for by Adelberger *et al.* (2011). These two challenges have been met in SF III and are described later.

C. Experimental progress on muon capture of the deuteron

Adelberger *et al.* (2011) also recommended carrying out the experimental determination of the muon capture rate on deuteron, as proposed in the MuSun experiment (Kammel, 2003; Salvat, 2017). This quantity could be used to constrain $S_{11}(0)$ without the need to rely on the three-body calculation of Γ_β^T. Theoretical calculations for the muon capture rate on the deuteron have been carried out in $\not\pi$EFT (Chen *et al.*, 2005) [it is possible to impose a neutron energy cut to isolate the low-energy neutron events such that $\not\pi$EFT is applicable (Kammel, 2003)], chiral hybrid EFT* (Ando *et al.*, 2002), the phenomenological potential model (Marcucci *et al.*, 2011), and, recently, in χEFT (Marcucci *et al.*, 2012, 2018; Acharya, Ekström, and Platter, 2018; Bonilla, Acharya, and Platter, 2023; Ceccarelli *et al.*, 2023; Gnech, Marcucci, and Viviani, 2024). However, the MuSun result has yet to be released. Note that the muon capture processes happen at a large momentum transfer compared to pp fusion. The momentum transfer dependence of the single nucleon axial coupling constant $g_A(q^2)$, with $g_A(q^2=0) \equiv g_A \equiv G_A/G_V$, was recently studied by Hill *et al.* (2018), who provided an experimental determination for the axial charge radius, given by $r_A^2 = 0.46(16)$ fm^2, where r_A is defined by the relation $g_A(q^2) = g_A(1 - r_A^2 q^2/6)$ for small q^2. The ∼30% uncertainty on r_A^2 has an impact on the ability of the MuSun experiment alone to directly constrain $S_{11}(0)$ (Acharya, Ekström, and Platter, 2018; Bonilla, Acharya, and Platter, 2023; Ceccarelli *et al.*, 2023; Gnech, Marcucci, and Viviani, 2024).

In the next few years, lattice quantum chromodynamics (QCD) calculations of $g_A(q^2)$ are expected to reduce the r_A uncertainty by a factor of 2 or more; see Meyer (2022) for the most recent review of the lattice results. Currently, lattice QCD results are consistent with those of Hill *et al.* (2018) on r_A, often with comparable uncertainties. At larger q^2 ($|q^2| \gtrsim 0.25$ GeV^2), there is a growing tension between lattice QCD predictions of $g_A(q^2)$ and the phenomenological determination from older neutrino-deuterium bubble chamber data (Meyer *et al.*, 2016), with the lattice QCD results yielding a 30% larger neutrino-nucleon cross section over a large range of q^2 (Meyer, Walker-Loud, and Wilkinson, 2022).

In any case, it is evident that accurate experimental determinations of muon capture rates on the deuteron and other light nuclei, which can be addressed theoretically via *ab initio* approaches, represent fundamental tests for the theoretical approaches themselves, within either χEFT or $\not\pi$EFT, and might be able to provide the necessary experimental information to fix the unknown parameters of the theory.

D. Progress in $S_{11}(0)$ calculations since SF II

We now summarize the $S_{11}(0)$ calculations performed after those of Adelberger *et al.* (2011) using different approaches.

1. χEFT

The pioneering work of Marcucci, Schiavilla, and Viviani (2013) used the next-to-next-to-next-to-leading-order (N^{3}LO) chiral two-nucleon potential (Entem and Machleidt, 2003; Machleidt and Entem, 2011) augmented with higher-order [$\mathcal{O}(\alpha^2)$] two-photon and vacuum-polarization electromagnetic interactions. These $\mathcal{O}(\alpha^2)$ corrections reduced $S_{11}(0)$ by ∼0.8%, due mainly to the vacuum-polarization-induced pp wave function distortion. This was consistent with the 0.84% result that was first found in the potential-model calculation of Schiavilla *et al.* (1998). This correction was also included in the EFT* calculation of Park *et al.* (2003). The relevant LECs were fitted to reproduce the $A = 3$ binding energies, magnetic moments, and GT matrix element in Γ_β^T to obtain $S_{11}(0) = 4.030(1 \pm 0.006) \times 10^{-25}$ MeV b, with the p-wave initial state contributing at ∼1%, which was approximately the accuracy level of the calculation (Marcucci, Schiavilla, and Viviani, 2013). However, using $\not\pi$EFT at the next-to-leading-order (NLO), Acharya, Platter, and Rupak (2019) later found that p waves contributed only at the order of 10^{-30} MeV b. Reexamining the computer programs, Marcucci, Schiavilla, and Viviani (2013) found an error in the determination of one of the p-wave reduced matrix elements (associated with the longitudinal multipole operator). Consequently, Marcucci, Schiavilla, and Viviani (2019) reported in the subsequent erratum that $S_{11} = 4.008(1 \pm 0.005) \times 10^{-25}$ MeV b.

In more recent work, Acharya *et al.* (2016) used chiral interactions and consistent currents up to N^{3}LO [called next-to-next-to-leading order (N^{2}LO) in the original literature since the second order vanished] and developed a robust procedure for the error quantification. In particular, they analyzed a family of 42 interactions (Carlsson *et al.*, 2016) with seven different cutoff values from 450 to 600 MeV. The 26 LECs were fitted to six different pools of input data including nucleon-nucleon (NN) and πN scatterings, as well as the binding energies and charge radii of ^{3}H and ^{3}He, the quadrupole moment of ^{2}H, and Γ_β^T. This thorough study yielded $S_{11}(0) = 4.047(1^{+0.006}_{-0.008}) \times 10^{-25}$ MeV b.

In both of the aforementioned χEFT calculations, a widely used relation first proposed by Gazit, Quaglioni, and Navrátil (2009) that linked the two-body axial current LEC $\hat{d}_R$ with the LEC c_D from the πNN vertex was employed. However, Marcucci *et al.* (2018) later found that there was a factor $-1/4$ missing in this $\hat{d}_R - c_D$ relation that was then acknowledged in the erratum of Gazit, Quaglioni, and Navrátil (2019). This error was unimportant in muon capture on the deuteron (Marcucci *et al.*, 2018) and it affected $S_{11}(0)$ only at the 0.1% level (Acharya, Marcucci, and Platter, 2023).

In the most recent and comprehensive χEFT study, Acharya, Marcucci, and Platter (2023) compared the aforementioned calculations of Acharya *et al.* (2016) and Marcucci, Schiavilla, and Viviani (2019) in detail. In addition to the

0.1% increase of $S_{11}(0)$ from using the correct $\hat{d}_R - c_D$ relation, updating the input parameters to their most recent values increased $S_{11}(0)$ by ∼1% in both calculations, due mainly to the 0.45% increase of G_A/G_V from the aforementioned value of Adelberger *et al.* (2011). Furthermore, Marcucci, Schiavilla, and Viviani (2019) received an ∼1% increase by removing the truncation error of the basis functions that effectively cut off the long-distance part of the wave functions, as Acharya *et al.* (2017) advocated. After these corrections the ∼1% difference between Acharya *et al.* (2016) and Marcucci, Schiavilla, and Viviani (2019) was reconciled, and the combined result was found to be (Acharya, Marcucci, and Platter, 2023)

$$S_{11}(0) = 4.100(1 \pm 0.007) \times 10^{-25}\ \text{MeV b}. \tag{6}$$

Acharya, Marcucci, and Platter (2023) obtained consistent values of $S_{11}(0)$ using four different χEFT models for the nuclear interaction. This value is also in agreement with the result obtained in $\not\pi$EFT by De-Leon and Gazit (2022), as later discussed. In estimating the order-by-order convergence, however, Acharya, Marcucci, and Platter (2023) used one of the χEFT models, which is already able to reproduce the deuteron properties at the leading order. Therefore, the χEFT error of Eq. (6) is likely to be an underestimate, warranting the enlarged error advocated in Sec. III D 4.

Finally, we mention the work of Liu, Peng *et al.* (2022), where the power counting of the χEFT weak current operator involved in the pp reaction was revisited using renormalization group (RG) invariance as the guideline. In particular, it is argued that the contact two-body axial current proportional to the $\hat{d}_R$ LEC must appear 1 order lower than assessed by naive dimensional analysis. Then it can be shown that RG invariance is fulfilled at N^{2}LO. However, the estimate for $\bar{\Lambda}$ obtained by Liu, Peng *et al.* (2022) does not use a value for $\hat{d}_R$ obtained by fitting Γ^T_β but rather is extracted in order to match the value of $\bar{\Lambda}$ obtained by Adelberger *et al.* (2011). Therefore, we do not consider the work of Liu, Peng *et al.* (2022) in this $S_{11}(0)$ evaluation.

2. $\not\pi$EFT

The universal two-body current coupling $L_{1,A}$ was determined using Γ^T_β in $\not\pi$EFT for the first time by De-Leon, Platter, and Gazit (2019). This calculation was carried out up to NLO using the dibaryon formulation of Beane and Savage (2001), which partially resumed higher-order effective-range contributions to improve the convergence. This result was then used by De-Leon and Gazit (2022), with updated input parameters, to obtain

$$S_{11}(0) = 4.12(1 \pm 0.015) \times 10^{-25}\ \text{MeV b}, \tag{7}$$

where the $\mathcal{O}(\alpha^2)$ electromagnetic correction was not calculated but was assumed to be the same as the potential-model value, 0.84% (Schiavilla *et al.*, 1998). While this number was not model independent, the model dependence was believed to be well below the assigned 1.5% error.

The small error assigned to this NLO result has been justified by drawing an analogy from the corresponding electromagnetic processes. Using the same approach, the $np \to d\gamma$ matrix element at threshold was predicted at NLO within 0.5% to the experimental value after the electromagnetic two-body current L_1 was fit to the magnetic moments of ^{3}He and ^{3}H. This indicates that the contribution of the three-body current at N^{2}LO is small in this electromagnetic case. The weak sector is shown to follow the same operator structure and hence provides support for the calculation procedure and the uncertainty estimate.

Note that the reason that the three-body current is an N^{2}LO effect in $\not\pi$EFT is related to the nontrivial renormalization of the nonderivative three-body contact interaction, which shows up at the leading order (LO) to absorb the cutoff dependence of Feynman diagrams. The subleading two-derivative three-body contact interaction is expected to show up at N^{2}LO. This interaction, combined with the one-body current, renormalizes the three-body current. Hence, the three-body current should also appear at the same order, N^{2}LO. However, if the nonderivative three-body contact interaction were counted as the higher order, such as N^{3}LO, as in χEFT (because cutoff independence is not strictly enforced order by order in χEFT), then the three-body current would contribute at much higher order. Although the χEFT power counting indeed yields good convergence in the expansions, it is unsatisfactory that one cannot remove the cutoff dependence at each order of the expansion. In addition, the uncertainty estimate of the χEFT still lacks a broad inspection of the specific nuclear χEFT potential implementation. As a consequence, we consider the $\not\pi$EFT 1.5% error a better estimate for the $S_{11}(0)$ theoretical uncertainty.

3. Lattice QCD and lattice EFT

Ideally, lattice QCD would provide a first principles prediction of the pp fusion rate and the GT matrix element of Γ^T_β both for pure QCD and with QED effects incorporated. However, such calculations are challenging and not yet available at the required precision. A proof-of-principle calculation was carried out by Savage *et al.* (2017) using a background field method to determine both the pp fusion GT matrix element and Γ^T_β. This exploratory calculation utilized a single pion mass at the SU(3)-flavor-symmetric point with $m_\pi \approx 806$ MeV, a single and relatively coarse lattice spacing of $a \approx 0.145$ fm, and a single volume. The calculation was performed under the assumption that the two- and three-nucleon systems were deeply bound. Without this assumption, matrix elements computed in the finite volume can be significantly different from those in infinite volume owing to Lellouch-Lüscher factors (Lellouch and Lüscher, 2001) that lead to power-law finite volume corrections. These can range from the few-percent level to O(1) (Briceño and Davoudi, 2013; Briceño *et al.*, 2015).

More recent lattice QCD calculations have shown that two-nucleon systems at heavy pion masses are in fact not bound (Iritani *et al.*, 2016; Francis *et al.*, 2019; Hörz *et al.*, 2021; Amarasinghe *et al.*, 2021). These efforts, which employ interpolating operators more sophisticated than those of

Savage *et al.* (2017), suggest that there could be large systematic uncertainties affecting the conclusions of Savage *et al.* (2017) stemming from misidentification of the spectrum and inaccurate Lellouch-Lüscher factors. In addition, Green *et al.* (2021) found that the two-baryon spectrum may be particularly sensitive to discretization effects, which would also have important implications for the continuum extrapolation of the matrix elements. These issues were discussed by Tews *et al.* (2022). Finally, results with pion masses $m_\pi \lesssim 300$ MeV are needed for accurate extrapolation to the physical pion mass.

Given these unresolved systematic issues, the result of Savage *et al.* (2017) is not included in this $S_{11}(0)$ evaluation—even though the extracted value $S_{11}(0) = 4.07(1 \pm 0.008) \times 10^{-25}$ MeV b is consistent with our recommended range quoted in Sec. III D 4.

The lattice EFT computation of Rupak and Ravi (2015) performed the pp fusion calculation by implementing $\not\pi$EFT on a spacetime lattice. The purpose of this leading-order study was to demonstrate that lattice EFT could reproduce the infinite volume and continuum result of $\not\pi$EFT such that it could be applied to various reactions of astrophysical interest in the future. Therefore, for $S_{11}(0)$ this result is considered a subset of the $\not\pi$EFT calculation.

4. Final recommendation of $S_{11}(0)$

The aforementioned discussions show that determinations of $S_{11}(0)$ from χEFT in Eq. (6), $\not\pi$EFT in Eq. (7), and lattice QCD (although with unquantified systematics) are consistent with each other. Furthermore, these values are also consistent with the recommended value of Adelberger *et al.* (2011) provided that the central value is increased[5] by 0.9% to $S_{11}(0) = 4.05(1 \pm 0.009) \times 10^{-25}$ MeV b to account for the G_A/G_V update. Averaging this value with the χEFT value in Eq. (6) and the $\not\pi$EFT value in Eq. (7) yields $S_{11}(0) = 4.09(1 \pm 0.005) \times 10^{-25}$ MeV b with χ^2 per degree of freedom to be 0.9. This shows that the χEFT and $\not\pi$EFT estimates and the $S_{11}(0)$ estimates of Adelberger *et al.* (2011) are mutually consistent.

In addition, we advocate adding an additional correlated error to account for any input that would tend to move all results in a coordinated way. For example, from Adelberger *et al.* (2011) to SF III, we experienced the ∼1% shift due to the update of the PDG value of G_A/G_V. It is not inconceivable that G_A/G_V or other input parameters or physics could change again by similar amounts: the large PDG inflation factor of 2.7 reflects the tension that continues to exist among G_A/G_V measurements (Workman *et al.*, 2022). Therefore, assigning an additional 1% correlated error seems reasonable. This is also in line with the subtleties discussed in Secs. III D 1 and III D 2, which call for an enlarged error. Therefore, our final recommended value for $S_{11}(0)$ is

$$S_{11}(0) = 4.09(1 \pm 0.015) \times 10^{-25}\ \text{MeV b}, \tag{8}$$

where we have added the correlated and uncorrelated errors linearly to be conservative.

E. Progress in $S'_{11}(0)$ and $S''_{11}(0)$

Using $\not\pi$EFT, Chen, Liu, and Yu (2013) computed $S_{11}(E)$ analytically with all partial waves included up to N^{2}LO. The Fermi matrix element contributed only at the 10^{-4} level and was neglected compared with the GT matrix element. The energy dependence of the phase factor f^R_{pp} of Eq. (5) was the dominant effect in $S'_{11}(0)$ and $S''_{11}(0)$, the energy dependence of pp scattering was subdominant, while the $L_{1,A}$ contribution was much less important in these derivatives than in $S_{11}(0)$. Therefore, these derivatives could be predicted more reliably than $S_{11}(0)$. Furthermore, the derivatives were computed analytically and were free from errors of fitting $S_{11}(E)$ to a polynomial. The result was $S'_{11}(0)/S_{11}(0) = (11.3 \pm 0.1)$ MeV^{-1} and $S''_{11}(0)/S_{11}(0) = (170 \pm 2)$ MeV^{-2}.

In χEFT, $S_{11}(E)$ for $E < 100$ keV was fit to polynomials of E (Marcucci, Schiavilla, and Viviani, 2019). Depending on whether a quadratic or quartic fit was used, $S'_{11}(0)/S_{11}(0)$ changed from 12.23 to 10.82 MeV^{-1} and $S''_{11}(0)/S_{11}(0)$ changed from 178.4 to 317.4 MeV^{-2}. Acharya *et al.* (2016) used a cubit fit and $E < 30$ keV to obtain $S'_{11}(0)/S_{11}(0) = 10.84(2)$ MeV^{-1} and $S''_{11}(0)/S_{11}(0) = 317.8(13)$ MeV^{-2}. Recently, Acharya, Marcucci, and Platter (2023) repeated the calculation of Marcucci, Schiavilla, and Viviani (2019) with the same energy range and cubic fit as Acharya *et al.* (2016), obtaining a result consistent with Acharya *et al.* (2016): $S'_{11}(0)/S_{11}(0) = 10.83$ MeV^{-1} and $S''_{11}(0)/S_{11}(0) = 313.72$ MeV^{-2}. We take these as the recommended values from χEFT.

Although the face values of $S'_{11}(0)/S_{11}(0)$ and $S''_{11}(0)/S_{11}(0)$ from $\not\pi$EFT and χEFT look much different, we remark that they actually agree on $S_{11}(E)/S_{11}(0)$ better than 0.1% below the ∼6 keV Gamow peak. For massive stars with central temperatures ∼15 keV, the agreement is better than 0.8% to the second order in the derivatives and 0.5% if $S'''_{11}(0)/S_{11}(0) = -5382$ MeV^{-3} is included in the χEFT result. Hence, we take the average of the $\not\pi$EFT and χEFT results as the recommended value,

$$\begin{aligned} S'_{11}(0) &= S_{11}(0)(11.0 \pm 0.2)\ \text{MeV}^{-1}, \\ S''_{11}(0) &= S_{11}(0)(242 \pm 72)\ \text{MeV}^{-2}. \end{aligned} \tag{9}$$

Finally, we comment on Gaspard *et al.* (2019), who performed a study of $S_{11}(E)$ in a wide energy range. The main focus of their work was to perform a proper energy-dependence analysis of the pp process in order to reliably extract $S'_{11}(0)/S_{11}(0)$ and $S''_{11}(0)/S_{11}(0)$. However, the calculation was performed within a phenomenological approach using a simplified model for the nuclear currents (i.e., not including two-body currents, which are well known to be significant) and structure (i.e., neglecting the d-wave components in the deuteron wave function). They found results for $S'_{11}(0)/S_{11}(0)$ and $S''_{11}(0)/S_{11}(0)$ that are compatible with those of Eq. (9). However, since these values were not obtained with state-of-the-art calculations, they have not been

[5]To know the precise shift requires an explicit calculation. However, if the shift is within the range of 0.8%–1.0%, the averaged value and χ^2 remain the same within the significant digits.

considered in the determination of $S'_{11}(0)/S_{11}(0)$ and $S''_{11}(0)/S_{11}(0)$.

IV. THE ^{2}H$(p,\gamma)^3$He REACTION (S_{12})

A. Introduction

The $^2\mathrm{H}(p,\gamma)^3\mathrm{He}$ reaction is the second step in the pp chain; see Fig. 1. Compared to the reactions mediated by the weak interaction, this reaction occurs much more rapidly. Consequently, on timescales relevant to solar energy generation, deuterium is effectively converted to ^{3}He instantaneously and thus is sensitive only to the Q value of the reaction and not to the uncertainties of the rate.

However, the $^2\mathrm{H}(p,\gamma)^3\mathrm{He}$ reaction plays an important role in the development of protostars because the onset of deuterium burning slows down the protostars' contraction and heating, thus increasing their lifespan. Accurate knowledge of the $^2\mathrm{H}(p,\gamma)^3\mathrm{He}$ reaction rate, particularly within the few keV range corresponding to the Gamow peak in protostars, is vital for effectively modeling protostellar evolution (Stahler, 1988).

Another astrophysical scenario where the $^2\mathrm{H}(p,\gamma)^3\mathrm{He}$ reaction plays a key role is big bang nucleosynthesis (BBN), which was responsible for the production of light elements during the first few minutes of the Universe. Among these elements deuterium is an excellent indicator of cosmological parameters because its primordial abundance is the most sensitive to the baryon density and critically depends on the radiation density of the early Universe; see the review of BBN by Cyburt *et al.* (2016). The reactions involved in the synthesis of deuterium are production via the well-known $p(n,\gamma)^2\mathrm{H}$ process and destruction via the $^2\mathrm{H}(^2\mathrm{H},n)^3\mathrm{He}$, $^2\mathrm{H}(^2\mathrm{H},p)^3\mathrm{H}$, and $^2\mathrm{H}(p,\gamma)^3\mathrm{He}$ reactions (Fields *et al.*, 2020).

Since the comprehensive review performed by Adelberger *et al.* (2011), there have been both new measurements and advances in the theoretical and phenomenological analysis of the $^2\mathrm{H}(p,\gamma)^3\mathrm{He}$ reaction. The new experimental results have been determined with accelerator-based measurements of the cross section (Tišma *et al.*, 2019; Mossa *et al.*, 2020b; Turkat *et al.*, 2021), as well as plasma-based, inertial confinement fusion measurements (Zylstra *et al.*, 2020; Mohamed, Kim, and Knauer, 2022), and are reviewed in Sec. IV B. On the theoretical side, there have been advances in *ab initio* calculations, where nucleons are the fundamental degrees of freedom interacting among themselves and with the external electromagnetic probe; see Ekström *et al.* (2023). Finally, Bayesian analysis methods have been used to model the energy dependence of the S factor, starting with the *ab initio* predictions and applying a polynomial approximation to it. We review these updates and provide recommended values and uncertainties of the S factor over the energy range of interest for solar fusion, based upon a Bayesian averaging of various models.

B. Datasets used in this review

The $^2\mathrm{H}(p,\gamma)^3\mathrm{He}$ reaction has a Q value of 5.5 MeV and proceeds through the radiative capture of a proton on deuterium. Different experimental approaches were followed to measure its cross section. Tišma *et al.* (2019) irradiated deuterated titanium targets with a proton beam and detected the γ rays with two high-purity germanium (HPGe) detectors placed at different angles. The final S factor is provided at four energies in the 47–210 keV range, with approximately 15% statistical uncertainty. More recently, the LUNA Collaboration performed a measurement in the energy range of 32–263 keV at the underground in the Gran Sasso Laboratories, exploiting the 6-order-of-magnitude suppression of the cosmic radiation background (Cavanna and Prati, 2018; Ferraro *et al.*, 2021). A windowless deuterium gas target was used and the γ rays emitted by the $^2\mathrm{H}(p,\gamma)^3\mathrm{He}$ reaction were detected by a large HPGe detector at 90° with respect to the beam axis. Great care was taken to minimize all sources of systematic uncertainties in the S-factor overall uncertainty at the 3% level (Mossa *et al.*, 2020a, 2020b). These new results provided stringent constraints on cosmological parameters obtained by comparing the precise primordial deuterium abundance predictions of the standard BBN model with astronomical observations (Cooke, Pettini, and Steidel, 2018). Deeper discussions of the LUNA results and their implications[6] were given by Moscoso *et al.* (2021), Pisanti *et al.* (2021), Pitrou *et al.* (2021), and Yeh, Olive, and Fields (2021)

Finally, a new measurement was performed at the Helmholtz-Zentrum Dresden-Rossendorf in the 300–1000 keV energy range using implanted deuterium targets on tantalum backings and two HPGe detectors (Turkat *et al.*, 2021). The resulting S factors show $\approx 1\sigma$ to 2σ tension with the analysis of the LUNA results extrapolated to $E \gtrsim 300$ keV (Mossa *et al.*, 2020b). However, they are affected by large systematic uncertainties. A new measurement of the $^2\mathrm{H}(p,\gamma)^3\mathrm{He}$ reaction is planned at the Felsenkeller laboratory in Germany (Bemmerer *et al.*, 2019).

In addition to the new accelerator-based results, two recent sets of measurements (Zylstra *et al.*, 2020; Mohamed, Kim, and Knauer, 2022) have also been performed using the inertial confinement fusion plasma-based platform (Gatu Johnson *et al.*, 2017; Mohamed, Kim, and Knauer, 2022; Gatu Johnson *et al.*, 2023), which has recently begun to be exploited for this type of work (Zylstra *et al.*, 2016; Casey *et al.*, 2017). Both measurements, which were performed at the OMEGA laser facility (see Sec. XIV D), used laser-driven implosions of spherical plastic-shell capsules filled with H_2D_2 gas and measured the emitted γ rays using a gas Cherenkov detector (Herrmann *et al.*, 2014) that was calibrated applying the technique described by Zylstra *et al.* (2019). The initial experiment obtained good statistics at an energy of 16 keV by making several repeated measurements, with a final statistical uncertainty of 6% and a systematic one of 17% (dominated by uncertainty in the absolute calibration of the detector) (Zylstra *et al.*, 2020). The second experiment obtained data at three different energies in the 17–37 keV region, with comparable systematic uncertainty but larger statistical uncertainty due to

[6]After the closing of this review, the Mossa *et al.* (2020b) data were reanalyzed to extract the experimental $^2\mathrm{H}(p,\gamma)^3\mathrm{He}$ γ-ray angular distribution (Stöckel *et al.*, 2024). The data confirm the *ab initio* angular distributions used in the original analysis by Mossa *et al.* (2020b).

fewer repeated measurements (Mohamed, Kim, and Knauer, 2022). The results obtained on this unique platform agree within error bars with the accelerator-based measurements.

C. Theoretical studies

Nuclear reactions of astrophysical interest in general and the $^2\mathrm{H}(p,\gamma)^3\mathrm{He}$ in particular are of great importance in nuclear theory because the available experimental data can be used to test the adopted theoretical framework. The $^2\mathrm{H}(p,\gamma)^3\mathrm{He}$ reaction has the great advantage of involving only $A \leq 3$ nuclear systems and can be addressed with a microscopic *ab initio* study. This means that the nuclear systems involved in the process are viewed as being made up of A nucleons, interacting among themselves and with the external electromagnetic probes. Within such an approach, the following ingredients are essential for the calculation: (i) realistic models for the nuclear interactions and currents, possibly rooted in QCD; (ii) a numerical technique able to solve the A-body bound and scattering state problem, including the Coulomb interaction without approximation. Such a technique is usually referred to as an *ab initio* method. The agreement (or disagreement) between *ab initio* theoretical predictions and experimental data represents a validation (or indicates the necessity of improvement) mostly for ingredient (i). In other words, are the models of the nuclear interactions and currents accurate within the precision specified by the *ab initio* method? This is why few-nucleon reactions can be used as an "ideal" laboratory, where the *ab initio* framework can be stringently tested in systems under more theoretical control.

The most recent *ab initio* calculation of the $^2\mathrm{H}(p,\gamma)^3\mathrm{He}$ reaction is that of Marcucci *et al.* (2016). They used the pair-correlated hyperspherical harmonics *ab initio* method to calculate the $A = 3$ initial scattering and final bound-state wave functions; see Kievsky *et al.* (2008) and Marcucci *et al.* (2020) for details. The nuclear interaction model adopted by Marcucci *et al.* (2016) to describe the $A = 3$ nuclear state consists of a two-nucleon term, the Argonne v_{18} (AV18) potential (Wiringa, Stoks, and Schiavilla, 1995), augmented by a three-nucleon contribution, the Urbana IX (UIX) potential (Pudliner *et al.*, 1995). The AV18 potential can reproduce the large two-nucleon database with a χ^2/datum ~ 1 (Wiringa, Stoks, and Schiavilla, 1995), while the combination AV18/UIX can accurately describe the properties of ^{3}He, the spectra of light p-shell nuclei (Pieper and Wiringa, 2001), and p-d scattering observables; see Wood *et al.* (2002). The electromagnetic current operator used by Marcucci *et al.* (2016) includes, in addition to the nonrelativistic one-body operator, two- and three-body terms required by gauge invariance in a system of interacting particles. These terms were constructed by Marcucci *et al.* (2005). The model was then tested against various electromagnetic observables to access the quality of its predictions. As a potential model, however, there is no systematic procedure for assigning uncertainties for observables whose values are unknown.

The results of Marcucci *et al.* (2016) have been found to be about 10% higher than the experimental data of Mossa *et al.* (2020b). Given the lack of a procedure for quantifying errors in calculations based on phenomenological interactions and currents, it is difficult to access the significance of this discrepancy. This leads us to make a pair of recommendations to the theory community. First, the $^2\mathrm{H}(p,\gamma)^3\mathrm{He}$ reaction should be studied within the framework of chiral effective field theory, which has reached a degree of accuracy and predictive power comparable to potential-based phenomenology. This approach is formally *ab initio* and rooted in QCD and, as an operator expansion, will provide an estimate of the theoretical uncertainty. Work along these lines is currently underway. Second, the angular distribution of the $^2\mathrm{H}(p,\gamma)^3\mathrm{He}$ capture reaction, and possibly also polarization observables, should be both calculated and measured. This would be valuable even if measurements were limited to higher energies, where they are less difficult. Such measurements would provide a further test of the predictive power of the theory.

D. Phenomenological and Bayesian analyses

In the energy range of astrophysical interest, the $^2\mathrm{H}(p,\gamma)^3\mathrm{He}$ reaction does not have any resonance or coupled channels that can give rise to nontrivial energy dependence, and the S factor can be modeled by a low-order polynomial in energy (Fowler, Caughlan, and Zimmerman, 1967). Moreover, the recent results from LUNA (Mossa *et al.*, 2020b), combined with previous measurements, place stringent constraints on the cross section, thus reducing the uncertainty over the range of interest to solar fusion and BBN (Casella *et al.*, 2002; Mossa *et al.*, 2020b; Pisanti *et al.*, 2021; Pitrou *et al.*, 2021; Yeh, Olive, and Fields, 2021).

A significant change since the work of Adelberger *et al.* (2011) has been the wide adoption of Bayesian analysis methods to evaluate thermonuclear reaction rates and provide more rigorous uncertainty estimates in a statistical sense (Iliadis *et al.*, 2016). This approach has been followed in the analysis presented here, which closely follows work on the $^2\mathrm{H}(p,\gamma)^3\mathrm{He}$ reaction reported by Moscoso *et al.* (2021) and references therein. The mathematical details of the Bayesian method are given in Appendix B. Here we focus on the application to $^2\mathrm{H}(p,\gamma)^3\mathrm{He}$ by the cited researchers.

Both the *ab initio* prediction from Marcucci *et al.* (2005) and a third-order polynomial in the energy were used to constrain the data, where we define an nth-order polynomial as

$$S_n(E;\lambda) = \sum_{i=0}^{n} \lambda_i E^i. \tag{10}$$

As noted in the literature, the energy dependence of Marcucci *et al.* (2005) is more reliable than the absolute normalization. Furthermore, the updated prediction by Marcucci *et al.* (2016), as noted, is ≈10% larger than that of Marcucci *et al.* (2005). Therefore, Moscoso *et al.* (2021) modeled the prediction of Marcucci *et al.* (2005), denoted $S_{\mathrm{nuc}}(E)$, as

$$S(E;\lambda) = aS_{\mathrm{nuc}}(E) + b, \tag{11}$$

where a and b are an unknown scale factor and offset to be determined in the analysis. While $S_{\mathrm{nuc}}(E)$ was not determined with theoretical uncertainty, model uncertainty is introduced

through the parameters a and b. The resulting mean values and uncertainties of $S(E;\lambda)$ determined from Eq. (11) were found to be comparable to those with the third-order polynomial.

E. Summary and recommendations

In this review we take the further step of applying Bayes model averaging to a number of reasonable models that describe the data, which systematically captures additional theoretical "model selection uncertainty." Details of the Bayesian analysis and model-averaging procedure are presented in Appendix B. The models that we explore include Eq. (11) with both a and b, as done[7] by Moscoso *et al.* (2021). In addition, we set $b = 0$ and then consider polynomials in energy of the order $n = 3$, 4, 5, and 6.

With such a Bayes model averaging, we can quantitatively compare and contrast the polynomial parametrizations of $^2\mathrm{H}(p,\gamma)^3\mathrm{He}$ along with *ab initio* results predicted by Marcucci *et al.* (2005, 2016), including the extra variance that arises from this set of reasonable models, for example, using polynomials of different order, as well as the phenomenological model of Eq. (11). Results are listed in Table III. The first column lists the model (i.e., polynomial or *ab initio*), the second column displays the natural logarithm of the Gaussian approximation to the Bayes factor (BF), and the third column lists the corresponding weight in the model averaging. From this model averaging, the resulting prediction for the $^2\mathrm{H}(p,\gamma)^3\mathrm{He}$ S factor at a few representative energies is provided in Table IV, where the first uncertainty arises from the first term in Eq. (B2) and the second uncertainty is from the second term, which we denote as model selection uncertainty. The resulting Bayes model average prediction of the S factor over the entire kinematic range considered is depicted in Fig. 5, with the gray band representing the 68% coverage probability. For this reaction it is interesting to note that the Bayesian analysis strongly favors the phenomenological models of Eq. (11) over the polynomial approximations. One reason for this might be that the scaled *ab initio* models have only one or two free parameters, and the energy dependence of $S_{\mathrm{nuc}}(E)$ given by Marcucci *et al.* (2005, 2016) is sufficient to accurately describe the various datasets. However, polynomial approximations are disfavored, as they require more parameters to capture the energy dependence. Note also that, in the model of Eq. (11) with $b = 0$ and using the work of Marcucci *et al.* (2016) for $S_{\mathrm{nuc}}(E)$, the scale factor is given by

$$a = 0.921(19), \tag{12}$$

indicating that the prediction of Marcucci *et al.* (2016) overestimates the $^2\mathrm{H}(p,\gamma)^3\mathrm{He}$ data by 7.9%, which is consistent with the aforementioned expectations. In comparison, the third-order polynomial fit predicts values of $S(E)$ that are 1σ higher at $E = 0$ and $2/3\sigma$ lower at $E = 91$ keV compared to those in Table IV.

TABLE III. Logarithm of the Gaussian approximation to the Bayes factor (logGBF) and corresponding weight [Eq. (B4)] for each model under investigation.

Model	logGBF	Weight
Ab initio, $aS_{\mathrm{nuc}}(E)$	1478.7	0.585
Ab initio, $aS_{\mathrm{nuc}}(E) + b$	1478.3	0.414
Third-order polynomial	1470.2	1.2×10^{-4}
Fourth-order polynomial	1469.2	4.6×10^{-5}
Fifth-order polynomial	1468.2	1.6×10^{-5}
Sixth-order polynomial	1464.1	2.9×10^{-7}

The analysis in Table III and Fig. 5 can be reproduced with the code linked in Table IV. The code also can provide a prediction of the mean value and uncertainty of $S_{12}(E)$ at any energy over the same kinematic range.

V. THE $^3\mathrm{He}(^3\mathrm{He},2p)^4\mathrm{He}$ REACTION (S_{33})

The $^3\mathrm{He}(^3\mathrm{He},2p)^4\mathrm{He}$ reaction terminates the pp-I chain. The ratio of its rate to that of the $^3\mathrm{He}(\alpha,\gamma)^7\mathrm{Be}$ reaction controls the branching to the pp-II and pp-III chains, so Adelberger *et al.* (1998) discussed increasing S_{33} as a potential solution to the solar neutrino problem. Subsequent experiments, notably, a very-low-energy measurement at the LUNA 50 kV accelerator deep underground in Gran Sasso (Bonetti *et al.*, 1999) and a complementary experiment at somewhat higher energies (Kudomi *et al.*, 2004), ruled out such an increase in S_{33}, as summarized by Adelberger *et al.* (2011).

A. Shape of the particle spectrum

Since no new absolute measurements of S_{33} have been reported since those of Adelberger *et al.* (2011), we consider the same four experiments (Krauss *et al.*, 1987; Junker *et al.*, 1998; Bonetti *et al.*, 1999; Kudomi *et al.*, 2004). However, there is new information on the energy spectrum of the emitted protons. This spectrum was recently measured using inertial confinement fusion plasmas for a Gamow peak energy of 165 keV (Zylstra *et al.*, 2017). The results show significant structure, indicating the presence of a sequential reaction mechanism passing through the unbound ground state of ^{5}Li. This spectrum is important for all of the S_{33} measurements since they determined cross sections by detecting only the protons above an energy threshold.

The efficiency correction by which Krauss *et al.* (1987) accounted for the threshold is not well documented, but the more recent measurements (Junker *et al.*, 1998; Bonetti *et al.*, 1999; Kudomi *et al.*, 2004) utilized the GENBOD event generator (James, 1968). It employs a simple reaction model without final-state interactions, the Pauli principle, or Coulomb effects that are important near the spectrum end point. The only angular correlations are those required by energy and momentum conservation, and together these simplifications give simple ellipses for the single energy distributions of the emitted nuclei. Published proton spectra obtained using accelerator beams do exist [see Fig. 2 of

[7]The implementation of the Bayesian analysis presented here is different than that of Moscoso *et al.* (2021) but was verified to produce the same results when the same implementation of the systematic uncertainties was made.

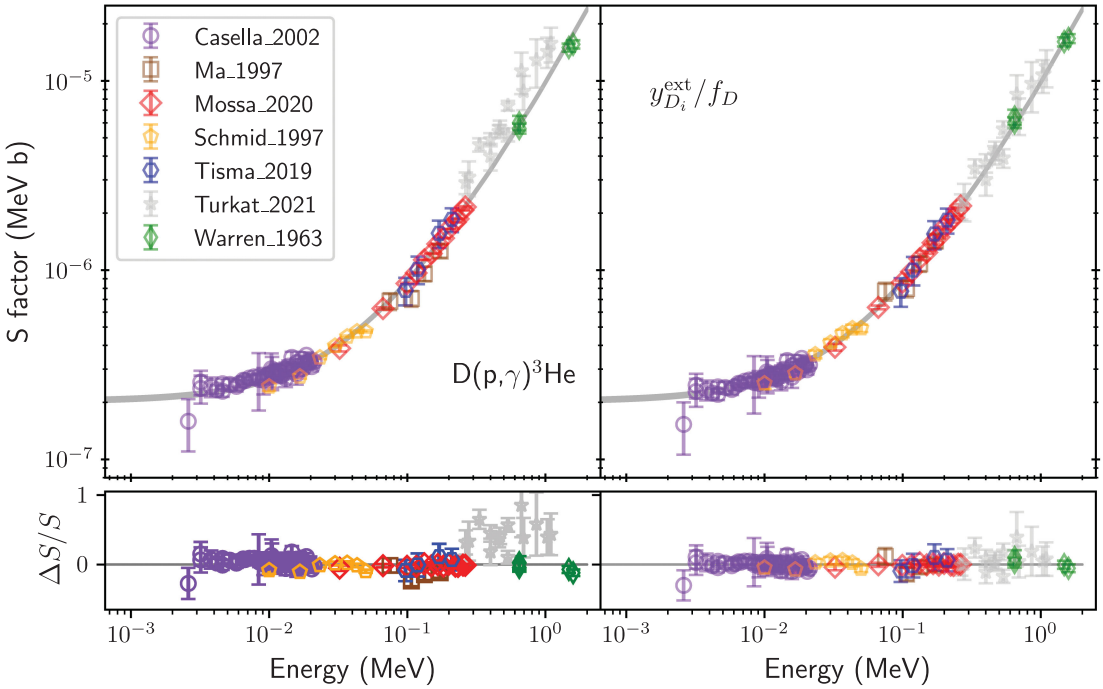

FIG. 5. S factor determined via Bayes model averaging (BMA) of the ^{2}H$(p,\gamma)^3$He datasets (Warren *et al.*, 1963; Ma *et al.*, 1997; Schmid *et al.*, 1997; Casella *et al.*, 2002; Tišma *et al.*, 2019; Mossa *et al.*, 2020b; Turkat *et al.*, 2021) analyzed as described in the text. Left panels: the original data with statistical uncertainties only. Right panels: the data after normalizing by BMA systematic uncertainty posteriors of f_D^{-1} for each dataset. The uncertainties correspond to the statistical, systematic, and extrinsic uncertainties added in quadrature. In most cases the quoted statistical uncertainty is the dominant uncertainty. The residual is defined as $\Delta S/S = (S_{\rm data} - S_{\rm fit}^{\rm BMA})/S_{\rm fit}^{\rm BMA}$ and is plotted for the original data with statistical uncertainty only on the left and the adjusted data (as described) on the right.

Dwarakanath (1974) and Fig. 3 of Krauss *et al.* (1987)], and although they are not corrected for instrumental effects, they do not appear to be well described by ellipses.

The ^{3}He$(^3$He$, 2p)^4$He reaction may proceed via several sequential mechanisms, including $p + {}^5$Li (with ^{5}Li in its ground or first excited state) and diproton $+ \alpha$ (where the diproton is two correlated protons in a singlet state) (Brune, Caggiano *et al.*, 2015). More complicated three-body decay channels, sometimes called direct decays, are also possible. Only a relatively narrow intermediate state (here the 1 MeV wide ^{5}Li ground state) could produce a peak in the energy spectrum, and precise classification of the reaction mechanism is in general both experimentally and theoretically ambiguous. When coincident detection of reaction products is used [as by Bonetti *et al.* (1999)], possible angular correlations between the reaction products also matter. A reaction through the $3/2^-$ ground state of ^{5}Li would emit the second proton preferentially either along or opposite to the direction of the first proton, while diproton emission would tend to send both protons in the same direction (Brune, Caggiano *et al.*, 2015).

The solid curves in Fig. 6 show two different R-matrix models of the proton energy spectrum at $E_{\rm c.m.} = 165$ keV, fitted to the spectrum measured by Zylstra *et al.* (2017) for $E_p \gtrsim 6$ MeV. The measured spectrum differs significantly from the elliptical spectrum of GENBOD. Based on their Fig. 6, the experiment of Junker *et al.* (1998) had a detection threshold of about 5 MeV proton energy. The measurements by Bonetti *et al.* (1999) required a coincidence between two detectors, with a detection threshold of 2 MeV proton energy in each detector. Finally, Fig. 19 of Kudomi *et al.* (2004) indicates a detection threshold of about 4 MeV proton energy. We have estimated their sensitivities to the assumed proton spectrum by integrating the curves shown in Fig. 6 above energy thresholds of 2, 4, and 6 MeV. These integrals vary from 3% below to 6% above the result from an elliptical spectrum, depending on the specific threshold and the assumed spectrum.

TABLE IV. The S factor of the ^{2}H$(p,\gamma)^3$He reaction at some selected energies determined from data using Bayesian model averaging as described in the text. The first uncertainty is the statistical one and the second is the model selection uncertainty..

$S_{12}(E)$ (10^{-7} MeV b)[a]							
$E = 0$ keV	$E = 10$ keV	$E = 20$ keV	$E = 40$ keV	$E = 80$ keV	$E = 91$ keV	$E = 100$ keV	$E = 120$ keV
2.028(51)(9)	2.644(60)(8)	3.276(70)(7)	4.579(94)(5)	7.31(15)(0)	8.11(16)(0)	8.77(18)(0)	10.24(21)(0)

The value at any energy in the fitted range can be obtained by running the analysis provided at https://github.com/nrp-g/leaner

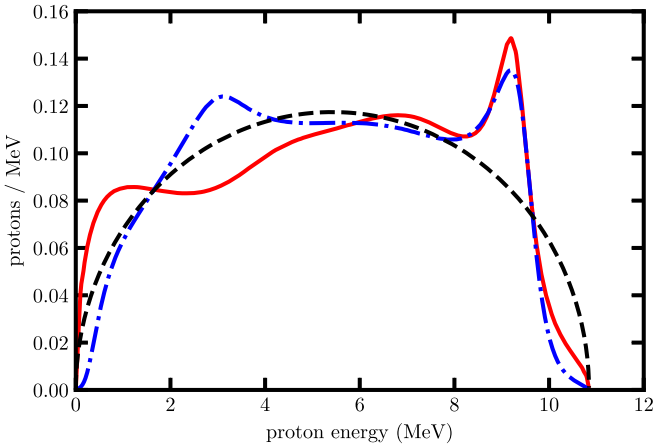

FIG. 6. Calculated proton energy spectra in the c.m. frame for the ^{3}He(^{3}He, $2p$)^{4}He reaction at $E_{\text{c.m.}} = 165$ keV. The solid red and dot-dashed blue curves are models 1 and 2, respectively, from Fig. 3(a) of Zylstra *et al.* (2017). The dashed black curve is the elliptical spectrum. The spectra are normalized to unit area.

B. Recommendation

Based on these investigations, our recommended S_{33} fit is the one from Adelberger *et al.* (2011), but with an additional 4% systematic uncertainty typical of the 3%–6% corrections to the extrapolated proton spectra estimated previously to take the uncertain spectral shape into account. This gives

$$S_{33}^{\text{best}}(E) = 5.21 - 4.90\left(\frac{E}{\text{MeV}}\right) + 11.21\left(\frac{E}{\text{MeV}}\right)^2 \text{ MeV b},$$

$$\delta S_{33}(E) = \left[0.118 - 1.516\left(\frac{E}{\text{MeV}}\right) + 14.037\left(\frac{E}{\text{MeV}}\right)^2 - 15.504\left(\frac{E}{\text{MeV}}\right)^3 + 71.640\left(\frac{E}{\text{MeV}}\right)^4\right]^{1/2} \text{ MeV b}.$$

Only the larger constant term in the uncertainty differs from the previous evaluation; this is due to the previously discussed spectral shape.

New measurements of this reaction could provide more accurate absolute cross sections using lower energy thresholds and could improve our understanding of the proton energy spectra and angular correlations. An analysis of new measurements should use Monte Carlo simulations considering a variety of plausible energy spectra and angular correlations in order to estimate the sensitivity to these effects. We note finally that the proton energy spectrum may depend on $E_{\text{c.m.}}$, as this has been found to be the case for neutrons from the mirror reaction ^{3}H$(t, 2n)\alpha$ (Gatu Johnson *et al.*, 2018).

VI. THE ^{3}He$(\alpha,\gamma)^7$Be REACTION (S_{34})

The ^{3}He$(\alpha, \gamma)^7$Be reaction proceeds via nonresonant capture to the ground and 429 keV first-excited states of ^{7}Be. It has been studied experimentally using three main methods, with references given in Secs. VI A and VI C: (1) by detecting at least two of the three γ rays from the reaction and taking the angular correlation with the α beam direction into account (the prompt-γ method); (2) by detecting the induced ^{7}Be radioactivity (the activation method) (Tilley *et al.*, 2002); and (3) by counting the ^{7}Be recoils (the recoil method).

A. Previous S_{34} recommendation in SF II

The ^{3}He$(\alpha, \gamma)^7$Be S factor recommended by Adelberger *et al.* (2011) was developed in multiple steps. To begin, a model was selected for the shape of $S(E)$ based on existing nucleon-level calculations (Kajino, 1986; Nollett, 2001). A rescaling of the curve was fitted to the data, but only at $E \leq 1.002$ MeV center of mass to minimize the role of short-distance physics in the models.

Adelberger *et al.* (1998) discussed a possible systematic discrepancy between previously used data from the two methods. By the time of Adelberger *et al.* (2011), in-depth studies from two groups using both activation and prompt methods were available, namely, the LUNA (Bemmerer *et al.*, 2006a; Confortola *et al.*, 2007; Gyürky *et al.*, 2007) and Seattle groups (Brown *et al.*, 2007). These studies did not have any discrepancies between activation and prompt-γ data in direct comparisons. Adelberger *et al.* (2011) limited the fitting to the data by the activation and recoil methods. The prompt-γ data were left out because of their somewhat larger common-mode errors, concerns about how well the γ-ray angular distribution was known, and avoidance of the correlated errors between activation and prompt data from the same experiment.

Adelberger *et al.* (2011) included only data published after 1998. The recommended value of Adelberger *et al.* (2011) was $S_{34}(0) = 0.56 \pm 0.02_{\text{expt}} \pm 0.02_{\text{theor}}$ based on the data from the Weizmann (Singh *et al.*, 2004), LUNA (Bemmerer *et al.*, 2006a; Confortola *et al.*, 2007; Gyürky *et al.*, 2007), Seattle (Brown *et al.*, 2007), and European Recoil Separator for Nuclear Astrophysics (ERNA) groups (Di Leva *et al.*, 2009).

B. Theory progress on S_{34}

Significant theoretical work on this reaction has occurred since the work of Adelberger *et al.* (2011), but the basic understanding of its mechanism remains unchanged from the 1960s (Tombrello and Parker, 1963). It is dominated by external nonresonant capture into the two bound states, and most of the dipole strength at low energy arises beyond the range of nuclear interaction. The external capture part of the cross section is determined by the asymptotic normalization constants (ANCs) of the bound states and by the scattering phase shifts; near threshold, most of the strength lies at ~5–20 fm (Neff, 2011). In models with explicit wave functions, the shorter-range strength largely cancels out owing to effects of nucleon-exchange antisymmetry. All models feature a shallow minimum of $S(E)$ near 1.25 MeV, where capture from d waves becomes comparable to that from s waves.

The first fully *ab initio* calculation (Neff, 2011) appeared just after the analysis of Adelberger *et al.* (2011) concluded; it used the fermionic molecular dynamics method and a softened representation of the Argonne v_{18} interaction (Wiringa, Stoks, and Schiavilla, 1995). This calculation agrees well with both the scale and the energy dependence of the modern S-factor data, and it is close to the energy dependence assumed by

Adelberger *et al.* (2011). Neff's elastic-scattering phase shifts also agree well with experiment. Notably, Neff found that the dipole strength distribution departs significantly from pure external capture at ^{3}He-^{4}He separations as large as 9 fm, compared with 3 to 4 fm in potential models.

Another *ab initio* model (Dohet-Eraly *et al.*, 2016; Vorabbi *et al.*, 2019) has also appeared, based on the no-core shell model with continuum method and the chiral interaction of Entem and Machleidt (2003), "softened" by the similarity renormalization group (SRG) procedure. Freedom to choose the SRG stopping point allowed exact reproduction of the ^{7}Be breakup energy, which corrects for the main effect on the external capture of omitting the three-nucleon potential. The results agree well with the overall scale of the modern data, but their energy dependence and phase shifts depart from the experiments, possibly owing to the omission of explicit three-body forces.

An important advance since the work of Adelberger *et al.* (2011) has been the application of halo EFT methods to astrophysical capture reactions (Bertulani, Hammer, and van Kolck, 2002; Higa, Rupak, and Vaghani, 2018; Premarathna and Rupak, 2020; Zhang, Nollett, and Phillips, 2020). EFTs are valid for systems with a natural separation between the momentum scales Q probed in low-energy experiments (for example, corresponding to a binding energy or a projectile energy) and the much larger momentum scale Λ where the low-energy degrees of freedom are no longer valid: the word *halo* here refers to nuclei with only shallow bound states. In halo EFT the only degrees of freedom are the initial- and final-state nuclei treated as point particles plus photons. For S_{34}, $\Lambda \sim 200$ MeV corresponds to the momentum needed to separate a proton from ^{3}He or to excite ^{4}He; the thresholds to separate the two ^{7}Be bound states into ^{3}He and ^{4}He correspond to momenta $Q = 71.4$ and 60.9 MeV.

Given a sufficient separation of scales, one constructs a Lagrangian that respects the system's symmetries and known qualitative features systematically, organized by powers of Q/Λ. This series can be truncated [at the LO, NLO, next-to-next-to-leading order (NNLO), etc.], and the precision of the resulting theory depends on the sizes of the omitted terms. The precision of a calculation and the energy where it breaks down can be estimated by assuming coefficients of the first omitted term to have a "natural" size. Coupling constants of the Lagrangian must be fitted to data, and the consistency of the power-counting scheme (identification of powers of Q/Λ for the main operator terms of a system) is tested by whether the fitted constants have natural sizes. Low-order coupling constants in a halo EFT can often be identified with familiar quantities like ANCs, scattering lengths, and effective ranges; the description of elastic scattering in halo EFT reproduces the Coulomb-modified effective-range expansion (Kong and Ravndal, 2000; Higa, Hammer, and van Kolck, 2008; Poudel and Phillips, 2022). When a separation of scales exists, halo EFT is well suited to data extrapolation because it avoids the tacit, difficult-to-test, and unavoidable prior assumptions present in the short-range parts of models based on explicit wave functions.

Two groups have studied S_{34} in halo EFT (Higa, Rupak, and Vaghani, 2018; Premarathna and Rupak, 2020; Zhang, Nollett, and Phillips, 2020). The sizes of the Coulomb interaction and the large s-wave scattering length make the correct power counting difficult to establish for this system. Higa, Rupak, and Vaghani (2018) and Premarathna and Rupak (2020) included careful examinations of possible power-counting schemes and strict adherence to a power counting once established, up to terms of NLO and NNLO, respectively, in two different power countings. They fitted EFTs to S-factor data, and they examined the effects of including or excluding elastic-scattering constraints in their fits. When they included scattering phase shifts from Boykin, Baker, and Hardy (1972) in their fits, they concluded that the large-scattering-length power counting of the NLO theory was favored. This result promotes two-body currents (i.e., contributions not equivalent to external nonresonant capture) to the leading order in the theory. The d-wave contribution that becomes important above 1 MeV first appears at NLO. In addition to data-fitting errors, these theories have errors estimated to be 10% from EFT truncation.

Zhang, Nollett, and Phillips (2020) followed a different approach to power counting up through NLO. At $E < 2$ MeV their derived expression for $S_{34}(E)$ is essentially the same as that from the NLO theory of Premarathna and Rupak (2020). Zhang, Nollett, and Phillips (2020) also developed some *ad hoc* (i.e., not systematically developed) higher-order EFT terms, referred to as partial-N4LO terms, to test for their impact on the fitting. The additional terms proved not to be required by the data and did not improve the fit; this result was taken to indicate that corrections from omitted terms are not large compared to experimental errors below 2 MeV. Scattering data were not considered in their work apart from broad priors on scattering length and effective range; the correlated errors in the S-factor data were taken into account.

Like halo EFT, the phenomenological R-matrix approach avoids a model of nuclear interactions and uses a systematic parametrization to fit data (Descouvemont and Baye, 2010). At the time of Adelberger *et al.* (2011), S_{34} had been the subject of little R-matrix fitting, apparently consisting only of the simple treatment of Descouvemont *et al.* (2004) that focused on BBN energies. After the work of Adelberger *et al.* (2011), an R-matrix analysis using `AZURE2` code (Azuma *et al.*, 2010; Uberseder and deBoer, 2015) was carried out on both elastic-scattering and S-factor data in conjunction with the Notre Dame experiment (Kontos *et al.*, 2013), and a more elaborate analysis using Monte Carlo sampling to estimate errors was later reported by deBoer *et al.* (2014). In the latter analysis, both the fitted value and the error bars were heavily influenced by the numerous scattering data of Barnard, Jones, and Phillips (1964). Recently, the `BRICK` software package was constructed to carry out Bayesian parameter estimations for `AZURE2` and applied to both capture and elastic scattering at all energies in the ^{7}Be system by Odell *et al.* (2022). They showed that markedly different $S_{34}(0)$ values result from the inclusion or absence of older scattering data (Barnard, Jones, and Phillips, 1964) alongside the recent SONIK scattering data of Paneru *et al.* (2024).

A small amount of additional theoretical work in more traditional frameworks has since appeared (Adelberger *et al.*, 2011). This includes fits of potential models to

S-factor data (Tursunov, Turakulov, and Kadyrov, 2018, 2021) and use of resonating-group methods (Solovyev and Igashov, 2017, 2019).

C. Experimental progress on S_{34}

Since the work of Adelberger *et al.* (2011), five new experiments have been reported: four from the Madrid and ATOMKI groups by the activation technique, at relatively high center-of-mass energies (Carmona-Gallardo *et al.*, 2012; Bordeanu *et al.*, 2013; Szücs, Kiss *et al.*, 2019; Tóth *et al.*, 2023), and one from the Notre Dame group using the prompt-γ method (Kontos *et al.*, 2013).

Following the approach adopted by Adelberger *et al.* (2011), we again only use the recoil and activation data for the S_{34} fits to follow. The γ-ray angular distribution is not known experimentally (Brown *et al.*, 2007), and the resultant uncertainty somewhat increases the common-mode error for the prompt-γ studies. ([An experiment to address previously raised concerns about angular distribution (Brown *et al.*, 2007) was recently concluded at Felsenkeller Dresden. The data suggest a higher than expected anisotropy but are currently available only in the form of a doctoral thesis (Turkat, 2023). If confirmed, they may lead to corrections of a few percent for some of the in-beam experiments where only one angle was instrumented.] In addition, all of the "modern" works reporting prompt-γ data except for the Notre Dame group (Kontos *et al.*, 2013) also include data obtained with other methods, leading to partial correlations between datasets that would complicate fitting.

Following this restriction, our data selection proceeds as follows. To begin, the four datasets previously used by Adelberger *et al.* (2011)—namely, the Weizmann (Singh *et al.*, 2004), LUNA (only the activation data) (Bemmerer *et al.*, 2006a; Confortola *et al.*, 2007; Gyürky *et al.*, 2007), Seattle (only the activation data) (Brown *et al.*, 2007), and ERNA groups (Di Leva *et al.*, 2009)—are carried over here.

Two of the archival datasets excluded by the 1998 cutoff date used by Adelberger *et al.* (2011) merit further discussion here: The data of Osborne *et al.* (1982, 1984) consist of two points measured by activation in a ^{3}He gas cell. However, their uncertainties are not separated into statistical and systematic components. Including them would have required an uncertain guess on how to divide the error bars, and the fit result would barely change, so we left them out. The work by Robertson *et al.* (1983) consists of one data point that was obtained by averaging two separate activation measurements with a ^{3}He and a ^{4}He gas cell, respectively. We do not use this result, because we lack details to verify the background subtraction, an issue that was raised by one of the researchers during our meeting. We also choose not to use the activation study by Volk *et al.* (1983). In that experiment there were thick entrance foils and the ^{4}He beam was completely stopped inside a high-pressure ^{3}He gas cell. This gave an integrated measurement over a wide energy range such that the analysis depended strongly on the assumed shape of the S_{34} curve, and the result was reported only as an extrapolated $S_{34}(0)$.

We now consider the new data since the work of Adelberger *et al.* (2011). An activation experiment in Madrid used a ^{3}He beam incident on a ^{4}He gas cell, reporting three data points (Carmona-Gallardo *et al.*, 2012). Another activation experiment, using a ^{4}He beam on ^{3}He gas cells, was reported by the ATOMKI group (Bordeanu *et al.*, 2013). Two higher-energy campaigns at ATOMKI were again performed using the activation method. The latter data are at $E = 2.5$–4.4 MeV (Szücs, Kiss *et al.*, 2019) and $E = 4.3$–8.3 MeV (Tóth *et al.*, 2023), respectively, above the energy range suitable for halo EFT and therefore not included.

A detailed study by the Notre Dame group reported 17 data points (Kontos *et al.*, 2013), using the primary γ ray from ground-state capture and the secondary γ ray from the deexcitation of the 429 keV first excited state of ^{7}Be. Kontos *et al.* reported no activation data, and the γ-ray detector was placed at just one angle, 90°. Since only prompt-γ data were reported, we did not include this dataset. To test the effects of this decision, we repeated some of our fits (see Sec. VI.D) with the modern prompt-γ experiments included: the 17 points from Kontos *et al.* (2013), the three prompt-γ points from the LUNA group (Confortola *et al.*, 2007), and the eight points from the Seattle group (Brown *et al.*, 2007). The extrapolated *S* factor changed by less than 1%, well within the error bars for the recommended S_{34} value.

Finally, an indirect experiment using the ^{6}Li(^{3}He, d)^{7}Be reaction and the ANC technique was recently reported (Kiss *et al.*, 2020). It is omitted from our fits owing to the additional normalization and theory uncertainties involved in determining an ANC from a transfer experiment, which are larger than the errors in the *S*-factor measurements used for these fits. All the data used in the fits are summarized in Table V.

As in the work of Adelberger *et al.* (2011), we model data uncertainties as consisting of a component that is independent for each point and a common-mode component that applies to all data from a given experiment as a multiplicative factor. This separation is well documented for all of the modern data and is also shown in Table V. Except at the lowest energies, the common-mode error typically dominates.

D. Data fitting

We base our recommended S_{34} on fits to the previously discussed halo EFT and *R*-matrix parametrizations. These avoid tacit assumptions present in potential models and conceptual difficulties involved in combining *ab initio* constraints with the data. The fits presented here differ from the previously published fits of Premarathna and Rupak (2020), Zhang, Nollett, and Phillips (2020), and Odell *et al.* (2022) mainly in the uniform use of the agreed-upon capture data and uncertainties from Sec. VI.C across all fits. We restricted the fitting to the $E < 2$ MeV range of validity for the NLO halo EFT expressions. Despite uniform handling of capture data, the fits in each framework handle scattering inputs differently for reasons discussed later.

In addition to the total capture cross-section and scattering data, the fitted data also include branching ratios for capture into the two ^{7}Be bound states, taken from Brown *et al.* (2007), Confortola *et al.* (2007), Di Leva *et al.* (2009), and Kontos *et al.* (2013). These are necessarily from prompt-γ experiments and suffer from the concerns about angular distribution

TABLE V. Experimental data used for the S_{34} fit. See the text for details. For each experimental dataset, the rescaling factors s_α are determined for Higa, Rupak, and Vaghani (2018), Zhang, Nollett, and Phillips (2020), and BRICK (Odell *et al.*, 2022) with or without the inclusion of elastic scattering.

Group and reference(s)	Energy range (keV)	Data points		Common-mode uncert.	Rescaling factor s_α			
		Used	Total		Higa EFT	Zhang EFT	BRICK	BRICK + S
Weizmann (Singh *et al.*, 2004)	420–950	4	4	2.2%	1.03(2)	1.02(2)	1.02(2)	1.03(2)
LUNA (Bemmerer *et al.*, 2006a; Confortola *et al.*, 2007; Gyürky *et al.*, 2007)	93–170	7	7	3.0%	1.02(2)	1.04(2)	1.05(2)	1.01(2)
Seattle (Brown *et al.*, 2007)	327–1235	8	8	3.0%	0.96(1)	0.95(2)	0.95(2)	0.98(2)
ERNA (Di Leva *et al.*, 2009)	650–2504	22	51	5.%	0.96(3)	0.94(2)	0.96(2)	0.99(2)
Madrid (Carmona-Gallardo *et al.*, 2012)	1054–2804	1	3	5.2%	0.99(3)	0.99(3)	0.97(2)	0.99(2)
ATOMKI (Bordeanu *et al.*, 2013)	1473–2527	2	5	5.9%	1.01(3)	1.00(3)	1.01(3)	1.04(3)

discussed in Sec. VI.C. However, their inclusion simplifies the fitting considerably by breaking parameter degeneracies between ground- and excited-state transitions (especially in the fitted ANCs), probably without strong impact on $S_{34}(0)$.

In constructing fits we split common-mode and point-to-point errors and "float the norms" of datasets using the cost function

$$\chi^2 = \sum_{\alpha=1}^{N_{\rm set}} \sum_{i=1}^{N} \frac{(y_i - \mu_i/s_\alpha)^2}{\sigma_{\alpha,i}^2} + \sum_{\alpha=1}^{N_{\rm set}} \frac{(1-s_\alpha)^2}{\omega_\alpha^2} \qquad (13)$$

to describe the goodness of fit (D'Agostini, 1994).

A rescaling factor s_α is fitted to each dataset α, with its deviation from unity penalized by the common-mode errors ω_α given in Table V. The index i sums over all points within a given dataset; y_i is a measured cross section, μ_i is a predicted cross section, and $\sigma_{\alpha,i}$ is the point-to-point error of the ith point in dataset α.

We carried out both frequentist fits that minimize χ^2 and Bayesian fits based on the posterior probability distribution of a likelihood function computed from $\exp(-\chi^2/2)$. In the Bayesian fits, parameters, extrapolated $S_{34}(0)$, and their errors were determined by Monte Carlo sampling of the parameter space. The relatively large number of model parameters and the significant fitting degeneracies between some of them make Bayesian analysis a natural choice for finding best fit and confidence intervals for the multiparameter models applied here. Two of the groups ran into serious difficulty with the frequentist fits due to parameter degeneracies and shallow local minima: during this study they were unable to produce frequentist fits in which they had confidence.

We performed multiple fits in the NLO halo EFT of Higa, Rupak, and Vaghani (2018) and Premarathna and Rupak (2020). These fits were carried out both with and without scattering constraints, which mainly impact $S_{34}(0)$ by removing parameter degeneracies that would otherwise leave the s-wave scattering length poorly constrained. The code base for this version of halo EFT incorporates scattering data through phase shifts. These fits, which were taken from the partial-wave analysis of Boykin, Baker, and Hardy (1972), at low energy are based mainly on the data of Barnard, Jones, and Phillips (1964).

One set of fits for the halo EFT of Higa, Rupak, and Vaghani (2018) was produced by χ^2 minimization, proceeding in two steps: first LO parameters were fitted to $E \leq 1000$ keV data, and then the results were taken as initial values in the search to minimize χ^2 over all parameters in the NLO theory for the full set of data. These fits gave $S_{34}(0) = 0.566 \pm 0.025$ keV b with the scattering constraint and $S_{34}(0) = 0.588 \pm 0.015$ keV b without (with uncertainties propagated in a linear approximation using covariances and partial derivatives). Formally, the EFT truncation error from stopping at NLO corresponds to an additional theoretical error that can shift S factors by 10%. However, any fitted curve is constrained by low-energy data, which in some sense become effectively renormalization conditions of the field theory. The error on extrapolated $S_{34}(0)$ should probably be smaller than 10% by an amount that is difficult to estimate.

A second set of fits to the halo EFT of Higa, Rupak, and Vaghani (2018) was carried out using Bayesian methods. Priors for the EFT parameters were developed based on previous experience, and data rescaling factors were incorporated as additional priors. The Bayesian results (including experimental error only) are $S_{34}(0) = 0.561^{+0.017}_{-0.018}$ keV b, including the phase shifts by Boykin, Baker, and Hardy (1972) and $S_{34}(0) = 0.559^{+0.018}_{-0.019}$ keV b excluding them, which is consistent with the χ^2 minimization.

Searches of the parameter space to minimize χ^2 for the NLO halo EFT of Zhang, Nollett, and Phillips (2020) ran into difficulties with parameter degeneracy and local minima in the χ^2 surface; for this formalism we report Bayesian results only. No experimental information about scattering was used, but flat priors on the scattering length and effective range were chosen over a 5σ range around a recent experiment. This fit differs from that of Zhang, Nollett, and Phillips (2020) mainly because it excludes the Notre Dame data and includes the ERNA activation data, and it gives $S_{34}(0) = 0.581 \pm 0.016$ keV b. The error associated with EFT truncation at NLO is estimated in this approach by separately fitting the previously discussed partial-N4LO theory. The result suggests that EFT truncation at NLO affects extrapolation from the data to threshold by ∼2% to 3%.

Our R-matrix fits are based mainly on sampling Bayesian posterior probabilities with the BRICK code. We also produced frequentist fits, but we were unable to estimate their

errors convincingly. The *R*-matrix fits used capture data both alone and in combination with the SONIK scattering data (Paneru *et al.*, 2024)—with the latter chosen because of concerns with the Barnard, Jones, and Phillips (1964) data that were discussed by Odell *et al.* (2022). Since BRICK fits elastic differential cross sections directly, it was not feasible to use the same phase-shift-based scattering constraints as our halo EFT fits. The *R*-matrix fit that includes scattering data is essentially the CS fit of Odell *et al.* (2022), but with a restriction to only the capture data described in Table V, only the scattering data below 2 MeV center of mass, and only the *R*-matrix parameters relevant below 2 MeV (no $7/2^-$ level or radiative widths for *d*-wave background poles).

Several of the fits are compared in Fig. 7. There it is apparent that they all agree within $\lesssim 5\%$ in the 0–2000 keV energy range and within $\lesssim 4\%$ in the astrophysically relevant range 0–500 keV. The fit to the NLO EFT of Higa, Rupak, and Vaghani (2018) lies in the middle of the range, so we adopt it as a reference in the lower panel of Fig. 7. Relative to that fit, the fits to the NLO EFT of Zhang, Nollett, and Phillips (2020) and the *R*-matrix fit without scattering rise up as much as 4% higher at 0–200 keV.

The most striking difference among the curves is between the BRICK *R*-matrix fit including the SONIK scattering data (Paneru *et al.*, 2024) and all the other fits. While the *R*-matrix fit with scattering finds rescaling factors somewhat closer to unity than the other fits do, its energy dependence in the 0–1000 keV range is qualitatively different, which is especially visible in the lower panel of Fig. 7, where residuals relative to the fitted EFT of Higa, Rupak, and Vaghani (2018) are shown. The BRICK fit without the scattering data is much closer to all the halo EFT fits, so the recent scattering data apparently have a large impact.

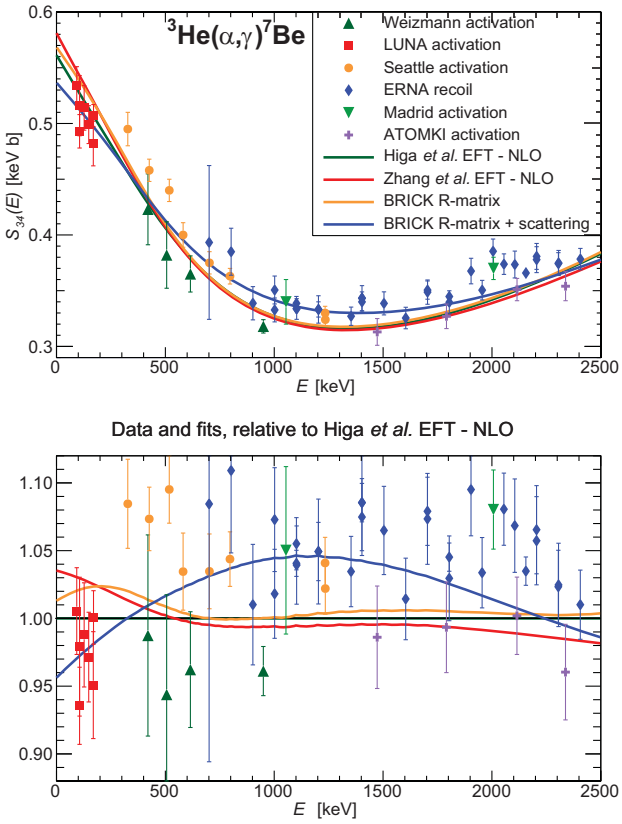

FIG. 7. Top panel: $^3\mathrm{He}(\alpha,\gamma)^7\mathrm{Be}$ astrophysical *S* factors from the experiments used for the fitting of the excitation function, namely, the Weizmann (Singh *et al.*, 2004), LUNA (Bemmerer *et al.*, 2006a; Confortola *et al.*, 2007; Gyürky *et al.*, 2007), Seattle (Brown *et al.*, 2007), Madrid (Carmona-Gallardo *et al.*, 2012), and ATOMKI experiments (Bordeanu *et al.*, 2013). The fit curves from two different EFT-based fits [approaches based on the work of Higa, Rupak, and Vaghani (2018) and Zhang, Nollett, and Phillips (2020)] and two *R*-matrix fits [BRICK (Odell *et al.*, 2022), with or without elastic-scattering data] are also shown. Bottom panel: experimental data and fits normalized to the EFT fit based on that of Higa, Rupak, and Vaghani (2018). See Table V and the text for details.

E. Recommended S_{34} value

Because the fit to the NLO EFT of Higa, Rupak, and Vaghani (2018) gives the central result among those attempted here, we adopt it for our recommended $S(E)$. For ease of adoption, it is noted that this recommended S_{34} curve can be empirically parametrized using the same shape as Adelberger *et al.* (2011) by the numerical equation [following a customary form in the past literature (Kajino, Austin, and Toki, 1987; Adelberger *et al.*, 2011)]

$$S_{34}(E) = (0.5610\ \mathrm{keV\,b})\exp(-0.5374E) \times [1 - 0.4829E^2 + 0.6310E^3 - 0.1527E^4]. \quad (14)$$

In Eq. (14) E is the center-of-mass energy in MeV. Equation (14) reproduces our recommended curve within 0.3% and is applicable only for $E = 0$–1600 keV.

Propagation of uncertainties from measurement to extrapolated $S_{34}(0)$ is relatively straightforward and unambiguous (at least in the Bayesian fitting). However, the uncertainty due to theoretical approximation is more complicated, and error estimation on extrapolated quantities in EFTs remains an open area of research; estimates from the groups working on S_{34} were previously discussed. We estimate the overall theoretical uncertainty on our recommended S factor to be the one measured via the 4% dispersion among fitted curves; this is comparable to the more formal estimates.

Our recommendations for the zero-energy astrophysical S factor and the low-energy slope are then

$$S_{34}(0) = 0.561 \pm 0.018_{\mathrm{expt}} \pm 0.022_{\mathrm{theor}}\ \mathrm{keV\,b}, \quad (15)$$

$$\frac{S'_{34}(0)}{S_{34}(0)} = -0.54 \pm 0.07\ \mathrm{MeV}^{-1}. \quad (16)$$

The given value of S'_{34}/S_{34} applies over $E = 0$–500 keV. Its considerable uncertainty is given by the full span of slopes among the four aforementioned fits, which is dominated by the inclusion of elastic scattering in one of the *R*-matrix fits. The $S_{34}(E)$ curve is straight at low energy in all models. Its second derivative is consistent with zero and difficult to compute for a given fit because of numerical cancellations.

TABLE VI. Main results of the Bayesian fits performed on the S_{34} data. The ANC refers to the sum of the ANCs for the ground- and excited-state transitions. See the text for details.

Fit	$S_{34}(23)$ (keV b)	S'_{34}/S_{34} (MeV^{-1})	a_0 (fm)	C^2 (fm^{-1})
EFT-NLO of Higa, Rupak, and Vaghani (2018)	0.554	−0.56	30^{+5}_{-2}	$26.9^{+4.5}_{-5.1}$
EFT-NLO of Zhang, Nollett, and Phillips (2020)	0.573	−0.61	46(6)	29(3)
BRICK R matrix	0.562	−0.57		24.4(9)
BRICK R matrix and scattering	0.531	−0.47		22.6(7)
ANC (Kiss *et al.*, 2020)				34 ± 1.6

The first error bar for $S_{34}(0)$ is given by the fit uncertainty, conservatively using the largest value among the various fits, and it encodes the experimental uncertainty. The second error bar reflects the 4% dispersion among theoretical formalisms. The two errors can be added in quadrature for applications. Our recommendation is essentially the same as that of Adelberger *et al.* (2011) but derived from completely different theoretical approaches that are much more directly connected to the data and much less dependent on model assumptions. It is also based on data over a wider energy range. The dispersion of S_{34} and S'_{34} among models at the solar Gamow peak is illustrated in Table VI, along with some indication of how fitted scattering lengths a_0 and squared ANCs C^2 vary among frameworks. [The latter are highly degenerate with short-range parameters in the fitting. In the EFT of Higa, Rupak, and Vaghani, 2018, they are sensitive to small variations in the p-wave effective ranges that are fitted instead of ANCs.]

F. Recommendations for future work on S_{34}

Here we present recommendations for further work that would improve understanding of the $^3\mathrm{He}(\alpha,\gamma)^7\mathrm{Be}$ reaction. Our first recommendation for the experiment concerns elastic $^3\mathrm{He} + {}^4\mathrm{He}$ scattering. New experiments over a wide energy range including at least part of the astrophysical range are needed to address the marked impact of the recent SONIK scattering data (Paneru *et al.*, 2024) on fitting for independent confirmation. Data below 2 MeV would be most useful for consistent fitting of halo EFTs.

Our second recommendation is that new measurements [besides the preliminary data of Turkat (2023)] are needed for the angular distribution of the emitted γ rays. This would relieve concerns in future fits about including prompt-γ data, most notably that of the Notre Dame group (Kontos *et al.*, 2013), that do not include activation measurements. These experiments should also be designed to provide new angle-corrected branching ratios for capture into the two bound states.

Our third recommendation is a study of the astrophysical S factor over a wide energy range, 50–1500 keV, and extending to even lower energies when technically feasible, with small point-to-point errors. Even with a large common-mode error, this would significantly constrain theoretical curve shapes near threshold and would provide an independent check on the influence of scattering data on $S(E)$.

On the theoretical side, further development of *ab initio* reaction calculations is desirable, improving on points of current difficulty like explicit inclusion of three-body potentials. Calculations with the same potential but by different methods would help to separate computational issues from the impact of potential choice. Further exploration of how *ab initio* inputs like ANCs and scattering lengths could serve as fitting priors would also be a useful avenue of research.

Authors of future theoretical calculations should consider including γ-ray angular distributions in their results; until recently, angular distributions were available from only two potential models (Tombrello and Parker, 1963; Kim, Izumoto, and Nagatani, 1981). New calculations would inform the analysis of experiments, and the angular distribution measurements that we recommend would provide tests of the calculations (or fitting constraints).

A source of complication here has been the need for a good meeting point between scattering data and theory. Given the difficulties of constructing a unique phase shift analysis without an underlying theory and the recent arrival of modern scattering data, theorists should consider including elastic differential cross sections directly as outputs and fitting constraints. In addition, efforts should be made to extend EFT fits to higher energies in order to take into account the 3 MeV resonance.

VII. THE hep REACTION (S_{hep})

The reaction $p + {}^3\mathrm{He} \to {}^4\mathrm{He} + e^+ + \nu_e$, also known as the hep reaction, is one of the possible processes taking place after the $^2\mathrm{H}(p,\gamma)^3\mathrm{He}$ reaction, and it produces the most energetic neutrinos, with an end point energy of 18.8 MeV. It is, however, the least probable, with its S factor—and consequently its rate—beyond the reach of even current experiments. This is due to the fact that the hep reaction is induced by the weak interaction and further suppressed by the Coulomb barrier and by the fact that the leading one-body axial (Gamow-Teller) current operator cannot connect the main s-state components of the $p + {}^3\mathrm{He}$ and $^4\mathrm{He}$ initial- and final-state wave functions. As a consequence, the one-body axial current nonzero contribution is due to the small components of the $^3\mathrm{He}$ and $^4\mathrm{He}$ wave functions. Furthermore, other contributions, such as weak magnetism and other one-body corrections to the vector current, two-body vector and axial currents, and the p waves in the $p + {}^3\mathrm{He}$ initial state, normally suppressed at solar temperatures, are significantly enhanced. This is further complicated by cancellations between the one- and two-body axial current contributions. As a consequence, as in the pp fusion, the hep reaction cross section is too small to be measured in a laboratory and only theoretical predictions are available.

The most recent studies of this reaction, which was previously evaluated by Adelberger *et al.* (2011), are those of Marcucci *et al.* (2000) and Park *et al.* (2003). The first one was performed within a phenomenological approach, similar to the calculation of Schiavilla *et al.* (1998) for the pp fusion. In this case the $p + {}^3\mathrm{He}$ and $^4\mathrm{He}$ initial and final nuclear wave functions were obtained with the correlated hyperspherical

harmonics (CHH) variational method (Viviani, Kievsky, and Rosati, 1995; Viviani, Rosati, and Kievsky, 1998) using the AV18 two-nucleon potential (Wiringa, Stoks, and Schiavilla, 1995) augmented by the UIX three-nucleon interaction (Pudliner *et al.*, 1995). In this way the binding energies of ^{3}He and ^{4}He and the singlet and triplet $p+{}^3$He scattering lengths were in good agreement with the experiment. The weak vector and axial transition operators were obtained within a phenomonological approach. In particular, the largest two-body contribution to the axial current arising from the excitation of intermediate Δ-isobar degrees of freedom was included using the transition-correlation operator scheme of Carlson *et al.* (1991) and Schiavilla *et al.* (1992) and fixing the nucleon-to-Δ axial coupling constant to reproduce Γ_β^T as in the pp case (Schiavilla *et al.*, 1998).

The second study of Park *et al.* (2003) was performed within the same hybrid EFT approach used for the pp fusion (EFT*), with the same nuclear weak current operators obtained within EFT as discussed in Sec. III and the LEC $\hat{d}^R$ fixed to reproduce Γ_β^T. The initial and final wave functions were derived using the CHH method with the AV18 or UIX potential, as in the derivation of Marcucci *et al.* (2000).

Following the results of Marcucci *et al.* (2000) and Park *et al.* (2003), Adelberger *et al.* (2011) recommended for the zero-energy S factor $S_{\rm hep}(0)$ the value $(8.6\pm2.6)\times10^{-20}$ keV b. The following three recommendations were also made: (i) to perform new studies with a broad spectrum of Hamiltonian models in order to properly access the theoretical uncertainty, (ii) to study other weak reactions for which experiments can test the predictions made by employing the same theoretical ingredients as those used for the hep reaction calculation, and (iii) to further understand the relation between the hep reaction and the so-called hen process ($n+{}^3\mathrm{He}\to{}^4\mathrm{He}+\gamma$). Of these recommended works, only the second one has been performed thus far, with the theoretical framework used for the hep study applied to the muon capture reactions on light nuclei (Marcucci *et al.*, 2011).

Given the lack of further studies on the hep reaction after the work of Adelberger *et al.* (2011), we decide to maintain

$$S_{\rm hep}(0)=(8.6\pm2.6)\times10^{-20}\ \text{keV b} \tag{17}$$

as the recommended value. Note that we could have increased $S_{\rm hep}(0)$ by ∼1%, in analogy with $S_{11}(0)$, owing to the updated values of the input parameters (mostly G_A/G_V). However, we decided not to apply such an increase, because it does not derive from a direct calculation and, most of all, because such an increase lies well within the quoted ∼30% uncertainty. However, given the advances in *ab initio* studies of the past decade and in the development of the EFT framework, we update the recommendations of Adelberger *et al.* (2011) as follows: (i) the hep process should be revisited within a fully consistent χEFT approach, as has been done for the pp fusion and other processes, such as muon captures on light nuclei (Marcucci *et al.*, 2012, 2018; Acharya, Ekström, and Platter, 2018; Bonilla, Acharya, and Platter, 2023; Ceccarelli *et al.*, 2023; Gnech, Marcucci, and Viviani, 2024); (ii) the initial and final wave functions should be calculated with the most accurate *ab initio* methods, as the uncorrelated hyperspherical harmonics (HH) method (Kievsky *et al.*, 2008; Marcucci *et al.*, 2020), which has been proven to provide more accurate $A=4$ bound and scattering wave functions than the CHH method while using both local and nonlocal interactions; (iii) the relation between the hep and hen processes should be understood. The hen process has been studied within χEFT and the HH method by Viviani *et al.* (2022), but a consistent parallel study of both $A=4$ reactions is still missing.

A relatively recent SNO Collaboration analysis of data from all three of the detector's running phases yielded a one-sided confidence-interval bound on the hep neutrino flux of Aharmim *et al.* (2020),

$$\phi_{\rm hep}<30\times10^3\ \text{cm}^{-2}\,\text{s}^{-1}\ (90\%\ \text{CL}), \tag{18}$$

a result that agrees with the SSM prediction. The lack of a definite measurement, however, has meant that there is no substantive experimental test of the predicted $S_{\rm hep}(0)$ value. Various global analyses of solar neutrino data have provided weak evidence for a nonzero flux, for example, from Bergstrom *et al.* (2016)

$$\phi_{\rm hep}|_{\text{global analysis}}=19^{+12}_{-9}\times10^3\ \text{cm}^{-2}\,\text{s}^{-1}, \tag{19}$$

which is consistent with the previously given experiment bound.

An extraction of the hep flux from the experiment will likely require a detailed shape analysis to separate hep neutrinos from the high-energy tail of the ^{8}B spectrum and the low-energy tail of atmospheric neutrinos. Typically the hep spectrum is assumed to have an allowed shape: indeed, in the work reported here, spectra are not provided, whereas p waves, weak magnetism, and similar corrections have been included. Because these corrections are unusually large for hep neutrinos, future studies should provide spectra and evaluate the impact of such corrections on the shape.

VIII. ELECTRON CAPTURE BY $p+p$ AND ^{7}Be

Electron-capture reactions are the sources of lines found in the solar neutrino spectrum. In particular, electron capture on $p+p$, i.e., the process $p+p+e^-\to d+\nu_e$, also known as the pep reaction, competes with $p+p$ fusion and depends on the same nuclear matrix element. Therefore, the ratio between the pp and pep rates is independent of nuclear physics. Based on this consideration, Adelberger *et al.* (2011) multiplied the result of Adelberger *et al.* (1998), which is based on the work of Bahcall and May (1969), by the radiative corrections calculated by Kurylov, Ramsey-Musolf, and Vogel (2003), leading to the final result given by

$$\begin{aligned}R(pep)&=1.130(1\pm0.01)\times10^{-4}(\rho/\mu_e)\\&\quad\times T_6^{-1/2}[1+0.02(T_6-16)]R(pp),\end{aligned} \tag{20}$$

where ρ is the density in units of g/cm^3, μ_e is the mean molecular weight per free electron, and T_6 is the temperature in megakelvins. The range of validity is $10<T_6<16$. Given

that no new evaluation of the pep rate has been performed since that of Adelberger *et al.* (2011), the result of Eq. (20) also represents the present recommended value.

Competition between electron and proton capture on ^{7}Be fixes the branching ratio of the pp-II and pp-III chains, and thereby the ^{7}Be and ^{8}B neutrino fluxes. Superallowed electron capture on the $J^\pi = 3/2^-$ ground state of ^{7}Be leads to the $J^\pi = 3/2^-$ ground state or the $J^\pi = 1/2^-$, 478 keV first excited state of ^{7}Li with a measured (terrestrial) branching ratio of 10.44(4)% (Tilley *et al.*, 2002). It is customary to calculate the solar decay rate in terms of the measured terrestrial decay rate, which has the advantage of removing the nuclear physics dependence, but it requires a proper calculation of the densities of electrons at the nucleus. This has usually been done by considering continuum and bound electrons separately, using the Debye-Hückel approximation pioneered by Salpeter (1954) for the screening of bound electrons in the solar plasma; the capture rate of continuum electrons is not significantly influenced by electron screening. Furthermore, it is necessary to calculate the atomic probability densities governing the K and L terrestrial electron-capture rates. Fretwell *et al.* (2020) measured the ratio of L to K capture using superconducting tunnel junctions. The recommendation of Adelberger *et al.* (1998, 2011) was

$$R(^7\mathrm{Be} + e^-) = 5.60(1 \pm 0.02) \times 10^{-9}(\rho/\mu_e)T_6^{-1/2}[1 + 0.004(T_6 - 16)]\ \mathrm{s}^{-1}, \tag{21}$$

which is valid for $10 < T_6 < 16$. Equation (21) is based on the continuum capture rate calculated by Bahcall and Moeller (1969), with the average ratio of the total capture rate to the continuum rate calculated using three solar models from Bahcall (1994) and the current value of the half-life given as 53.22(6) d (Tilley *et al.*, 2002). It agrees within 1% with a density matrix calculation of the rate that makes no assumptions regarding the nature of electronic quantum states in the solar plasma and allows for aspherical fluctuations in the spatial distributions of plasma ions (Gruzinov and Bahcall, 1997). The estimated uncertainty of 2% accounts for possible corrections to the Debye-Hückel approximation due to thermal fluctuations in the small number of ions in the Debye sphere and breakdowns in the adiabatic approximation (Johnson *et al.*, 1992).

Although calculations have appeared in the literature claiming new plasma effects based on model calculations [see Simonucci *et al.* (2013) and Vescovi *et al.* (2019), we continue to regard the arguments of Bahcall *et al.* (2002) as definitive. They presented five distinct derivations demonstrating that the Salpeter formula for screening corrections is valid for pp-chain reactions and solar conditions up to corrections on the order of a few percent.

IX. THE ^{7}Be$(p,\gamma)^8$B REACTION (S_{17})

A. Introduction

Radiative proton capture on ^{7}Be ($J^\pi = 3/2^-$) at solar energies proceeds through nonresonant capture to the ground state of ^{8}B ($J^\pi = 2^+$). This capture occurs predominantly at separations well beyond the range of the strong interaction via $E1$ transitions from s and d partial waves, as the $M1$ amplitude and contributions from higher partial waves are negligible in the energy range of interest (Christy and Duck, 1961). The importance of this reaction for the determination of the high-energy solar neutrino spectrum and the experimental data reviewed by Adelberger *et al.* (1998) inspired several experiments that, taken together, provided a consistent picture of the energy dependence of the reaction cross section, despite discrepancies in absolute scale. Prior to the review of Adelberger *et al.* (2011), most direct measurements were performed using a radioactive target and an intense proton beam. In spite of the great care taken in evaluating the systematic energy-independent uncertainties, in the following referred to as common-mode errors (CMEs), a noteworthy discrepancy persisted even in the most recent experiments that was finally handled by Adelberger *et al.* (2011) by inflating the stated experimental uncertainties. Indirect measurements of the cross section of ^{7}Be$(p,\gamma)^8$B based on Coulomb dissociation were considered but not included in the final recommendation of Adelberger *et al.* (2011) for the zero-energy astrophysical S factor $S_{17}(0)$. However, despite the experimental issues, the uncertainty on the recommended value of $S_{17}(0)$ given by Adelberger *et al.* (2011) is dominated by the theoretical contribution. Therefore, our analysis focused on these aspects (discrepancies in the experimental data, indirect measurements, and theoretical uncertainties), as discussed in the remainder of Sec. IX.

B. Experimental data

1. Direct measurements

The thorough review of published work done by Adelberger *et al.* (2011) investigated the influence of beam-target overlap, target stoichiometry, beam energy loss, and the backscattering of ^{8}B recoils on CMEs and led to the selection of a homogeneous group of well-documented datasets. Since then, no further information has become available on these aspects of direct measurements. The data that formed the basis of the recommendation of Adelberger *et al.* (2011) were those of Hammache *et al.* (1998, 2001), Hass (1999), Strieder *et al.* (2001), and Baby *et al.* (2003a, 2003b) and the BE3 dataset of Junghans *et al.* (2003). We considered the complete set of radiative-capture measurements that were the basis of the recommendation of Adelberger *et al.* (2011) for $S_{17}(0)$, where we adopted the revised BE3 data presented by Junghans *et al.* (2010), which were reanalyzed using a more sophisticated model of the target and more accurate stopping powers. In addition, we included in our analysis the only new experiment reported thereafter of Buompane *et al.* (2022), which used a radioactive ^{7}Be ion beam and the recoil mass separator ERNA to detect the ^{8}B recoils. While these new results contribute to the determination of S_{17} with

different, well controlled systematics (Buompane *et al.*, 2018), their large statistical uncertainty relative to the other experiments, owing to the low counting statistics, limits their impact.

New scattering data have been published. Elastic- and inelastic-scattering cross sections at relative kinetic energies between 474 keV and 2.74 MeV were measured and s-wave scattering lengths were inferred by Paneru *et al.* (2019). At higher energies between 1.6 and 3.4 MeV, thick-target elastic and inelastic-scattering excitation function measurements were used to infer the existence of new resonances above 1.8 MeV (Mitchell *et al.*, 2013). These high-lying resonances have no direct influence on $S_{17}(0)$, because of their small partial widths in the $^7\mathrm{Be}_{\mathrm{gs}} + p$ channel and/or because they cannot be populated by s- or d-wave capture at low energy.

2. Indirect measurements

Adelberger *et al.* (2011) considered Coulomb dissociation measurements based on the formalism developed by Baur, Bertulani, and Rebel (1986) (Motobayashi *et al.*, 1994; Kikuchi *et al.*, 1997, 1998; Iwasa *et al.*, 1999; Davids *et al.*, 2001; Davids, Austin *et al.*, 2001; Schümann *et al.*, 2003) where, in some cases, the most recent publications supersede the previously published ones. Finally, the results of these experiments were not included in the determination of $S_{17}(0)$, owing to disagreements over whether the analyses of the various measurements properly accounted for the contributions of $E2$ transitions. We disagree with these reservations and find the agreement of these measurements with radiative-capture measurements significant. However, to include these consistent data in formulating our recommendation for $S_{17}(0)$, we inflated the CMEs of the Coulomb breakup measurements to adequately account for the uncertainty in the $E2$ components assumed in each analysis.

The common-mode errors are obtained from a linear sum of those given in the manuscripts and an additional common-mode error due to the estimated size of the $E2$ component in each measurement. This additional error is applicable in one direction only, downward for the analyses of Kikuchi *et al.* (1998) and Schümann *et al.* (2006) of the RIKEN and GSI measurements, respectively, and upward for the analysis of Davids and Typel (2003) of the Michigan State University (MSU) measurement, dependeing upon whether the $E2$ component was included or excluded. Though the analysis of Davids and Typel (2003) did include a common-mode error contribution of 2.5% due to the $E2$ component (which represented 5% of the total cross section), we have included an additional 2.5% contribution to the MSU experiment. The size of the additional common-mode errors for the RIKEN and GSI measurements was based on scaling this 2.5% according to the predicted size of the $E2$ contribution to the cross section in these measurements relative to that in the MSU measurement, evaluated using first-order perturbation theory and the $E1$ and $E2$ S factors calculated in a potential model of ^{8}B (Bertulani, 1996). Thus, the additional single-sided common-mode errors added to the GSI, MSU, and RIKEN measurements are −2.1%, 2.5%, and −4.3%, respectively.

C. Theory

The size of the theoretical contribution to the uncertainty in the $S_{17}(0)$ estimate of Adelberger *et al.* (2011) was twice that of the experimental contribution. Since that estimate, significant progress has been made. A new potential-model calculation was performed by Dubovichenko *et al.* (2019). The large-scale computational demands of calculations using high-quality NN and three-nucleon (3N) interactions beyond $A = 5$ hindered the *ab initio* approach in the past. Nevertheless, progress has been rapid, and it has been possible to extend *ab initio* calculations to $^7\mathrm{Be}(p,\gamma)^8\mathrm{B}$, albeit without 3N forces. Navrátil, Roth, and Quaglioni (2011) performed such a calculation using the no-core shell model in the continuum with a nucleon-nucleon interaction derived from chiral EFT at the fourth order. The calculation converged with respect to the model space size and reproduces experimental data for the S factor despite having virtually no free parameters (though the similarity renormalization group evolution parameter was tuned to reproduce the binding energy of ^{8}B). The final value of $S_{17}(0) = 19.4(7)$ eV b agrees with the reecommendation of Adelberger *et al.* (2011) and, as later shown, with our analysis. More recently, a new approach was introduced to combine experimental measurements with *ab initio* predictions, resulting in an "*ab initio*–informed evaluation" (Kravvaris *et al.*, 2023) that arrived at a value of $S_{17}(0) = 19.8(3)$ eV b.

A significant theoretical advance was the application of the formalism of halo EFT developed by Bertulani, Hammer, and van Kolck (2002) to $^7\mathrm{Be}(p,\gamma)^8\mathrm{B}$ calculations by Zhang, Nollett, and Phillips (2015, 2018) and Higa, Premarathna, and Rupak (2022). This application treats the incoming p and ^{7}Be as pointlike particles and the ^{8}B final state as a bound state of the two. The calculation and the associated errors depend upon the accuracy with which one is able to describe the incoming scattering states, the final bound state, and the relevant electromagnetic currents. The relative kinetic or c.m. energy range $E \lesssim 1$ MeV, corresponding to a relative momentum $p \lesssim 40$ MeV/c, is considered to be within the domain of applicability of halo EFT. The two cluster physical description of $^7\mathrm{Be}(p,\gamma)^8\mathrm{B}$ is expected to hold at ^{3}He-α relative momenta below the physical cutoff $\Lambda \sim 70$ MeV/c set by the threshold (binding momentum) for breaking the ^{7}Be core into these constituents. Further, at energies above the excitation energy of the first excited state, $E_\star = 0.4291$ MeV, including the contribution of the excited core $^7\mathrm{Be}^\star$ is imperative in the EFT.

Zhang, Nollett, and Phillips (2015, 2018) included such an excited ^{7}Be contribution. Higa, Premarathna, and Rupak (2022) provided a calculation without the $^7\mathrm{Be}^\star$ contribution below $E_\star$ and one with it above $E_\star$ that also included an $M1$ contribution to the 1^+ resonance. The two groups' halo EFT calculations with the $^7\mathrm{Be}^\star$ contributions differ in several respects that were elaborated by Higa, Premarathna, and Rupak (2022). Differences in the final bound-state calculation affect the treatment of the short-range interactions and divergences in the EFTs. The interpretation of the ANCs in terms of the elastic-scattering parameters is affected. However, the momentum dependence of the capture cross section is not impacted by the ANCs, which are fitted to capture data.

Thus, there is no effect on the cross section. In the incoming channel, Higa, Premarathna, and Rupak (2022) used a more general form of the s-wave short-range interaction involving the ^{7}Be* core based on the low-energy symmetry that is included only at NNLO. In contrast, Zhang, Nollett, and Phillips (2015, 2018) included a short-range interaction at LO that could make a difference in the momentum dependence of the cross section. However, as shown in an order-by-order calculation (Higa, Premarathna, and Rupak, 2022), the short-range interaction is a subleading effect, so the two halo EFTs should have a similar low-momentum dependence. The third important difference is in the treatment of two-body currents, which affects EFT error estimates. Zhang, Nollett, and Phillips (2015, 2018) included this at NLO, whereas Higa, Premarathna, and Rupak (2022) estimated it to be an N^{3}LO effect. Bayesian estimates of the two-body current (Zhang, Nollett, and Phillips, 2015, 2018) are not strongly constrained by capture data, which is consistent with this being a higher-order contribution.

Another widely used approach for describing the cross sections of low-energy nuclear reactions is R-matrix theory. In R-matrix theory, the $^7\mathrm{Be}(p,\gamma)^8\mathrm{B}$ cross section can be parametrized in terms of a few parameters representing either "real" or "background" poles. The real poles correspond to the observed states and resonances, while the background terms correspond to the mean-field effects that are of the nonresonant type. In this case a background pole in the 1^- channel is needed to reproduce the nonresonant $E1$ part of the capture. The parameters of the real pole corresponding to the bound state are determined by the binding energy and the two ANCs, while the 1^+ resonance parameters are determined by its energy and partial decay widths (both proton and radiative). The R-matrix analysis of this reaction carried out by Barker (1995) arrived at a value of $S_{17}(0) = 17(3)$ eV b. However, it was based on data that were excluded by Adelberger *et al.* (2011) and here, with the exception of those of Filippone *et al.* (1983).

We fit data using R-matrix theory and halo EFTs, with both frequentist and Bayesian approaches, investigating the impact of different choices for the energy range in which data were fitted, and obtained consistent results. Our recommended $S_{17}(0)$ value and its uncertainty are based on a Bayesian fit of both direct and Coulomb dissociation data taken at energies $E \leq 1250$ keV using the halo EFT$_\star$ of Higa, Premarathna, and Rupak (2022). This theory provides a good description of capture data over a wide energy range, including the $M1$ contribution from the 1^+ resonance. The theoretical uncertainties are well understood. Further, the contributions of the $S = 1$ and 2 spin channels to the capture cross section are self-consistently parametrized with the elastic-scattering information contained in the known ANCs for this system.

The Bayesian formalism incorporates prior information concerning the ANCs in the fits. The upper limit on the energy in the fit was determined to be high enough to include some data from all the modern experiments, yet low enough that the contribution of the wide 3^+ resonance at $E \approx 2456$ keV does not exceed 1% of the total cross section at any energy, as estimated by our R-matrix analysis. The fitting procedure is described in Sec. IX.D, whereas the details, as well as the results of the fits done at different energy ranges and with different theories, are reported in the Supplemental Material (681).

D. Fitting procedures

Adelberger *et al.* (2011) noted that the different $S_{17}(E)$ datasets had similar energy dependences. The discrepancies among the datasets were due primarily to different absolute normalizations. We address the normalization issue by introducing scaling factors associated with the CMEs. This contrasts with the approach of Adelberger *et al.* (2011), in which the errors were inflated by the factor $\sqrt{\chi^2/\chi^2(P=0.5)}$. The procedure for handling discrepant datasets adopted here is mathematically rigorous and naturally aligns with the method of estimating theoretical uncertainty discussed later. We prefer this approach to the inflation factor method used by Adelberger *et al.*, 2011) since the absolute scales of the different datasets can be used as constraints for each other, while there is no information available for a reevaluation of the CMEs. The procedure that we used (described later) can be applied to both frequentist and Bayesian analyses.

Although our final recommendation is based on Bayesian analysis alone, both χ^2 minimization (a frequentist approach) and Bayesian posterior probability distribution function evaluation were performed to fit EFTs to the data. In the R-matrix analysis, only the former was used. The likelihood function defined as the conditional probability $P(D|\boldsymbol{\theta})$ for the data D given theoretical parameters $\boldsymbol{\theta}$ enters both fitting procedures. It can be derived from the χ^2 expression given by D'Agostini (1994),

$$P(D|\boldsymbol{\theta},\boldsymbol{s}) = \prod_{\alpha=1}^{N_{\mathrm{set}}} \frac{1}{\sqrt{2\pi\omega_\alpha^2}} \exp\left[-\frac{(1-s_\alpha)^2}{2\omega_\alpha^2}\right] \times \prod_{i=1}^{N_\alpha} \frac{1}{\sqrt{2\pi\sigma_{\alpha,i}^2}} \exp\left\{-\frac{[y_{\alpha,i}-\mu_{\alpha,i}(\boldsymbol{\theta})/s_\alpha]^2}{2\sigma_{\alpha,i}^2}\right\}, \quad (22)$$

with $\alpha = 1, \ldots, N_{\mathrm{set}}$ labeling the different experimental datasets and $i = 1, \ldots, N_\alpha$ labeling the individual data points of each experiment. In the second term of Eq. (22), we divide theoretical predictions $\mu_{\alpha,i}(\boldsymbol{\theta})$ for the data points of the experiment α by a scaling factor s_α and consider the combination as our full model for $y_{\alpha,i}$, the ith data point of experiment α with point-to-point uncertainty $\sigma_{\alpha,i}$.

In the first term of Eq. (22), we assign s_α a Gaussian distribution centered at 1 with a width equal to the CME ω_α. For the GSI, MSU, and RIKEN data shown in Table VIII, asymmetric Gaussians are used with ω_α depending on the sign of $1 - s_\alpha$. In our χ^2 minimization, the χ^2 definition is derived from equating the full exponents in Eq. (22) to $-\chi^2/2$. In the absence of CMEs with $s_\alpha = 1$, Eq. (22) leads to the usual uncorrelated least-squares minimization formula.

In the Bayesian analysis, the terms in the first exponential are considered as part of the prior distribution $P(\boldsymbol{\theta},\boldsymbol{s})$ that are conditioned on prior knowledge and assumptions such as the CMEs $\boldsymbol{\omega}$ in the scaling factors $\boldsymbol{s}$ or estimates of theoretical

parameters $\boldsymbol{\theta}$ in the EFT. The posterior distribution for the theoretical parameters is then derived via Bayes's theorem,

$$P(\boldsymbol{\theta}, \boldsymbol{s}|D) = \frac{P_{\text{Bayes}}(D|\boldsymbol{\theta})P(\boldsymbol{\theta}, \boldsymbol{s})}{P(D)}, \tag{23}$$

where the likelihood function $P_{\text{Bayes}}(D|\boldsymbol{\theta})$ is defined without the first exponential in Eq. (22). However, since the GSI, MSU and RIKEN data have asymmetric CMEs, we draw priors from a uniform distribution spanning 50% to 150% of the central values for these that are then used in the asymmetric normalization exponentials in the likelihood function. This was computationally simpler than generating asymmetric Gaussian priors that span the entire $(-\infty, \infty)$ range, which is neither necessary nor physical for a normalization constant.

The constant $P(D)$ in Eq. (23), known as the Bayesian evidence, guarantees the correct normalization of the posterior distribution. It is useful in comparisons of different theories but does not affect the estimation of parameters.

E. Data analysis and S_{17} determination

We performed χ^2 fits using several theoretical expressions over multiple energy ranges: $E \leq 475$ keV, $E \leq 1250$ keV, and over a nonresonant energy range $E \leq 490$ keV and 805 keV $\leq E \leq 1250$ keV, in which the $M1$ contribution from the 1^+ resonance can be ignored. Fits with and without Coulomb dissociation data were performed that resulted in overlapping $S_{17}(0)$ determinations within the estimated fitting uncertainties. The different low-energy $E \leq 475$ keV fits included one using the halo EFT from Zhang, Nollett, and Phillips (2018) and one using the halo EFT$_\star$ from Higa, Premarathna, and Rupak (2022), with both including the excited ^{7}Be contribution. The simpler halo EFT$_{\text{gs}}$ expressions, not including an excited component ^{7}Be*, were also fitted in this low-energy region with comparable results. For the fits in the other two energy ranges, halo EFT expressions with excited ^{7}Be* contributions from both Zhang, Nollett, and Phillips (2018) and Higa, Premarathna, and Rupak (2022) were used. The halo EFT expression of Zhang, Nollett, and Phillips (2018), which does not include an $M1$ contribution, was supplemented with a Breit-Wigner resonance (Rolfs and Rodney, 1988) with its energy (around the 1^+ resonance energy $E \approx 630$keV), width, and proton-decay branching ratio determined by the fits. An R-matrix model was fitted to data in the three energy regions with the AZURE2 code (Azuma *et al.*, 2010), again resulting in an $S_{17}(0)$ consistent with the halo EFT values. The results from the various fits are included in the Supplemental Material (681).

Bayesian fits were performed with halo EFT expressions from both Higa, Rupak, and Vaghani (2018) and Zhang, Nollett, and Phillips (2020) that are compatible with the various χ^2 fits. The Bayesian analysis had advantages over the χ^2 fits in exploring parameter space and in determining realistic uncertainties (King *et al.*, 2019).

The $^7\text{Be}(p,\gamma)^8\text{B}$ capture proceeds through the $S = 2$ and 1 channels. The reaction is known to be peripheral, resulting in an $S_{17}(0)$ that has a subleading dependence on the strong interaction in the initial state (Baye, 2000). This behavior was shown to persist away from the threshold in halo EFT, in which for $E1$ capture the strong interaction in the incoming s-wave channel contributes only at NNLO.

Therefore, to the high order, the capture is sensitive only to the sum of the squares of the ANCs in the $S = 2$ and 1 channels. This results in an arbitrariness in the relative contributions from the two spin channels in the χ^2 fits without affecting the final S_{17} determination. R-matrix, EFT$_{\text{gs}}$, and EFT$_\star$ fits confirm this behavior. However, the ANCs have been extracted experimentally (Trache *et al.*, 2003; Tabacaru *et al.*, 2006) and also theoretically (Nollett and Wiringa, 2011; Zhang, Nollett, and Phillips, 2018) in *ab initio* calculations. Although the determination of $S_{17}(0)$ is insensitive to the relative contributions of the two spin channels, knowledge of the relative contributions of the ANCs is important in the EFT framework. It establishes the hierarchy of different contributions in the perturbative expansion. This is crucial in developing a self-consistent expansion that is necessary to quantify the theoretical errors at any finite order of the perturbation. Prior knowledge of the ANCs and other parameters can be accounted for naturally in the Bayesian framework in which one specifies the prior probabilities $P(\boldsymbol{\theta}, \boldsymbol{s})$. Similar constraints can be included in the χ^2 fit by modifying the first exponential in Eq. (22) to center the theoretical parameters around known values.

The Bayesian fits involved six theoretical parameters and 11 normalization constants s_α for the datasets. The priors for the normalization constants were as described earlier. The priors for the theoretical parameters are based on the underlying EFT assumptions (Higa, Premarathna, and Rupak, 2022) about the expansion in a small ratio Q/Λ, where $Q \sim 40$ MeV$/c$ represents the low momentum of infrared physics and $\Lambda \sim 70$ MeV$/c$ indicates the cutoff of the theory. The $^5S_2$ and $^3S_1$ scattering lengths $a_0^{(2)} = -3.18^{+0.55}_{-0.50}$ fm and $a_0^{(1)} = 17.34^{+1.11}_{-1.33}$ fm (Paneru *et al.*, 2019) are taken as inputs. For $E1$ capture at LO, the only fit parameter, the $^5P_2$ effective momentum ρ, is assumed to scale as Q, and accordingly we assume a uniform prior for ρ between -100 and 1.5 MeV$/c$, where the upper limit is set by the physical constraint that the ANC squares have to be positive. At NLO the $^3P_2$ ANC^2 $C_{1,1}^2$ is a fit parameter whose prior is taken from a normal distribution determined by experiment. At NNLO we use the *ab initio* calculation of Zhang, Nollett, and Phillips (2018) to draw the $^3P_2^\star$ ANC^2 from a normal distribution. A ratio of the s-wave scattering lengths in the coupled-channel $^3S_1$-$^3S_1^\star$ that is assumed to be $\mathcal{O}(1)$ in the EFT is drawn from a normal distribution with a mean of 0 and a standard deviation of 10 to cover a wide range. The $M1$ capture is dominated by the transition $^5P_1 \to {}^5P_2$, and it requires three parameters: a p-wave scattering volume a_1, an effective momentum r_1, and a two-body current to regulate divergences. Higa, Premarathna, and Rupak (2022) determined $a_1 = -108.13$ fm^3 and $r_1 = -111.23$ MeV from the narrow 1^+ resonance energy and width. Here we kept a_1 fixed while drawing r_1 from a uniform distribution between -150 and -50 MeV. The Bayesian fit gave $r_1 \sim -111.23$ MeV. The two-body coupling was drawn from a uniform distribution, and the fits gave a

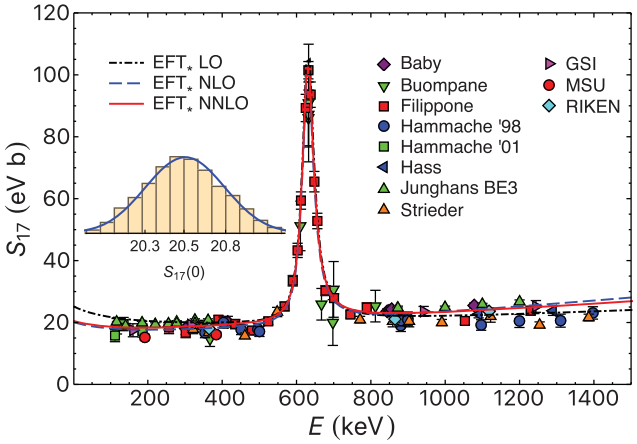

FIG. 8. Astrophysical S factor for $^7\mathrm{Be}(p,\gamma)^8\mathrm{B}$. Data with $E \leq 1250$ keV were included in the Bayesian fits shown here, which use the halo EFT of Higa, Premarathna, and Rupak (2022) that includes an excited ^{7}Be component. The dot-dashed black curve is the LO calculation, the dashed blue curve is NLO, and the solid red curve is NNLO. Inset: posterior probability distribution function for $S_{17}(0)$ in eV b. The median as well as the 16th and 84th percentiles of the distribution are specified.

numerical value consistent with the EFT estimate. We obtain the posterior distribution $P(\boldsymbol{\theta}, \boldsymbol{s}|D)$ using a probabilistic integration method called nested sampling (Skilling, 2006) implemented in `Python` (Feroz, Hobson, and Bridges, 2009) that calculates both the posterior and the evidence.

The experimental data and EFT$_\star$ fits at LO, NLO, and NNLO are shown in Fig. 8. S_{17}, and its derivatives at threshold are given in Table VII. The quality of the fits, the consistency of the numerical values of the fit parameters with EFT assumptions, and the order-by-order improvement in the numerical value of the fitted capture cross section and S factor give us confidence in the estimated theoretical uncertainty. We find the posterior probability distribution functions to be symmetric and well described by Gaussians, and as such we report the mean and standard deviation in Table VII. Table VIII gives the scaling factors for the experimental datasets determined from the NNLO fit along with their common-mode errors.

F. Theoretical uncertainty

The theoretical uncertainties in halo EFT are estimated from the perturbative expansion in Q/Λ (Higa, Premarathna, and Rupak, 2022). Q is associated with the physics at low momenta of interest: relative momentum $p \lesssim 40$ MeV$/c$, binding momentum $\gamma \sim 15$ MeV$/c$, inverse Bohr radius $\kappa_C \sim 24$ MeV$/\hbar c$, excitation momentum $\gamma_\Delta \sim 27$ MeV$/c$, and resonance momentum $p_R \sim 32$ MeV$/c$. The cutoff scale of $\Lambda \sim 70$ MeV is estimated as previously described. Except for a narrow momentum range around the 1^+ resonance, capture is dominated by $E1$ transitions from s and d waves that preserve the channel spin. Thus, the threshold theoretical estimates of $S_{17}(0)$ are based on $E1$ capture. The ANC for the $^5P_2$ final bound channel is known to be about 5 times larger than the $^3P_2$ bound channel, so capture in the $S = 2$ channel dominates. The LO contribution in the Q/Λ expansion comes only from s-wave Coulomb interactions in the $S = 2$ channel. The weakly bound ^{8}B state enables peripheral capture without initial-state strong interactions.

At NLO d-wave Coulomb interactions in the $S = 2$ channel and s-wave Coulomb interactions in the $S = 1$ channel are added. Strong interactions in the initial s and d waves of the $S = 1$ channel contribute at NNLO. Perturbatively, the s-wave scattering lengths $a_0^{(1)}$ and $a_0^{(2)}$ contribute at this order. Though $a_0^{(1)}$ is much larger than $a_0^{(2)}$, the $S = 1$ channel is 1 order higher in the perturbation, making these contributions comparable. We also see mixing in the coupled $^3S_1$-$^3S_1^\star$ channels due to the excited core contribution, which is parametrized by scattering lengths. The mixing requires the $^3P_2^\star$ ANC in the capture cross section. The theory error is estimated as 30% at LO, 10% at NLO, and 3% at NNLO from an estimated $Q/\Lambda \sim 1/3$. This is validated by the relative sizes of the cross section at different orders of the perturbation, and also by the sizes of the fitted parameters that are consistent with theoretical estimates.

The uncertainty from the higher-order contributions is estimated as follows. Two-body currents make a relative contribution $\sim k_0 a_0 L_{E1}$ with photon energy $k_0 = (p^2+\gamma^2)/(2\mu) \sim Q^3/\Lambda^2$. In the $S = 2$ channel, $a_0^{(2)} \sim 1/\Lambda$, so this is a N^{3}LO contribution. In the $S = 1$ channel, the larger $a_0^{(1)} \sim 1/Q$ makes this a Q^2/Λ^2 contribution; however, this spin channel is suppressed by 1 order in the perturbation. Thus, two-body currents constitute a N^{3}LO 3% uncertainty; s-wave effective-range corrections would also constitute a N^{3}LO

TABLE VII. S_{17} and its first two energy derivatives at $E = 50$ eV determined from Bayesian fits of experimental data below 1250 keV using the halo EFT of Higa, Premarathna, and Rupak (2022) that includes an excited ^{7}Be component. The first error in each is from the fit. The second error is the estimated LO (30%), NLO (10%), and NNLO (3%) EFT error, respectively, from higher-order corrections.

Theory	S_{17} (eV b)	S'_{17}/S_{17} (MeV^{-1})	S''_{17}/S_{17} (MeV^{-2})
LO	25.2(3)(76)	−2.44(4)(73)	35.8(6)(108)
NLO	20.2(2)(20)	−2.02(4)(20)	33.3(6)(33)
NNLO	20.5(3)(6)	−1.86(4)(6)	31.9(6)(10)

TABLE VIII. Scaling factors for the datasets at NNLO, the number of data points used in the $E \leq 1250$ keV fits, and the common-mode errors.

Dataset	Scaling	Data points	CME
Baby	0.97(1)	8	2.22%
Buompane	1.08(3)	9	4.0%
Filippone	1.03(2)	25	11.9%
Hammache '98	1.11(3)	12	5.7%
Hammache '01	1.06(4)	3	11.5%
Hass	1.02(3)	1	3.6%
Junghans BE3	0.93(1)	18	2.67%
Strieder	1.13(2)	9	8.3%
GSI	0.99(3)	4	(−7.7%, +5.6%)
MSU	1.16(4)	2	(−7.1%, +9.6%)
RIKEN	1.05(2)	3	(−12.7%, +8.4%)

uncertainty. Initial-state d-wave interactions (suppressed by 2 powers of momentum) in the $S = 2$ channel also constitute a N^{3}LO uncertainty. The uncertainty in the experimental determination of the s-wave scattering lengths is included in the 3% N^{3}LO uncertainty.

G. Conclusions and recommendation for S_{17}

R-matrix and EFT fits of direct and Coulomb dissociation data below 1250 keV, where the influence of resonances other than the 1^+ can be neglected, were carried out. Many different theories and energy ranges were considered, and consistent results were obtained. Our recommendation was obtained using the halo EFT of Higa, Premarathna, and Rupak (2022) that includes an excited ^{7}Be component. This theory was selected owing to the generality and rigor of its treatment of short-range interactions in the initial and final states and of two-body currents, as well as its inclusion of $M1$ transitions and robust uncertainty quantification. The resulting recommendation is $S_{17}(0) = 20.5(3)(6)$ eV b, where the first error is due to fitting and the second is due to neglected higher-order contributions. For the purposes of solar modeling, we intend that the two errors be added together in quadrature and recommend $S_{17}(0) = 20.5(7)$ eV b.

The recommended $S_{17}(0)$ has a notably smaller uncertainty than the value of Adelberger *et al.* (2011) for two primary reasons. Significant theoretical developments in halo EFT with a NNLO calculation have reduced the theoretical uncertainty by a factor of 2. The use of floating data normalization factors allows discrepant datasets to be brought into agreement for low-energy extrapolation without inflating the measurement uncertainties. In the Bayesian fits, the normalization factors are assigned priors, as is done for some of the theoretical parameters. Frequentist fits presented in the Supplemental Material (681) include these in the definition of the χ^2 cost function. Normalization factors other than unity increase the cost, but the overall cost is lowered by bringing precise measurements from different datasets into agreement. This is effective because the number of scale factors is much less than the number of high-precision data points. Owing to the small uncertainties and large number of data points, the measurement of Junghans *et al.* (2010) exerted a strong influence on the fit. Planned measurements, such as those recently approved at $E = 1$ and 1.2 MeV using a ^{7}Be beam and the DRAGON recoil separator at TRIUMF, must have comparably small statistical and systematic uncertainties in order to compete effectively.

X. THE ^{14}N$(p,\gamma)^{15}$O REACTION (S_{114})

The ^{14}N$(p,\gamma)^{15}$O reaction proceeds through a number of bound-state transitions, but the total capture cross section is dominated by the capture to the 6.79 MeV state ($3/2^+$) in ^{15}O. [In this section the reported level energies are taken from the most recent compilation of Ajzenberg-Selove (1991).] The contribution of this transition to the total reaction cross section at solar energies is 71%–78% (Azuma *et al.*, 2010; Adelberger *et al.*, 2011). The second-strongest transition, with a contribution of 16% to 17%, is the capture to the ground state of ^{15}O, while the capture to the 6.18 MeV state ($3/2^-$) is responsible for about 7% to 8% of the total cross section. The remaining 5%–7% is attributed to the capture to the other bound states (i.e., 5.18 MeV, $1/2^+$; 5.24 MeV, $5/2^+$; 6.86 MeV, $5/2^+$; and 7.28 MeV, $7/2^+$).

Adelberger *et al.* (2011) recommended a lower value, with a greatly reduced uncertainty, for $S_{114}(0)$ of 1.66(12) keV b compared to that of Adelberger *et al.* (1998), $3.5^{+0.4}_{-1.6}$ keV b. This was the result of the following: the new implementation of the more rigorous R-matrix technique (Angulo and Descouvemont, 2001) over the previously used Breit-Wigner analysis, higher precision low-energy capture datasets (Formicola *et al.*, 2004; Imbriani *et al.*, 2005; Runkle *et al.*, 2005; Bemmerer *et al.*, 2006b; Lemut *et al.*, 2006; Marta *et al.*, 2008) over the yields presented by Schröder *et al.* (1987), transfer measurements of proton ANCs for the bound states (Bertone *et al.*, 2002; Mukhamedzhanov *et al.*, 2003), and constraints on the lifetime of the 6.79 MeV bound state (Bertone *et al.*, 2001; Schürmann *et al.*, 2008). Since the work of Adelberger *et al.* (2011), several new experiments and R-matrix calculations have been completed, but our understanding of the ground-state transition remains incomplete.

A. Current status and results

Since the work of Adelberger *et al.* (2011), several new measurements have been reported for the capture reaction (Daigle *et al.*, 2016; Li *et al.*, 2016; Wagner *et al.*, 2018; Gyürky, Halász *et al.*, 2019; Sharma *et al.*, 2020; Frentz *et al.*, 2022; Gyürky *et al.*, 2022), the lifetime of the 6.79 MeV state (Galinski *et al.*, 2014; Sharma *et al.*, 2020; Frentz *et al.*, 2021), the proton bound-state ANCs (Artemov *et al.*, 2012), and a measurement of the low-energy ^{14}N$(p,p)^{14}$N scattering cross section (deBoer *et al.*, 2015). These and past works have included several R-matrix fits (Angulo and Descouvemont, 2001; Formicola *et al.*, 2004; Imbriani *et al.*, 2005; Runkle *et al.*, 2005; Li *et al.*, 2016; Wagner *et al.*, 2018; Frentz *et al.*, 2022), resulting in a range of different approaches to the fitting, which gives insight into the systematic uncertainties of the model.

The recommended partial $S(0)$ values are discussed in Sec. X.E. The 6.79 MeV transition, as it is the strongest, has received a great deal of experimental attention. Its ease of measurement and relatively well-understood reaction contributions result in a small uncertainty in the low-energy extrapolation of the S factor of ≈3%. The ground-state and 6.18 MeV transitions have uncertainties of ≈40%, owing mainly to the complexity of the underlying reaction contributions and the much smaller cross section.

B. Absolute strength of the 259 keV resonance

The $E = 259$ keV resonance in ^{14}N$(p,\gamma)^{15}$O is used as a reference for normalization in many experiments because it is a narrow resonance, it has a precisely known strength, and it has γ-ray transitions that span a wide energy range. The absolute strength of the resonance has been determined in three works (Daigle *et al.*, 2016; Gyürky, Halász *et al.*, 2019; Sharma *et al.*, 2020) since the work of Adelberger *et al.*

TABLE IX. Summary of the $E = 259$ keV resonance strength values along with their total uncertainties. The last row gives the recommended value with its total uncertainty.

Reference or note	$\omega\gamma_{259}$ (meV)
Becker *et al.* (1982)[a]	13.7 ± 1.0
Runkle *et al.* (2005)[a]	12.4 ± 0.9
Imbriani *et al.* (2005)	12.9 ± 0.9
Bemmerer *et al.* (2006b)	12.8 ± 0.6
Daigle *et al.* (2016)	12.6 ± 0.6
Gyürky, Halász *et al.* (2019)	13.4 ± 0.8
Sharma *et al.* (2020)	12.8 ± 0.9
SF III recommended value	12.9 ± 0.5

[a]As given by Daigle *et al.* (2016).

(2011). Based largely on the work of Daigle *et al.* (2016), a new resonance strength of $\omega\gamma_{259} = 12.86 \pm 0.45$ meV, which is consistent with the previous value but with higher precision thanks to the new datasets, is recommended. For the averaging we adopted the approach followed by Adelberger *et al.* (2011). The common systematic uncertainty of the nitrogen stopping power of 2.9% (Ziegler, Ziegler, and Biersack, 2010) was excluded from the weighted mean calculation and summed in quadrature with the weighted mean uncertainty to obtain the final uncertainty. In addition, the stopping-power- and branching-ratio-corrected resonance strengths from Daigle *et al.* (2016) were used in the calculations instead of the originally quoted values. The resonance strength determination is summarized in Table IX. Regarding the branching ratios, those of Daigle *et al.* (2016) are recommended.

C. Indirect studies

There are several indirect techniques that have been used to help constrain the extrapolation of the low-energy cross section. A new transfer study of proton ANCs was reported by Artemov *et al.* (2012). Since the 6.79 MeV level also acts a subthreshold resonance in the ground-state transition, its lifetime is also needed. New lifetime measurements were made by Galinski *et al.* (2014), Sharma *et al.* (2020), and Frentz *et al.* (2021) in addition to the previously avaliable data by Bertone *et al.* (2001) and Schürmann *et al.* (2008). Because the lifetime is in a range that is difficult to access experimentally ($t_{1/2} < 2$ fs), these works still report values either with large uncertainties or upper limits only. Scattering cross sections can also be helpful in constraining both bound and unbound level parameters for the R-matrix fit to the capture data. A consistent set of scattering measurements was made by deBoer *et al.* (2015) that superseded the unutilizable data for $^{14}\mathrm{N}(p, p)$ and showed large discrepancies (Gurbich, 2008). In the new work, only yield ratios are reported in order to reduce the uncertainties associated with target degradation. This scattering data give added constraint to the broad, high-energy $3/2^+$ resonance at $E \approx 2.2$ MeV.

D. *R*-matrix considerations

The phenomenological R matrix has been the primary model used to fit and extrapolate cross-section data, following the analysis of Angulo and Descouvemont (2001). Many investigations have used the same multichannel R-matrix code, AZURE2, which was introduced by Azuma *et al.* (2010). The model has proven to be popular because it is flexible in its level structure description yet, at the same time, retains enough physical constraints that it can be used for extrapolations into unobserved regions of the cross section. This flexibility also allows for additional complications like overfitting, mistaking experimental resolution effects for inconsistencies between datasets, and needing additional reaction components (Wiescher, deBoer, and Reifarth, 2023), to give a few common examples.

In the R-matrix framework, the cross section is described by including a number of reaction components that include resonances, subthreshold states, and background levels. For radiative-capture reactions, an additional component is introduced, external capture (Holt *et al.*, 1978; Barker and Kajino, 1991; Angulo and Descouvemont, 2001), which is used to model the nonresonant capture process. Figure 9 shows an example of a multichannel AZURE2 R-matrix fit to scattering data and the three strongest transitions of the $^{14}\mathrm{N}(p,\gamma)\mathrm{O}$ reaction: 6.79 MeV, the ground state, and 6.17 MeV.

When one uses the alternative R-matrix parametrization of Brune (2002), the resonance components are characterized by observable energies and partial widths, while subthreshold resonances have their strength quantified by the state's ANC. The strength of the external capture contributions are likewise given by ANCs.

The strongest transition, to the 6.79 MeV state, is dominated by external capture at solar fusion energies. As pointed out by Adelberger *et al.* (2011), discrepancies among the datasets over the higher energy range make it unclear whether an additional contribution is needed from a background level. However, as Wagner *et al.* (2018) showed, even when a background level is introduced, it has a small effect on the low-energy extrapolation owing to the dominance of the external capture component.

The next strongest transition is to the ground state, where the R-matrix description of the low-energy cross section is complicated. It is thought to have significant competing and interfering contributions from the 6.79 MeV subthreshold state, the narrow $E = 259$ keV resonance, external capture, a background level, and the broad, higher-energy resonance at $E = 2.2$ MeV. Despite all of these contributions, which give the R-matrix fit a considerable amount of flexibility for this transition, a satisfactory fit to the ground-state transition data remains elusive (Li *et al.*, 2016; Wagner *et al.*, 2018; Frentz *et al.*, 2022).

Finally, the 6.18 MeV transition is dominated by the narrow $E = 259$ keV resonance and external capture contributions at low energies. A contribution from the 6.79 MeV subthreshold state may also be significant.

E. Partial *S* factors

In this compilation a different approach than that of Adelberger *et al.* (2011) is adopted to determine the $S(0)$ value for the two strongest transitions. Because several calculations are already available in recent publications, no new R-matrix calculation was performed. Instead, the reported

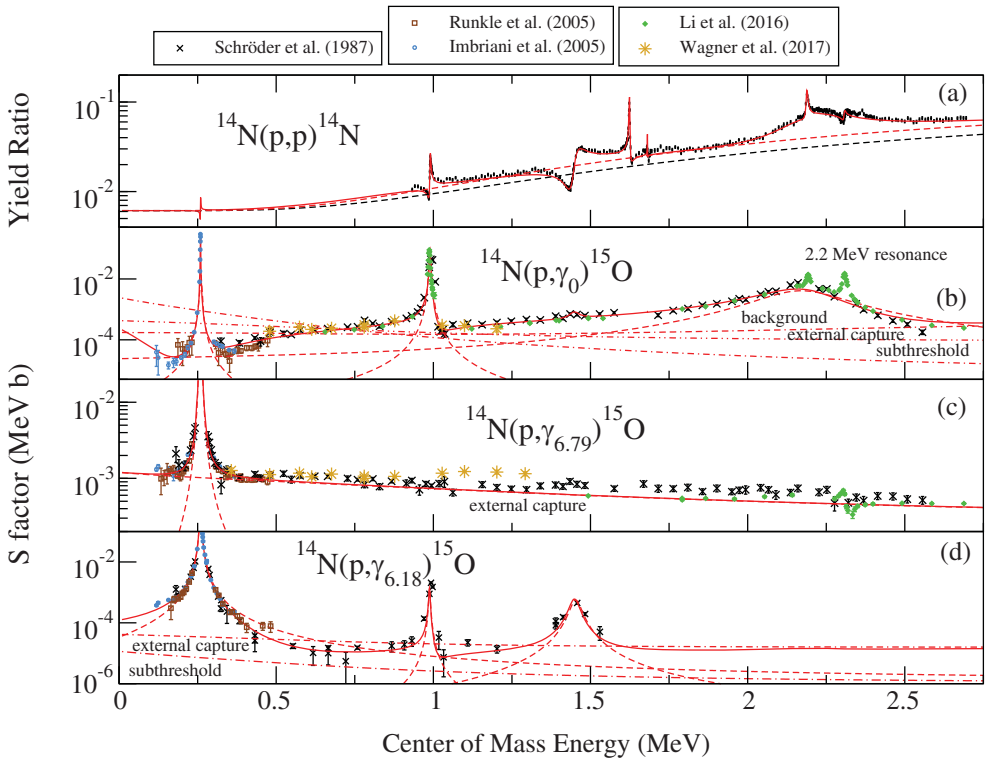

FIG. 9. (a) Representative yield ratio for the ^{14}N-p scattering cross section (deBoer *et al.*, 2015). Low-energy S factors for the three strongest transitions in the $^{14}\mathrm{N}(p,\gamma)^{15}\mathrm{O}$ reaction to the (b) ground state and (c) 6.79 MeV and (d) 6.18 MeV final states (Schröder *et al.*, 1987; Imbriani *et al.*, 2005; Runkle *et al.*, 2005; Li *et al.*, 2016; Wagner *et al.*, 2018). An example of an R-matrix fit is shown, with individual resonance contributions indicated by dashed lines, external capture indicated by dot-dashed lines, and cross sections indicated by solid lines.

$S(0)$ values from the original publications are considered (Imbriani *et al.*, 2005; Runkle *et al.*, 2005; Li *et al.*, 2016; Wagner *et al.*, 2018; Frentz *et al.*, 2022). Runkle *et al.* (2005), Li *et al.* (2016), and Frentz *et al.* (2022) normalized the datasets to the strength of the 259 keV resonance. Therefore, the reported $S(0)$ values were renormalized by the ratios of the resonance strengths used in each work and the present recommended one. In contrast, Imbriani *et al.* (2005) and Wagner *et al.* (2018) established an absolute normalization, independent of the 259 keV resonance strength.

1. Ground-state transition

The ground-state transition cross section of the $^{14}\mathrm{N}(p,\gamma)^{15}\mathrm{O}$ reaction is challenging to measure accurately and to high precision because the cross section is low and most experiments perform measurements with high efficiency γ-ray detectors in close geometry. This increases the yield for these measurements but also greatly increases the effect of γ-ray summing into the ground-state transition, with the largest contribution from the 6.79 MeV transition at low energies. In addition, the cross section on the high-energy side of the strong, low-energy 259 keV resonance is inconsistent between different measurements, likely a result of nitrogen diffusion into the thick-target backing material.

Adelberger *et al.* (2011) included the R-matrix fit the data of Schröder *et al.* (1987), Imbriani *et al.* (2005), Runkle *et al.* (2005), and Marta *et al.* (2008) below 2 MeV. A good description of the data was obtained over most of this energy region, with the exception of a consistent overestimation of the experimental data from ≈300 to 500 keV. The fit there favored the higher cross sections of Marta *et al.* (2008), consistently overestimating the data of Runkle *et al.* (2005) throughout this energy range. Note that the data of Schröder *et al.* (1987) were clarified to be yields that were uncorrected for experimental effects. Cross sections were deduced for these data by Adelberger *et al.* (2011) but where never published.

Since the work of Adelberger *et al.* (2011), there have been three new datasets reporting partial cross sections (Li *et al.*, 2016; Wagner *et al.*, 2018; Frentz *et al.*, 2022), all of which used the AZURE2 R-matrix code to derive $S(0)$. These values are considered here as an indication of the uncertainty in the low-energy extrapolation. Li *et al.* (2016) concentrated on differential cross-section measurements between 0.5 and 3.5 MeV, while both Wagner *et al.* (2018) and Frentz *et al.* (2022) focused on bridging the gap between the measurements of Li *et al.* (2016) and the lower-energy LUNA (Imbriani *et al.*, 2005) and Laboratory for Experimental Nuclear Astrophysics (LENA) measurements (Runkle *et al.*, 2005).

The new data and accompanying R-matrix fits have repeatedly confirmed a discrepancy between the R-matrix fit and the experimental data for the ground-state transition, especially when the high-energy data of Schröder *et al.* (1987) and Li *et al.* (2016) are included in the fit. On the R-matrix

TABLE X. Total $S_{114}(0)$ values as the sum of the partial transitions.

Transition	$S_{114}(0)$ (keV b)	$\Delta S_{114}(0)$	Reference
tr → 0	0.30 ± 0.11	37%	This review
tr → 6.79	1.17 ± 0.03	2.9%	This review
tr → 6.17	0.13 ± 0.05	38%	Adelberger *et al.* (2011)
tr → 5.18	0.010 ± 0.003	30%	Adelberger *et al.* (2011)
tr(5.24) → 0	0.068 ± 0.020	30%	Adelberger *et al.* (2011)
R-matrix sum	1.68 ± 0.13[a]	7.6%	
Additional system uncertainty[b]		3.5%	
Total	1.68 ± 0.14	8.4%	

[a]The uncertainty is the sum of the partial transition uncertainties.

[b]From the normalization to the $E = 259$ keV resonance strength.

side, this could point to a missing reaction component (i.e., missing resonance or subthreshold state) or an incorrect spin-parity assignment. On the data side, the close geometry setups of most experiments result in large summing corrections. Inaccurate corrections for angular distributions could also play a role. Because of this unresolved inconsistency between data and model, a larger uncertainty has been attributed to this transition compared to Adelberger *et al.* (2011); see Table X.

2. 6.79 MeV transition

In contrast to the ground state, repeated measurements of the 6.79 MeV transition continue to produce consistent results, especially at very low energies. The measurements of Wagner *et al.* (2018) do show a more rapidly increasing cross section at high energies than those of previous works, but they are consistent in the low-energy region. In addition, the ANC determined from the normalization of the external capture cross section used to model the nonresonant capture in the *R*-matrix fit yields consistent results with those determined from transfer studies (Bertone *et al.*, 2002; Mukhamedzhanov *et al.*, 2003). Because of this continued consistency across measurements, the value adopted here is the weighted average of the reported values, where the uncertainty has been further reduced from that of Adelberger *et al.* (2011).

3. Other transitions

For the three weaker transitions reported by Adelberger *et al.* (2011), there were no new experimental data. Here the values of $S(0)$ have been determined by scaling those from Adelberger *et al.* (2011) by the ratio of the 259 keV resonance strengths adopted here and from Adelberger *et al.* (2011).

F. Total *S* factor and conclusions

Figure 9 shows the low-energy *S* factors and *R*-matrix fits to the strongest capture transitions and the scattering yields at a representative angle, and Table X summarizes the uncertainties estimated for the zero-energy *S* factor $S_{114}(0)$ for each of the significant capture transitions. Their sum gives the adopted total $S(0)$ value. The absolute uncertainty of the *R*-matrix sum is the quadratic sum of the absolute uncertatinties of the partial transitions, while the recommended uncertainty conservatively includes an additional 3.5% relative uncertainty from the resonance strength (see Table IX) to which most of the datasets were normalized. As described in Sec. X.E.1, the uncertainty in the ground-state transition increased to 37% over the 19% estimate of Adelberger *et al.* (2011) owing to repeated confirmation of a tension between different experimental datasets and the *R*-matrix description of the cross section. The uncertainty in the 6.79 MeV transition decreased from 4.0% to 2.9% owing to the consistency of the various measurements for this transition.

In addition, the new total capture cross section of Gyürky *et al.* (2022), performed using the activation technique over the energy range from 0.55 to 1.4 MeV, is larger than the sum of the partial *R*-matrix cross sections by ≈25%, a significant margin compared to the systematic uncertainties of the different datasets. However, we emphasize that, for several of the transitions, the only data available are those of Schröder *et al.* (1987), which are yields, not cross sections, and often give only upper limits. For example, the capture to the 7.56 MeV level in this energy range may be significant.

Given the previous considerations, a somewhat larger uncertainty of 8.4% has been estimated for $S_{114}(0)$ compared to the 7% uncertainty recommended by Adelberger *et al.* (2011). As one of the main sources of uncertainty remains the ground-state transition, far geometry angular distribution measurements extending the differential measurements of Li *et al.* (2016) to lower energies are recommended. These measurements will both reduce the effect of summing and provide more information on the underlying reaction mechanisms at these low energies. Further, as the data of Schröder *et al.* (1987) have significant uncorrected experimental effects, new measurements covering the same wide energy range should be undertaken. Such measurements are planned at both the LUNA and JUNA underground facilities. At very low energies, the LUNA and LENA measurements of the ground-state transition by Imbriani *et al.* (2005) and Runkle *et al.* (2005), respectively, remain the only measurements. The discrepancy between the two measurements and the tension between the *R*-matrix fits also make new measurements in this range of high priority. Despite several additional attempts since the work of Adelberger *et al.* (2011), the lifetime of the 6.79 MeV transition remains unmeasured. This is still a high priority, as having a well constrained value will greatly improve our understanding of the low-energy behavior of the ground-state transition cross section. Finally, we recommend that the cross section to the 6.18 and 7.56 MeV final states be measured at high energies in order to address the tension between the measured total cross section and the sum of the partial cross sections.

XI. OTHER CNO, NE-NA REACTIONS

In the following we provide information on the proton-induced reactions involving the target nuclei ^{12,13}C, ^{15}N, ^{16,17,18}O, ^{19}F, ^{20,21,22}Ne, and ^{23}Na. Unless otherwise noted, we focus here on the low-energy region, i.e., below 150 keV in

TABLE XI. Overview of the CNO and NeNa reactions.

Reaction	Category[a]	$S(0) \pm \Delta S(0)$ (keVb)	E_0[b] (keV)	Most recent reference	Comment
$^{12}C(p,\gamma)^{13}N$	B	1.44 ± 0.06	25	Skowronski *et al.* (2023a)	SF II (Adelberger *et al.*, 2011): $S(0) = 1.34 \pm 0.21$ keV b
$^{13}C(p,\gamma)^{14}N$	B	6.1 ± 0.4	25	Skowronski *et al.* (2023a)	SF II (Adelberger *et al.*, 2011): $S(0) = 7.6 \pm 1.0$ keV b
$^{15}N(p,\gamma)^{16}O$	B	40 ± 3	28	deBoer *et al.* (2013)	SF II (Adelberger *et al.*, 2011): $S(0) = 36 \pm 6$ keV b
$^{15}N(p,\alpha)^{12}C$	B	$73\,000 \pm 5000$	28	La Cognata *et al.* (2009)	SF II (Adelberger *et al.*, 2011): $S(0) = 73\,000 \pm 5000$ keV b
$^{16}O(p,\gamma)^{17}F$	B	10.92 ± 0.44	30	Iliadis, Palanivelrajan, and de Souza (2022)	SF II (Adelberger *et al.*, 2011): $S(0) = 10.6 \pm 0.8$ keV b
$^{17}O(p,\gamma)^{18}F$	B	4.7 ± 1.0	31	Gyürky *et al.* (2017)	SF II (Adelberger *et al.*, 2011): $S(0) = 6.2 \pm 3.1$ keV b
$^{17}O(p,\alpha)^{14}N$	A	⋯	31	Bruno *et al.* (2016)	Near-threshold resonances
$^{18}O(p,\gamma)^{19}F$	B	23.0 ± 3.8	31	Pantaleo *et al.* (2021)	Also in the literature, $S(0) = 7.1$ and 15.7 keV b
$^{18}O(p,\alpha)^{15}N$	B	⋯	31	Bruno *et al.* (2019)	Low-energy resonances
$^{19}F(p,\gamma)^{20}Ne$	A	⋯	33	Zhang *et al.* (2022)	Possible resonance near threshold
$^{19}F(p,\alpha)^{16}O$	B	⋯	33	Zhang, López *et al.* (2021)	Possible resonance near threshold
$^{20}Ne(p,\gamma)^{21}Na$	B	6776 ± 550	36	This review	
$^{21}Ne(p,\gamma)^{22}Na$	A	≈20	36	Rolfs *et al.* (1975)	Factor of 3 uncertainty in $S(0)$
$^{22}Ne(p,\gamma)^{23}Na$	A	415 ± 91	36	Ferraro *et al.* (2018)	Subthreshold resonance at −130 keV
$^{23}Na(p,\gamma)^{24}Mg$	B	18 ± 9	38	Boeltzig *et al.* (2022)	
$^{23}Na(p,\alpha)^{20}Ne$	A	⋯	38	Iliadis *et al.* (2010)	

[a]Categories for the dominant rate contribution at the central temperature of the Sun. A: narrow resonances. B: broad resonant or nonresonant contributions. We define a narrow resonance by the criterion that its full contribution to the reaction rate can be calculated from the resonance energy and strength alone.
[b]Central energy location (center-of-mass system) of the Gamow peak at the solar core.

the center of mass. The reactions on lighter target nuclei up to and including ^{16}O are of direct relevance for solar neutrinos; the other reactions play a role in hydrogen burning at somewhat higher temperatures, including asymptotic giant branch (AGB) stars.

Table XI lists, where applicable, the S factor at zero energy, the Gamow peak location, and relevant references. Table XII provides recommended values for the S factor and the corresponding uncertainty on a grid of seven energy values. These results are displayed in Fig. 10 together with their polynomial fits. The fit coefficients are listed in Table I. Table XIII gives the values of recommended strengths of the narrow resonances. A discussion of each reaction is now provided.

A. Reactions of the CNO-I cycle

1. $^{12}C(p,\gamma)^{13}N$

The low-energy reaction cross section is influenced by the tail of a broad resonance and the nonresonant capture in the ground state of ^{13}N. The results of six new direct measurements have been published since the work of Adelberger *et al.* (2011) (Nesaraja *et al.*, 2001; Csedreki, Gyürky, and Szücs,

TABLE XII. S factors vs center-of-mass energy. The data are also plotted in Fig. 10.

Reaction	$S(E)$ (keV b) (% uncertainty)						
	5 keV	10 keV	20 keV	40 keV	60 keV	100 keV	140 keV
$^{12}C(p,\gamma)^{13}N$[a]	1.46(4.1%)	1.47(4.1%)	1.51(4.1%)	1.58(4.1%)	1.67(4.1%)	1.89(4.0%)	2.19(4.1%)
$^{13}C(p,\gamma)^{14}N$[a]	6.16(6.0%)	6.22(6.0%)	6.34(6.1%)	6.60(6.1%)	6.89(6.1%)	7.58(6.1%)	8.47(6.1%)
$^{15}N(p,\gamma)^{16}O$	40.8(7.5%)	41.7(7.5%)	43.0(7.5%)	45.8(7.5%)	50.0(7.5%)	59.0 (7.5%)	73.4(7.5%)
$^{15}N(p,\alpha)^{12}C$	7.7×10^4 (6.8%)	8.0×10^4 (6.8%)	8.5×10^4 (6.8%)	1.00×10^5 (6.8%)	1.18×10^5 (6.8%)	1.66×10^5 (6.8%)	2.53×10^5 (6.8%)
$^{16}O(p,\gamma)^{17}F$[b]	10.64(4.0%)	10.38(4.0%)	9.92(4.0%)	9.15(4.0%)	8.56(4.0%)	7.67(4.0%)	7.05(4.0%)
$^{20}Ne(p,\gamma)^{21}Na$[c]	2586(8%)	1365(8%)	593 (7%)	226(7%)	128(7%)	69(6%)	45(6%)
$^{23}Na(p,\gamma)^{24}Mg$	18(50%)	18(50%)	18(50%)	18(50%)	18(50%)	18(50%)	18(50%)

[a]From Skowronski *et al.*, 2023a.
[b]From Iliadis, Palanivelrajan, and de Souza, 2022.
[c]From this review.

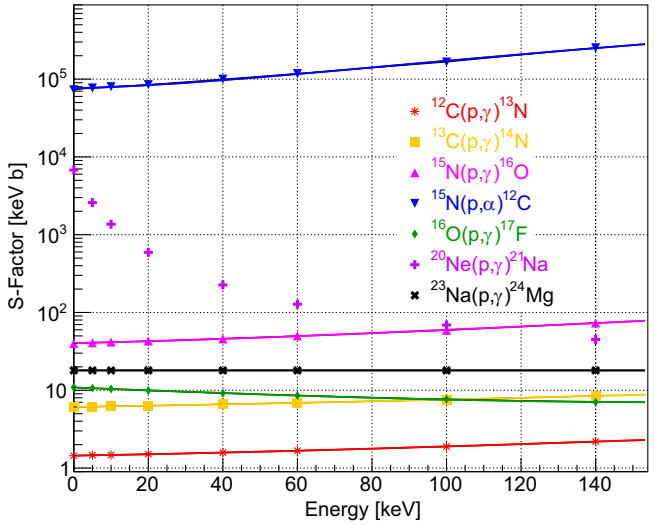

FIG. 10. Astrophysical S factors of CNO and NeNa cycle reactions. The circles represent the values listed in Table XII. The solid lines represent polynomial (quadratic) fits of the S-factor values. The fit coefficients are listed in Table I. The S factor of the $^{20}\mathrm{Ne}(p,\gamma)^{21}\mathrm{Na}$ reaction cannot be accurately fit with a quadratic (or cubic) polynomial function.

2023; Gyürky *et al.*, 2023; Kettner *et al.*, 2023; Skowronski *et al.*, 2023a, 2023b).

The first experiment by Nesaraja *et al.* (2001) reported the reaction cross section relative to that of the $^{13}\mathrm{C}(p,\gamma)^{14}\mathrm{N}$ reactions at $E_p^{\mathrm{lab}} = 160$ keV to be 0.24 ± 0.03.

Two of the newest experiments were performed at ATOMKI (Csedreki, Gyürky, and Szücs, 2023; Gyürky *et al.*, 2023). The first employed the activation method in a wide laboratory bombarding energy range, $E_p^{\mathrm{lab}} = 300$–1900 keV, to provide a dataset with an absolute normalization having uncertainties that are distinct from those of the older datasets obtained using in-beam γ-ray spectroscopy. The main focus of the second experiment was the precise determination of the energies and widths of the two low-energy resonances using in-beam γ-ray spectroscopy with detectors located at several angles.

The fourth experiment, by Skowronski *et al.* (2023b), was performed at the Felsenkeller underground accelerator facility in Dresden, Germany, using in-beam γ-ray spectroscopy. The focus was on determining the parameters of the lowest-lying resonance employing a detector in close geometry with high solid-angle coverage. The data covered the energy range of $E_p^{\mathrm{lab}} = 345$–670 keV and allowed for an extrapolation to solar and stellar energies using R-matrix theory. The absolute normalization of this dataset is about 25% lower than the previous results. The low-energy slope of the S factor also changed, resulting in an extrapolated value of $S(25\ \mathrm{keV}) = 1.34 \pm 0.09$ keV b in the solar Gamow peak.

The fifth experiment, by Kettner *et al.* (2023), was performed at Bochum and Notre Dame and focused on the second resonance in the reaction. Differential cross sections at 0° and 55°, thick-target yields, and angular distributions at selected energies were measured in the energy range of $E_p^{\mathrm{lab}} = 1000$–$2500$ keV. A comprehensive R-matrix fit of the available data was also performed and resulted in $S(25\ \mathrm{keV}) = 1.48 \pm 0.09$ keV b.

The sixth experiment, by the LUNA Collaboration (Skowronski *et al.*, 2023a), obtained data in the range of $E_p = 80$–400 keV, reaching the lowest bombarding energies to date. Both the activation technique and in-beam γ-ray spectroscopy were applied, with a consistent absolute normalization of the data, despite the different systematic uncertainties introduced by the two methods. Their S factor in the solar Gamow peak, $S(25\ \mathrm{keV}) = 1.53 \pm 0.06$ keV b, is in good agreement with the finding of Kettner *et al.* (2023) and is compatible within 2σ with the result of Skowronski *et al.* (2023b).

Apart from the previously discussed direct measurements, the ground-state ANC was determined in a recent particle transfer experiment by Artemov *et al.* (2022). They also reported a fit of the radiative-capture data available at the time. The R-matrix fits to the data of Kettner *et al.* (2023) and Skowronski *et al.* (2023a, 2023b) gave ANC values consistent with the result of the transfer work.

Thanks to the high consistency of all recent datasets, the extrapolation of the cross section to solar energies has now improved uncertainty. Owing to the self-consistency between the methods used and the precise data covering the lowest energies to date, we adopt the S factor recommended by Skowronski *et al.* (2023a); see Tables XI and XII.

2. $^{13}\mathrm{C}(p,\gamma)^{14}\mathrm{N}$

This reaction proceeds to the ground state and five excited states in ^{14}N. The low-energy cross section is influenced by the tail of a broad resonance at laboratory bombarding energy of $E_r^{\mathrm{lab}} \approx 558$ keV. Previously, only a single work reported cross sections for all transitions (King *et al.*, 1994), which was the basis of the S-factor recommendations by Adelberger *et al.* (1998, 2011).

Later, a comprehensive study by the LUNA Collaboration (Skowronski *et al.*, 2023a) provided data in the energy range of $E_p^{\mathrm{lab}} = 80$–400 keV. One of their datasets was obtained with HPGe detectors to study partial cross sections. Their second dataset was obtained with a γ-ray calorimeter to measure the total reaction cross sections. The results from both datasets agree in the absolute cross-section scale, despite major differences in the systematic uncertainties of the two methods. The new results are about 30% lower than the previous results of King *et al.* (1994). Despite this scale difference the calculated S-factor ratio for the $^{12}\mathrm{C}(p,\gamma)^{13}\mathrm{N}$ and $^{13}\mathrm{C}(p,\gamma)^{14}\mathrm{N}$ reactions at $E_p^{\mathrm{lab}} = 160$ keV is 0.26 ± 0.02, which is in perfect agreement with the experimental one of 0.24 ± 0.03 reported by Nesaraja *et al.* (2001).

The adopted S factor given in Tables XI and XII is based on the result of Skowronski *et al.* (2023a) owing to its self-consistency between the different methods for measuring the cross sections and the higher precision of the dataset compared to that of King *et al.* (1994).

3. $^{15}\mathrm{N}(p,\alpha)^{12}\mathrm{C}$

Following (Adelberger *et al.*, 2011), the experimental and phenomenological work on the $^{15}\mathrm{N}(p,\alpha)^{12}\mathrm{C}$ reaction can be divided into the following three groups, which address different aspects: (i) new (p,α_0) data (deBoer *et al.*, 2012), (ii) new

TABLE XIII. Recommended strengths and relative kinetic energies of narrow resonances. We define a *narrow resonance* by the criterion that its full contribution to the total rate can be calculated from the resonance energy and strength alone.

Reaction	$E_r^{\text{c.m.}}$ (keV)	$\omega\gamma$ (eV)[a]	Comment or reference(s)
$^{17}\text{O}(p,\gamma)^{18}\text{F}$	65	$15.6^{+18.3}_{-4.0} \times 10^{-12}$	See the text for details
	183	$(1.77 \pm 0.09) \times 10^{-6}$	See the text for details
$^{17}\text{O}(p,\alpha)^{14}\text{N}$	65	$4.6^{+5.4}_{-1.2} \times 10^{-9}$	See the text for details
	183.9	$(1.68 \pm 0.03_{\text{stat}} \pm 0.12_{\text{syst}}) \times 10^{-3}$	Chafa *et al.* (2007) and Bruno *et al.* (2015)
$^{18}\text{O}(p,\gamma)^{19}\text{F}$	20	5.7×10^{-22}	Champagne and Pitt (1986)
	90	$(0.53 \pm 0.07_{\text{stat}} \pm 0.07_{\text{syst}}) \times 10^{-9}$	Best *et al.* (2019)
	143	$(0.98 \pm 0.03) \times 10^{-3}$	See the text for details
$^{18}\text{O}(p,\alpha)^{15}\text{N}$	20	$8.3^{+3.8}_{-2.6} \times 10^{-19}$	La Cognata *et al.* (2008)
	90	$2.0^{+13.7}_{-0.4} \times 10^{-7}$	See the text for details
	143	$(166 \pm 8) \times 10^{-3}$	See the text for details
$^{19}\text{F}(p,\gamma)^{20}\text{Ne}$	11.0	$\leq 8.5 \times 10^{-29}$	Betts, Fortune, and Middleton (1975) and Kious (1990)
	212.7	$\leq 4.2 \times 10^{-6}$	Spyrou *et al.* (2000) and Zhang *et al.* (2022)
	225.2	$(4.19 \pm 0.33) \times 10^{-5}$	Spyrou *et al.* (2000) and Zhang *et al.* (2022)
	323.9	$(3.16 \pm 0.33) \times 10^{-3}$	Couture *et al.* (2008), Williams *et al.* (2021), and Zhang *et al.* (2022)
$^{19}\text{F}(p,\alpha\gamma)^{16}\text{O}$	11.0	$(7.5 \pm 3.0) \times 10^{-29}$	Zhang, López *et al.* (2021)
	212.7	0.0126 ± 0.0013	Spyrou *et al.* (2000) and Zhang, López *et al.* (2021)
	225.2	0.0011 ± 0.0004	Spyrou *et al.* (2000) and Zhang, López *et al.* (2021)
	323.9	23.5 ± 0.6	Zhang, López *et al.* (2021) and Zhang *et al.* (2022)
$^{21}\text{Ne}(p,\gamma)^{22}\text{Na}$	16.6	$\leq 6.2 \times 10^{-24}$	Iliadis *et al.* (2001)
	94.6	$\leq 6.4 \times 10^{-10}$	Iliadis *et al.* (2001)
	126	$(3.75 \pm 0.75) \times 10^{-5}$	Görres *et al.* (1982)
$^{22}\text{Ne}(p,\gamma)^{23}\text{Na}$	5	$\leq 2.1 \times 10^{-51}$	Hale *et al.* (2001)
	28	$\leq 3.2 \times 10^{-25}$	Hale *et al.* (2001)
	35	$(3.1 \pm 1.2) \times 10^{-15}$	Iliadis *et al.* (2010)
	68	$\leq 6 \times 10^{-11}$	Ferraro *et al.* (2018)
	100	$\leq 7 \times 10^{-11}$	Ferraro *et al.* (2018)
	150	$(3.9 \pm 0.9) \times 10^{-9}$	Santra, Chakraborty, and Roy (2020)
	151	$(1.97 \pm 0.12) \times 10^{-7}$	See the text for details
	181	$(2.39 \pm 0.12) \times 10^{-6}$	See the text for details
$^{23}\text{Na}(p,\gamma)^{24}\text{Mg}$	133	$1.46^{+0.58}_{-0.53} \times 10^{-9}$	Boeltzig *et al.* (2019) and Marshall *et al.* (2021)
	240.6	$5.3(1) \times 10^{-4}$	Switkowski *et al.* (1975) and Keinonen *et al.* (1989)
	295.90	$1.05(19) \times 10^{-1}$	Switkowski *et al.* (1975) and Endt *et al.* (1990)
$^{23}\text{Na}(p,\alpha)^{20}\text{Ne}$	133	$\leq 1.5 \times 10^{-8}$	Rowland *et al.* (2004), Iliadis, Champagne, and José (2005), and Marshall *et al.* (2021)
	240.6	≤ 0.1	Hale *et al.* (2001)
	295.90	$1.03(26) \times 10^{-2}$	Iliadis *et al.* (2010)

[a]The resonance strength in the center-of-mass system for the reactions listed here is defined as $\omega\gamma \equiv (2J+1)(2j_t+1)^{-1}(2j_p+1)^{-1}\Gamma_p\Gamma_x/\Gamma$, with J, j_t, and j_p the spins of the resonance, target, and projectile, respectively, and Γ_p, Γ_x, and Γ the proton partial width, the γ-ray or α-particle partial width, and the total resonance width, respectively.

$(p,\alpha\gamma)$ data (Imbriani *et al.*, 2012a, 2012b; Reinhardt *et al.*, 2016; Gyürky, Fülöp *et al.*, 2019; deBoer *et al.*, 2021), and (iii) R-matrix analyses of existing datasets (deBoer *et al.*, 2013; Brune and deBoer, 2020).

Other studies have been conducted for laboratory bombarding energies above 400 keV. Reinhardt *et al.* (2016) tabulated the strength of a resonance at $E_r^{\text{c.m.}} \approx 403$ keV (2^-, $E_x = 12\,530$ keV), and their value was in agreement with previous determinations. Gyürky, Fülöp *et al.* (2019) showed the thick-target yield for the $E_r^{\text{c.m.}} = 841$ keV resonance, but no further details were reported. New cross-section data for the $(p,\alpha_1\gamma)$ reaction down to about 900 keV center-of-mass energy were displayed by deBoer *et al.* (2021). They used the data for a comprehensive R-matrix fit and reported parameters of resonances above about 1500 keV center-of-mass energy.

Imbriani *et al.* (2012a, 2012b) measured the $^{15}\text{N}(p,\alpha\gamma)^{12}\text{C}$ reaction down to about 140 keV laboratory bombarding energy and showed that the S factor of the $(p,\alpha_1\gamma)$ channel is orders of magnitude lower than the (p,α_0) channel.

Finally, deBoer *et al.* (2013) provided a detailed analysis of all available channels populating the ^{16}O compound nucleus, expanding the results presented by deBoer *et al.* (2012). They considered a wide range of experimental data leading to a single consistent R-matrix fit that accurately describes the broad level structure of ^{16}O below $E_x = 13\,500$ keV. The resulting fit was used to extract an improved determination of the low-energy S factor for the $^{15}\text{N}(p,\alpha)^{12}\text{C}$ reaction. In addition, Brune and deBoer (2020) developed the partial-wave formalism for calculating the angular distributions of secondary γ rays following particle emission, providing the

framework needed for future studies that can directly utilize differential measurements of the $^{15}\mathrm{N}(p,\alpha_1\gamma)^{12}\mathrm{C}$ reaction.

The available evidence confirms that the (p,α_0) channel dominates the total S factor. The global R-matrix analysis of deBoer *et al.* (2013) provided results that slightly exceed the experimental data of Redder *et al.* (1982) and also estimated a slightly larger value, $S(0) = (95 \pm 6) \times 10^3$ keV b, than previous works [see Table VII of deBoer *et al.* (2013), thus calling for additional low-energy measurements. The extrapolated S factor of deBoer *et al.* (2013) agrees with the findings of La Cognata *et al.* (2009), who conducted the most recent indirect study, determining the S factor down to 20 keV center-of-mass energy. The global R-matrix analysis suggests a renormalization of the S factor of La Cognata *et al.* (2009) by 6%, which is within the quoted uncertainty. Based on the previously provided information, we adopt the S factor of La Cognata *et al.* (2009), $S(0) = (73 \pm 5) \times 10^3$ keV b, which was also adopted by Adelberger *et al.* (2011).

B. Reactions of the NO or CNO-II cycle

1. $^{15}\mathrm{N}(p,\gamma)^{16}\mathrm{O}$

The low-energy $^{15}\mathrm{N}(p,\gamma)^{16}\mathrm{O}$ cross section is dominated by its ground-state transition (Leblanc *et al.*, 2010; Imbriani *et al.*, 2012b). This transition's cross section is enhanced by the constructively interfering tails of two broad resonances at laboratory proton energies of $E^{\mathrm{lab}} = 338$ and 1028 keV, which correspond to 1^- levels in the $^{16}\mathrm{O}$ compound system. In addition to ground-state proton and γ-ray deexcitation, these levels also decay strongly through the α_0 and α_1 channels. For the 338 keV resonance, $\Gamma_\gamma/\Gamma_\alpha = (6.7 \pm 0.3) \times 10^{-5}$ (deBoer *et al.*, 2013). Because of interference effects, this ratio does not directly translate to the rate of passage from the CNO-IV to the NeNa cycle. Currently, the favored framework for the analysis and extrapolation of the available data is the phenomenological R matrix. Here the main components that are used to model the low-energy cross section of the $^{15}\mathrm{N}(p,\gamma)^{16}\mathrm{O}$ reaction are the two broad 1^- resonances, external capture, and a 1^- background level. The strength of the external capture can be characterized by the ground-state proton ANC of $^{16}\mathrm{O}$, which has been experimentally determined via a proton-transfer reaction (Mukhamedzhanov *et al.*, 2008). In addition, γ-ray deexcitation to the ground state has been observed through a 2^+ level in this energy region in the $^{12}\mathrm{C} + \alpha$ reactions but has been shown to be negligibly weak for $^{15}\mathrm{N}(p,\gamma)^{16}\mathrm{O}$ (deBoer *et al.*, 2013).

The cross-section measurements used by Adelberger *et al.* (2011) were those of Hebbard (1960), Rolfs and Rodney (1974), and Bemmerer *et al.* (2009). While the then-newly-measured data of Bemmerer *et al.* (2009) represented significant improvements in accuracy over the results of Rolfs and Rodney (1974) and in precision over the findings of Hebbard (1960), they cover only a limited energy range. Adelberger *et al.* (2011) adopted the two-level R-matrix fit of Mukhamedzhanov *et al.* (2008), which simultaneously fit $^{15}\mathrm{N}(p,\alpha)^{12}\mathrm{C}$ data, giving $S(0) = 36 \pm 6$ keV b for the $^{15}\mathrm{N}(p,\gamma)^{16}\mathrm{O}$ reaction; see also Barker (2008). The fit shows that the extrapolation performed by Rolfs and Rodney (1974), which yielded 64 ± 6 keV b, overestimated $S(0)$.

Following Adelberger *et al.* (2011), Leblanc *et al.* (2010) carried out a comprehensive measurement campaign at LUNA and the University of Notre Dame covering a laboratory energy range from $E^{\mathrm{lab}} = 130$ to 1800 keV. They used a three-level R-matrix fit, but the ground-state proton ANC of Mukhamedzhanov *et al.* (2008) was not considered, resulting in a somewhat larger extrapolated value of $S(0) = 39.6(26)$ keV b than that adopted by Adelberger *et al.* (2011). Mukhamedzhanov, La Cognata, and Kroha (2011) subsequently showed that a three-level R-matrix fit of equal quality could be obtained with the ANC and reported an extrapolated value of $S(0)$ that ranged from 33 to 40 keVb.

Caciolli *et al.* (2011) expanded the energy range of Bemmerer *et al.* (2009) by measuring the cross section up to $E_{\mathrm{c.m.}} = 370$ keV. Their experiment scanned over the top of the lowest-energy broad resonance at $E_{\mathrm{c.m.}} = 312$ keV. The data were found to be consistent with the ground-state data of Leblanc *et al.* (2010).

deBoer *et al.* (2013) performed a comprehensive R-matrix fit that included not only the $^{15}\mathrm{N} + p$ data but also a wide range of $^{12}\mathrm{C} + \alpha$ data over a similar excitation energy range; see also Sec. XI.A.3). The value from this analysis, $S(0) = 40 \pm 3$ keV b, was slightly above that of Leblanc *et al.* (2010) and agreed with the upper limit of Mukhamedzhanov, La Cognata, and Kroha (2011). However, it is lower than the recent potential-model extrapolation of $S(0) = 45^{+9}_{-7}$ keV b found in the NACRE II compilation (Xu *et al.*, 2013). The difference between the two fits is likely due to the fact that NACRE II disregarded the higher-energy part of the Leblanc *et al.* (2010) data, which map the interference pattern between the two 1^- resonances more accurately than older datasets. To reproduce experimental data in that region, a 1^- background level was added in the R-matrix fits of Leblanc *et al.* (2010) and later works. Here we adopt the value of $S(0) = 40 \pm 3$ keV b from deBoer *et al.* (2013), as it considers the most comprehensive set of available data.

While low-energy future measurements are recommended, experiments at high energy are highly desirable for better understanding the reaction mechanisms responsible for the interference pattern that is observed between the two well-known 1^- resonances, which cannot be completely reproduced unless some background contribution is also included.

2. $^{16}\mathrm{O}(p,\gamma)^{17}\mathrm{F}$

Below a laboratory energy of about 2700 keV, i.e., the energy of the lowest-lying resonance (Tilley, Weller, and Cheves, 1993), the $^{16}\mathrm{O}(p,\gamma)^{17}\mathrm{F}$ reaction is a prime example of the nonresonant direct radiative-capture process. This reaction has been measured many times using a variety of techniques, including activation, prompt γ-ray detection, and inverse-kinematics experiments. The $E1$ capture can proceed to the ground or first excited state in $^{17}\mathrm{F}$, with the latter being the dominant transition. Adelberger *et al.* (2011) adopted a value of $S(0) = 10.6 \pm 0.8$ keV b with a 7.5% uncertainty. This result was obtained by normalizing the microscopic-model calculations of Baye, Descouvemont, and Hesse (1998) to the data of Rolfs (1973) and Morlock *et al.* (1997).

A recent statistically rigorous evaluation of the S-factor data of Hester, Pixley, and Lamb (1958), Chow, Griffiths, and Hall (1975), Becker *et al.* (1982), and Morlock *et al.* (1997) was presented by Iliadis, Palanivelrajan, and de Souza (2022). Their analysis, including a discussion of experimental uncertainties, used a combined fit of the transitions to the ground and first excited states in ^{17}F and their sum and was performed using a Bayesian model. The physical model was a single-particle model employing a Woods-Saxon potential for generating the radial bound-state wave function. The fit had three adjustable parameters: the radius parameter and diffuseness of the Woods-Saxon potential and the ANCs for scaling the theoretical nonresonant capture S factors. It was also found that a poor fit was obtained when using spectroscopic factors instead as scaling parameters. As the $^{16}\mathrm{O}(p,\gamma)^{17}\mathrm{F}$ reaction at low bombarding energies is peripheral, the analysis of the S factor in terms of the ANCs greatly reduced the sensitivity of the fit to the single-particle potential parameters. For the ANCs of the ground and first-excited-state transitions, Iliadis, Palanivelrajan, and de Souza (2022) found values of $C^2_{\mathrm{gs}} = 1.115\ \mathrm{fm}^{-1}$ ($\pm 4.0\%$) and $C^2_{\mathrm{fes}} = 7063\ \mathrm{fm}^{-1}$ ($\pm 4.0\%$), respectively. These results agree with those measured in the $^{16}\mathrm{O}(^3\mathrm{He}, d)^{17}\mathrm{F}$ reaction by Gagliardi *et al.* (1999). It is not surprising that the uncertainties given by Gagliardi *et al.* ($\approx 10\%$) are significantly larger than for the previously quoted values, because the distorted-wave Born approximation (DWBA) analysis of Gagliardi *et al.* (1999) was subject to ambiguities in the choice of optical model potentials for the incoming and outgoing channels.

The total S factor at zero energy reported by Iliadis, Palanivelrajan, and de Souza (2022) was $S_{\mathrm{tot}}(0) = 10.92$ keV b ($\pm 4.0\%$). The uncertainty is significantly smaller than the results published by Iliadis *et al.* (2008), which were derived from an analysis that was not statistically rigorous. We adopt the results of Iliadis, Palanivelrajan, and de Souza (2022) in this review. Their S factor is presented in Table XII.

We endorse the two recommendations made by Iliadis, Palanivelrajan, and de Souza (2022). First, they advocated for a new low-energy measurement of the $^{16}\mathrm{O}(p,\gamma)^{17}\mathrm{F}$ reaction, specifically, at center-of-mass energies below 200 keV, which thus far have been reached only in the experiment of Hester, Pixley, and Lamb (1958), albeit with a relatively large systematic uncertainty of 14%. Second, it would be interesting to compare their results to those from a future R-matrix analysis of the same datasets.

3. $^{17}\mathrm{O}(p,\gamma)^{18}\mathrm{F}$

Adelberger *et al.* (2011) discussed only the nonresonant component of the $^{17}\mathrm{O}(p,\gamma)^{18}\mathrm{F}$ reaction cross section, which dominates the total cross section at solar temperatures. At the time the results of Chafa *et al.* (2007) were recommended. Since the publication of the work by Adelberger *et al.* (2011), several new S-factor measurements have been reported, at both low and high energies (Newton *et al.*, 2010; Hager *et al.*, 2012; Kontos *et al.*, 2012; Scott *et al.*, 2012; Di Leva *et al.*, 2014; Buckner *et al.*, 2015; Gyürky *et al.*, 2017). Despite differences in the techniques exploited and energy ranges covered, the derived $S(0)$ values agree across different experiments, for both the nonresonant capture and the total S factor, where the latter quantity includes the low-energy tails of two broad resonances ($E_r^{\mathrm{c.m.}} = 557$ and 677 keV). Here we recommend the total S factor from the most recent analysis of Gyürky *et al.* (2017). The $^{17}\mathrm{O}(p,\gamma)^{18}\mathrm{F}$ reaction cross section was measured in the laboratory bombarding energy range of 500–1800 keV, with a typical total uncertainty of 10% using the activation method. A comparison with other independent results, when possible, at $Ep^{\mathrm{lab}} = 500$ keV resulted in good agreement with the results of Hager *et al.* (2012) and Kontos *et al.* (2012), while a 20% difference is observed with respect to the results of Newton *et al.* (2010). An R-matrix analysis was performed while considering all the low-energy data, resulting in a value of $S(0)\mathrm{tot} = (4.7 \pm 1.0)$ keV b.[8]

At temperatures near 60 MK, which is typical for hydrogen-shell burning in AGB stars, the $^{17}\mathrm{O}(p,\gamma)^{18}\mathrm{F}$ reaction rate is dominated by the $E_r^{\mathrm{c.m.}} = 65$ keV resonance, which was not considered by Adelberger *et al.* (2011). No direct measurements are reported for the resonance strength $\omega\gamma$, which is presently estimated from experimental values of the partial and total widths. Partial widths of $\Gamma_\alpha = (130 \pm 5)$ eV and $\Gamma_\gamma = (0.44 \pm 0.02)$ eV were measured using the $^{14}\mathrm{N} + \alpha$ reaction (Berka *et al.*, 1977; Mak *et al.*, 1980). The most uncertain quantity is the proton partial width Γ_p, which is estimated from the measured strength of the corresponding resonance in the (p,α) channel. Our best estimate for the (p,α) strength is $\omega\gamma_{p\alpha} = 4.6^{+5.4}_{-1.2} \times 10^{-9}$ eV (see Table XIII and Sec. XI.B.4 for details), which leads to $\Gamma_p = 18.5^{+21.7}_{-4.7} \times 10^{-9}$ eV. Hence, our recommended value is $\omega\gamma_{p\gamma} = 15.6^{+18.3}_{-4.0} \times 10^{-12}$ eV; see Table XIII. This value is consistent with the strength recommended by Palmerini *et al.* (2013), though we have inflated the error to account for the uncertain status of the proton width. A direct measurement of the (p,γ) strength of the $E_r^{\mathrm{c.m.}} = 65$ keV resonance is ongoing at LUNA (Ciani, Piatti, and Gesuè, 2022). Moreover, the 65 keV (1^-) resonance is expected to interfere with the -2.0 keV (1^-) subthreshold resonance. We recommend the treatment of the interference contribution described by Buckner *et al.* (2015). At typical temperatures of classical novae, the main contributor to the $^{17}\mathrm{O}(p,\gamma)^{18}\mathrm{F}$ reaction rate is the $E_r^{\mathrm{c.m.}} = 183.9$ keV resonance, which was first observed by Fox *et al.* (2004). It was subsequently remeasured by Chafa *et al.* (2007), Scott *et al.* (2012), Di Leva *et al.* (2014), and Buckner *et al.* (2015). Here we recommend the weighted mean adopted by Buckner *et al.* (2015), $\omega\gamma = (1.77 \pm 0.09) \times 10^{-6}$ eV.[9]

4. $^{17}\mathrm{O}(p,\alpha)^{14}\mathrm{N}$

The $^{17}\mathrm{O}(p,\alpha)^{14}\mathrm{N}$ reaction rate is determined by the contributions of the narrow resonances. At solar energies the dominant contributions originate from resonances at $E_r^{\mathrm{c.m.}} = -2$ and 65 keV. At typical temperatures of AGB stars

[8] Gyürky *et al.* (2017) referred to the uncertainty to as statistical only. However, it in fact represents the total uncertainty (Gyürky, 2024).

[9] The article by Gesuè *et al.* (2024) reported an $\omega\gamma$ bare value of $[30 \pm 6(\mathrm{stat}) \pm 2(\mathrm{syst})] \times 10^{-12}$ eV for the 64.5 keV resonance strength.

and classical novae, the main contributor to the rate is a resonance at $E_r^{\text{c.m.}} = 183.9$ keV. Concerning the subthreshold resonance, no new results have been published since (Adelberger *et al.*, 2011).

The $E_r^{\text{c.m.}} = 65$ keV resonance was recently studied both in a direct experiment [$\omega\gamma = (10.0 \pm 1.4_{\text{stat}} \pm 0.7_{\text{syst}}) \times 10^{-9}$ eV (Bruno *et al.*, 2016)] and with the Trojan horse indirect method [$\omega\gamma = (3.42 \pm 0.60) \times 10^{-9}$ eV (Sergi *et al.*, 2015)]. The resonance strength reported by Bruno *et al.* (2016) deviates by a factor of 2.5 from that of Sergi *et al.* (2015) and by a factor of 2 from the value used prior to the work of Adelberger *et al.* (2011) given by Fox *et al.* (2005), who included a revised analysis of the data from Blackmon *et al.* (1995). Because the values disagree by more than their uncertainties, we recommend an approximate value of $\omega\gamma = 4.6^{+5.4}_{-1.2} \times 10^{-9}$ eV, which encompasses all values in the literature.

The resonance at $E_r^{\text{c.m.}} = 183.9$ keV, in contrast, is well known. The most recent determination of its strength, as reported by Bruno *et al.* (2015), was $\omega\gamma = (1.68 \pm 0.03_{\text{stat}} \pm 0.12_{\text{syst}}) \times 10^{-3}$ eV, which is in excellent agreement with previous results (Chafa *et al.*, 2007; Moazen *et al.*, 2007; Newton *et al.*, 2007).

C. Reactions of the CNO-III cycle

1. ^{18}O$(p,\gamma)^{19}$F

Important components for this reaction channel are a $E_r^{\text{c.m.}} = 20$ keV resonance, for which only indirect data exist (Wiescher *et al.*, 1980; Champagne and Pitt, 1986; La Cognata *et al.*, 2008), the resonances at $E_r^{\text{c.m.}} = 90$ keV and $E_r^{\text{c.m.}} = 143$ keV, and the nonresonant capture process. Reported strengths of the $E_r^{\text{c.m.}} = 20$ keV resonance vary by 1 order of magnitude between 1.4×10^{-22} eV (Lorenz-Wirzba *et al.*, 1979) and 1.9×10^{-21} eV (Wiescher *et al.*, 1980), depending on the assumed proton widths. We recommend a value of $\omega\gamma = 5.7 \times 10^{-22}$ eV, based on the results of Champagne and Pitt (1986). A comprehensive measurement was done by Wiescher *et al.* (1980) covering the 80–2200 keV range at multiple angles and measuring branching ratios, the direct component (extrapolated from high-energy data), and strengths down to the $E_r^{\text{c.m.}} = 143$ keV resonance. The strength of the latter resonance, $\omega\gamma = (0.98 \pm 0.03) \times 10^{-3}$ eV, has been remeasured multiple times with consistent results (Wiescher *et al.*, 1980; Becker *et al.*, 1982; Vogelaar *et al.*, 1990; Dermigny *et al.*, 2016; Best *et al.*, 2019; Pantaleo *et al.*, 2021). The strength of the $E_r^{\text{c.m.}} = 90$ keV resonance was controversial (Buckner *et al.*, 2012; Fortune, 2013), but a measurement by Best *et al.* (2019) found it to be of insignificant strength [$\omega\gamma = (0.5 \pm 0.1) \times 10^{-9}$ eV]. The nonresonant component was determined by Wiescher *et al.* at an energy of $E^{\text{c.m.}} = 1752$ keV and extrapolated to a value of $S(0) = 15.7$ keV b. Buckner *et al.* normalized a nonresonant capture model calculation to the experimental value at $E^{\text{c.m.}} = 1752$ keV, resulting in $S(0) = 7.1$ keV b. No uncertainties were given for these two S factors. Best *et al.* (2019) extracted the nonresonant component from a cross-section fit at center-of-mass energies between 85 and 150 keV, resulting in $S(0) = (23 \pm 3.8)$ keV b. Here we adopt this value, but further investigation of the low-energy cross section is necessary to resolve these discrepancies.

2. ^{18}O$(p,\alpha)^{15}$N

The low-energy trend of the $^{18}\text{O}(p,\alpha)^{15}\text{N}$ cross section is determined by three resonances, at 20, 90, and 143 keV; see Table XIII. The most recent determination of the strength of the 20 keV resonance comes from a Trojan horse method (THM) experiment by La Cognata *et al.* (2008). Their result had already been recommended by Adelberger *et al.* (2011); we maintain the same recommendation. The resonance at 90 keV was investigated in the past with direct (Lorenz-Wirzba *et al.*, 1979) and indirect techniques (La Cognata *et al.*, 2008), finding consistent results. Nevertheless, a new direct measurement reported a resonance strength 1 order of magnitude higher than the previously adopted value (Bruno *et al.*, 2019). Since no clear explanation can be found for such a discrepancy, here we adopt a weighted average of the three resonance strengths, but we inflate the uncertainty so that it embraces all three values. New experiments to solve this discrepancy are advised. The resonance at 143 keV is well known, and different experiments have provided consistent results (Lorenz-Wirzba *et al.*, 1979; Becker *et al.*, 1995; Bruno *et al.*, 2015). Here we adopt a weighted average of Becker *et al.* (1995) and Bruno *et al.* (2015), which have independent systematic uncertainties (while no information on individual contributions to the total uncertainty was given by Lorenz-Wirzba *et al.* (1979). The nonresonant differential cross section was measured down to $E_{\text{c.m.}} = 55$ keV by Bruno *et al.* (2019). At overlapping energies the S factor is consistent with the previous measurement by Lorenz-Wirzba *et al.* (1979). Bruno *et al.* (2019) found a broad structure at $E \approx 110$ keV that they could explain only by assuming the existence of an as-yet-unobserved resonance at $E_r^{\text{c.m.}} = 106$ keV. Further investigations are needed to shed light on this supposed resonance.

3. ^{19}F$(p,\gamma)^{20}$Ne

The $^{19}\text{F}(p,\gamma)^{20}\text{Ne}$ reaction has been challenging to access experimentally because it has a much smaller cross section than the competing $^{19}\text{F}(p,\alpha\gamma)^{16}\text{O}$ reaction. The cross section of both reactions is dominated by a mixture of narrow and broad resonances corresponding to mostly unnatural parity states in ^{20}Ne (mainly $J^\pi = 1^+$ and 2^-). At very low energies, the cross section may be enhanced by a near-threshold state at $E_{\text{c.m.}} \approx 11$ keV, and subthreshold and nonresonant capture contributions may also contribute significantly but have not yet been well characterized (deBoer, Clarkson *et al.*, 2021), as few particle transfer studies have been published (Betts, Fortune, and Middleton, 1975; Kious, 1990).

The first low-energy cross-section measurement was that of Couture *et al.* (2008), who measured only the $^{19}\text{F}(p,\gamma_1)^{20}\text{Ne}$ transition. While this was likely a strong transition, there can certainly be other transitions with sizable contributions. Couture *et al.* (2008) covered the center-of-mass energy range from 200 to 760 keV, where three strong resonances were observed, at $E_r^{\text{c.m.}} = 323.9$, 564, and 634 keV. Only an upper

limit was reported for an expected resonance at $E_r^{\text{c.m.}} = 213$ keV. In addition, no evidence of either a near-threshold state, a subthreshold state, or nonresonant capture has been observed.

An investigation of the γ-ray branching ratios of the $E_r^{\text{c.m.}} = 323.9$ keV resonance was undertaken by Williams *et al.* (2021), who used the DRAGON recoil separator at TRIUMF. Recoil detection provided an effective method of discriminating the large background from the $^{19}\text{F}(p,\alpha\gamma)^{16}\text{O}$ reaction. It was found that the primary transitions to both the ground and the 4967 keV state dominate over the primary transition to the 1633 keV first excited state.

Finally, a new direct measurement of the low-energy cross section reported by Zhang *et al.* (2022) overlaps with the previous low-energy data of Couture *et al.* (2008). A new resonance was discovered at $E_r^{\text{c.m.}} = 225.2$ keV in the $^{19}\text{F}(p,\gamma_1)^{20}\text{Ne}$ cross section and was attributable to a 3^- state that corresponds to a weak resonance observed in the $^{19}\text{F}(p,\alpha\gamma)^{16}\text{O}$ data of Spyrou *et al.* (2000) at the same energy. This low-energy resonance increases the $^{19}\text{F}(p,\gamma)^{20}\text{Ne}$ reaction rate by about an order of magnitude at $T \approx 0.1$ GK. Like Williams *et al.* (2021), Zhang *et al.* (2022) observed a sizable ground-state transition for the $E_r^{\text{c.m.}} = 323.9$ keV resonance. As in the $^{19}\text{F}(p,\alpha\gamma)^{16}\text{O}$ reaction (see Sec. XI.C.4), an upper limit was also estimated for the proposed $E_r^{\text{c.m.}} = 11$ keV resonance.

We have therefore adopted the resonance energies and strengths of Zhang *et al.* (2022), which are in good agreement with the previous measurements of Couture *et al.* (2008) and Williams *et al.* (2021) in the overlapping energy region; see Tables XI and XIII.

4. $^{19}\text{F}(p,\alpha)^{16}\text{O}$

The $^{19}\text{F}(p,\alpha)^{16}\text{O}$ reaction was not included by Adelberger *et al.* (2011). NACRE (Angulo *et al.*, 1999) pointed out that the total astrophysical S factor was dominated by the nonresonant (p,α_0) channel, though underscoring the large uncertainties (≈50%) affecting the reaction rate at low temperatures. After NACRE the situation greatly changed following the publication of a large number of papers addressing the measurement of the α_0 channel (La Cognata *et al.*, 2011, 2015; Lombardo *et al.*, 2013, 2015; Indelicato *et al.*, 2017), of the $\alpha\gamma$ channel (Fessler *et al.*, 2000; Spyrou *et al.*, 2000; Ding, Xu, and Wang, 2002; Zhang *et al.*, 2019, 2021; Pham *et al.*, 2021). In addition, some researchers attempted to reach a consensus astrophysical factor carrying out refined analyses using, for instance, the phenomenological R matrix (He *et al.*, 2018; Lombardo, 2019; Lombardo *et al.*, 2019; deBoer, Clarkson *et al.*, 2021; Zhang, López *et al.*, 2021), and carried out new theoretical calculations of the astrophysical S factor (Sahoo and Basu, 2021).

Regarding the measurement of the astrophysical factor for the α_0 channel, populating the ^{16}O ground state, indirect [using the THM (Tribble *et al.*, 2014)] and direct methods were used, leading to consistent results. While the direct measurement (Lombardo *et al.*, 2015) could reach about 170 keV in the center of mass, the THM measurements (La Cognata *et al.*, 2011, 2015; Indelicato *et al.*, 2017) could reach 5 keV and provide an extrapolated $S(0) = (17.4 \pm 2.7) \times 10^3$ keV b. The most striking feature of both direct and indirect measurements is the evidence of resonances populating the $E_{\text{c.m.}} \lesssim 600$ keV energy region, which is at odds with the NACRE extrapolation.

Until the work of Zhang *et al.* (2021), direct measurements of the $\alpha\gamma$ channel stopped at energies well above the Gamow energy. Zhang *et al.* (2021) could reach energies as low as ≈72 keV in the center of mass, which is still above the Gamow window for solar fusion, thanks to the use of the Jinping Underground Nuclear Astrophysics (JUNA) experimental facility. Although the lowest-energy point is affected by a large uncertainty (87%) and no correction for the electron screening effect is reported [for instance, Assenbaum, Langanke, and Rolfs (1987) estimated a 20% enhancement at 70 keV center-of-mass energy for proton-induced reactions on oxygen], the R-matrix analysis carried out by Zhang *et al.* indicates the presence of a resonance at $E_r^{\text{c.m.}} = 11$ keV, corresponding to a ^{20}Ne excitation energy of 12.855 MeV. This 1^+ level could significantly increase the S factor, yielding $S(0) \approx 200$ MeV b. If this result is confirmed, the $\alpha\gamma$ channel will dominate the low-energy total S factor for $^{19}\text{F}(p,\alpha)^{16}\text{O}$ at center-of-mass energies below ≈ 50 keV. Alternatively, if the $E_r^{\text{c.m.}}$ resonance is excluded from the fit, the deduced value will be $S(0) \approx 1$ MeV b.

The presence of new datasets triggered the publication of reviews aiming to provide the best fit of the available data. In particular, Lombardo *et al.* (2019) carried out a comprehensive R-matrix analysis spanning an energy range from about $E^{\text{c.m.}} = 200$ keV to 12 000 keV. The R-matrix fit predicts a $S(0) \approx 10$ MeV b result for the α_0 channel, with a conservative uncertainty of about 20%, which is lower than the value from Indelicato *et al.* (2017). An additional interesting result from their work is that the α_1 channel, corresponding to the population of the 0^+ ^{16}O first excited state, is negligible with respect to the α_0 one below about $E^{\text{c.m.}} = 50$ keV, yet if the 2^+ state at 13 095 keV is assumed to contribute, as supported by the $^{16}\text{O}(\alpha,\alpha_1)^{16}\text{O}^*$ data, the α_1 channel may significantly contribute to the aforementioned total astrophysical factor about $E^{\text{c.m.}} = 50$ keV, calling for new data at low energies.

The most comprehensive R-matrix analysis, however, not including the results of Zhang *et al.* (2021), is the one carried out in deBoer, Clarkson *et al.* (2021). For the α_1 channel, the results are consistent with those of Lombardo *et al.* (2019). For the $\alpha\gamma$ channel, the conclusions are that the α_2 channel is the major one and, as shown by Zhang *et al.* (2021), low-threshold and subthreshold resonances can enhance the astrophysical factor to dominate over the α_0 channel at astrophysical energies. Finally, the result of the R-matrix analysis for the α_0 channel supports a flat S factor devoid of resonances, which is in contrast to the findings of La Cognata *et al.* (2011, 2015), Lombardo *et al.* (2013, 2015), and Indelicato *et al.* (2017) but in agreement with the analysis of Herndl *et al.* (1991). However, this is based on the data from Lorenz-Wirzba (1978), which were excluded from the NACRE compilation owing to a likely large underestimate of reported absolute cross sections (by about a factor of 2).

In summary, while the situation for the α_0 and α_1 channels is well constrained, the contribution of higher ^{16}O excited

states—and, in particular, of the α_2 channel—needs further studies to confirm the occurrence of the $E_r^{\text{c.m.}} = 11$ keV resonance. This represents the largest source of uncertainty to date. Therefore, the recommended reaction rate lower limit is conservatively set by the Indelicato *et al.* (2017) one, while the upper limit is given by Zhang, López *et al.* (2021), assuming the existence of the $E_r^{\text{c.m.}} = 11$ keV resonance.

D. Reactions of the neon-sodium (NeNa) cycle

1. ^{20}Ne$(p,\gamma)^{21}$Na

The low-energy S factor of the $^{20}\text{Ne}(p,\gamma)^{21}\text{Na}$ reaction is dominated by the high-energy tail of a subthreshold resonance only a few keV below the reaction threshold. In addition, the nonresonant capture into two additional states is relevant and provides the largest contribution in the energy range where data are available. All three transitions were measured over a wide range of energies by two direct experiments (Rolfs *et al.*, 1975; Lyons *et al.*, 2018), and the results can be used to arrive at S-factor recommendations. However, no consistent parametrizations have been published that could be used for comparison of the results.

S-factor data from these two experiments were extracted either from their accompanying supplemental materials or from digitized forms of the published figures. The results were normalized to the strength of the $E_r^{\text{c.m.}} = 1113$ keV resonance [$\omega\gamma = 0.94$ eV (Lyons *et al.*, 2018)]. The resonant capture into the tail of the subthreshold resonance [$E_r^{\text{c.m.}} = -7.9$ keV (Firestone, 2015)] can be described using the Breit-Wigner equation, as shown by Rolfs and Rodney (1988) and Iliadis (2015). To additionally account for the nonresonant capture to the ground state, a constant value of $S(E) = 0.0463$ keV b, as recommended in the indirect experiment of Mukhamedzhanov *et al.* (2006), was included in the fit to the data of Rolfs *et al.* (1975) and Lyons *et al.* (2018). For the two direct-capture transitions, the energy dependence of the S factor was calculated with the program DIRCAP (Iliadis, 2022) using a Woods-Saxon potential with a diffuseness of $a = 0.65$ fm to achieve S-factor magnitudes comparable to the experimental data. These S factors were fit individually to the experimental data and then summed to the total S factor. The results are listed in Table XII. Uncertainties from the individual contributions were added in quadrature.

However, significant and unquantifiable uncertainties likely exist because the results of the two experiments differ systematically in both magnitude and energy dependence (Lyons *et al.*, 2018). This may be caused by experimental or data-analysis errors in either experiment (or in both). In addition, the experiments at low energies measured in only a small angular range and relied on sparse angular distribution measurements at higher energies to infer angular correlation effects. In addition, the experiments did not reach sufficiently low energies to conclusively determine the potential parameters to be used in the DIRCAP calculation. Consequently, this will contribute to the S-factor uncertainty when the energy range of stellar burning, which depends on the temperature, is located far below the experimental range.

A new measurement of the $^{20}\text{Ne}(p,\gamma)^{21}\text{Na}$ direct-capture cross section down to $E^{\text{c.m.}} = 250$ keV was recently published by the LUNA Collaboration (Masha *et al.*, 2023). The potential-model results agree with the new experimental data.

2. ^{21}Ne$(p,\gamma)^{22}$Na

At temperatures below 0.1 GK, the reaction rate is dominated by three narrow resonances, at 16.6, 94.6, and 126 keV. The 16.6 and 94.6 keV resonances have never been observed directly in the (p,γ) channel (Görres *et al.*, 1982). Upper limits on their strengths were derived from a $^{21}\text{Ne}(d,p)^{22}\text{Na}$ experiment (Neogy, Middleton, and Scholz, 1972; Iliadis *et al.*, 2001). The results are reported in Table XIII. The nonresonant capture S factor at zero energy was estimated by Rolfs *et al.* (1975) using single-particle spectroscopic factors of the bound states in ^{22}Na. According to Rolfs *et al.*, the result, $S(0) \approx 20$ keV b, is uncertain by a factor of 3.

3. ^{22}Ne$(p,\gamma)^{23}$Na

The $^{22}\text{Ne}(p,\gamma)^{23}\text{Na}$ reaction used to be the most uncertain of the NeNa cycle because of a number of poorly known low-lying resonances. At temperatures below 30 MK, the reaction rate is dominated by a resonance at 36 keV. Its strength was determined from a proton-transfer experiment (Hale *et al.*, 2001; Iliadis *et al.*, 2010). Two near-threshold resonances are expected, at 5 and 28 keV, but the existing upper limits on their strengths are so low that they do not contribute significantly to the reaction rate (Hale *et al.*, 2001). Two resonances, at 68 and 100 keV, were reported by Powers *et al.* (1971), generating a great deal of discussion in the literature. Subsequent searches included direct experiments (Cavanna *et al.*, 2015; Depalo *et al.*, 2016; Ferraro *et al.*, 2018), a proton-transfer reaction (Hale *et al.*, 2001), and inelastic scattering (Carrasco-Rojas *et al.*, 2023). No evidence for the resonances emerged from these searches. The latest direct upper limits on their strength have suggested that, even if the two resonances exist, their contribution to the mean (recommended) thermonuclear reaction rate is negligible (Ferraro *et al.*, 2018). A resonance doublet dominates the reaction rate at temperatures around 0.1 GK. The strength of the stronger resonance in the doublet was measured in both direct (Kelly *et al.*, 2017; Cavanna *et al.*, 2018; Lennarz *et al.*, 2020; Williams *et al.*, 2020) and proton-transfer experiments [data from Powers *et al.* (1971) and Hale *et al.* (2001) reanalyzed by Santra, Chakraborty, and Roy (2020)]. The value adopted in Table XIII is an average of all previously mentioned literature values. The strength of the weaker resonance in the doublet was inferred from proton-transfer data (Santra, Chakraborty, and Roy, 2020).

At 0.2 GK the reaction rate is determined mainly by a resonance at 181 keV. Its strength was measured in four independent experiments (Kelly *et al.*, 2017; Cavanna *et al.*, 2018; Ferraro *et al.*, 2018; Williams *et al.*, 2020). The strength recommended in Table XIII is a weighted average of all four values. The most intense higher-lying resonances relevant to nova and supernova explosions were recently addressed by Longland *et al.* (2010), Depalo *et al.* (2015), Kelly *et al.* (2017), and Williams *et al.* (2020). The nonresonant capture cross section has been measured by different groups (Kelly *et al.*, 2017; Ferraro *et al.*, 2018; Williams *et al.*, 2020). The

low-energy trend of the ground-state capture is described by a constant value of $S = (50 \pm 12)$ keV b plus the contribution of a broad subthreshold state at −130 keV ($E_x = 8664$ keV) (Ferraro *et al.*, 2018).

4. ^{23}Na$(p,\gamma)^{24}$Mg

The $^{23}\mathrm{Na}(p,\gamma)^{24}\mathrm{Mg}$ reaction has elicited several recent studies (Caciolli *et al.*, 2011; Boeltzig *et al.*, 2019, 2022; Marshall *et al.*, 2021). The cross section is dominated by three narrow resonances over the lowest experimentally measured energy range, which are located at $E_r^{\mathrm{c.m.}} = 133$, 240.6, and 295.9 keV. Below the lowest known resonance, nonresonant components are thought to dominate.

Several indirect measurements have been made to characterize energies and proton spectroscopic factors of bound and unbound states in ^{24}Mg. The measurement of Hale *et al.* (2004) used the $^{23}\mathrm{Na}(^3\mathrm{He}, \mathrm{d})^{24}\mathrm{Mg}$ reaction to investigate unbound states ($11\,690 < E_x < 12\,520$ keV) near the proton separation energy ($S_p = 11\,693$ keV). For lower-energy bound states that were not measured, the spectroscopic factors of Garrett *et al.* (1978) were adopted. A direct-capture model was used to calculate the nonresonant component of the cross section. This was followed by an investigation of the lowest-energy resonance at $E_r^{\mathrm{c.m.}} \approx 133$ keV by Cesaratto *et al.* (2013), where an upper limit for the resonance strength was determined. A subsequent study at the LUNA facility (Boeltzig *et al.*, 2019) was able to make a first measurement of the resonance strength, $1.46^{+0.58}_{-0.53} \times 10^{-9}$ eV. A recent $^{23}\mathrm{Na}(^3\mathrm{He}, d)^{24}\mathrm{Mg}$ transfer study at the Triangle Universities Nuclear Laboratory (TUNL) revised the energy of the ≈133 keV resonance to $E_r^{\mathrm{c.m.}} = 133(3)$ keV (Marshall *et al.*, 2021).

Direct cross-section measurements of the $^{23}\mathrm{Na}(p,\gamma)^{24}\mathrm{Mg}$ reaction at energies between $E^{\mathrm{lab}} = 500$ and 1000 keV were made at the University of Notre Dame by Boeltzig *et al.* (2022). Two broad, strong resonances were observed in several γ-ray transitions at $E_r^{\mathrm{c.m.}} = 841$ and 981 keV whose low-energy tails contribute in the low-energy region. Note that the energy uncertainties presented here reflect the uncertainty in the beam calibration of the accelerator, which was neglected by Boeltzig *et al.* (2022). Further, measurements of the $E_x = 10\,740$ keV primary transition in ^{24}Mg, predicted to have the largest nonresonant capture component based on the spectroscopic factors of Garrett *et al.* (1978), observed a trend in the off-resonance cross section that was highly suggestive of nonresonant capture. Given the level of consistency observed between the nonresonant capture S factors calculated from the spectroscopic factors of Garrett *et al.* (1978) and the external capture S factors from the R-matrix analysis, an uncertainty in the nonresonant S factor of 50% was recommended. We have adopted the nonresonant component of Boeltzig *et al.* (2022) in this review, which, like all previous calculations, relies heavily on the spectroscopic factors of Garrett *et al.* (1978).

5. ^{23}Na$(p,\alpha)^{20}$Ne

The $^{23}\mathrm{Na}(p,\alpha)^{20}\mathrm{Ne}$ reaction rate is dominated by narrow resonances, with a total of 52 resonances in the center-of-mass energy interval 6–2328 keV.

After NACRE the state-of-the-art tabulation of the resonance strengths is the one given by Iliadis *et al.* (2010). It is based mostly on the $(^3\mathrm{He}, d)$ proton-transfer measurement by Hale *et al.* (2004), which supplied both the excitation energies and the spectroscopic factors of the near-threshold states. In detail, below $E^{\mathrm{c.m.}} = 968$ keV, all the resonance strengths are taken from Table VI of Hale *et al.* (2004), with the exception of the $E_r^{\mathrm{c.m.}} = 133$ keV resonance strength (Marshall *et al.*, 2021), for which the upper limit directly determined by Rowland *et al.* (2004) and Iliadis, Champagne, and José (2005), which is equal to 1.5×10^{-8} eV, is adopted. Above $E^{\mathrm{c.m.}} = 968$ keV, the strengths of Hale *et al.* (2004) are rescaled to that of the $E_r^{\mathrm{c.m.}} = 338$ keV resonance determined by Rowland *et al.* (2002). This result is considered the reference value since it provides the most recent directly measured strength.

Besides the aforementioned works, two more should be considered. One was by Iliadis, Champagne, and José (2005), whose data were not used by Iliadis *et al.* (2010), because the same upper limit for the $E_r^{\mathrm{c.m.}} = 133$ keV resonance is reported as was used by Rowland *et al.* (2004). The other work was by Cesaratto *et al.* (2013), who used the upper limit on the (p,γ) resonance strength and the upper limit on the α branching ratio (equal to 0.13 at the 95% CL), to provide an upper limit on the (p,α) strength of the $E_r^{\mathrm{c.m.}} = 133$ keV resonance equal to 0.88×10^{-9} eV. This implies a negligible contribution to the reaction rate and confirms the conclusions drawn by Iliadis *et al.* (2010).

Note that below 10^9 K, the resonances dominating the total $^{23}\mathrm{Na}(p,\gamma)^{24}\mathrm{Mg}$ S factor differ from those determining the total $^{23}\mathrm{Na}(p,\alpha)^{20}\mathrm{Ne}$ S factor. Consequently, the S factors of these two competing reactions are not correlated.

XII. ELECTRON SCREENING OF NUCLEAR REACTIONS

Nuclear fusion reactions measured in the laboratory and those occurring in the solar core are both affected by the electronic environments in which they take place. The effects are, however, different, requiring special care in deriving the appropriate solar reaction rates. As long as these rates cannot be measured under solar plasma conditions in the laboratory, the usual two-step strategy is to remove the laboratory screening effects from the data to obtain the bare nuclear cross section σ^{b}, which is then modified to incorporate the solar plasma screening modifications. Thus, one must address the differential effects of screening for the solar cross section σ^{solar} and the laboratory results σ^{lab}.

A. Screening in laboratory experiments

Screening diminishes the Coulomb barriers that retard interactions between bare nuclei, thus enhancing cross sections, with the effects becoming more pronounced with decreasing center-of-mass energy. Nuclear astrophysics has advanced rapidly over the past two decades with the deployment of underground accelerators and other low-background techniques (Broggini *et al.*, 2010) that have enabled low-energy, low-counting-rate experiments. In particular, laboratory measurements of the pp-chain reactions $^2\mathrm{H}(p,\gamma)^3\mathrm{He}$ and $^3\mathrm{He}(^3\mathrm{He}, 2p)^4\mathrm{He}$ have been made at energies corresponding

to the solar Gamow peak. A treatment of the distorting effects of screening then becomes important in extracting the bare S factor $S^b(E)$.

The bare cross section is given by

$$\sigma^b(E) = \frac{1}{E} S(E) P(E), \qquad P(E) \equiv \exp\left[-2\pi\eta(E)\right], \quad (24)$$

with $\eta(E) = Z_1 Z_2 \alpha \sqrt{\mu/2E}$, where μ is the reduced mass and E is the center-of-mass energy. The effects of screening can be incorporated into the Gamow penetration factor $P(E)$ through an energy shift, $E \to E + U_e$, where the screening potential U_e has the net effect of lowering the Coulomb barrier. At the lowest accessible energies in laboratory measurements, the separation of target and projectile during tunneling is much smaller than the atomic radius. Thus, the electrons, which were originally bound to the target (assuming a projectile beam of bare nuclei), are attracted by the joint charge of target and projectile during the fusion. The screening potential can then be replaced by a constant screening energy U_e. This picture was confirmed in simulations of the electron dynamics in low-energy fusion reactions (Shoppa *et al.*, 1993). After expanding the argument of the exponential in Eq. (24) to the first order in U_e one obtains the following relation between the laboratory and bare S factors (Assenbaum, Langanke, and Rolfs, 1987):

$$S^{\rm lab}(E) = S^{\rm b}(E) \exp\left(\frac{\pi\eta(E) U_e}{E}\right). \quad (25)$$

Equation (25) neglects a small normalization correction associated with the effects U_e on the matching of the external wave function to that in the Coulomb region.

The $1/E$ dependence of the exponent is responsible for the growing importance of the screening correction at low energies. Although the screening potential U_e can in principle be calculated from the electron charge distribution, in most applications it is treated as a free constant parameter that is determined along with $S^{\rm b}(0)$ and its derivatives from a fit to data. Figure 4 of Adelberger *et al.* (2011) shows the results for $S_{33}(E)$, where the fit yielded $U_e = 305 \pm 90$ eV. The exponential dependence of the screening correction leads to a rapid increase in $S_{33}^{\rm lab}(E)$ relative to $S_{33}^{\rm b}$, reaching ~40% at the lowest data point measured. This example also underscores the potential for screening to complicate the extraction of $S^{\rm b}(E)$ for energies relevant to the solar core, even in cases where measurements are restricted to higher energy than the Gamow window.

In principle, one can test the adequacy of Eq. (25) by doing laboratory experiments at low energies—even if the reactions studied are not directly relevant to nuclear astrophysics. Such studies began more than 30 years ago (Assenbaum, Langanke, and Rolfs, 1987), when gaseous targets were used to limit energy loss effects and other systematics. Subsequent studies have varied greatly in their configurations, with targets ranging from atomic and molecular gases to metals,[10] thin and thick targets, and the use of direct and inverse kinematics (Aliotta *et al.*, 2022). The experiments can be challenging at the energies needed, subject to backgrounds from both intrinsic activities in detectors and external sources such as cosmic rays.

The values of U_e extracted from experiment using gaseous targets have often exceeded the adiabatic limit, which is defined in atomic physics as the difference between the electron binding energies of the separate atoms in the entrance channel and that of the composite atom (Engstler *et al.*, 1988, 1992; Angulo *et al.*, 1993; Prati *et al.*, 1994; Greife *et al.*, 1995; Aliotta *et al.*, 2001; Rolfs, 2001; Rolfs and Somorjai, 1995). This in turn has generated unease about the reliability of the values for $S^{\rm b}(E)$ extracted from laboratory measurements for use in astrophysics (Balantekin, Bertulani, and Hussein, 1997).

Several suggestions have been made to resolve this apparent discrepancy. For example, an error in the estimated stopping power could result in a smaller reaction effective energy, so the experimentally deduced screening would be larger than the true value (Bang *et al.*, 1996; Langanke *et al.*, 1996). Indeed, such deviations have been found between theoretical calculations of stopping powers and the tabulation that is traditionally being used in the analysis of low-energy fusion data (Golser and Semrad, 1991; Bertulani and de Paula, 2000; Bertulani, 2004). An accurate experimental determination of stopping powers for gaseous hydrogen and helium targets would be desirable. Corrections associated with the nonuniform distribution of the electron cloud around the nucleus (Carraro, Schafer, and Koonin, 1988) and the effects of electron-electron interactions (Shoppa *et al.*, 1993) have also been suggested as potential generators of unidentified systematic error. For molecular targets the screening energy shows a significant dependence on the scattering angle, being smallest if the projectile passes the spectator nucleus before fusion (Shoppa *et al.*, 1996). Furthermore, the experimental deduction of screening energies requires assumptions about the bare nuclear cross sections, which is another source of uncertainty. This was demonstrated by Tumino *et al.* (2014, 2021), who, after constraining fits by the addition of higher-energy data (from a Trojan horse measurement), obtained a lower value of U_e. Clusterization and polarization effects have also been proposed to effect the deduced screening energies in specific low-energy reactions (Spitaleri *et al.*, 2016, 2017)

For resonances both the energy and the width can be affected by screening (Salpeter, 1954; Zinner, 2007). Particular care has to be taken for narrow, low-energy resonances, where the assumption of a constant screening energy is not valid and the radial dependence of the screening potential has to be considered, which leads to a significant reduction of screening on the resonance width (Iliadis, 2023).

Particularly large screening energies were observed in deuteron- and proton-induced fusion reactions if the projectile was implanted in metals (Czerski *et al.*, 2001, 2006; Kasagi *et al.*, 2002; Raiola *et al.*, 2002a, 2002b; Cvetinovic *et al.*, 2015; Lipoglavsek and Cvetinović, 2020). While the $d + d$ fusion data obtained with a gaseous target (Greife *et al.*, 1995) were compatible with the adiabatic limit [$U_e = 20$ eV (Bracci, Fiorentini, and Mezzorani, 1990; Bracci *et al.*, 1991)], screening energies obtained for various metal hosts varied among themselves and could reach values of several

[10] In this section, the word *metals* is used with the traditional meaning from chemistry, not the astrophysical one.

hundred eV. As the adiabatic limit derived for the fusion on individual atoms in a gas does not apply to reactions with targets implanted in a host material, an appropriate model has been developed (Czerski *et al.*, 2004; Huke *et al.*, 2008) that agrees favorably with recent screening energies obtained under high-vacuum conditions (Czerski *et al.*, 2016; Czerski, 2022). Huke *et al.* (2008) identified oxygen and carbon contamination as the source for some particularly large deduced screening energies. We note that the studies of $d + d$ low-energy fusion were motivated by the quest to enhance nuclear fusion rates by environmental effects (Czerski, 2022).

The potential discrepancy between observed and theoretical screening energies would become astrophysically irrelevant if it were possible to measure reaction rates directly under solar plasma conditions. This may prove to be possible using high-intensity lasers. First measurements of light-ion reactions in plasma have been performed, though under plasma conditions for which screening effects are expected to be negligible (Barbui *et al.*, 2013; Zylstra *et al.*, 2016, 2020; Casey *et al.*, 2023). A direct measurement of bare nuclear cross section, thus avoiding screening effects, is proposed for storage ring experiments, in which a stored beam of ions can collide with a transverse beam (Glorius and Bruno, 2023).

B. Screening in the solar core

The energy-generating reactions that occur in the solar core involve nuclei that are almost completely ionized. Consequently, the atomic environment differs substantially from that of the terrestrial experiments in which these same reactions are measured. Once $S^{\mathrm{b}}(E)$ is determined from these laboratory measurements, the screening effects of the plasma must be folded in to yield $S^{\mathrm{solar}}(e)$. Adopting the notation of Adelberger *et al.* (2011), one can define the correction factor as

$$f_0(E) = \frac{\sigma^{\mathrm{solar}}(E)}{\sigma^{\mathrm{b}}(E)}. \tag{26}$$

In the weak screening approximation (Salpeter, 1954), the ion-ion Coulomb potential is screened on a length scale given by the Debye radius R_D,

$$V(r) = \frac{\alpha Z_1 Z_2}{r} \exp\left(-\frac{r}{R_D}\right), \tag{27}$$

yielding

$$f_0 \sim \exp\left(\frac{\alpha Z_1 Z_2}{R_D kT}\right). \tag{28}$$

See Adelberger *et al.* (2011) for the functional dependence of R_D on temperature, density, and the mass fractions X_i and for discussions of corrections for electron degeneracy and incomplete ionization.

Adelberger *et al.* (2011) discussed the conditions under which the weak screening approximation is valid; under solar core conditions, this requires $Z_1 Z_2 < 10$, a condition satisfied by pp-chain and CNO bi-cycle reactions. Yet, corrections are expected at some level, as the interion potential is not completely negligible in all collisions compared to the relative kinetic energy of the ions (Salpeter, 1954; Salpeter and van Horn, 1969; Itoh *et al.*, 1979; Carraro, Schafer, and Koonin, 1988; Brown and Sawyer, 1997; Ogata, 1997; Bahcall *et al.*, 2002; Fiorentini *et al.*, 2003).

Dynamic corrections—nonadiabatic effects that arise when the velocities of reacting nuclei momentarily exceed typical plasma velocities—have been a point of some controversy that Adelberger *et al.* (1998, 2011) addressed. However, the absence of such dynamic corrections even for large Gamow energies has been shown to be a consequence of the nearly exact thermodynamic equilibrium of the solar plasma (Brown and Sawyer, 1997; Gruzinov, 1998; Gruzinov and Bahcall, 1998). Specifically, Bahcall *et al.* (2002) found that corrections to the Salpeter formula under solar conditions would be approximately at the few-percent level and pointed to specific errors in several papers that had come to contrary conclusions.

Some researchers have advocated for changes in solar rates due to dynamical corrections, including Mao, Mussack, and Däppen (2009), Mussack and Däppen (2010), Mussack (2011), Simonucci *et al.* (2013), Wood, Mussack, and Guzik (2018), and Vescovi *et al.* (2019). The approaches employed are based on modeling the plasma, and in general the researchers do not relate their conclusions to earlier work [particularly Bahcall *et al.* (2002)], making them difficult to evaluate. The essential point of Bahcall *et al.* (2002) was that the conceptual simplifications that result from recognizing that screening in the solar plasma can be formulated as a problem in equilibrium statistical mechanics. This approach removes all need to classified rates as fast or slow relevant to some plasma timescale, as there is no time in equilibrium statistical mechanics. Consequently, we continue to regard the work of Bahcall *et al.* (2002) as the most realistic estimate of corrections to the Salpeter formula.

XIII. RADIATIVE OPACITIES

A. Introduction

Opacity is a measure of the photon absorption of matter and is an essential quantity for understanding radiative heat transfer in the Sun. Radiative heat transfer occurs through the absorption and emission processes taking place within the material that the radiation traverses. In local thermodynamic equilibrium (LTE),[11] the emission and absorption are straightforwardly related through the Planck function. In this scenario determining the absorption coefficients or opacity, denoted as κ_ν, provides a complete description of how radiation is transported through the material.

[11]Local thermodynamic equilibrium can be defined as the situation where the thermodynamic properties of a microscopic volume of matter are the same as their thermodynamic equilibrium values corresponding to the local electron temperature and density. The assumption of LTE is commonly used in stellar modeling, and the discussion of opacities in this section is limited to LTE conditions. In some circumstances (such as solar coronal modeling), non-LTE conditions should be given careful consideration, but they are not discussed in this review.

For example, in the equilibrium diffusion limit, the radiation heat flux F_R is directly related to the Rosseland mean opacity (RMO) κ_R through the following equation (Huebner and Barfield, 2014):

$$F_R = -\frac{16\pi}{3}\frac{\sigma T^3}{\kappa_R \rho}\nabla T, \tag{29}$$

where T represents temperature, ∇T denotes its gradient, ρ is the mass density, and σ is the Stefan-Boltzmann constant. The quantity κ_R is the solar RMO. Thus, any error in this quantity introduces an error in the radiative heat transport and the simulated solar evolution. Quantifying the error in κ_R is challenging because κ_R is a weighted mean of a complex solar mixture opacity,

$$\frac{1}{\kappa_R} = \int_0^\infty \frac{1}{\kappa_\nu} w_\nu d\nu, \tag{30}$$

where w_ν is a weighting function related to the temperature derivative of the Planck function B_ν,

$$B_\nu = \frac{2h\nu^3}{c^2}(e^{h\nu/kT})^{-1}, \tag{31}$$

where ν denotes the photon frequency, h is the Planck constant, k is the Boltzmann constant, and c is the speed of light. Moreover, the frequency-resolved solar opacity κ_ν is a sum of elemental opacities $\kappa_{\nu,i}$ weighted by their mass fractions (b_i),

$$\kappa_\nu = \sum_i b_i \kappa_{\nu,i}\,. \tag{32}$$

Equation (30) reveals that the accuracy of κ_ν is especially important over the spectral range where w_ν is high and κ_ν is low (owing to the inverse weighting). Equation (32) shows that accuracy in κ_ν requires good knowledge of both element opacities $\kappa_{\nu,i}$ and mass fractions b_i.

Figure 11 shows the total monochromatic opacity of the Sun at three different solar radii, highlighting the variations in w_ν (gray lines), κ_ν (black lines), and some of the leading individual element contributions $\kappa_{\nu,i}$ (red, green, and blue lines) to the RMO determination [Eq. (30)] as a function of the radius. Figure 11 was made while assuming the GS98 solar abundances and using Opacity Library (OPLIB) opacities (Colgan *et al.*, 2016) and is included primarily for illustrative purposes. As shown in the figure, the solar opacity varies considerably in both magnitude (note the log axes) and shape across different solar radii. Moreover, each element contributes distinctively to the overall monochromatic opacity, with either a dominant continuous opacity spectrum or strong lines that arise from bound-bound transitions. If there is an error in the calculated solar opacity κ_ν, it would stem from inaccuracies in the calculated element opacities and/or abundances. In addition, the error is expected to be a complex function of photon energy and would vary at each radius owing to changes in temperature and density. As a result, it is not possible to provide a single factor for uncertainty or correction. It is crucial to assess the accuracy of the intricate spectral features depicted in Fig. 11 in order to better understand the nature of the errors.

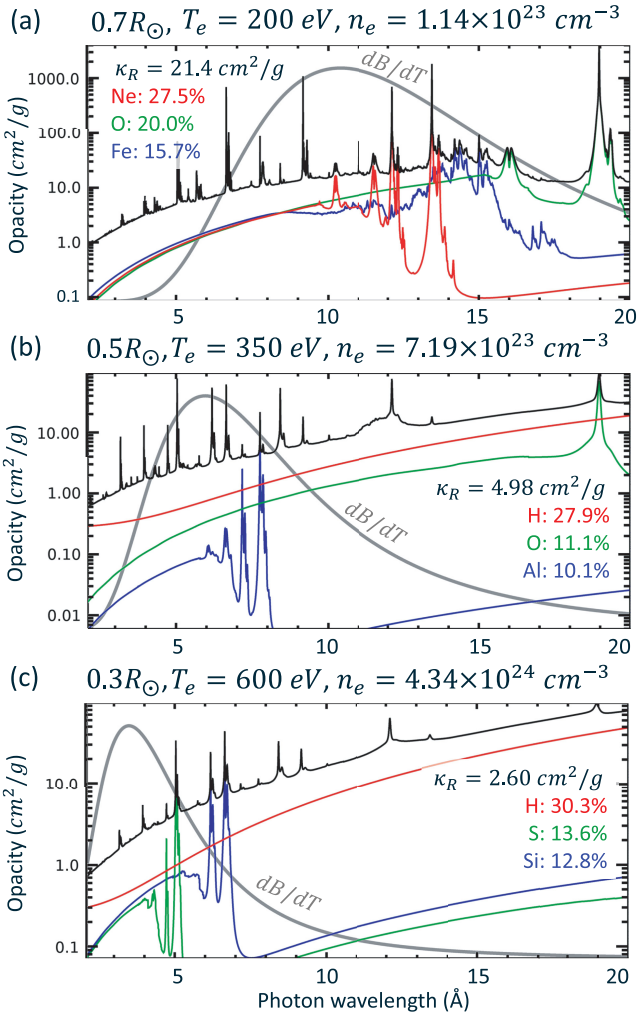

FIG. 11. Monochromatic opacity of the Sun at three different solar radii as indicated. The temperature and electron density at each solar radius are displayed, as are some of the major elemental opacity contributions at these conditions. Note that, for clarity, not all contributions are plotted. The percentages of three elements displayed indicate the leading elemental contributors to the RMO at these conditions. They are roughly quantified by calculating how much the RMO is reduced if each element is completely removed. Sketches were made using the GS98 solar abundances and OPLIB opacities and are mainly intended to show the spectral complexity of the solar opacity.

These complex spectral features arise from microscopic physics at the atomic level—that is, the absorption of radiation through quantum mechanical processes. If one knows the atomic energy levels and transition probabilities of all the relevant atomic states (of each atom or atomic ion of each material in the Sun), then the opacity of that material can be computed.[12] Since atomic structure and transition

[12]We note that the opacity of molecules and dust, or grains, can be important in some circumstances (Huebner and Barfield, 2014); however, they play a minor role in stellar modeling and thus are not discussed here.

probabilities can be predicted (under various approximations), starting with the Schrödinger (or Dirac) equation, this seems like an achievable goal. However, complications quickly arise from a multitude of factors, such as how to deal with the infinity of atomic states that may be populated in each atom or atomic ion, how to account for the perturbations caused by the plasma environment on the atomic states, and how to handle the large quantities of data that arise with such calculations, particularly for multielectron atoms and ions. In solar modeling one requires the opacity of all relevant elements (around 30) at all plasma conditions that are found at all radii throughout the solar evolution. Thus, the opacity must be tabulated as a function of species, plasma temperature, plasma density, and photon energy.

Nevertheless, steady progress has been made in determining the opacity of solar mixtures over the past five decades. In the 1980s insufficient accuracy in stellar-envelope opacity was hypothesized through multiple astrophysical puzzles (Simon, 1982), and opacity models were subsequently improved by incorporating more detailed atomic physics and a more complete set of states (Berrington *et al.*, 1987; Seaton, 1987; Magee *et al.*, 1995; Iglesias and Rogers, 1996). The improved accuracy was confirmed through a few benchmark experiments (Davidson *et al.*, 1988; Perry *et al.*, 1991; Springer *et al.*, 1992; Winhart *et al.*, 1996) and improved agreement with some astrophysical observations (Iglesias and Rogers, 1991; Daszyńska-Daszkiewicz and Walczak, 2009, 2010). However, the calculated solar opacities are not experimentally validated at most radii, particularly more deeply into the Sun, where the conditions (temperature and density) are more extreme.

In the past decade, experimental methods have steadily improved, in concert with the availability of powerful x-ray sources, such as the Sandia Z facility. Monochromatic opacities were successfully measured at multiple conditions relevant to solar convection-base conditions (Bailey *et al.*, 2007, 2015). Systematic experimental studies performed on chromium, iron, and nickel helped narrow down hypotheses for the discrepancies (Nagayama *et al.*, 2019). All of these experimental results provided essential clues for testing various approximations for solar-interior-opacity calculations; however, the reported model-data disagreements also raised significant controversy. This led to various theoretical investigations and the development of independent experimental methods (Perry *et al.*, 2020; Opachich *et al.*, 2022). Ongoing theoretical and experimental investigations are primarily focused on understanding the origins of reported disagreements as a first step toward reaching a consensus in this field. Our aim here is to provide a status report for the field, summarizing past work on solar opacity calculations and experiments while identifying some of the open questions that are the focus of current work.

B. Opacity models

Over the years a wide range of approximations has been used for the various components of opacity calculations. To help navigate these approximations, it may be useful to summarize the key components of a frequency-dependent opacity. Opacities are often broken down into various components. The first of these is *bound-bound* absorption (a photoexcitation transition between two levels of an atomic ion), which manifests as strong line features in the opacity spectrum (such as the black "spikes" in Fig. 11). The *bound-free* absorption (photoionization of the ground or excited level of an atomic ion) is normally a continuous (wavelength-dependent) contribution, such as the smooth hydrogen opacity contribution depicted as red lines in Figs. 11(b) and 11(c). The *free-free* absorption (also known as inverse bremsstrahlung) is where a free electron absorbs a photon and, finally, *scattering* (the scattering of a photon by a free electron) contributions can be important at high photon energies. Other contributions may be important in molecules or other material. Equation (30) shows that, owing to the harmonic mean inherent in the RMO, the most important photon energy range is when the spectral opacity is low and when the weighting function w_ν is high. In the solar case, at a given solar radius, it is important to know which elements dominate the opacity at such a region, which will depend on the elemental abundance and its contribution at that distance, as illustrated in Fig. 11.

The determination of opacities usually starts with one of two fundamental approaches. The first approach, which was used in the first opacity computations (Huebner and Barfield, 2014), starts with a mean ion model, where a fictitious "average" atom or ion of a given element is conceived, with fractional occupation numbers, which is consistent with the given temperature and density of the species under consideration. The fractional occupation numbers, usually determined through a self-consistent iterative approach, inform the real (physical) ion stages of importance at such conditions. The average atom can then be unfolded through various procedures to the physical ion stages of relevance, and the opacity of such ions can be determined. In this model the plasma effects (in particular, the perturbation of the average atom by the fields produced by the surrounding plasma ions and electrons) can be included in a natural way, and this approach is often most useful at high densities, where plasma perturbations on the atoms or ions are most important. The infinity of atomic states are naturally truncated by plasma effects that remove bound states from consideration. The old inferno model (Liberman, 1979) and the more recent STAR tables (Krief, Feigel, and Gazit, 2016b; Krief, Feigel, and Gazit, 2018) are based on this method. We note that recent work (Gill, Fontes, and Starrett, 2023) has considerably improved some of the approximations used in related approaches.

The second approach is often referred to as detailed configuration (or term) accounting, where one determines all possible ion stages of the species and then determines all possible ground and (multiply) excited states of each ion, each with a corresponding population that is condition dependent. This method is often more spectroscopically accurate than the mean ion model because it considers the structure of each ion separately but can require enormous computational resources for complex species. The structure of each ion is determined from a solution of the Schrödinger (or Dirac) equation, which can then also produce transition probabilities. Within this procedure many computational difficulties must be overcome to produce acceptably accurate data for all ion stages of all relevant elements. A few examples are given for illustration. Within the solution of the Schrödinger equation, it is desirable

to include configuration interaction (CI), a two-body term in the Hamiltonian that accounts for electron-electron interactions (Cowan, 1981), which results in an accurate description of atomic energy levels. However, the inclusion of this term for atomic ions with large numbers of configurations can quickly result in a computationally intractable problem. Therefore, approximations in which CI is included in only a limited manner are often employed. Furthermore, careful consideration has to be given to the number of states that should be included in the calculations. A compromise is always necessary between including as many states as possible versus the computational resources available for the calculation. Convergence checks are necessary to ensure that sufficient states are included. However, the rate of convergence of the opacity with respect to the number of states included will depend on the plasma conditions of interest, so this in itself is not necessarily a straightforward matter. The computer codes that are used to generate the opacity must also be able to efficiently process large amounts of atomic data.

Similarly, when considering photoexcitation and photoionization of atomic ions, it is desirable to include coupling of the bound electrons to the continuum electron(s). Often called close coupling, this may be accomplished through techniques such as the *R*-matrix approach (Seaton, 1987; Burke, 2011) or other related methods. However, such approaches are also computationally intensive and can be severely limited in the number of terms that can be included in the resulting close-coupling expansions. It is also not clear how to include plasma perturbations within such approaches. As a result, perturbative approaches, such as distorted-wave methods (Cowan, 1981; Badnell *et al.*, 2005; Sampson, Zhang, and Fontes, 2009), are often employed. They are much more computationally tractable and are of sufficient accuracy for midionized and highly ionized ions.

In concert with an atomic model, the thermodynamics of the system must be considered. That is, an equation-of-state (EOS) description of the material is required so that the thermodynamic properties and atomic state populations can be determined for a given material temperature and density. In the mean ion approach, the thermodynamic quantities arise naturally through the description of the atom or ion in a plasma. In a detailed configuration accounting approach, a common approach to EOS calculations starts with a chemical picture based on a minimization of the chemical free energy (Däppen, Anderson, and Mihalas, 1987; Hummer and Mihalas, 1988; Rogers and Iglesias, 1992; Hakel and Kilcrease, 2004). Such a model has to treat a wide range of physical conditions ranging from ideal gas through high-density conditions where pressure ionization may rapidly strip ions of all their electrons. The number of atomic states retained in the partition function is a key quantity in determining whether the EOS is complete at the conditions of interest. This assessment of completeness will strongly depend on the plasma conditions.

The final important aspect of opacity models that we want to discuss concerns line broadening. Photoabsorption lines in a plasma become broadened because of a number of factors, such as natural and Doppler broadening. Collisional broadening (often known as Stark broadening) is often a dominant broadening mechanism. This is broadening due to the plasma microfields caused by the motion of electrons and ions in a plasma. As before, line broadening is an important part of any opacity model, but any treatment of this effect has to be tractable for all ions and all conditions encountered when building an opacity table. While accurate line broadening models exist for one- and two-electron systems (Lee, 1988; Stambulchik *et al.*, 2019; Gomez *et al.*, 2022), the treatment of broadening for multielectron systems often requires a number of approximations (Dimitrijevic and Konjevic, 1986, 1987).

C. Production of tables

Some of the earliest determinations of opacity for stellar physics started by the pioneering work in the UK of Berrington *et al.* (1987) and Seaton (1987)). This development led to the Opacity Project (OP), which in time produced a set of opacity tables for stellar modeling that are still in common use today (Badnell *et al.*, 2005). At around the same time, Opacity Astrophysical Library (OPAL) opacity tables were published by Lawrence Livermore National Laboratory (LLNL) (Iglesias and Rogers, 1996). Both of these sets of tables were widely adopted by the stellar modeling community. Some early theoretical opacity work was performed at Los Alamos National Laboratory (LANL) (Huebner and Barfield, 2014), starting with pioneering work by Mayer and continuing with Arthur Cox in the 1960s. In the 1990s the LANL work resulted in OPLIB tables produced from the `LEDCOP` code (Magee *et al.*, 1995). In the mid-2010s, the modern `ATOMIC` code was used to produce a new generation of opacity tables that improved the computation of opacities in a number of ways (Colgan *et al.*, 2016). All of these tables are available electronically in various formats. Other important opacity tables have been produced in France (the OPAS and SCO-RCG opacity efforts) (Blancard, Cossé, and Faussurier, 2012; Mondet *et al.*, 2015; Pain, 2021), Israel (using the STAR code) (Krief, Feigel, and Gazit, 2016b, 2018), and elsewhere. Differences among these tables and their underlying opacity models have been the focus of dedicated workshops and conferences (Mendoza, Turck-Chiéze, and Colgan, 2018).

Many of these tables (primarily the OP and OPAL) were quickly adopted by the solar modeling community and were useful in solving the Cepheid variability puzzle (Simon, 1982), where updated opacities helped resolve a previous disagreement between observation and modeling of Cepheid variables. Detailed comparisons between these two sets of tables have been made on numerous occasions, regarding both individual opacities (Badnell *et al.*, 2005) and how solar models that use these tables compare (Delahaye and Pinsonneault, 2006). Overall, the agreement between the various opacity tables was deemed to be satisfactory (within 5%) for the accepted solar models of the late 1990s (Magee *et al.*, 1995). This paradigm was shaken when new determinations of the elemental solar abundances were reported (Asplund, Grevesse, and Sauval, 2005), which implied that solar models disagreed with helioseismology observations. It was suggested (Serenelli *et al.*, 2009) that changes in the opacity of a few species (mainly Fe, Ne, and O) could reconcile the solar models with the observations. Since then, intensive work has been performed in exploring some of the

approximations made in the older opacity tables. The OP effort has focused on new and larger R-matrix calculations for important ions of Fe (Nahar and Pradhan, 2016; Delahaye *et al.*, 2021), primarily Fe^{17+}. At Los Alamos the modern ATOMIC code was used to create a new generation of opacity tables for H through Zn (Colgan *et al.*, 2016). Although significant improvements in many aspects of the calculations were incorporated, the resulting opacity tables did not significantly improve the comparison of solar modeling with helioseismology. Krief, Feigel, and Gazit (2016a) showed that one possible way to produce larger opacities under solar conditions would be if line broadening effects were significantly increased—by several orders of magnitude. Opacity increases of ≈10% near the solar convective zone and ≈2% in the solar core have been attributed to ionic correlations (Krief *et al.*, 2018). Such topics require further investigation.

D. Experimental testing of calculated iron opacity

Errors in calculated solar opacity can arise from inaccuracies in both the abundance and calculated element opacities in a complex way. Therefore, it is important to investigate the accuracy of abundance and elemental opacities separately. The accuracy of elemental opacities can best be evaluated by examining the frequency-resolved (monochromatic) opacity. Since each spectral feature of the element opacity often relies on different physics and approximations, disagreements between model predictions and experimental data on a frequency-resolved basis can help identify which approximations are invalid and guide refinements in opacity theory. Here we provide an overview of the fundamentals as well as previous investigations into measurements of solar-interior opacity. A more general and tutorial discussion of the experimental methods and a historical overview can be found elsewhere (Bailey *et al.*, 2009).

The material opacity κ_ν is related to its transmission T_ν via the following equation:

$$T_\nu = \frac{I_\nu - \epsilon_\nu}{B_\nu - \epsilon_\nu} = e^{-\kappa_\nu \rho L}, \tag{33}$$

where B_ν is the backlight spectrum, I_ν is the backlight transmitted through the sample, ϵ_ν is a sum of the sample plasma emission and other backgrounds, and ρL is the areal density of the opacity sample. Thus, sample opacity κ_ν can be experimentally determined by heating the sample and accurately measuring the following quantities: the backlight with and without the heated sample (B_ν and I_ν), the plasma self-emission and background (ϵ_ν), and the sample areal density (ρL).

Several challenging criteria must be met if opacity measurements are to be both interpretable and useful. First, the elements, conditions, and spectral ranges of interest must be identified. Second, a macroscopic opacity sample must be uniformly heated to the desired conditions to achieve local thermodynamic equilibrium. Third, the heated sample must be backlit with a bright and spectrally smooth radiation B_ν to accurately determine frequency-resolved absorption. It is critical that the backlight is significantly brighter than the sample plasma emission or other background signals ϵ_ν. Fourth, the absorption spectrum must be recorded with spectrometers that provide sufficient signals and spectral resolving power for the opacity study. Fifth, the condition of the heated sample (T_e, n_e, and ρL) must be diagnosed independently of the opacity in question. Simulated conditions are not appropriate for this purpose, since their accuracy heavily depends on the accuracy of the opacity in question. Finally, the opacity spectrum and its uncertainty must be accurately determined from the measured I_ν, B_ν, ϵ_ν, and ρ_ν values and their uncertainties.

After the revision of solar abundance in 2005 (Asplund, Grevesse, and Sauval, 2005), solar models and helioseismology disagreed, and the accuracy of solar-interior opacity was called into question. This disagreement was primarily due to a significant reduction in solar opacity resulting from the reduced metallicity, and it was the greatest at the base of the solar convection zone [hereafter, convection-zone base (CZB)]. Since then, solar abundance has been continuously revised, with the latest abundances determined by two groups being $Z/X = 0.0225$ (Asplund, Amarsi, and Grevesse, 2021) and $Z/X = 0.0187$ (Magg *et al.*, 2022), which still disagree with each other, leaving significant uncertainty in the solar abundance. For determining the accuracy of calculated solar opacities, the accuracy of calculated element opacities must also be experimentally scrutinized. Since Fe and O are the two dominant sources of opacity at the CZB, their opacities must be experimentally tested at CZB conditions (i.e., $T_e = 182$ eV, $n_e = 9 \times 10^{22}$ $e\,\mathrm{cm}^{-3}$). Previous experimental approaches were not suitable for this purpose, because their backlighters were not bright enough to mitigate the bright self-emission produced at these conditions.

Over the past two decades, experimental methods have been refined using one of the brightest x-ray sources, Z pinch. In 2007 iron opacities were successfully measured at 150 eV and 7×10^{21} $e\,\mathrm{cm}^{-3}$, providing support for the accuracy of calculated Fe opacities under these specific conditions. In 2015 iron opacities were measured at larger temperatures and densities. This study revealed a significant discrepancy between the calculated and measured opacities as the temperature and density approached the CZB conditions, as shown in Fig. 12. This is a significant concern since the experimental density was still approximately 3 times lower than the actual

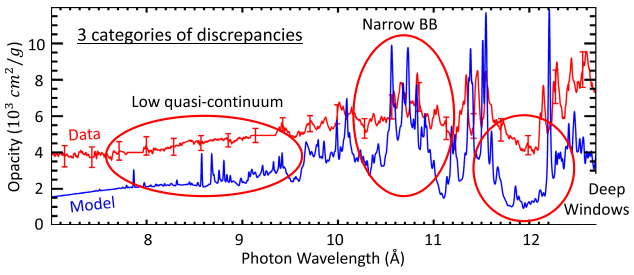

FIG. 12. Comparison of measured opacity (in red) and calculated opacity [in blue (Badnell and Seaton, 2003)] at a temperature of 182 eV and an electron density of 3.1×10^{22} $e\,\mathrm{cm}^{-3}$. Three types of measured-vs-modeled opacity disagreements are shown: (i) a lower quasicontinuum, (ii) narrower bound-bound line features, and (iii) deeper opacity windows. These trends were observed in all opacity models compared by Bailey *et al.* (2015).

density at the CZB. Opacity models employ approximations to account for density effects such as line broadening and pressure ionization. If these approximations are incorrect, the disagreement between calculated and measured opacities could be even more pronounced at the densities found at the CZB.

The disagreement observed in the iron opacity was complex, as depicted in Fig. 12. The modeled opacities were lower in the quasicontinuum region at short wavelengths (< 10 Å), narrower in bound-bound lines, and deeper in the opacity valleys known as windows. These discrepancies are likely caused by various factors, but it is difficult to disentangle different sources of discrepancies based solely on the disagreement in iron opacity alone.

In 2019 a comprehensive study was conducted to measure opacities for Cr, Fe, and Ni at solar-interior temperatures (Nagayama *et al.*, 2019). This systematic study helped narrow down hypotheses on the sources of disagreement by observing how the discrepancies change as a function of atomic number. The measurements revealed that measured opacities for all three elements had narrower line features than the model predictions, suggesting potentially inaccurate density effects in opacity models. Disagreement in the opacity windows was observed for Cr and Fe, while Ni did not show significant disagreement. At the experimental conditions used in the study, Cr and Fe were in an open L-shell configuration, whereas Ni was closer to a closed L-shell configuration. It is known that the calculations of both population and EOS are more challenging in open L-shell configurations. Therefore, the observed trend in window disagreement may suggest a connection to the difficulties associated with EOS calculations in such configurations.

One interesting finding from this systematic study was the disagreement observed in the quasicontinuum region. Unlike the discrepancies observed in bound-bound linewidth and window opacities, no clear trend was observed in the quasicontinuum disagreement. The model and data agree well for Cr and Ni, but not for Fe, at high temperatures. Two possible explanations have been proposed for this unexpected behavior. The first hypothesis suggests the presence of missing physics in the opacity models that becomes significant under the conditions encountered by high-temperature Fe-opacity experiments. The second hypothesis proposes that the opacity experiments or analyses are flawed, but only for Fe at high temperatures. Until opacity experiments and theories are reconciled, neither possibility can be definitively ruled out.

Despite numerous investigations, the discrepancies between experimental and theoretical iron opacities remain unresolved (Nagayama, Bailey, Loisel, Hansen *et al.*, 2014; Nagayama, Bailey, Loisel, Rochau, and Falcon, 2014; Bailey *et al.*, 2015; Kilcrease *et al.*, 2015; Blancard *et al.*, 2016; Colgan *et al.*, 2016; Mancini, 2016; Nagayama *et al.*, 2016, 2017, 2019; Nagayama, Bailey *et al.*, 2016; Nahar and Pradhan, 2016). On the experimental side, measurements of sample spatial gradients have been conducted and found to be negligible (Nagayama, Bailey, Loisel, Hansen *et al.*, 2014). Numerical tests have also shown that temporal gradients, self-emission, and the presence of tamping material do not have significant impact on the results (Nagayama, Bailey, Loisel, Rochau, and Falcon, 2014; Nagayama, Bailey *et al.*, 2016; Nagayama *et al.*, 2017). Furthermore, the uncertainties in temperature and density diagnostics resulting from the choice of spectral model have been determined, and it has been found that these uncertainties are too small to account for the reported discrepancies (Nagayama *et al.*, 2016). In addition, background measurements have also been performed and found to be negligible (Dunham *et al.*, 2021).

The persistent differences between experiments (Bailey *et al.*, 2015; Nagayama *et al.*, 2019) and opacity models have led to a sustained effort to reconcile these discrepancies. The experimental efforts were previously discussed. On the theoretical side, tests of some of the approximations used in the opacity tables have been conducted (Blancard *et al.*, 2016; Colgan *et al.*, 2016; Nahar and Pradhan, 2016; Delahaye *et al.*, 2021), particularly in assessing the convergence of opacity models with respect to the number of configurations included in the calculations. However, no significant changes in the final opacity have been reported from such studies.

Several groups have postulated new physical effects that could produce more opacity contributions than in previous works. Of particular note is the possibility of two-photon opacity contributions, where an atom or ion could simultaneously absorb two photons (possibly of different frequencies) (More, Hansen, and Nagayama, 2017; More *et al.*, 2020). All current opacity tables omit such contributions, as they are believed to be a minor contribution to the overall opacity. Preliminary studies by More, Hansen, and Nagayama (2017) and More *et al.* (2020) have suggested that this could be a factor in the comparison of theory with the Z measurements, but other studies found that such a contribution should be small (Iglesias, 2015; Pain, 2018; Kruse and Iglesias, 2019, 2021).

Another interesting study reported that transient spatial localization may result in increased opacities (Liu *et al.*, 2018; Zeng *et al.*, 2022). This is a density-dependent effect where the plasma effects localize the continuum wave functions near the absorbing ion, potentially resulting in increased broadening and bound-free cross sections. While Zeng *et al.* (2022) suggested that this effect is significant, other studies cast doubt on this claim (Iglesias, 2023).

Opacity theorists and experimentalists continue to collaborate closely to address discrepancies and uncertainties in the calculated solar RMO. They carefully examine each other's work, seeking to resolve the discrepancies and accurately quantify the uncertainty associated with calculated solar opacities.

E. Future opacity work

The continuing disagreement between the Z Fe experiments (Bailey *et al.*, 2015; Nagayama *et al.*, 2019) and theoretical models is by far the largest concern of the opacity community. New theoretical efforts, while interesting, have not yet resolved these differences. New experimental results, particularly the opacity-on-NIF campaign [a project of the National Ignition Facility (NIF)] (Perry *et al.*, 2020; Opachich *et al.*, 2022), are eagerly anticipated to shed some light on the current impasse. New approaches are also being developed for opacity measurements using the APOLLON laser at LULI

(France) and on the GEKKO XII laser (Japan) (Fujioka *et al.*, 2005). There has been a suggestion for measuring heat conductivity under thermodynamic conditions resembling those found deeper in the radiative zone using hydrocarbon foams doped to imitate the solar composition (Krief *et al.*, 2018). Such progress will have implications for solar modeling, as the combination of opacity and elemental abundances is key to resolving the significant discrepancy between helioseismology and solar models. As noted, the abundance of solar elements is also the subject of renewed scrutiny (Asplund, Amarsi, and Grevesse, 2021; Magg *et al.*, 2022).

XIV. EXPERIMENTAL FACILITIES FOR SOLAR FUSION STUDIES

Improved experimental facilities have led to significant progress in nuclear astrophysics research in recent years, and future instrumental developments will likely continue to push the boundaries in the next decade. Key goals driving technological developments include tests of the weak interactions and of solar properties that make use of high-precision solar neutrino measurements, helioseismological mappings of the core metallicity, and detailed solar modeling. There is also a host of related open questions in different areas, such as big bang nucleosynthesis, red giant evolution, the evolution of supernova progenitors, and a variety of transient explosive phenomena in astrophysics where a quantitative understanding of the nuclear physics is essential. Owing to the small cross sections of low-energy charged-particle reactions, experiments must be designed to achieve signal rates significantly lower than the background rates from cosmic rays, natural radioactivity in the laboratory, and induced activity from beam interactions with target impurities. In Secs. XIV.A–XIV.E, we outline current experiences and future facilities—either in development or planned—that will possibly pave the way for major breakthroughs in the coming years.

A. Aboveground facilities

Aboveground facilities always play a crucial role in investigating nuclear reactions of astrophysical interest. Various methods are applied to minimize background. A prevalent approach involves employing passive shielding around the detection area, typically utilizing a layered configuration of lead, copper, and polyethylene. This setup helps to decrease unwanted signals and neutron background in detectors with relatively small capacities. However, there are additional techniques that can be utilized to further diminish background interference, enabling measurements at energy levels closer to those pertinent to astrophysics.

1. LENA

LENA is part of the Triangle Universities Nuclear Laboratory, located on the campus of Duke University, in North Carolina. LENA features two accelerators: a 230 keV ECR accelerator that produces the world's most intense low-energy proton beams (Cooper *et al.*, 2018) and the 2 MV Singletron accelerator from High Voltage Engineering Europa B.V. (Shornikov *et al.*, 2023). These machines deliver ion beams with significant intensity—up to 20 mA dc proton current at lower energies and 2 mA at several MeV—along with advanced beam pulsing capabilities. Each accelerator has dedicated transport systems and control mechanisms for simultaneous operation. A key component of LENA is the γ-ray coincidence spectrometer, which allows measurements with sensitivities comparable to underground facilities (Buckner *et al.*, 2015). The detector setup includes a 130% p-type HPGe detector, HPGe clover detectors, and a 16-segment NaI(Tl) annulus, along with the APEX detector featuring 24 position-sensitive NaI(Tl) bars for enhanced measurements. Recently, LENA added a cosmic-ray veto system with nine plastic scintillators to reduce the cosmic-ray muon background, conveniently positioned owing to its wheeled assembly.

2. NSL

The Nuclear Science Laboratory (NSL) at the University of Notre Dame hosts a number of low-energy accelerators and the TriSOL radioactive beam facility to maintain a rigorous experimental program in nuclear astrophysics, nuclear structure physics, and fundamental symmetries, as well as in a broad range of nuclear physics and nuclear chemistry applications. The 5 MV single-ended pelletron provides high-intensity proton, helium, and $A \leq 40$ heavy-ion beams for nuclear astrophysics related experiments in forward kinematics using solid and gas target technologies and in inverse kinematics using the St. George recoil separator. The 10 MV FN pelletron tandem is the main machine for nuclear structure physics experiments but also serves that accelerator mass spectrometry program for analyzing long-lived radioactivities in terrestrial and meteoritic samples. The FN is also used for indirect measurements of reactions of astrophysical interest and serves as a driver for the production of light radioactive isotope beams ($A \leq 40$) for nuclear astrophysics and fundamental symmetry studies.

B. Underground facilities

Underground facilities are essential for pushing the boundaries of direct measurements toward the lowest energies of astrophysical interest (tens to hundreds of keV). In particular, capture-reaction measurements leading to neutron- or γ-ray emissions are severely hampered in surface laboratories because of the overwhelming background associated with cosmic rays. This background can be suppressed by many orders of magnitude by exploiting the natural shielding provided by the rock overburden in underground sites. The improvements possible with this strategy have been demonstrated by pioneering work at the LUNA at INFN-LNGS, first with a 50 kV accelerator (LUNA I) and then with a 400 kV one (LUNA II) still in operation today (Aliotta, Boeltzig *et al.*, 2022). Since the last solar fusion review, a new accelerator has been installed at INFN-LNGS, and other underground laboratories have become operational in China (JUNA), the U.S. [Compact Accelerator System for Performing Astrophysical Research (CASPAR)], and Germany (Felsenkeller). These are now described.

FIG. 13. Photo of the 3.5 MV Singletron accelerator recently installed at LNGS. From Matthias Junker.

1. Bellotti Ion Beam Facility

INFN-LNGS recently expanded its accelerator capabilities with the installation of a new 3.5 MV Singletron machine designed and set up by High Voltage Engineering Europe (HVEE) (Sen *et al.*, 2019); see Fig. 13. The 3.5 MV machine is equipped with two independent beam lines that can be operated with solid and gas target systems. Acceptance tests at HVEE demonstrated that the machine can deliver intense proton, helium, and carbon beams (1, 0.5, and 0.15 mA, respectively) with well-defined energy resolution (0.01% of a teravolt) and stability (0.001% h^{-1} of a teravolt) (Di Leva, 2020). The 1.4 km of rock overburden at LNGS, equivalent to about 3000 meters of water equivalent (m.w.e.), significantly reduces the flux of muons and associated secondaries; see Aliotta, Boeltzig *et al.* (2022) for a review. A first experimental proposal presented by the LUNA Collaboration focuses on measurements of the reactions $^{14}N(p,\gamma)^{15}O$, $^{12}C+{}^{12}C$, $^{13}C(\alpha,n)^{16}O$, and $^{22}Ne(\alpha,n)^{25}Mg$, with the last in the context of the ERC Starting Grant SHADES. The 3.5 MV accelerator is now part of the Bellotti Ion Beam Facility (Junker *et al.*, 2023) and is open to external users.[13]

2. JUNA

JUNA is part of the China Jinping Underground Laboratory, established on the site of hydropower plants in the Jinping mountain in Sichuan, China (Liu *et al.*, 2022). The laboratory, located near the middle of a traffic tunnel, is shielded by 2400 m of mainly marble overburden (6720 m.w.e.). In December 2020 the JUNA Collaboration installed a 400 kV accelerator capable of delivering H^+ and He^+ beams with intensities of up to 10 particle mA and a He^{2+} beam with an intensity of up to 1 particle mA. Some important results have already been published. For example, the lowest-energy study to date of the $^{19}F(p,\gamma)^{20}Na$ reaction advocates a breakout from the CNO cycle as a possible route for calcium production in population III stars (Zhang *et al.*, 2022).

[13]See https://www.lngs.infn.it/en/pagine/bellotti-facility-en.

3. CASPAR

CASPAR laboratory is the only U.S.-based deep underground accelerator and is operated by a collaboration of the University of Notre Dame and the South Dakota School of Mines and Technology (Robertson *et al.*, 2016). The accelerator system has been fully operational since 2018 and is located 1480 m below the surface at SURF[14] in Lead, SD, formerly the Homestake gold mine. The rock overburden results in a 4300 m.w.e shielding effect, significantly decreasing cosmic-ray-induced background with a muon flux level of 4×10^{-9} cm^{-2} s^{-1}. The residual neutron flux consists primarily of low-energy (<10 MeV) neutrons generated by (α,n) reactions induced by the decay of naturally occurring uranium and thorium radionuclides in the surrounding rock and is generally of the order of 10^{-6} neutrons/cm^{-2} s^{-1} (Mei and Hime, 2006; Mei, Zhang, and Hime, 2009). The CASPAR accelerator is a 1 MV Van de Graaff style JN accelerator with a 150–1100 kV operational rangeis that well suited for overlap with higher-energy measurements. The accelerator provides proton and α beams with up to ~250 μA on target. The scientific program continues to explore stellar neutron sources and expands the present studies into the magnesium range probing α capture reactions on ^{24}Mg, ^{25}Mg, and ^{26}Mg isotopes. A new program has been initiated to explore the end point of nova nucleosynthesis, studying proton capture reactions in the Ar to Fe range. CASPAR is well suited for these measurements but will be complemented by a new low-energy machine that is presently under development at Notre Dame.

4. Felsenkeller

The Felsenkeller laboratory is hosted within a network of tunnels, excavated into hornblende monzonite rock, previously used as a cool storage place for the homonymous nearby brewery. Jointly funded and built by Technische Universität Dresden and Helmholtz-Zentrum Dresden-Rossendorf, the laboratory operates a 5 MV Pelletron-type accelerator built by NEC. With the addition of a rf ion source in the high-voltage terminal, the accelerator can be operated in tandem mode or as a single-ended machine and is capable of delivering proton, α-particle, and carbon beams with currents up to several tens of microamperes. Unlike the other sites mentioned in this section, Felsenkeller is a shallow underground laboratory, with a rock overburden of only 140 m.w.e.[15] Such a depth is sufficient to shield all components of cosmic-ray-induced radiation, except muons, for which further active shielding is generally required (Ludwig *et al.*, 2019). Detailed studies of muon, neutron, and γ backgrounds have been carried out (Ludwig *et al.*, 2019; Szücs, Bemmerer *et al.*, 2019; Grieger *et al.*, 2020; Turkat *et al.*, 2023), and the $^{12}C(p,\gamma)^{13}N$ reaction has also been studied (Skowronski *et al.*, 2023b). The further scientific program of Felsenkeller foresees the study of several reactions of astrophysical interest, including $^{3}He(\alpha,\gamma)^{7}Be$ and $^{12}C(\alpha,\gamma)^{16}O$.

[14]See http://www.sanfordlab.org.

[15]A comprehensive description of the laboratory was recently published (Bemmerer *et al.*, 2025).

C. Indirect methods

Indirect methods are also pivotal in nuclear astrophysics owing to the challenges associated with directly measuring reactions at extremely low energies. They can have systematic uncertainties that are different from those of direct measurements, and they provide supplementary information that can constrain R-matrix and other models used in the extrapolation of data from direct measurements. For this review it is worth further exploring here the ANC and THM methods. For a detailed description of the methods, see Tribble *et al.* (2014) and Tumino *et al.* (2021).

The ANC method determines the zero-energy cross section for radiative-capture reactions by exploiting their peripheral nature. This means that the reaction depends mostly on the long-distance behavior of the wave function. The ANC is extracted from transfer reactions using the DWBA, with uncertainties arising primarily from the optical model description that are still much smaller than those affecting spectroscopic factors. While the method is focused to zero energy, it complements direct measurements and can be applied to loosely bound nuclei. The method has been applied to the $^3\mathrm{He}(\alpha,\gamma)^7\mathrm{Be}$; see Sec. VI.C.

The THM is a powerful technique for indirectly measuring astrophysical $S(E)$ factors of reactions involving charged particles. By studying a related reaction with a spectator particle, the THM allows for the extraction of the desired cross section without the need for extrapolation. The THM relies on the assumption of quasifree kinematics, where the spectator particle has a minimal effect on the reaction of interest. The method requires careful selection of beam energy and momentum transfer to ensure that the Coulomb barrier is overcome and the spectator particle remains relatively undisturbed. Since Solar Fusion II, significant advancements have been made, focused on improving the model's accuracy and assessing its systematic uncertainties (Tribble *et al.*, 2014; Tumino *et al.*, 2021). For reactions dominated by broad resonances, the modified R-matrix approach allows for the incorporation of half-off-energy-shell and energy resolution effects within a well-established framework (La Cognata *et al.*, 2015; Trippella and Cognata, 2017). This method enables multichannel descriptions of reactions, such as in the $^{12}\mathrm{C}+{}^{12}\mathrm{C}$ fusion studies (Tumino *et al.*, 2018), and includes a DWBA-based normalization procedure that does not rely on direct data (La Cognata *et al.*, 2010). The modified R-matrix framework has been applied to the $^{15}\mathrm{N}(p,\alpha)^{12}\mathrm{C}$ (see Sec. XI.A.3), $^{19}\mathrm{F}(p,\alpha)^{16}\mathrm{O}$ (see Sec. XI.C.4), and $^{23}\mathrm{Na}(p,\alpha)^{20}\mathrm{Ne}$ (see Sec. XI.D.5) reactions. For narrow resonance reactions, a simplified approach has been introduced to deduce resonance strengths (La Cognata *et al.*, 2022). This method reduces systematic errors from normalization and theory to the percent level through multiresonance normalization and covariance in error propagation. The narrow resonance approach has been used to analyze the $^{17}\mathrm{O}(p,\gamma)^{18}\mathrm{F}$ (see Sec. XI.B.3), $^{17}\mathrm{O}(p,\alpha)^{14}\mathrm{N}$ (see Sec. XI.B.4), and $^{18}\mathrm{O}(p,\alpha)^{15}\mathrm{N}$ (see Sec. XI.C.2) reactions.

D. Plasma facilities

1. NIF and OMEGA

Several efforts have recently been devoted to studying nuclear reactions in a plasma environment reminiscent of stellar conditions (Gatu Johnson *et al.*, 2017) using the two large laser facilities: OMEGA at the Laboratory for Laser Energetics, University of Rochester (Boehly *et al.*, 1997), and the NIF at Lawrence Livermore National Laboratory (Wonterghem *et al.*, 2016). Both facilities use high-power lasers to implode spherical capsules containing reactants of interest to high temperatures (of the order 1–20 keV) and densities [up to 10^3 g cm^{-3} in the extreme case of implosions with a fuel ice layer (Abu-Shawareb *et al.*, 2022)]. The OMEGA laser has the capability of delivering 30 kJ of laser energy divided between 60 laser beams to the target; the NIF can deliver up to 2.0 MJ using 192 laser beams and can thus be used to implode larger amounts of materials at more extreme conditions than OMEGA. Nuclear experiments at these two facilities are enabled by an extensive suite of nuclear diagnostics, originally developed to do inertial confinement fusion experiments (Cerjan *et al.*, 2018). Initial results have been obtained on the $^2\mathrm{H}(p,\gamma)^3\mathrm{He}$ reaction (Zylstra *et al.*, 2020; Mohamed, Kim, and Knauer, 2022), the $^3\mathrm{He}(^3\mathrm{H},\gamma)^6\mathrm{Li}$ reaction (Zylstra *et al.*, 2016), and the $^3\mathrm{H}(^3\mathrm{H},2n)\alpha$ reaction (Casey *et al.*, 2017). Proton spectra have also been measured for the $^3\mathrm{He}(^3\mathrm{He},2p)\alpha$ reaction (Zylstra *et al.*, 2017). In addition to low-Z reaction nuclear S-factor studies, the NIF and OMEGA facilities are also promising for studies of plasma effects on nuclear reactions, including screening (Aliotta and Langanke, 2022; Casey *et al.*, 2023); for studies of charged-particle-induced reactions (Wiescher, deBoer, and Görres, 2022); and, thanks to the high neutron fluxes achievable [up to 5×10^{27} neutrons/cm^{-2} s^{-1} (Abu-Shawareb *et al.*, 2022)], for studying reactions on excited states (Thompson, 2022). However, there are challenges still to be addressed in fully developing this new platform for nuclear experiments, including the impact on the results of rapid gradients in space and time (Crilly *et al.*, 2022).

2. PANDORA

PANDORA is a device conceived for multidisciplinary studies, including many of astrophysical interest (Mascali *et al.*, 2022); see Fig. 14. Two of its main objectives are (a) to perform the first measurements of β decays in plasmas of astrophysical relevance in order to verify the results obtained in storage rings with ^{187}Re (a lifetime reduction by 9 orders of magnitude) and (b) to measure the opacities of plasmas of astrophysical interest (kilonova ejecta). PANDORA will mainly consist of the three following subsystems:

(i) An innovative superconducting magnetic plasma trap, able to produce and confine plasmas with an electron-ion density up to 10^{13} cm^{-3} and an electron temperature of $T_e\sim0.1$–30 keV.

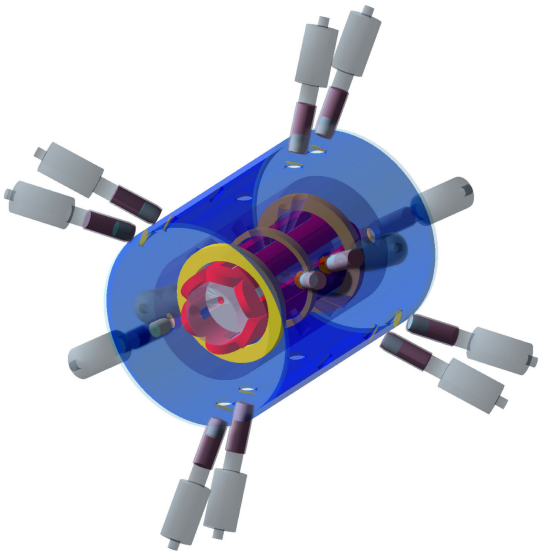

FIG. 14. Schematic of the PANDORA trap with holes to house the HPGe detectors. From Domenico Santonocito.

(ii) An advanced plasma multidiagnostic system consisting of a set of noninvasive diagnostic tools capable of operating simultaneously for nonintrusive monitoring of the thermodynamic plasma properties and parameters.
(iii) An array of 14 HPGe detectors for γ-ray spectroscopy surrounding the plasma trap.

The next development steps will involve preliminary numerical simulation studies to assess the possibility of measuring opacities in astrophysical plasmas (relevant for kilonova ejecta), the study of expected abundances and constraints in AGB stars for some key nuclides of interest, experimental investigation of magnetic confinement and turbulence in plasma using an existing trap at ATOMKI–Debrecen, and a definition of the analysis algorithm for x-ray imaging and spatially resolved spectroscopy.

Initial physics cases to be investigated include ^{176}Lu (a potential cosmochronometer), ^{134}Cs (to adequately reproduce the observed abundance ratio of the two *s*-only isotopes ^{134}Ba and ^{136}Ba), and ^{94}Nb (to solve the puzzle about the exact contribution of *s* processing to ^{94}Mo).

3. Sandia Z

The Sandia National Laboratories Z machine is the world's largest pulsed power accelerator (Sinars *et al.*, 2020). It charges 22 MJ of electrical energy into a capacitor and then discharges it all at once (over approximately 100 ns) into targets ranging from millimeters to centimeters in size. The peak electrical power reached is 80 TW, 15 times the steady-state electrical power generated by all of the world's power plants combined. By concentrating this massive power into small targets, the Z machine can convert them into a state of high-energy density (HED), which refers to an extreme state of matter with a pressure exceeding 10^6 times atmospheric pressure.

The Z machine has been used for a wide range of HED science, including inertial confinement fusion, dynamic material properties, and laboratory astrophysics. In particular, the Sandia Z machine can convert this electrical power into x-ray power using a scheme called the *Z*-pinch dynamic hohlraum (Rochau *et al.*, 2014). This is the most energetic x-ray source on Earth and has been used by academic collaborations such as the Wooton Center for Astrophysical Plasma Properties and the Center for Laboratory Astrophysics. For the stellar opacity project (see Sec. XIII.D), they heat iron or oxygen to the conditions relevant to the base of the convection zone and measure their frequency-resolved opacities to test hypotheses for the solar-opacity-abundance problem (Basu and Antia, 2008; Bailey *et al.*, 2009, 2015; Nagayama *et al.*, 2019). For the accretion disk projects, they heat silicon, iron, and neon photoionized plasmas to conditions similar to those at black hole accretion disks to experimentally test the validity of calculated atomic data, kinetics, and spectral formation (Loisel *et al.*, 2017). This is important for accurately interpreting high-resolution data from upcoming x-ray space telescopes such as XRISM. For the white dwarf photosphere project, they reproduce its photosphere conditions and validate spectroscopic methods used for understanding the age of the Universe as well as constraining its evolutionary paths and supernova remnants (Falcon *et al.*, 2015; Montgomery *et al.*, 2015; Schaeuble *et al.*, 2019, 2021). These experiments reach temperatures ranging from 10^4 to 2×10^6 K and densities ranging from 10^{16} to 10^{23} electrons/cm^{-3} and are performed simultaneously by placing their samples at different locations from the *Z*-pinch dynamic hohlraum.

E. Storage rings for nuclear astrophysics studies

1. CRYRING

A main limitation of experimental studies involving unstable nuclei arises from the difficulty of producing radioactive ion beams of adequate intensity and purity at the energies of interest for astrophysical applications. Storage rings offer a key advantage over traditional isotope separation online and in-flight approaches, as they allow for storing and recirculating radioactive ions over and over again, thus allowing for multiple interactions of unreacted beam particles with an in-ring target (Steck and Litvinov, 2020). Beam recirculation significantly improves the quality of the beam as it results in orders-of-magnitude increased intensity (typical boosting factors of $\sim10^5$), limited only by the duty cycle of the measurement (Bruno *et al.*, 2023) and in improved purity of the stored beam, as only beam particles with the right mass-to-charge ratio will survive in the beam orbit.

One of the main technical challenges of storage rings comes from the requirement of UHV conditions ($< 10^{-10}$ mbar) necessary to guarantee that ions can be recirculated with minimal losses. This in turn translates into a requirement for sufficiently thin targets (i.e., typically $\leq 10^{11}$–10^{14} atoms/cm^{-2}) to minimize beam ion losses through scattering or electron capture; see Bruno *et al.* (2023) for further details.

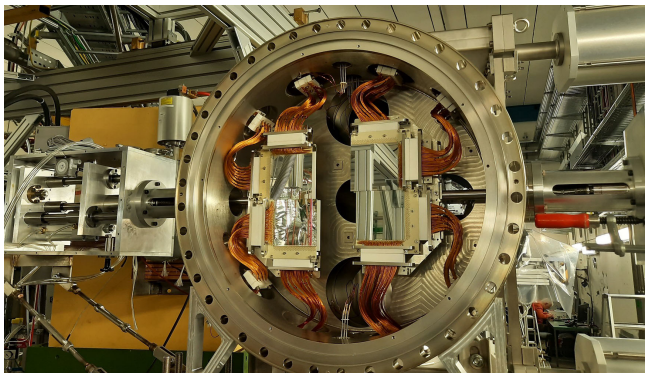

FIG. 15. Photo of the CARME chamber recently installed at CRYRING. Four silicon-strip detectors are visible at the center of the chamber. From Carlo Bruno.

A dedicated low-energy storage ring, CRYRING (Lestinsky *et al.*, 2016), inherited from Stockholm University, was installed at GSI in 2016 as a Swedish in-kind contribution to the FAIR facility. The facility allows nuclear astrophysics studies to be done with radioactive nuclei. After its initial recommissioning (Herfurth *et al.*, 2018), CRYRING now serves as a low-energy extension for experimental storage ring beams, as well as a stand-alone machine with a local ion source (Geithner *et al.*, 2017). After in-flight production in the fragment recoil separator at relativistic energies, rare ions can now be cooled, post-decelerated and stored in the full range down to about 100 keV/u. A study is underway to reach lower energy by means of a transverse low-energy beam line from the FISIC project (Schury *et al.*, 2020; Glorius and Bruno, 2023). CRYRING is now equipped with an in-ring microdroplet gas target, whose low density ($\lesssim 10^{14}$ atoms/cm^{-2}) ensures minimal beam energy loss and straggling through the target, a unique advantage for charged-particle spectroscopy at storage rings compared to standard techniques.

In addition, a new detection chamber (see Fig. 15), CRYRING Array for Reaction Measurements (CARME), was recently installed at CRYRING and fully commissioned in early 2022. Specifically designed to fulfill requirements of stored beam experiments and operating at a pressure of 10^{-12} mbar, CARME can host up to eight double-sided silicon-strip detectors with excellent angular and energy resolution.

Finally, the upcoming installation of the FISIC transverse beam line (Schury *et al.*, 2020) will allow the beam stored in CRYRING to be intercepted, thus opening up unprecedented opportunities for crossed-beam experiments. An interesting application may be the study of nuclear reactions between ion beams, i.e., reactions unaffected by the electron screening, directly at the energies of astrophysical interest. Initial proposals for the study of nuclear astrophysics reactions have already been approved.

XV. CLOSING REMARKS

A. Summary

This review summarizes the significant progress that has been made in the past decade in understanding the nuclear reactions that govern energy production in solar and stellar hydrogen burning. It also describes some of the plasma and atomic physics that effects the solar environment in which these reactions take place, as well as the diagnostic tools—solar neutrinos and helioseismology—by which we can probe that environment.

For S_{11} and S_{12}, cross sections have been derived from first principles using both potential theory and effective field theory. In the case of S_{12}, new experimental data agree well with the theoretical predictions. $S_{\rm hep}$, which governs a minor branch of solar fusion, must also be taken from theory.

The S factors for other pp-chain reactions are based on laboratory measurements. In some cases, notably including S_{17}, most of the studies reviewed here are relatively far from the solar Gamow peak energies, underlining the need for theoretical and experimental tools to bridge the gap.

The nuclear physics of the pp chain remains a significant uncertainty in SSM predictions of the individual neutrino fluxes: pp, pep, hep, ^{7}Be, ^{8}B, and CNO. The nuclear errors are comparable to, and in the case of the hep neutrinos much greater than, the "environmental" errors that are generated by other uncertainties in the SSM (Orebi Gann *et al.*, 2021).

For several reactions including S_{33} and S_{114}, the SF III recommended values are less precise than those of Adelberger *et al.* (2011). This fact should be taken not as a sign of regression but instead as indicative of a more cautious treatment of uncertainties. In some of the error estimates made in this review, we have been mindful of past lessons on the potential impact of unidentified systematics.

The status of our understanding of radiative opacities has been reviewed here, the first time the subject has been included in the solar fusion series. The debate generated by the solar composition problem has brought renewed attention to the complicated interplay between opacities and composition in the SSM. Given new experimental opportunities, especially luminous x-ray sources coupled with plasma targets, there is the expectation of rapid progress in this field over the next decade.

There has been only limited progress on electron screening since the work of Adelberger *et al.* (2011). This field has important practical implications not only for the Sun but also for laboratory experiments and may merit additional attention in the coming decade. Progress may depend on achieving a better understanding of low-energy stopping powers.

B. Recommended values for S factors and their derivatives

The SF III recommendations for nuclear reaction S factors and their derivatives are presented in Table I of the Introduction. In the sections following the Introduction, we presented the details leading to these results and identified opportunities for future work, which are now summarized.

C. General recommendations for future work

For all of the solar fusion reactions, obtaining high-precision experimental data in the Gamow window remains an elusive goal, one that may not be reached in the foreseeable future. However, such direct measures are just one of many avenues for improving our understanding of the nuclear

physics of the Sun. The following recommendations are in most cases summaries of more detailed discussions presented in this review; see the relevant sections for additional details.

(1) For all of the experimentally accessible pp-chain reactions and for S_{114}, which determines the CNO-cycle rate, there is a need for at least one experimental dataset spanning the entire energy range, encompassing the more limited datasets that currently exist. This will provide an important cross-check on the normalizations of those datasets. Experimentalists can now tackle this challenge owing to the new generation of underground accelerators that have the dynamic range needed for such studies.

(2) We recommended continued effort on reaction theory relevant to pp-chain reactions. The needs go beyond rates to include both astrophysical (for example, precise neutrino spectra) and laboratory (for example, γ-ray angular distributions) observables.

(3) We urge the community to set an ambitious goal for the precision of future S-factor measurements: reduce the nuclear physics uncertainties to a factor of 2 below current SSM environmental uncertainties such that they are no longer a significant contributor to SSM neutrino flux uncertainties. With the exception of the hep neutrinos, this goal could be reached via a future reduction of a factor ∼2, typically, in the individual S-factor uncertainties (Orebi Gann *et al.*, 2021). As solar neutrino data are an important input into global neutrino oscillation analyses, nuclear uncertainties will continue to feed into that program until this goal is achieved. Improvements in S_{114} and other CNO-cycle S factors are needed, as the current 8.4% uncertainty would be a limiting factor in extracting the solar core's metallicity from a future large-volume CN neutrino experiment. The progress reported here on S_{17}, with the uncertainty reduced significantly from that of Adelberger *et al.* (2011) to 3.4%, should be continued given the current and future ^{8}B neutrino programs of Super-K and Hyper-K: these neutrinos are our best solar core thermometer. Finally, ongoing Super-K efforts to detect hep neutrinos provide strong motivation for improving estimates of S_{hep} and the associated neutrino spectrum. (Uncertainties in the high-energy tail of the ^{8}B spectrum must also be reduced, as discussed in Sec. II.)

(4) New experimental methods are becoming available that could help us better understand electron screening in terrestrial and solar reactions. Plasma conditions resembling those of the Sun can now be produced in the laboratory. Reactions can be studied in rings, using ions stripped of their atomic shells. The level of theory activity in this field has declined over the past decade, so we hope that experimental progress will help renew interest.

(5) To break the degeneracy between solar abundances and solar opacities, efforts should be made to improve our understanding of radiative opacities for the Sun's principal metals. A high priority is the resolution of the current discrepancy between measured and modeled iron opacities. Solar physicists need access to state-of-the-art, open-source opacity codes.

(6) We recommend that resources be available to extend the use of current and next-generation dark matter detectors to solar neutrino detection. This includes designing new detectors so that they are highly capable for both applications. Some of the high-priority goals of solar neutrino physics—such as a 1% measurement of the pp neutrinos to check the luminosity constraint—might be achieved with a dual-purpose detector.

(7) The solar fusion program to periodically review the nuclear physics of the Sun and other hydrogen-burning stars should be continued, with the separation between studies being no more than ten years. The format should continue to be open, giving all researchers working in the field an opportunity to contribute, and broadly international.

(8) Future solar fusion studies should continue to strengthen the connections between this community and others interested in main-sequence stars. SF III has placed increased emphasis on hydrogen burning at higher temperatures, plasma physics, opacities, and asteroseimology. However, with observations now being made of solarlike stars in their formation stages, we anticipate additional connections developing that will extend well beyond the limits of this study.

D. Outlook

Six decades after the initial observations of solar neutrinos by Davis (2003), significant advances have been made in our understanding of the SSM and, indeed, of hydrogen-burning stars in general. The driver of this progress has been experiment: the observations made of all of the principal solar neutrino sources; our improved understanding of the flavor physics of those neutrinos; the advances made in helioseismology through a second quantitative probe of the solar interior; and our improved knowledge of the input microphysics of the SSM, including nuclear cross sections and opacities. Despite this progress, improvements are still needed. In several cases the dominant uncertainty in our solar neutrino flux predictions stems from the limited precision of the nuclear S factors. Similarly, uncertainties remain in our understanding of radiative transport in the Sun, including the continuing debate about the Sun's primordial composition. As changes in composition often can be mimicked by changes in radiative opacities, our imperfect knowledge of the latter has slowed resolution of the solar composition problem.

The prospects for substantial progress in the next decade are bright. Whereas at the time of Adelberger *et al.* (2011) there was only one underground ion accelerator worldwide, now there are five, opening up possibilities for independently cross-checking important nuclear data. The low background that can be achieved underground led to the first measurements of reactions in the Gamow window. Other new experimental capabilities have come online that are advancing our understanding of solar atomic physics, including low-energy storage rings and new plasma facilities, the latter made possible in part by advances in high-power lasers. The field is approaching the point where opacity measurements can be made under conditions closely approximating those of the solar interior.

Theory has progressed as well, including advances in neutrino flavor physics that have once again made neutrinos a precise probe of solar physics. Techniques with a firmer footing in first principles, such as effective field theory and lattice QCD, are being employed in the extraction of pp-chain S factors. Conventional approaches like the R matrix can now be applied to complex nuclear systems where the inclusion of multiple reaction channels is important.

On the observational side, several large neutrino detectors are under construction, including Hyper-Kamiokande, JUNO, and DUNE. Certain direct-detection dark matter experiments have reached a sensitivity where nuclear recoils due to the coherent solar neutrino scattering have become a background, leading to discussions of how such detectors might be optimized for solar neutrino detection (Essig, Sholapurkar, and Yu, 2018). This underscores the noteworthy radiopurity of these underground detectors. Finally, the helioseismic studies that proved so important in establishing the credibility of the SSM are now being extended to other stars—a major reason why SF III was undertaken at this time. Asteroseismic studies have the potential to tell us what is special and what is common about the Sun as a star.

Given the current excitement about the emerging field of multimessenger astrophysics, it is perhaps fitting to remember that the Sun was the prototype for this field. An array of physical measurements of the Sun—its mass, radius, luminosity, and abundances—were combined with neutrino flux and helioseismic measurements to constrain and then test the SSM. The result was the discovery of neutrino mass and flavor mixing.

This success was a multidisciplinary effort that has not yet run its course. We still have uncertainties in our characterization of the Sun's nuclear, atomic, and weak interaction physics that, if improved, would make the Sun an even more powerful laboratory. As our best-known and nearest star, the Sun is the test of our understanding of the structure and evolution of other main-sequence stars. If the past is any indicator of the future, the efforts that we carry out over the next decade to make the Sun an even more precisely calibrated reference will yield a rich return in our understanding of physics.

LIST OF SYMBOLS AND ABBREVIATIONS

ANC	asymptotic normalization coefficient
BBN	big bang nucleosythesis
CME	common-mode error
EFT	effective field theory and variants: chiral (χEFT), pionless ($\not\pi$EFT), hybrid (EFT*), etc.
LO	leading order
NLO	next-to-leading order
NNLO	next-to-next-to-leading order
SSM	standard solar model

ACKNOWLEDGMENTS

We gratefully acknowledge discussions with many colleagues. The help that they provided contributed significantly to this review.

We thank the following institutions for their support of the SF III effort:

Physics Frontier Center Network for Neutrinos, Nuclear Astrophysics, and Symmetries (N3AS), University of California, Berkeley, host of the SF III workshop;

Institute for Nuclear Theory, University of Washington;

European Union, Chemical Elements as Tracers of the Evolution of the Cosmos—Infrastructures for Nuclear Astrophysics (ChETEC-INFRA), Horizon 2020 Project No. 101008324; and

The Heising-Simons Foundation, Grant No. 2017-228.

N3AS is supported by the U.S. National Science Foundation under Cooperative Agreement No. 2020275. The INT is supported by the U.S. Department of Energy under Grant No. DE-FG02-00ER41132

The authors of SF III acknowledge the following support:

U.S. National Science Foundation, through

Grants No. PHY-1430152 (Joint Institute for Astrophysics) and No. OISE-1927130 (IReNA), Michigan State University;

Grants No. PHY-1913620 and No. PHY-2209184, Mississippi State University;

Grants No. PHY-2011890 and No. PHY-2310059, University of Notre Dame;

Grant No. PHY-2111426, University of Tennessee; and

Grant No. PHY-2108339, University of Wisconsin.

U.S. Department of Energy, through

Contract No. DE-AC02-07CH11359, Fermi National Accelerator Laboratory (Fermilab);

Contract No. DE-AC02-05CH11231, Lawrence Berkeley National Laboratory (LBNL);

Contract No. DE-AC52-07NA27344, Lawrence Livermore National Laboratory (LLNL);

Contract No. 89233218NCA000001, Los Alamos National Laboratory (LANL);

Contract No. DE-NA0003525, Sandia National Laboratories; and

Contract No. DE-AC05-00OR22725, Oak Ridge National Laboratory (ORNL).

Fermilab is operated by Fermi Research Alliance, LLC for the Office of Science. LBNL is operated by the University of California for the Office of Science. LLNL is operated by the Lawrence Livermore National Security, LLC for the National Nuclear Security Administration (NNSA). LANL is operated by Triad National Security, LLC for NNSA. Sandia National Laboratories are managed and operated by National Technology and Engineering Solutions of

Sandia (NTESS) for the NNSA. ORNL is operated by UT-Battelle, LLC for the Office of Science.

U.S. Department of Energy, through

Awards No. DE-FG02-00ER41138 and No. DE-SC0004658, University of California, Berkeley;

Award No. DE-FG02-93ER40789, Colorado School of Mines;

Award No. DE-FG02-97ER41033 (TUNL), Duke University;

Award No. DE-SC0013617 (FRIB Theory Alliance), Michigan State University;

Award No. DE-FG02-97ER41041, University of North Carolina;

Awards No. DE-FG02-88ER40387, No. DE-NA0003883, and No. DE-NA0004065, Ohio University;

Award No. DE-FG02-08ER41533, Texas A&M University, Commerce;

Award No. DE-FG02-97ER41020 (CENPA), University of Washington;

Award No. DE-SC0019465, University of Wisconsin;

Award No. DE-SC0023692, Iowa State University; and

Award No. DE-SC0019257, San Diego State University.

Helmholtz Research Academy Hesse for FAIR, Germany.

Hungarian Scientific Research Fund Grant No. FK134845, National Research, Development, and Innovation Office.

Israel Science Foundation Grant No. 889/23.

Italian Ministero dell'Università e della Ricerca (MUR) Grants No. 2022E2J4RK (program PRIN 2022) and No. 2017W4HA7S (program PRIN 2017).

The Natural Sciences and Engineering Research Council of Canada (NSERC).

Unidad de Excelencia María de Maeztu Grant No. CEX2020-001058-M, Generalitat de Catalunya Grant No. 2021-SGR-1526, and MICINN Grant No. PID2023-149918NB-I00, Spain.

UK Science and Technology Facilities Council Grant No. ST/V001051/1.

This paper describes objective technical results and analysis. Any subjective views or opinions that might be expressed in the paper do not necessarily represent the views of the U.S. Department of Energy, the United States Government, or any other previously listed agency.

APPENDIX A: GALLIUM NEUTRINO SOURCE CROSS SECTIONS

Here we describe in more detail the constraint that the electron-capture rate for ^{71}Ge places on the ^{51}Cr and ^{37}Ar neutrino source cross sections for ^{71}Ga, in the process expanding on the discussion of Sec. II.A.2. We discuss both the early treatment of Bahcall and the more recent analysis of Elliott *et al.* (2023) and Elliott, Gavrin, and Haxton (2024), which was performed in support of the BEST experiment

Following Bahcall (1978), the electron-capture rate can be written in terms of a dimensionless phase-space factor $f_{\rm EC}$,

$$f_{\rm EC} = 2\pi^2 \left(\frac{\hbar}{mc}\right)^3 \left(\frac{q}{mc^2}\right)^2 |\psi(R)|^2, \tag{A1}$$

where q is the energy available to the neutrino and we have omitted atomic shell effects for brevity. The last factor in Eq. (A1) is the electron density at the nucleus within the radius R. Multiplying this by the experimentally determined half-life $t_{1/2}$ yields the traditional ft value needed to calculate the neutrino cross section. Bahcall (1978) defined a characteristic scale σ_0 for neutrino cross sections on ^{71}Ga in the form

$$\sigma_0 = 1.2429 \times 10^{-47} \left(\sum\nolimits_i q_i^2 g_i^2\right)^{-1} \tag{A2}$$

$$= 8.611 \times 10^{-46}\ \text{cm}^2, \tag{A3}$$

where $g_i = \psi(R)$. Bahcall (1997) reported the aforementioned number and stated, "[I]t is about 0.5% less than the value 8.8012×10^{-46} I have used since 1984." Since these numbers differ by 2.2%, there is clearly an error in one of the three numbers.

Recently, Elliott *et al.* (2023) and Elliott, Gavrin, and Haxton (2024) recast the derivations with fundamental constants replacing numerical values and correction terms explicitly stated. They concluded that the ground-state cross section is 2.5% lower, and the excited-state contributions somewhat larger, than the values used in the anomaly analysis. The adjusted net anomaly is minimally reduced.

They found the following expression for the neutrino cross section on ^{71}Ga leading to the ground state (gs) of ^{71}Ge:

$$\sigma_{\rm gs} = \frac{G_F^2 \cos^2\theta_C g_A^2}{\pi} p_e E_e \mathcal{F}(Z_f, E_e) \mathrm{B}_{\rm GT}^{(\nu,e)}(\text{gs})[1 + g_{v,b(\nu,e)}][1 + \epsilon_q], \tag{A4}$$

where $E_e = q - Q_{\rm EC} + m_e - \Delta_0$ and $\Delta_0 \simeq 90$ eV is a small correction introduced by Bahcall for the energy lost to electronic rearrangement in the charge-changing reaction. The Gamow-Teller matrix element $B_{\rm GT}^{(\nu,e)}(\text{gs})$ is determined from the measured

half-life $\tau_{1/2}$ of the electron-capture decay of ^{71}Ge,

$$\omega = \frac{\ln[2]}{\tau_{1/2}} = \frac{G_F^2 \cos^2\theta_C g_A^2}{2\pi} |\phi_{1s}|^2_{\rm avg} q_{1s}^2 \left[2(1+\epsilon_o^{1s})\left(1+\frac{P_L+P_M}{P_K}\right)\right]\left[2B_{\rm GT}^{(\nu,{\rm e})}({\rm gs})\right][1+g_{v,b({\rm EC})}][1+\epsilon_q]. \tag{A5}$$

In Eq. (A5) $\epsilon_o^{1s} \simeq 0.013$ is a correction for overlap and exchange to account for the differences in the wave functions of the initial and final atomic states, $g_{v,b}$ is a radiative correction, and $\epsilon_q \simeq 5\times10^{-4}$ is a correction for the weak magnetism contribution to the transition probability. The factor 2 with $B_{\rm GT}^{(\nu,{\rm e})}({\rm gs})$ is a spin statistical factor. Hence,

$$\sigma_{\rm gs} = \omega \frac{p_e E_e \mathcal{F}(Z_f, E_e)}{|\phi_{1s}|^2_{\rm avg} q_{1s}^2}[1+g_{v,b({\rm EC})}]^{-1}\left[2(1+\epsilon_o^{1s})\left(1+\frac{P_L+P_M}{P_K}\right)\right]^{-1} \tag{A6}$$

$$\equiv \sigma_0 \frac{p_e E_e \mathcal{F}(Z_f, E_e)}{m_e^2 c^3}\frac{1}{2\pi\alpha Z}. \tag{A7}$$

Equation (A7) extracts the Bahcall cross-section scale σ_0 and inserts the dimensionful parameters needed to scale the energy and momentum. The atomic factors of Elliott *et al.* (2023) are equivalent to those of Bahcall,

$$\sum_i |\phi_i|^2_{\rm avg} q_i^2 = 0.014\,43 \frac{(m_e c^2)^5}{4\pi(\hbar c)^3}. \tag{A8}$$

None of the three most advanced calculations referenced by Bahcall (1997) of the densities g_i have been published, so the numerical factor 0.014 43 is taken from the ratio in Eq. (A3). [The computer code GRASP (Dyall *et al.*, 1989) may still be available.] Rather than use the theoretical electron density of each subshell at the nucleus, Elliott *et al.* used the experimentally measured subshell ratios, which has the advantage that only a single overlap and exchange correction and a single energy are needed, for the $1s$ state. As Bahcall stated, overlap and exchange have little effect on the total electron-capture (EC) rate, so Elliott *et al.* wrote Eq. (A8) as follows, with the inclusion of a small Q-value update:

$$\sum_i |\phi_i|^2_{\rm avg} q_i^2 (1+\epsilon_0^i) = |\phi_{1s}|^2_{\rm avg} q_{1s}^2 \left[(1+\epsilon_o^{1s})\left(1+\frac{P_L+P_M}{P_K}\right)\right]. \tag{A9}$$

The resulting expression is

$$\sigma_0 = \frac{8\pi^2 \ln(2)\alpha Z}{|\phi_{1s}|^2_{\rm avg} q_{1s}^2 t_{1/2}}[1+g_{v,b({\rm EC})}]^{-1}\left[2(1+\epsilon_o^{1s})\left(1+\frac{P_L+P_M}{P_K}\right)\right]^{-1} \tag{A10}$$

$$= \left(\frac{\hbar c}{m_e c^2}\right)^3 \frac{4\pi^2 \ln(2)\alpha Z}{0.01440 c\, t_{1/2}}\left(\frac{0.2221\ {\rm MeV}}{q_{1s}}\right)^2 [1+g_{v,b({\rm EC})}]^{-1} \tag{A11}$$

$$= 8.63\times10^{-46}[1+g_{v,b({\rm EC})}]^{-1}\ {\rm cm}^2, \tag{A12}$$

which is only 0.3% larger than the value given by Bahcall (1997).

The aforementioned cross-section expressions give a ground-state cross section that is 2.6% lower than in the cross-section table, Table II of Bahcall (1997). Whether this extends to the solar neutrino rates has not yet been evaluated, but in any scenario some reconsideration of the low-energy solar neutrino data may be required once a resolution to the Ga anomaly has emerged.

APPENDIX B: BAYESIAN METHODS

The treatment of uncertainties when dealing with multiple datasets was addressed in the appendix of Adelberger *et al.* (2011), including the inflation factor method used by the Particle Data Group that was adopted by most of the working groups of Adelberger *et al.* (2011). Interested readers are directed there. We now extend that discussion to include the Bayesian methods used by several of the SF III work groups. For example, in the analysis of the ^{2}H$(p,\gamma)^3$He reaction presented in Sec. IV.D, both Bayesian analysis and Bayes model averaging were utilized.

Consider an optimization that utilizes Gaussian-distributed priors in a constrained Bayesian analysis. With such priors, maximizing the likelihood amounts to minimizing an augmented χ^2,

$$\chi^2_{\rm aug} \equiv \sum_{D,i} \frac{[y_{D_i} - f_D S(E;\lambda)]^2}{\sigma^2_{D_i} + (\sigma^{\rm ext}_{D_i})^2} + \sum_p \left(\frac{\lambda_p - \tilde{\mu}_p}{\tilde{\sigma}_p}\right)^2. \quad \text{(B1)}$$

The first term in Eq. (B1) is the standard χ^2, and the second term derives from the Bayesian constraint on the parameters (λ_p) with prior mean ($\tilde{\mu}_p$) and width ($\tilde{\sigma}_p$), which are chosen with some prior knowledge or can be optimized as subsequently described. Care must be taken when choosing values for the priors ($\tilde{\mu}_p$ and $\tilde{\sigma}_p$). In the absence of prior information, it is common to set $\tilde{\mu}_p = 0$. Similarly, one should not make $\tilde{\sigma}_p$ too small unless one has prior knowledge to do so; otherwise, this will bias the determination of λ_p.

In the first term of Eq. (B1), the double sum runs over the datasets (D) and individual results from each dataset (D_i), with the mean value and stochastic uncertainty of each data point given by y_{D_i} and σ_{D_i}, respectively.

The theoretical model describing the S-factor data, $S(E;\lambda)$, is a function of the energy (E) and a set of parameters (λ) that must be determined. The quoted systematic uncertainties are parametrized by the normalization factors f_D, with a prior of unit normalization and a width characterized by the quoted systematic uncertainty. It is straightforward within a Bayesian framework to utilize distribution functions for f_D that are not Gaussian, such as a log-normal or other distributions. The parameters f_D represent a normalization of the model function for a given dataset that, viewed from a non-Bayesian perspective, can also be interpreted as normalization factors that must be applied to the data to match the "true" underlying distribution.

Finally, $\sigma^{\rm ext}_{D_i}$ are unknown *extrinsic uncertainties* (de Souza *et al.*, 2019). If one assumes that a smooth function of energy can accurately describe the data, then the data in a given experimental set may scatter about this presumed "true" value by more than is reflected by the quoted statistical uncertainties. de Souza *et al.* (2019) suggested that this extra scatter might be explained by some additional source of statistical uncertainty unbeknownst to the experimenter or by some unknown systematic uncertainty that is different for each data point in the same dataset, as opposed to a correlated systematic that affects all data points similarly. In either case this extrinsic uncertainty can be accommodated in a Bayesian analysis framework by adding the additional uncertainty as a normal-distributed source of noise with a width that is constrained by the data. de Souza *et al.* (2019) and Moscoso *et al.* (2021) added $\sigma^{\rm ext}_{D_i}$ as an absolute uncertainty, regardless of the energy. For some data Odell, Brune, and Phillips (2022) suggested to instead adopt a relative uncertainty such that the scale of the extrinsic fluctuations is proportional to the mean value of $S(E)$. This strategy of adding extra extrinsic uncertainty to the datasets can be viewed as an alternative to that of inflating the quoted statistical uncertainties by $\sqrt{\chi^2_\nu}$, which is often used for seemingly incompatible datasets (Workman *et al.*, 2022), where χ^2_ν is the χ^2 per degree of freedom. An advantage of the extrinsic uncertainty method is that it uses the observed scatter within a given dataset as a measure of the possible size of unreported uncertainties, as opposed to uniformly increasing the uncertainty in all datasets by the same relative amount.

One can further perform a Bayes model averaging, which we implement and describe here. For a given model, after optimizing the posterior parameter distributions, the BF is proportional to the probability of the model given the data (Hilbe, de Souza, and Ishida, 2017). Therefore, for a fixed dataset, the BF can be used as a relative probability of each model, thus enabling a weighted model-averaging procedure. If we assume a uniform likelihood for each model, the expectation value and variance of a quantity Y is given by

$$\mathrm{E}[Y] = \sum_k \mathrm{E}[Y|M_k] P[M_k|D], \quad \text{(B2)}$$

$$\mathrm{Var}[Y] = \sum_k \mathrm{Var}[Y|M_k] P[M_k|D] + \sum_k \mathrm{E}^2[Y|M_k] P[M_k|D] - \mathrm{E}^2[Y], \quad \text{(B3)}$$

where $\mathrm{E}[Y|M_k]$ denotes the expectation of Y given the model M_k and $P[M_k|D]$ denotes the probability of the model M_k given the data (D), which is given by

$$P[M_k|D] = \frac{\mathrm{BF}_{M_k}}{\sum_l \mathrm{BF}_{M_l}}, \quad \text{(B4)}$$

with BF_{M_l} the Bayes factor of model l. Similarly, for a given model, in the absence of prior information on the size of an unknown parameter, the optimal width of its prior can be estimated by finding the value of $\tilde{\sigma}_p$ that maximizes the BF, which typically provides a reasonable approximation to marginalizing over the prior width.

REFERENCES

Abazov, A. I., *et al.*, 1991, Phys. Rev. Lett. **67**, 3332.
Abe, K., *et al.*, 2016, Phys. Rev. D **94**, 052010.
Abe, K., *et al.* (Hyper-Kamiokande Proto-Collaboration), 2018, arXiv:1805.04163.
Abu-Shawareb, H., *et al.*, 2022, Phys. Rev. Lett. **129**, 075001.
Acciarri, R., *et al.*, 2016, arXiv:1601.02984.
Acharya, B., B. D. Carlsson, A. Ekström, C. Forssén, and L. Platter, 2016, Phys. Lett. B **760**, 584.
Acharya, B., A. Ekström, D. Odell, T. Papenbrock, and L. Platter, 2017, Phys. Rev. C **95**, 031301.
Acharya, B., A. Ekström, and L. Platter, 2018, Phys. Rev. C **98**, 065506.
Acharya, B., L. E. Marcucci, and L. Platter, 2023, arXiv:2304.03327.
Acharya, B., L. Platter, and G. Rupak, 2019, Phys. Rev. C **100**, 021001.
Adam, T., *et al.*, 2015, arXiv:1508.07166.
Adelberger, E. G., *et al.*, 1998, Rev. Mod. Phys. **70**, 1265.
Adelberger, E. G., *et al.*, 2011, Rev. Mod. Phys. **83**, 195.
Agarwalla, S. K., *et al.* (Borexino Collaboration), 2020a, J. High Energy Phys. 02, 038.
Agostini, M., *et al.*, 2017, Phys. Rev. D **96**, 091103.
Agostini, M., *et al.* (Borexino Collaboration), 2018, Nature (London) **562**, 505.
Agostini, M., *et al.*, 2019, Phys. Rev. D **100**, 082004.
Agostini, M., *et al.*, 2020a, Phys. Rev. D **101**, 012009.
Agostini, M., *et al.*, 2020b, Phys. Rev. D **101**, 062001.

Agostini, M., *et al.* (Borexino Collaboration), 2020c, Nature (London) **587**, 577.
Aharmim, B., *et al.*, 2006, Astrophys. J. **653**, 1545.
Aharmim, B., *et al.*, 2018, Phys. Rev. D **98**, 112013.
Aharmim, B., *et al.*, 2019a, Phys. Rev. D **99**, 032013.
Aharmim, B., *et al.*, 2019b, Phys. Rev. D **100**, 112005.
Aharmim, B., *et al.*, 2019c, Phys. Rev. D **99**, 112007.
Aharmim, B., *et al.*, 2020, Phys. Rev. D **102**, 062006.
Ahmad, Q. R., *et al.*, 2001, Phys. Rev. Lett. **87**, 071301.
Ahmad, Q. R., *et al.*, 2002a, Phys. Rev. Lett. **89**, 011301.
Ahmad, Q. R., *et al.*, 2002b, Phys. Rev. Lett. **89**, 011302.
Ahmed, S. N., *et al.*, 2004, Phys. Rev. Lett. **92**, 181301.
Ajzenberg-Selove, F., 1991, Nucl. Phys. **A523**, 1.
Akhmedov, E., and A. Y. Smirnov, 2022, J. High Energy Phys. 11, 082.
Akimov, D., *et al.*, 2017, Science **357**, 1123.
Aliotta, M., A. Boeltzig, R. Depalo, and G. Gyürky, 2022, Annu. Rev. Nucl. Part. Sci. **72**, 177.
Aliotta, M., and K. Langanke, 2022, Front. Phys. **10**.
Aliotta, M., *et al.*, 2001, Nucl. Phys. **A690**, 790.
Aliotta, M., *et al.*, 2022, J. Phys. G **49**, 010501.
Allega, A., *et al.* (SNO+ Collaboration), 2022, Phys. Rev. D **105**, 112012.
Allega, A., *et al.* (SNO+ Collaboration), 2023, Phys. Rev. Lett. **130**, 091801.
Allega, A., *et al.* (SNO+ Collaboration), 2024, Phys. Rev. D **109**, 072002.
Alonso, J. R., *et al.*, 2014, Brookhaven National Laboratory Report No. BNL-106082-2014-JA [arXiv:1409.5864].
Amarasinghe, S., R. Baghdadi, Z. Davoudi, W. Detmold, M. Illa, A. Parreno, A. V. Pochinsky, P. E. Shanahan, and M. L. Wagman, 2021, arXiv:2108.10835.
An, F., *et al.*, 2016, J. Phys. G **43**, 030401.
Anderson, M., *et al.* (SNO+ Collaboration), 2019a, Phys. Rev. D **99**, 032008.
Anderson, M., *et al.* (SNO+ Collaboration), 2019b, Phys. Rev. D **99**, 012012.
Anderson, M. R., *et al.* (SNO+ Collaboration), 2020, Phys. Rev. C **102**, 014002.
Ando, S., T. S. Park, K. Kubodera, and F. Myhrer, 2002, Phys. Lett. B **533**, 25.
Angulo, C., and P. Descouvemont, 2001, Nucl. Phys. **A690**, 755.
Angulo, C., S. Engstler, G. Raimann, C. Rolfs, W. H. Schulte, and E. Somorjai, 1993, Z. Phys. A **345**, 231.
Angulo, C., *et al.*, 1999, Nucl. Phys. **A656**, 3.
Anselmann, P., *et al.*, 1992, Phys. Lett. B **285**, 376.
Antia, H. M., and S. Basu, 2006, Astrophys. J. **644**, 1292.
Appel, S., *et al.*, 2022, Phys. Rev. Lett. **129**, 252701.
Aprile, E., *et al.*, 2024, arXiv:2408.02877.
Arpesella, C., *et al.* (Borexino Collaboration), 2008, Phys. Lett. B **658**, 101.
Artemov, S. V., S. B. Igamov, Q. I. Tursunmakhatov, and R. Yarmukhamedov, 2012, Phys. At. Nucl. **75**, 291.
Artemov, S. V., *et al.*, 2022, Eur. Phys. J. A **58**, 24.
Askins, M., *et al.*, 2020, Eur. Phys. J. C **80**, 416.
Askins, M., *et al.*, 2022, arXiv:2202.12839.
Asplund, M., 2005, Annu. Rev. Astron. Astrophys. **43**, 481.
Asplund, M., A. M. Amarsi, and N. Grevesse, 2021, Astron. Astrophys. **653**, A141.
Asplund, M., N. Grevesse, and A. J. Sauval, 2005, in *Cosmic Abundances as Records of Stellar Evolution and Nucleosynthesis*, Astronomical Society of the Pacific Conference Series Vol. 336, edited by T. G. Barnes III and F. N. Bash (Astronomical Society of the Pacific, San Francisco), p. 25.
Asplund, M., N. Grevesse, and A. J. Sauval, 2006, Nucl. Phys. **A777**, 1.
Asplund, M., N. Grevesse, A. J. Sauval, and P. Scott, 2009, Annu. Rev. Astron. Astrophys. **47**, 481.
Asplund, M., Å. Nordlund, R. Trampedach, C. Allende Prieto, and R. F. Stein, 2000, Astron. Astrophys. **359**, 729, https://ui.adsabs.harvard.edu/abs/2000A&A...359..729A.
Assenbaum, H. J., K. Langanke, and C. Rolfs, 1987, Z. Phys. A **327**, 461.
Azuma, R. E., *et al.*, 2010, Phys. Rev. C **81**, 045805.
Baby, L. T., *et al.*, 2003a, Phys. Rev. C **67**, 065805.
Baby, L. T., *et al.*, 2003b, Phys. Rev. Lett. **90**, 022501.
Badnell, N. R., M. A. Bautista, K. Butler, F. Delahaye, C. Mendoza, P. Palmeri, C. J. Zeippen, and M. J. Seaton, 2005, Mon. Not. R. Astron. Soc. **360**, 458.
Badnell, N. R., and M. J. Seaton, 2003, J. Phys. B **36**, 4367.
Bahcall, J. N., 1966, Phys. Rev. Lett. **17**, 398.
Bahcall, J. N., 1978, Rev. Mod. Phys. **50**, 881.
Bahcall, J. N., 1990, Phys. Rev. D **41**, 2964.
Bahcall, J. N., 1994, Phys. Rev. D **49**, 3923.
Bahcall, J. N., 1997, Phys. Rev. C **56**, 3391.
Bahcall, J. N., 2002, Phys. Rev. C **65**, 025801.
Bahcall, J. N., S. Basu, M. Pinsonneault, and A. M. Serenelli, 2005, Astrophys. J. **618**, 1049.
Bahcall, J. N., L. S. Brown, A. Gruzinov, and R. F. Sawyer, 2002, Astron. Astrophys. **383**, 291.
Bahcall, J. N., J. Davis, Raymond, and L. Wolfenstein, 1988, Nature (London) **334**6182, 487.
Bahcall, J. N., E. Lisi, D. E. Alburger, L. de Braeckeleer, S. J. Freedman, and J. Napolitano, 1996, Phys. Rev. C **54**, 411.
Bahcall, J. N., and R. M. May, 1968, Astrophys. J. **152**, L17.
Bahcall, J. N., and R. M. May, 1969, Astrophys. J. **155**, 501.
Bahcall, J. N., and C. P. Moeller, 1969, Astrophys. J. **155**, 511.
Bahcall, J. N., A. M. Serenelli, and S. Basu, 2005, Astrophys. J. **621**, L85.
Bahcall, J. N., and A. Ulmer, 1996, Phys. Rev. D **53**, 4202.
Bailey, J. E., G. A. Rochau, R. C. Mancini, C. A. Iglesias, J. J. MacFarlane, I. E. Golovkin, C. Blancard, P. Cosse, and G. Faussurier, 2009, Phys. Plasmas **16**, 058101.
Bailey, J. E., *et al.*, 2007, Phys. Rev. Lett. **99**, 265002.
Bailey, J. E., *et al.*, 2015, Nature (London) **517**, 56.
Balantekin, A. B., C. A. Bertulani, and M. S. Hussein, 1997, Nucl. Phys. **A627**, 324.
Bang, J. M., L. S. Ferreira, E. Maglione, and J. M. Hansteen, 1996, Phys. Rev. C **53**, R18.
Barbui, M., *et al.*, 2013, Phys. Rev. Lett. **111**, 082502.
Barinov, V., B. Cleveland, V. Gavrin, D. Gorbunov, and T. Ibragimova, 2018, Phys. Rev. D **97**, 073001.
Barinov, V. V., *et al.*, 2022a, Phys. Rev. Lett. **128**, 232501.
Barinov, V. V., *et al.*, 2022b, Phys. Rev. C **105**, 065502.
Barker, F. C., 1995, Nucl. Phys. **A588**, 693.
Barker, F. C., 2008, Phys. Rev. C **78**, 044612.
Barker, F. C., and T. Kajino, 1991, Aust. J. Phys. **44**, 369.
Barnard, A. C. L., C. M. Jones, and G. C. Phillips, 1964, Nucl. Phys. **50**, 629.
Basilico, D., *et al.*, 2023, Phys. Rev. D **108**, 102005.
Basu, S., and H. M. Antia, 2004, Astrophys. J. **606**, L85.
Basu, S., and H. M. Antia, 2008, Phys. Rep. **457**, 217.
Batkin, I. S., and M. K. Sundaresan, 1995, Phys. Rev. D **52**, 5362.

Baur, G., C. A. Bertulani, and H. Rebel, 1986, Nucl. Phys. **A458**, 188.

Baye, D., 2000, Phys. Rev. C **62**, 065803.

Baye, D., P. Descouvemont, and M. Hesse, 1998, Phys. Rev. C **58**, 545.

Beacom, J. F., *et al.*, 2017, Chin. Phys. C **41**, 023002.

Beane, S. R., and M. J. Savage, 2001, Nucl. Phys. **A694**, 511.

Becker, H. W., W. E. Kieser, C. Rolfs, H. P. Trautvetter, and M. Wiescher, 1982, Z. Phys. A **305**, 319.

Becker, H. W., *et al.*, 1995, Z. Phys. A **351**, 453.

Bedaque, P. F., H. W. Hammer, and U. van Kolck, 1999, Phys. Rev. Lett. **82**, 463.

Bellini, G., *et al.* (Borexino Collaboration), 2014, Nature (London) **512**7515, 383.

Bemmerer, D., *et al.*, 2006a, Phys. Rev. Lett. **97**, 122502.

Bemmerer, D., *et al.*, 2006b, Nucl. Phys. **A779**, 297.

Bemmerer, D., *et al.*, 2009, J. Phys. G **36**, 045202.

Bemmerer, D., *et al.*, 2019, in *Solar Neutrinos*, edited by M. Meyer and K. Zuber (World Scientific, Singapore), pp. 249–263.

Bemmerer, D., *et al.*, 2025, Eur. Phys. J. A **61**, 19.

Bergemann, M., *et al.*, 2021, Mon. Not. R. Astron. Soc. **508**, 2236.

Bergstrom, J., M. C. Gonzalez-Garcia, M. Maltoni, C. Pena-Garay, A. M. Serenelli, and N. Song, 2016, J. High Energy Phys. 03, 132.

Berka, I., K. P. Jackson, C. Rolfs, A. M. Charlesworth, and R. E. Azuma, 1977, Nucl. Phys. **A288**, 317.

Berrington, K. A., P. G. Burke, K. Butler, M. J. Seaton, P. J. Storey, K. T. Taylor, and Y. Yan, 1987, J. Phys. B **20**, 6379.

Bertone, P. F., A. E. Champagne, M. Boswell, C. Iliadis, S. E. Hale, V. Y. Hansper, and D. C. Powell, 2002, Phys. Rev. C **66**, 055804.

Bertone, P. F., A. E. Champagne, D. C. Powell, C. Iliadis, S. E. Hale, and V. Y. Hansper, 2001, Phys. Rev. Lett. **87**, 152501.

Bertulani, C. A., 1996, Z. Phys. A **356**, 293.

Bertulani, C. A., 2004, Phys. Lett. B **585**, 35.

Bertulani, C. A., and D. T. de Paula, 2000, Phys. Rev. C **62**, 045802.

Bertulani, C. A., H. W. Hammer, and U. van Kolck, 2002, Nucl. Phys. **A712**, 37.

Best, A., *et al.*, 2019, Phys. Lett. B **797**, 134900.

Betts, R. R., H. T. Fortune, and R. Middleton, 1975, Phys. Rev. C **11**, 19.

Bhattacharya, M., E. G. Adelberger, and H. E. Swanson, 2006, Phys. Rev. C **73**, 055802.

Bhupal Dev, P. S., *et al.*, 2019, SciPost Phys. Proc. **2**, 001.

Blackmon, J. C., A. E. Champagne, M. A. Hofstee, M. S. Smith, R. G. Downing, and G. P. Lamaze, 1995, Phys. Rev. Lett. **74**, 2642.

Blancard, C., P. Cossé, and G. Faussurier, 2012, Astrophys. J. **745**, 10.

Blancard, C., *et al.*, 2016, Phys. Rev. Lett. **117**, 249501.

Boehly, T. R., *et al.*, 1997, Opt. Commun. **133**, 495.

Boeltzig, A., *et al.*, 2019, Phys. Lett. B **795**, 122.

Boeltzig, A., *et al.*, 2022, Phys. Rev. C **106**, 045801.

Bonetti, R., *et al.*, 1999, Phys. Rev. Lett. **82**, 5205.

Bonilla, J., B. Acharya, and L. Platter, 2023, Phys. Rev. C **107**, 065502.

Bordeanu, C., G. Gyürky, Z. Halász, T. Szücs, G. G. Kiss, Z. Elekes, J. Farkas, Z. Fülöp, and E. Somorjai, 2013, Nucl. Phys. **A908**, 1.

Boykin, W., S. Baker, and D. Hardy, 1972, Nucl. Phys. **A195**, 241.

Bracci, L., G. Fiorentini, V. S. Melezhik, G. Mezzorani, and P. Pasini, 1991, Phys. Lett. A **153**, 456.

Bracci, L., G. Fiorentini, and G. Mezzorani, 1990, Phys. Lett. A **146**, 128.

Brdar, V., J. Gehrlein, and J. Kopp, 2023, J. High Energy Phys. 05, 143.

Briceño, R. A., and Z. Davoudi, 2013, Phys. Rev. D **88**, 094507.

Briceño, R. A., J. J. Dudek, R. G. Edwards, C. J. Shultz, C. E. Thomas, D. J. Wilson, and Hadron Spectrum Collaboration, 2015, Phys. Rev. Lett. **115**, 242001.

Broggini, C., D. Bemmerer, A. Caciolli, and D. Trezzi, 2018, Prog. Part. Nucl. Phys. **98**, 55.

Broggini, C., D. Bemmerer, A. Guglielmetti, and R. Menegazzo, 2010, Annu. Rev. Nucl. Part. Sci. **60**, 53.

Brown, L. S., and R. F. Sawyer, 1997, Rev. Mod. Phys. **69**, 411.

Brown, T. A. D., C. Bordeanu, K. A. Snover, D. W. Storm, D. Melconian, A. L. Sallaska, S. K. L. Sjue, and S. Triambak, 2007, Phys. Rev. C **76**, 055801.

Brune, C. R., 2002, Phys. Rev. C **66**, 044611.

Brune, C. R., J. A. Caggiano, D. B. Sayre, A. D. Bacher, G. M. Hale, and M. W. Paris, 2015, Phys. Rev. C **92**, 014003.

Brune, C. R., and R. J. deBoer, 2020, Phys. Rev. C **102**, 024628.

Bruno, C. G., *et al.*, 2015, Eur. Phys. J. A **51**, 94.

Bruno, C. G., *et al.*, 2016, Phys. Rev. Lett. **117**, 142502.

Bruno, C. G., *et al.*, 2019, Phys. Lett. B **790**, 237.

Bruno, C. G., *et al.*, 2023, Nucl. Instrum. Methods Phys. Res., Sect. A **1048**, 168007.

Buckner, M. Q., C. Iliadis, J. M. Cesaratto, C. Howard, T. B. Clegg, A. E. Champagne, and S. Daigle, 2012, Phys. Rev. C **86**, 065804.

Buckner, M. Q., C. Iliadis, K. J. Kelly, L. N. Downen, A. E. Champagne, J. M. Cesaratto, C. Howard, and R. Longland, 2015, Phys. Rev. C **91**, 015812.

Buldgen, G., A. Noels, V. A. Baturin, A. V. Oreshina, S. V. Ayukov, R. Scuflaire, A. M. Amarsi, and N. Grevesse, 2024, Astron. Astrophys. **681**, A57.

Buompane, R., *et al.*, 2018, Eur. Phys. J. A **54**, 92.

Buompane, R., *et al.*, 2022, Phys. Lett. B **824**, 136819.

Burke, P. G., 2011, *R-Matrix Theory of Atomic Collisions* (Springer, Berlin), p. 3.

Butler, M., and J.-W. Chen, 2001, Phys. Lett. B **520**, 87.

Butler, M., J.-W. Chen, and X. Kong, 2001, Phys. Rev. C **63**, 035501.

Butler, M., J.-W. Chen, and P. Vogel, 2002, Phys. Lett. B **549**, 26.

Caciolli, A., *et al.*, 2011, Astron. Astrophys. **533**, A66.

Caffau, E., H. G. Ludwig, M. Steffen, B. Freytag, and P. Bonifacio, 2011, Sol. Phys. **268**, 255.

Capozzi, F., S. W. Li, G. Zhu, and J. F. Beacom, 2019, Phys. Rev. Lett. **123**, 131803.

Capozzi, F., E. Lisi, A. Marrone, and A. Palazzo, 2018, Prog. Part. Nucl. Phys. **102**, 48.

Carlson, J., D. O. Riska, R. Schiavilla, and R. B. Wiringa, 1991, Phys. Rev. C **44**, 619.

Carlsson, B. D., A. Ekström, C. Forssén, D. F. Strömberg, G. R. Jansen, O. Lilja, M. Lindby, B. A. Mattsson, and K. A. Wendt, 2016, Phys. Rev. X **6**, 011019.

Carmona-Gallardo, M., *et al.*, 2012, Phys. Rev. C **86**, 032801.

Carraro, C., A. Schafer, and S. E. Koonin, 1988, Astrophys. J. **331**, 565.

Carrasco-Rojas, D. P., *et al.*, 2023, Phys. Rev. C **108**, 045802.

Casella, C., *et al.*, 2002, Nucl. Phys. **A706**, 203.

Casey, D. T., *et al.*, 2017, Nat. Phys. **13**, 1227.

Casey, D. T., *et al.*, 2023, Front. Phys. **10**.

Castro, M., S. Vauclair, and O. Richard, 2007, Astron. Astrophys. **463**, 755.

Cavanna, F., and P. Prati, 2018, Int. J. Mod. Phys. A **33**, 1843010.

Cavanna, F., *et al.*, 2015, Phys. Rev. Lett. **115**, 252501.

Cavanna, F., *et al.*, 2018, Phys. Rev. Lett. **120**, 239901.

Ceccarelli, L., A. Gnech, L. E. Marcucci, M. Piarulli, and M. Viviani, 2023, Front. Phys. **10**, 1049919.

Cerjan, C. J., *et al.*, 2018, J. Phys. G **45**, 033003.

Cesaratto, J. M., A. E. Champagne, M. Q. Buckner, T. B. Clegg, S. Daigle, C. Howard, C. Iliadis, R. Longland, J. R. Newton, and B. M. Oginni, 2013, Phys. Rev. C **88**, 065806.
Chafa, A., *et al.*, 2007, Phys. Rev. C **75**, 035810.
Champagne, A. E., and M. L. Pitt, 1986, Nucl. Phys. **A457**, 367.
Chen, J.-W., K. M. Heeger, and R. G. Robertson, 2003, Phys. Rev. C **67**, 025801.
Chen, J.-W., T. Inoue, X. Ji, and Y. Li, 2005, Phys. Rev. C **72**, 061001.
Chen, J.-W., C. P. Liu, and S.-H. Yu, 2013, Phys. Lett. B **720**, 385.
Chen, J.-W., G. Rupak, and M. J. Savage, 1999, Nucl. Phys. **A653**, 386.
Chow, H. C., G. M. Griffiths, and T. H. Hall, 1975, Can. J. Phys. **53**, 1672.
Christensen-Dalsgaard, J., 2002, Rev. Mod. Phys. **74**, 1073.
Christensen-Dalsgaard, J., M. P. di Mauro, G. Houdek, and F. Pijpers, 2009, Astron. Astrophys. **494**, 205.
Christy, R. F., and I. Duck, 1961, Nucl. Phys. **24**, 89.
Ciani, G. F., D. Piatti, and R. M. Gesuè, 2022, EPJ Web Conf. **260**, 11003.
Cleveland, B. T., T. Daily, J. Davis, Raymond, J. R. Distel, K. Lande, C. K. Lee, P. S. Wildenhain, and J. Ullman, 1998, Astrophys. J. **496**, 505.
Colgan, J., D. P. Kilcrease, N. H. Magee, M. E. Sherrill, J. A. Jr., P. Hakel, C. J. Fontes, J. A. Guzik, and K. A. Mussack, 2016, Astrophys. J. **817**, 116.
Collar, J. I., and S. G. Yoon, 2023, Phys. Rev. C **108**, L021602.
Coloma, P., M. C. Gonzalez-Garcia, M. Maltoni, J. P. Pinheiro, and S. Urrea, 2023, J. High Energy Phys. 08, 032.
Confortola, F., *et al.*, 2007, Phys. Rev. C **75**, 065803.
Cooke, R. J., M. Pettini, and C. C. Steidel, 2018, Astrophys. J. **855**, 102.
Cooper, A. L., *et al.*, 2018, Rev. Sci. Instrum. **89**, 083301.
Couture, A., *et al.*, 2008, Phys. Rev. C **77**, 015802.
Cowan, R. D., 1981, *The Theory of Atomic Structure and Spectra* (University of California Press, Berkeley), p. 3.
Crilly, A., I. Garin-Fernandez, B. Appelbe, and J. Chittenden, 2022, Front. Phys. **10**.
Csedreki, L., G. Gyürky, and T. Szücs, 2023, Nucl. Phys. **A1037**, 122705.
Cumming, A., and W. C. Haxton, 1996, Phys. Rev. Lett. **77**, 4286.
Cvetinovic, A., M. Lipoglavsek, S. Markelj, and J. Vesic, 2015, Phys. Rev. C **92**, 065801.
Cyburt, R. H., B. D. Fields, K. A. Olive, and T.-H. Yeh, 2016, Rev. Mod. Phys. **88**, 015004.
Czerski, K., 2022, Phys. Rev. C **106**, L011601.
Czerski, K., A. Huke, A. Biller, P. Heide, M. Hoeft, and G. Ruprecht, 2001, Europhys. Lett. **54**, 449.
Czerski, K., A. Huke, P. Heide, and G. Ruprecht, 2004, Europhys. Lett. **68**, 363.
Czerski, K., A. Huke, P. Heide, and G. Ruprecht, 2006, Eur. Phys. J. A **27**, 83.
Czerski, K., D. Weissbach, A. I. Kilic, G. Ruprecht, A. Huke, M. Kaczmarski, and N. Targosz-Ślęczka, and K. Maass, 2016, Europhys. Lett. **113**, 22001.
D'Agostini, G., 1994, Nucl. Instrum. Methods Phys. Res., Sect. A **346**, 306.
Daigle, S., K. J. Kelly, A. E. Champagne, M. Q. Buckner, C. Iliadis, and C. Howard, 2016, Phys. Rev. C **94**, 025803.
Däppen, W., L. Anderson, and D. Mihalas, 1987, Astrophys. J. **319**, 195.
Daszyńska-Daszkiewicz, J., and P. Walczak, 2009, Mon. Not. R. Astron. Soc. **398**, 1961.
Daszyńska-Daszkiewicz, J., and P. Walczak, 2010, Mon. Not. R. Astron. Soc. **403**, 496.
Davids, B., S. M. Austin, D. Bazin, H. Esbensen, B. M. Sherrill, I. J. Thompson, and J. A. Tostevin, 2001, Phys. Rev. C **63**, 065806.
Davids, B., and S. Typel, 2003, Phys. Rev. C **68**, 045802.
Davids, B., *et al.*, 2001, Phys. Rev. Lett. **86**, 2750.
Davidson, S. J., J. M. Foster, C. C. Smith, K. A. Warburton, and S. J. Rose, 1988, Appl. Phys. Lett. **52**, 847.
Davis, R., 2003, Rev. Mod. Phys. **75**, 985.
Davis, R., D. S. Harmer, and K. C. Hoffman, 1968, Phys. Rev. Lett. **20**, 1205.
deBoer, R. J., O. Clarkson, A. J. Couture, J. Görres, F. Herwig, I. Lombardo, P. Scholz, and M. Wiescher, 2021, Phys. Rev. C **103**, 055815.
deBoer, R. J., J. Görres, G. Imbriani, P. J. LeBlanc, E. Uberseder, and M. Wiescher, 2013, Phys. Rev. C **87**, 015802.
deBoer, R. J., J. Görres, K. Smith, E. Uberseder, M. Wiescher, A. Kontos, G. Imbriani, A. Di Leva, and F. Strieder, 2014, Phys. Rev. C **90**, 035804.
deBoer, R. J., P. J. Leblanc, S. Falahat, G. Imbriani, J. Görres, S. O'Brien, E. Uberseder, and M. Wiescher, 2012, Phys. Rev. C **85**, 038801.
deBoer, R. J., *et al.*, 2015, Phys. Rev. C **91**, 045804.
deBoer, R. J., *et al.*, 2021, Phys. Rev. C **103**, 065801.
de Braeckeleer, L., *et al.*, 1995, Phys. Rev. C **51**, 2778.
Delahaye, F., C. P. Ballance, R. T. Smyth, and N. R. Badnell, 2021, Mon. Not. R. Astron. Soc. **508**, 421.
Delahaye, F., and M. H. Pinsonneault, 2006, Astrophys. J. **649**, 529.
De-Leon, H., and D. Gazit, 2022, arXiv:2207.10176.
De-Leon, H., L. Platter, and D. Gazit, 2019, Phys. Rev. C **100**, 055502.
Depalo, R., *et al.*, 2015, Phys. Rev. C **92**, 045807.
Depalo, R., *et al.*, 2016, Phys. Rev. C **94**, 055804.
Dermigny, J. R., C. Iliadis, M. Q. Buckner, and K. J. Kelly, 2016, Nucl. Instrum. Methods Phys. Res., Sect. A **830**, 427.
Descouvemont, P., A. Adahchour, C. Angulo, A. Coc, and E. Vangioni-Flam, 2004, At. Data Nucl. Data Tables **88**, 203.
Descouvemont, P., and D. Baye, 2010, Rep. Prog. Phys. **73**, 036301.
de Souza, R. S., S. R. Boston, A. Coc, and C. Iliadis, 2019, Phys. Rev. C **99**, 014619.
Di Leva, A., 2020 (private communication).
Di Leva, A., *et al.*, 2009, Phys. Rev. Lett. **102**, 232502.
Di Leva, A., *et al.* (LUNA Collaboration), 2014, Phys. Rev. C **89**, 015803.
Dimitrijevic, M., and N. Konjevic, 1986, Astron. Astrophys. **163**, 297.
Dimitrijevic, M. S., and N. Konjevic, 1987, Astron. Astrophys. **172**, 345.
Ding, S., K. Xu, and H. Wang, 2002, Appl. Radiat. Isot. **56**, 877.
Dohet-Eraly, J., P. Navrátil, S. Quaglioni, W. Horiuchi, G. Hupin, and F. Raimondi, 2016, Phys. Lett. B **757**, 430.
Dubovichenko, S. B., N. A. Burkova, A. V. Dzhazairov-Kakhramanov, and A. S. Tkachenko, 2019, Nucl. Phys. **A983**, 175.
Dunham, G. S., T. Nagayama, J. E. Bailey, and G. P. Loisel, 2021, Rev. Sci. Instrum. **92**, 083512.
Dwarakanath, M. R., 1974, Phys. Rev. C **9**, 805.
Dyall, K., I. Grant, C. Johnson, F. Parpia, and E. Plummer, 1989, Comput. Phys. Commun. **55**, 425.
Eguchi, K., *et al.*, 2003, Phys. Rev. Lett. **90**, 021802.

Ekström, A., C. Forssén, G. Hagen, G. R. Jansen, W. Jiang, and T. Papenbrock, 2023, Front. Phys. **11**, 1129094.

Elliott, S., V. Gavrin, and W. Haxton, 2024, Prog. Part. Nucl. Phys. **134**, 104082.

Elliott, S. R., V. N. Gavrin, W. C. Haxton, T. V. Ibragimova, and E. J. Rule, 2023, Phys. Rev. C **108**, 035502.

Endt, P. M., C. Alderliesten, F. Zijderhand, A. A. Wolters, and A. G. M. Van Hees, 1990, Nucl. Phys. **A510**, 209.

Engstler, S., A. Krauss, K. Neldner, C. Rolfs, U. Schröder, and K. Langanke, 1988, Phys. Lett. B **202**, 179.

Engstler, S., G. Raimann, C. Angulo, U. Greife, C. Rolfs, U. Schröder, E. Somorjai, B. Kirch, and K. Langanke, 1992, Z. Phys. A **342**, 471.

Entem, D. R., and R. Machleidt, 2003, Phys. Rev. C **68**, 041001.

Essig, R., M. Sholapurkar, and T.-T. Yu, 2018, Phys. Rev. D **97**, 095029.

Esteban, I., M. C. Gonzalez-Garcia, M. Maltoni, T. Schwetz, and A. Zhou, 2020, J. High Energy Phys. 09, 178.

Falcon, R. E., G. A. Rochau, J. E. Bailey, T. A. Gomez, M. H. Montgomery, D. E. Winget, and T. Nagayama, 2015, Astrophys. J. **806**, 214.

Feroz, F., M. P. Hobson, and M. Bridges, 2009, Mon. Not. R. Astron. Soc. **398**, 1601.

Ferraro, F., G. F. Ciani, A. Boeltzig, F. Cavanna, and S. Zavatarelli, 2021, Front. Astron. Space Sci. **7**, 119.

Ferraro, F., *et al.*, 2018, Phys. Rev. Lett. **121**, 172701.

Fessler, A., T. N. Massey, B. J. Micklich, and D. L. Smith, 2000, Nucl. Instrum. Methods Phys. Res., Sect. A **450**, 353.

Fetisov, V. N., and Y. S. Kopysov, 1972, Phys. Lett. **40B**, 602.

Fields, B. D., K. A. Olive, T.-H. Yeh, and C. Young, 2020, J. Cosmol. Astropart. Phys. 03, 010.

Filippone, B. W., A. J. Elwyn, C. N. Davids, and D. D. Koetke, 1983, Phys. Rev. C **28**, 2222.

Fiorentini, G., C. Rolfs, F. L. Villante, and B. Ricci, 2003, Phys. Rev. C **67**, 014603.

Firestone, R. B., 2015, Nucl. Data Sheets **127**, 1.

Formicola, A., *et al.*, 2004, Phys. Lett. B **591**, 61.

Fortune, H. T., 2013, Phys. Rev. C **88**, 015801.

Fowler, W. A., 1972, Nature (London) **238**, 24.

Fowler, W. A., G. R. Caughlan, and B. A. Zimmerman, 1967, Annu. Rev. Astron. Astrophys. **5**, 525.

Fox, C., C. Iliadis, A. E. Champagne, A. Coc, J. José, R. Longland, J. Newton, J. Pollanen, and R. Runkle, 2004, Phys. Rev. Lett. **93**, 081102.

Fox, C., C. Iliadis, A. E. Champagne, R. P. Fitzgerald, R. Longland, J. Newton, J. Pollanen, and R. Runkle, 2005, Phys. Rev. C **71**, 055801.

Francis, A., J. R. Green, P. M. Junnarkar, C. Miao, T. D. Rae, and H. Wittig, 2019, Phys. Rev. D **99**, 074505.

Frentz, B., *et al.*, 2021, Phys. Rev. C **103**, 045802.

Frentz, B., *et al.*, 2022, Phys. Rev. C **106**, 065803.

Fretwell, S., *et al.*, 2020, Phys. Rev. Lett. **125**, 032701.

Fujioka, S., *et al.*, 2005, Phys. Rev. Lett. **95**, 235004.

Fukuda, Y., *et al.*, 1996, Phys. Rev. Lett. **77**, 1683.

Fukuda, Y., *et al.*, 1998a, Phys. Rev. Lett. **81**, 1562.

Fukuda, Y., *et al.* (Super-Kamiokande Collaboration), 1998b, Phys. Rev. Lett. **81**, 1562.

Gagliardi, C. A., *et al.*, 1999, Phys. Rev. C **59**, 1149.

Galinski, N., *et al.*, 2014, Phys. Rev. C **90**, 035803.

Garrett, J. D., H. T. Fortune, R. Middleton, and W. Scholz, 1978, Phys. Rev. C **18**, 2032.

Gaspard, D., J.-M. Sparenberg, Q. Wenda, and D. Baye, 2019, Phys. Rev. C **100**, 035805.

Gatu Johnson, M., G. Hale, M. Paris, M. Wiescher, and A. Zylstra, 2023, Front. Phys. **11**, 1180821.

Gatu Johnson, M., *et al.*, 2017, Phys. Plasmas **24**, 041407.

Gatu Johnson, M., *et al.*, 2018, Phys. Rev. Lett. **121**, 042501.

Gazit, D., S. Quaglioni, and P. Navrátil, 2009, Phys. Rev. Lett. **103**, 102502.

Gazit, D., S. Quaglioni, and P. Navrátil, 2019, Phys. Rev. Lett. **122**, 029901(E).

Geithner, W., *et al.*, 2017, Hyperfine Interact. **238**, 13.

Gesuè, R. M., *et al.*, 2024, Phys. Rev. Lett. **133**, 052701.

Gill, N. M., C. J. Fontes, and C. E. Starrett, 2023, J. Phys. B **56**, 015001.

Giunti, C., Y. F. Li, C. A. Ternes, O. Tyagi, and Z. Xin, 2022, J. High Energy Phys. 10, 164.

Giunti, C., Y. F. Li, C. A. Ternes, and Z. Xin, 2023, Phys. Lett. B **842**, 137983.

Glorius, J., and C. G. Bruno, 2023, Eur. Phys. J. A **59**, 81.

Gnech, A., L. E. Marcucci, and M. Viviani, 2024, Phys. Rev. C **109**, 035502.

Goldhagen, K., M. Maltoni, S. E. Reichard, and T. Schwetz, 2022, Eur. Phys. J. C **82**, 116.

Golser, R., and D. Semrad, 1991, Phys. Rev. Lett. **66**, 1831.

Gomez, T. A., T. Nagayama, P. B. Cho, D. P. Kilcrease, C. J. Fontes, and M. C. Zammit, 2022, J. Phys. B **55**, 034002.

Gonzalez-Garcia, M. C., M. Maltoni, J. P. Pinheiro, and A. M. Serenelli, 2024, J. High Energy Phys. 02, 064.

Görres, J., C. Rolfs, P. Schmalbrock, H. P. Trautvetter, and J. Keinonen, 1982, Nucl. Phys. **A385**, 57.

Green, J. R., A. D. Hanlon, P. M. Junnarkar, and H. Wittig, 2021, Phys. Rev. Lett. **127**, 242003.

Greife, U., F. Gorris, M. Junker, C. Rolfs, and D. Zahnow, 1995, Z. Phys. A **351**, 107.

Grevesse, N., and A. Noels, 1993, in *Origin and Evolution of the Elements*, edited by N. Prantzos, E. Vangioni-Flam, and M. Cassé (Cambridge University Press, Cambridge, England), pp. 15–25.

Grevesse, N., and A. J. Sauval, 1998, Space Sci. Rev. **85**, 161.

Gribov, V., and B. Pontecorvo, 1969, Phys. Lett. **28B**, 493.

Grieger, M., *et al.*, 2020, Phys. Rev. D **101**, 123027.

Gruzinov, A. V., 1998, Astrophys. J. **496**, 503.

Gruzinov, A. V., and J. N. Bahcall, 1997, Astrophys. J. **490**, 437.

Gruzinov, A. V., and J. N. Bahcall, 1998, Astrophys. J. **504**, 996.

Gurbich, A., 2008, Nucl. Instrum. Methods Phys. Res., Sect. B **266**, 1193.

Guzik, J. A., and K. Mussack, 2010, Astrophys. J. **713**, 1108.

Guzik, J. A., L. S. Watson, and A. N. Cox, 2005, Astrophys. J. **627**, 1049.

Gyürky, G., 2024 (private communication).

Gyürky, G., L. Csedreki, T. Szücs, G. G. Kiss, Z. Halász, and Z. Fülöp, 2023, Eur. Phys. J. A **59**, 59.

Gyürky, G., Z. Fülöp, F. Käppeler, G. G. Kiss, and A. Wallner, 2019, Eur. Phys. J. A **55**, 41.

Gyürky, G., Z. Halász, G. G. Kiss, T. Szücs, A. Csík, Z. Török, R. Huszánk, M. G. Kohan, L. Wagner, and Z. Fülöp, 2019, Phys. Rev. C **100**, 015805.

Gyürky, G., Z. Halász, G. G. Kiss, T. Szücs, and Z. Fülöp, 2022, Phys. Rev. C **105**, L022801.

Gyürky, G., A. Ornelas, Z. Fülöp, Z. Halász, G. G. Kiss, T. Szücs, R. Huszánk, I. Hornyák, I. Rajta, and I. Vajda, 2017, Phys. Rev. C **95**, 035805.

Gyürky, G., *et al.*, 2007, Phys. Rev. C **75**, 035805.

Hager, U., *et al.*, 2012, Phys. Rev. C **85**, 035803.

Hagstotz, S., P. F. de Salas, S. Gariazzo, S. Pastor, M. Gerbino, M. Lattanzi, S. Vagnozzi, and K. Freese, 2021, Phys. Rev. D **104**, 123524.

Hakel, P., and D. P. Kilcrease, 2004, in *Proceedings of the 14th APS Topical Conference on Atomic Processes in Plasmas, Santa Fe, 2004*, edited by J. S. Cohen, D. P. Kilcrease, and S. Mazevet (AIP Publishing, Melville, NY), pp. 190–196.
Hale, S. E., A. E. Champagne, C. Iliadis, V. Y. Hansper, D. C. Powell, and J. C. Blackmon, 2001, Phys. Rev. C **65**, 015801.
Hale, S. E., A. E. Champagne, C. Iliadis, V. Y. Hansper, D. C. Powell, and J. C. Blackmon, 2004, Phys. Rev. C **70**, 045802.
Hammache, F., *et al.*, 1998, Phys. Rev. Lett. **80**, 928.
Hammache, F., *et al.*, 2001, Phys. Rev. Lett. **86**, 3985.
Hampel, W., and L. P. Remsberg, 1985, Phys. Rev. C **31**, 666.
Harada, M., *et al.*, 2023, Astrophys. J. Lett. **951**, L27.
Hardy, J. C., and I. S. Towner, 2009, Phys. Rev. C **79**, 055502.
Hardy, J. C., and I. S. Towner, 2020, Phys. Rev. C **102**, 045501.
Hass, M., 1999, Phys. Lett. B **462**, 237.
Haxton, W. C., 1995, Annu. Rev. Astron. Astrophys. **33**, 459.
Haxton, W. C., and A. M. Serenelli, 2008, Astrophys. J. **687**, 678.
He, J.-J., I. Lombardo, D. Dell'Aquila, Y. Xu, L.-Y. Zhang, and W.-P. Liu, 2018, Chin. Phys. C **42**, 015001.
Hebbard, D. F., 1960, Nucl. Phys. **15**, 289.
Herfurth, F., *et al.*, 2018, *Proceedings of the 11th Workshop on Beam Cooling and Related Topics (COOL2017), Bonn, 2017*, edited by V. R. W. Schaa, M. Marx, and M. Tilmont (JACoW, Geneva).
Herndl, H., H. Abele, G. Staudt, B. Bach, K. Grün, H. Scsribany, H. Oberhummer, and G. Raimann, 1991, Phys. Rev. C **44**, R952.
Herrera, Y., and A. Serenelli, 2023, ChETEC-INFRA WP8: Astro-nuclear Library—Standard Solar Models B23, 10.5281/zenodo.10174170.
Herrmann, H. W., *et al.*, 2014, Rev. Sci. Instrum. **85**, 11E124.
Hester, R. E., R. E. Pixley, and W. A. Lamb, 1958, Phys. Rev. **111**, 1604.
Higa, R., H. W. Hammer, and U. van Kolck, 2008, Nucl. Phys. **A809**, 171.
Higa, R., P. Premarathna, and G. Rupak, 2022, Phys. Rev. C **106**, 014601.
Higa, R., G. Rupak, and A. Vaghani, 2018, Eur. Phys. J. A **54**, 89.
Hilbe, J. M., R. S. de Souza, and E. E. O. Ishida, 2017, *Bayesian Models for Astrophysical Data Using* `R, JAGS, Python, and Stan` (Cambridge University Press, Cambridge, England).
Hill, R. J., P. Kammel, W. J. Marciano, and A. Sirlin, 2018, Rep. Prog. Phys. **81**, 096301.
Hirata, K. S., *et al.*, 1989, Phys. Rev. Lett. **63**, 16.
Holt, R. J., H. E. Jackson, R. M. Laszewski, J. E. Monahan, and J. R. Specht, 1978, Phys. Rev. C **18**, 1962.
Hörz, B., *et al.*, 2021, Phys. Rev. C **103**, 014003.
Huebner, W. F., and W. D. Barfield, 2014, *Opacity*, Astrophysics and Space Science Library Vol. 402 (Springer, New York), 10.1007/978-1-4614-8797-5.
Huke, A., K. Czerski, P. Heide, G. Ruprecht, N. Targosz, and W. Żebrowski, 2008, Phys. Rev. C **78**, 015803.
Hummer, D., and D. Mihalas, 1988, Astrophys. J. **331**, 794.
Iglesias, C. A., 2015, High Energy Density Phys. **15**, 4.
Iglesias, C. A., 2023, High Energy Density Phys. **47**, 101043.
Iglesias, C. A., and F. J. Rogers, 1991, Astrophys. J. Lett. **371**, L73.
Iglesias, C. A., and F. J. Rogers, 1996, Astrophys. J. **464**, 943.
Iliadis, C., 2015, *Nuclear Physics of Stars* (Wiley-VCH, Weinheim).
Iliadis, C., 2022 (private communication).
Iliadis, C., 2023, Phys. Rev. C **107**, 044610.
Iliadis, C., K. S. Anderson, A. Coc, F. X. Timmes, and S. Starrfield, 2016, Astrophys. J. **831**, 107.
Iliadis, C., C. Angulo, P. Descouvemont, M. Lugaro, and P. Mohr, 2008, Phys. Rev. C **77**, 045802.
Iliadis, C., A. Champagne, and J. José, 2005, J. Phys. G **31**, S1785.
Iliadis, C., J. M. D'Auria, S. Starrfield, W. J. Thompson, and M. Wiescher, 2001, Astrophys. J. Suppl. Ser. **134**, 151.
Iliadis, C., R. Longland, A. E. Champagne, and A. Coc, 2010, Nucl. Phys. **A841**, 251.
Iliadis, C., V. Palanivelrajan, and R. S. de Souza, 2022, Phys. Rev. C **106**, 055802.
Imbriani, G., *et al.*, 2005, Eur. Phys. J. A **25**, 455.
Imbriani, G., *et al.*, 2012a, Phys. Rev. C **86**, 039902.
Imbriani, G., *et al.*, 2012b, Phys. Rev. C **85**, 065810.
Indelicato, I., *et al.*, 2017, Astrophys. J. **845**, 19.
Iritani, T., *et al.*, 2016, J. High Energy Phys. 10, 101.
Itoh, N., H. Totsuji, S. Ichimaru, and H. E. Dewitt, 1979, Astrophys. J. **234**, 1079.
Iwasa, N., *et al.*, 1999, Phys. Rev. Lett. **83**, 2910.
James, F., 1968, CERN Report No. 68-15, https://cds.cern.ch/record/275743/files/CERN-68-15.pdf.
Johnson, C. W., E. Kolbe, S. E. Koonin, and K. Langanke, 1992, Astrophys. J. **392**, 320.
Junghans, A. R., K. A. Snover, E. C. Mohrmann, E. G. Adelberger, and L. Buchmann, 2010, Phys. Rev. C **81**, 012801.
Junghans, A. R., *et al.*, 2003, Phys. Rev. C **68**, 065803.
Junker, M., G. Imbriani, A. Best, A. Boeltzig, A. Compagnucci, A. Di Leva, F. Ferraro, D. Rapagnani, and V. Rigato, 2023, Front. Phys. **11**, 1291113.
Junker, M., *et al.*, 1998, Phys. Rev. C **57**, 2700.
Kajino, T., 1986, Nucl. Phys. **A460**, 559.
Kajino, T., S. M. Austin, and H. Toki, 1987, Astrophys. J. **319**, 531.
Kammel, P., 2003, in *Proceedings of the International Workshop on Exotic Atoms—Future Perspectives (EXA 2002), Vienna, 2002*, edited by P. Kienle, J. Marton, and J. Zmeskal (Austrian Academy of Sciences Press, Vienna) [arXiv:nucl-ex/0304019].
Kaplan, D. B., 1996, talk, *Annual Meeting of the APS Division of Nuclear Physics, Cambridge, MA, 1996* (unpublished), p. BA.03.
Kasagi, J., H. Yuki, T. Baba, T. Noda, T. Ohtsuki, and A. G. Lipson, 2002, J. Phys. Soc. Jpn. **71**, 2881.
Keinonen, J., P. Tikkanen, A. Kuronen, Á. Z. Kiss, E. Somorjai, and B. H. Wildenthal, 1989, Nucl. Phys. **A493**, 124.
Kelly, K. J., A. E. Champagne, L. N. Downen, J. R. Dermigny, S. Hunt, C. Iliadis, and A. L. Cooper, 2017, Phys. Rev. C **95**, 015806.
Kettner, K. U., H. W. Becker, C. R. Brune, R. J. deBoer, J. Görres, D. Odell, D. Rogalla, and M. Wiescher, 2023, Phys. Rev. C **108**, 035805.
Kievsky, A., S. Rosati, M. Viviani, L. E. Marcucci, and L. Girlanda, 2008, J. Phys. G **35**, 063101.
Kikuchi, T., *et al.*, 1997, Phys. Lett. B **391**, 261.
Kikuchi, T., *et al.*, 1998, Eur. Phys. J. A **3**, 213.
Kilcrease, D., J. Colgan, P. Hakel, C. Fontes, and M. Sherrill, 2015, High Energy Density Phys. **16**, 36.
Kim, B. T., T. Izumoto, and K. Nagatani, 1981, Phys. Rev. C **23**, 33.
King, G. B., A. E. Lovell, L. Neufcourt, and F. M. Nunes, 2019, Phys. Rev. Lett. **122**, 232502.
King, J. D., R. E. Azuma, J. B. Vise, J. Görres, C. Rolfs, H. P. Trautvetter, and A. E. Vlieks, 1994, Nucl. Phys. **A567**, 354.
Kious, M., 1990, Ph.D. thesis (Université de Paris-Sud).
Kirsebom, O. S., *et al.*, 2011, Phys. Rev. C **83**, 065802.
Kiss, G. G., *et al.*, 2020, Phys. Lett. B **807**, 135606.
Kong, X., and F. Ravndal, 2000, Nucl. Phys. **A665**, 137.
Kong, X., and F. Ravndal, 2001, Phys. Rev. C **64**, 044002.
Kontos, A., E. Uberseder, R. deBoer, J. Görres, C. Akers, A. Best, M. Couder, and M. Wiescher, 2013, Phys. Rev. C **87**, 065804.
Kontos, A., *et al.*, 2012, Phys. Rev. C **86**, 055801.

Krauss, A., H. W. Becker, H. P. Trautvetter, and C. Rolfs, 1987, Nucl. Phys. **A467**, 273.
Kravvaris, K., P. Navrátil, S. Quaglioni, C. Hebborn, and G. Hupin, 2023, Phys. Lett. B **845**, 138156.
Krief, M., A. Feigel, and D. Gazit, 2016a, Astrophys. J. **824**, 98.
Krief, M., A. Feigel, and D. Gazit, 2016b, Astrophys. J. **821**, 45.
Krief, M., A. Feigel, and D. Gazit, 2018, Atoms **6**, 35.
Krief, M., Y. Kurzweil, A. Feigel, and D. Gazit, 2018, Astrophys. J. **856**, 135.
Krueger, R., and T. Schwetz, 2023, Eur. Phys. J. C **83**, 578.
Kruse, M. K., and C. A. Iglesias, 2019, High Energy Density Phys. **31**, 38.
Kruse, M. K., and C. A. Iglesias, 2021, High Energy Density Phys. **41**, 100976.
Kudomi, N., M. Komori, K. Takahisa, S. Yoshida, K. Kume, H. Ohsumi, and T. Itahashi, 2004, Phys. Rev. C **69**, 015802.
Kunitomo, M., T. Guillot, and G. Buldgen, 2022, Astron. Astrophys. **667**, L2.
Kurylov, A., M. J. Ramsey-Musolf, and P. Vogel, 2003, Phys. Rev. C **67**, 035502.
La Cognata, M., V. Z. Goldberg, A. M. Mukhamedzhanov, C. Spitaleri, and R. E. Tribble, 2009, Phys. Rev. C **80**, 012801.
La Cognata, M., S. Palmerini, C. Spitaleri, I. Indelicato, A. M. Mukhamedzhanov, I. Lombardo, and O. Trippella, 2015, Astrophys. J. **805**, 128.
La Cognata, M., *et al.*, 2008, Phys. Rev. Lett. **101**, 152501.
La Cognata, M., *et al.*, 2010, Astrophys. J. **708**, 796.
La Cognata, M., *et al.*, 2011, Astrophys. J. Lett. **739**, L54.
La Cognata, M., *et al.*, 2022, Astrophys. J. **941**, 96.
Langanke, K., T. D. Shoppa, C. A. Barnes, and C. Rolfs, 1996, Phys. Lett. B **369**, 211.
Leblanc, P. J., *et al.*, 2010, Phys. Rev. C **82**, 055804.
Lee, R., 1988, J. Quant. Spectrosc. Radiat. Transfer **40**, 561.
Lellouch, L., and M. Lüscher, 2001, Commun. Math. Phys. **219**, 31.
Lemut, A., *et al.* (LUNA Collaboration), 2006, Phys. Lett. B **634**, 483.
Lennarz, A., *et al.*, 2020, Phys. Lett. B **807**, 135539.
Lestinsky, M., *et al.*, 2016, Eur. Phys. J. Special Topics **225**, 797.
Li, Q., J. Görres, R. J. deBoer, G. Imbriani, A. Best, A. Kontos, P. J. LeBlanc, E. Uberseder, and M. Wiescher, 2016, Phys. Rev. C **93**, 055806.
Liberman, D. A., 1979, Phys. Rev. B **20**, 4981.
Lipoglavsek, M., and A. Cvetinović, 2020, in EPJ Web Conf. **227**, 01012.
Liu, P., C. Gao, Y. Hou, J. Zeng, and J. Yuan, 2018, Commun. Phys. **1**, 95.
Liu, T.-X., R. Peng, S. Lyu, and B. Long, 2022, Phys. Rev. C **106**, 055501.
Liu, W. P., *et al.*, 2022, Few-Body Syst. **63**, 43.
Loisel, G. P., J. E. Bailey, D. A. Liedahl, C. J. Fontes, T. R. Kallman, T. Nagayama, S. B. Hansen, G. A. Rochau, R. C. Mancini, and R. W. Lee, 2017, Phys. Rev. Lett. **119**, 075001.
Lombardo, I., 2019, Acta Phys. Pol. B **50**, 393.
Lombardo, I., D. Dell'Aquila, L. Campajola, E. Rosato, G. Spadaccini, and M. Vigilante, 2013, J. Phys. G **40**, 125102.
Lombardo, I., D. Dell'Aquila, J.-J. He, G. Spadaccini, and M. Vigilante, 2019, Phys. Rev. C **100**, 044307.
Lombardo, I., *et al.*, 2015, Phys. Lett. B **748**, 178.
Longfellow, B., *et al.*, 2023, Phys. Rev. C **107**, L032801.
Longland, R., C. Iliadis, J. M. Cesaratto, A. E. Champagne, S. Daigle, J. R. Newton, and R. Fitzgerald, 2010, Phys. Rev. C **81**, 055804.
Lorenz-Wirzba, H., 1978, Ph.D. thesis (Westfälischen Wilhelms-Universität zu Münster).
Lorenz-Wirzba, H., P. Schmalbrock, H. P. Trautvetter, M. Wiescher, C. Rolfs, and W. S. Rodney, 1979, Nucl. Phys. **A313**, 346.
Ludwig, F., L. Wagner, T. Al-Abdullah, G. G. Barnaföldi, D. Bemmerer, D. Degering, K. Schmidt, G. Surányi, T. Szücs, and K. Zuber, 2019, Astropart. Phys. **112**, 24.
Ludwig, H. G., E. Caffau, M. Steffen, B. Freytag, P. Bonifacio, and A. Kučinskas, 2009, Mem. Soc. Astron. Ital. **80**, 711.
Lyons, S., *et al.*, 2018, Phys. Rev. C **97**, 065802.
Ma, L., H. J. Karwowski, C. R. Brune, Z. Ayer, T. C. Black, J. C. Blackmon, E. J. Ludwig, M. Viviani, A. Kievsky, and R. Schiavilla, 1997, Phys. Rev. C **55**, 588.
Machleidt, R., and D. R. Entem, 2011, Phys. Rep. **503**, 1.
Magee, N. H., *et al.*, 1995, in *Astrophysical Applications of Powerful New Databases*, edited by S. J. Adelman and W. L. Wiese, Astronomical Society of the Pacific Conference Series Vol. 78 (Astronomical Society of the Pacific, San Francisco), p. 51.
Magg, E., *et al.*, 2022, Astron. Astrophys. **661**, A140.
Mak, H. B., G. T. Ewan, H. C. Evans, J. D. MacArthur, W. McLatchie, and R. E. Azuma, 1980, Nucl. Phys. **A343**, 79.
Mancini, R. C., 2016, J. Phys. Conf. Ser. **717**, 012069.
Mao, D., K. Mussack, and W. Däppen, 2009, Astrophys. J. **701**, 1204.
Marcucci, L. E., J. Dohet-Eraly, L. Girlanda, A. Gnech, A. Kievsky, and M. Viviani, 2020, Front. Phys. **8**, 69.
Marcucci, L. E., A. Kievsky, S. Rosati, R. Schiavilla, and M. Viviani, 2012, Phys. Rev. Lett. **108**, 052502.
Marcucci, L. E., A. Kievsky, S. Rosati, R. Schiavilla, and M. Viviani, 2018, Phys. Rev. Lett. **121**, 049901.
Marcucci, L. E., G. Mangano, A. Kievsky, and M. Viviani, 2016, Phys. Rev. Lett. **116**, 102501.
Marcucci, L. E., M. Piarulli, M. Viviani, L. Girlanda, A. Kievsky, S. Rosati, and R. Schiavilla, 2011, Phys. Rev. C **83**, 014002.
Marcucci, L. E., R. Schiavilla, and M. Viviani, 2013, Phys. Rev. Lett. **110**, 192503.
Marcucci, L. E., R. Schiavilla, and M. Viviani, 2019, Phys. Rev. Lett. **123**, 019901(E).
Marcucci, L. E., R. Schiavilla, M. Viviani, A. Kievsky, S. Rosati, and J. F. Beacom, 2000, Phys. Rev. C **63**, 015801.
Marcucci, L. E., M. Viviani, R. Schiavilla, A. Kievsky, and S. Rosati, 2005, Phys. Rev. C **72**, 014001.
Marshall, C., K. Setoodehnia, F. Portillo, J. H. Kelley, and R. Longland, 2021, Phys. Rev. C **104**, L032801.
Marta, M., *et al.*, 2008, Phys. Rev. C **78**, 022802.
Mascali, D., *et al.*, 2022, Universe **8**, 80.
Masha, E., *et al.*, 2023, Phys. Rev. C **108**, L052801.
McKeown, R. D., G. T. Garvey, and C. A. Gagliardi, 1980, Phys. Rev. C **22**, 738.
Mei, D. M., and A. Hime, 2006, Phys. Rev. D **73**, 053004.
Mei, D. M., C. Zhang, and A. Hime, 2009, Nucl. Instrum. Methods Phys. Res., Sect. A **606**, 651.
Mendoza, C., S. Turck-Chiéze, and J. Colgan, 2018, in *Workshop on Astrophysical Opacities*, Astronomical Society of the Pacific Conference Series Vol. 515, edited by J. Colgan (Astronomical Society of the Pacific, San Francisco).
Meyer, A., 2022, Proc. Sci. LATTICE2022, 240.
Meyer, A. S., M. Betancourt, R. Gran, and R. J. Hill, 2016, Phys. Rev. D **93**, 113015.
Meyer, A. S., A. Walker-Loud, and C. Wilkinson, 2022, Annu. Rev. Nucl. Part. Sci. **72**, 205.
Mitchell, J. P., G. V. Rogachev, E. D. Johnson, L. T. Baby, K. W. Kemper, A. M. Moro, P. Peplowski, A. S. Volya, and I. Wiedenhöver, 2013, Phys. Rev. C **87**, 054617.
Moazen, B. H., *et al.*, 2007, Phys. Rev. C **75**, 065801.

Mohamed, Z. L., Y. Kim, and J. P. Knauer, 2022, Front. Phys. **10**, 944339.
Mondet, G., C. Blancard, P. Cossé, and G. Faussurier, 2015, Astrophys. J. Suppl. Ser. **220**, 2.
Montalbán, J., A. Miglio, A. Noels, N. Grevesse, and M. P. di Mauro, 2004, in *Proceedings of the SOHO 14/GONG 2004 Workshop, New Haven, 2004*, ESA Special Publications Vol. 559, edited by D. Danesy (European Space Agency, Noordwijk, Netherlands), pp. 574–576.
Montgomery, M. H., R. E. Falcon, G. A. Rochau, J. E. Bailey, T. A. Gomez, A. L. Carlson, D. E. Bliss, T. Nagayama, M. Stein, and D. E. Winget, 2015, High Energy Density Phys. **17**, 168.
More, R., J.-C. Pain, S. Hansen, T. Nagayama, and J. Bailey, 2020, High Energy Density Phys. **34**, 100717.
More, R. M., S. B. Hansen, and T. Nagayama, 2017, High Energy Density Phys. **24**, 44.
Morlock, R., R. Kunz, A. Mayer, M. Jaeger, A. Müller, J. W. Hammer, P. Mohr, H. Oberhummer, G. Staudt, and V. Kölle, 1997, Phys. Rev. Lett. **79**, 3837.
Moscoso, J., R. S. de Souza, A. Coc, and C. Iliadis, 2021, Astrophys. J. **923**, 49.
Mossa, V., *et al.*, 2020a, Eur. Phys. J. A **56**, 144.
Mossa, V., *et al.*, 2020b, Nature (London) **587**, 210.
Motobayashi, T., *et al.*, 1994, Phys. Rev. Lett. **73**, 2680.
Mukhamedzhanov, A. M., M. La Cognata, and V. Kroha, 2011, Phys. Rev. C **83**, 044604.
Mukhamedzhanov, A. M., *et al.*, 2003, Phys. Rev. C **67**, 065804.
Mukhamedzhanov, A. M., *et al.*, 2006, Phys. Rev. C **73**, 035806.
Mukhamedzhanov, A. M., *et al.*, 2008, Phys. Rev. C **78**, 015804.
Mussack, K., 2011, Astrophys. Space Sci. **336**, 111.
Mussack, K., and W. Däppen, 2010, Astrophys. Space Sci. **328**, 153.
Nagayama, T., J. E. Bailey, G. Loisel, S. B. Hansen, G. A. Rochau, R. C. Mancini, J. J. MacFarlane, and I. Golovkin, 2014, Phys. Plasmas **21**, 056502.
Nagayama, T., J. E. Bailey, G. Loisel, G. A. Rochau, and R. E. Falcon, 2014, Rev. Sci. Instrum. **85**, 11D603.
Nagayama, T., J. E. Bailey, G. Loisel, G. A. Rochau, J. J. MacFarlane, and I. Golovkin, 2016, Phys. Rev. E **93**, 023202.
Nagayama, T., J. E. Bailey, G. P. Loisel, G. A. Rochau, J. J. MacFarlane, and I. E. Golovkin, 2017, Phys. Rev. E **95**, 063206.
Nagayama, T., *et al.*, 2016, High Energy Density Phys. **20**, 17.
Nagayama, T., *et al.*, 2019, Phys. Rev. Lett. **122**, 235001.
Nahar, S. N., and A. K. Pradhan, 2016, Phys. Rev. Lett. **116**, 235003.
Napolitano, J., S. J. Freedman, and J. Camp, 1987, Phys. Rev. C **36**, 298.
Navrátil, P., R. Roth, and S. Quaglioni, 2011, Phys. Lett. B **704**, 379.
Neff, T., 2011, Phys. Rev. Lett. **106**, 042502.
Neogy, P., R. Middleton, and W. Scholz, 1972, Phys. Rev. C **6**, 885.
Nesaraja, C. D., C. R. Brune, B. T. Crowley, J. H. Kelley, S. O. Nelson, R. M. Prior, K. Sabourov, D. R. Tilley, A. Tonchev, and H. R. Weller, 2001, Phys. Rev. C **64**, 065804.
Newton, J. R., C. Iliadis, A. E. Champagne, J. M. Cesaratto, S. Daigle, and R. Longland, 2010, Phys. Rev. C **81**, 045801.
Newton, J. R., C. Iliadis, A. E. Champagne, R. Longland, and C. Ugalde, 2007, Phys. Rev. C **75**, 055808.
Nollett, K. M., 2001, Phys. Rev. C **63**, 054002.
Nollett, K. M., and R. B. Wiringa, 2011, Phys. Rev. C **83**, 041001.
Norman, E. B., A. Drobizhev, N. Gharibyan, K. E. Gregorich, Y. G. Kolomensky, B. N. Sammis, N. D. Scielzo, J. A. Shusterman, and K. J. Thomas, 2024, Phys. Rev. C **109**, 055501.
Odell, D., C. R. Brune, and D. R. Phillips, 2022, Phys. Rev. C **105**, 014625.
Odell, D., C. R. Brune, D. R. Phillips, R. J. deBoer, and S. N. Paneru, 2022, Front. Phys. **10**, 888476.
Ogata, S., 1997, Astrophys. J. **481**, 883.
Opachich, Y. P., *et al.*, 2022, Rev. Sci. Instrum. **93**, 113515.
Orebi Gann, G. D., K. Zuber, D. Bemmerer, and A. Serenelli, 2021, Annu. Rev. Nucl. Part. Sci. **71**, 491.
Osborne, J. L., C. A. Barnes, R. W. Kavanagh, R. M. Kremer, G. J. Mathews, J. L. Zyskind, P. D. Parker, and A. J. Howard, 1982, Phys. Rev. Lett. **48**, 1664.
Osborne, J. L., C. A. Barnes, R. W. Kavanagh, R. M. Kremer, G. J. Mathews, J. L. Zyskind, P. D. Parker, and A. J. Howard, 1984, Nucl. Phys. **A419**, 115.
Pain, J.-C., 2018, High Energy Density Phys. **26**, 23.
Pain, J.-C., 2021, Plasma **4**, 42.
Palmerini, S., M. L. Sergi, M. L. Cognata, L. Lamia, R. G. Pizzone, and C. Spitaleri, 2013, Astrophys. J. **764**, 128.
Paneru, S. N., *et al.*, 2019, Phys. Rev. C **99**, 045807.
Paneru, S. N., *et al.*, 2024, Phys. Rev. C **109**, 015802.
Pantaleo, F. R., *et al.*, 2021, Phys. Rev. C **104**, 025802.
Park, T. S., L. E. Marcucci, R. Schiavilla, M. Viviani, A. Kievsky, S. Rosati, K. Kubodera, D. P. Min, and M. Rho, 2003, Phys. Rev. C **67**, 055206.
Particle Physics Project Prioritization Panel, 2023, report, https://www.usparticlephysics.org/2023-p5-report/; accessed on April 27, 2024.
Perry, T., *et al.*, 2020, High Energy Density Phys. **35**, 100728.
Perry, T. S., *et al.*, 1991, Phys. Rev. Lett. **67**, 3784.
Pham, M. V., L. A. Kesler, K. B. Woller, and Z. S. Hartwig, 2021, Nucl. Instrum. Methods Phys. Res., Sect. B **499**, 118.
Pieper, S. C., and R. B. Wiringa, 2001, Annu. Rev. Nucl. Part. Sci. **51**, 53.
Pisanti, O., G. Mangano, G. Miele, and P. Mazzella, 2021, J. Cosmol. Astropart. Phys. 04, 020.
Pitrou, C., A. Coc, J.-P. Uzan, and E. Vangioni, 2021, Mon. Not. R. Astron. Soc. **502**, 2474.
Poudel, M., and D. R. Phillips, 2022, J. Phys. G **49**, 045102.
Powers, J. R., H. T. Fortune, R. Middleton, and O. Hansen, 1971, Phys. Rev. C **4**, 2030.
Prati, P., *et al.*, 1994, Z. Phys. A **350**, 171.
Premarathna, P., and G. Rupak, 2020, Eur. Phys. J. A **56**, 166.
Pudliner, B. S., V. R. Pandharipande, J. Carlson, and R. B. Wiringa, 1995, Phys. Rev. Lett. **74**, 4396.
Raiola, F., *et al.*, 2002a, Phys. Lett. B **547**, 193.
Raiola, F., *et al.*, 2002b, Eur. Phys. J. A **13**, 377.
Rauer, H., *et al.*, 2014, Exp. Astron. **38**, 249.
Redder, A., H. W. Becker, H. Lorenz-Wirzba, C. Rolfs, P. Schmalbrock, and H. P. Trautvetter, 1982, Z. Phys. A **305**, 325.
Reinhardt, T. P., S. Akhmadaliev, D. Bemmerer, K. Stöckel, and L. Wagner, 2016, Nucl. Instrum. Methods Phys. Res., Sect. B **381**, 58.
Renshaw, A., *et al.*, 2014, Phys. Rev. Lett. **112**, 091805.
Robertson, D., M. Couder, U. Greife, F. Strieder, and M. Wiescher, 2016, talk, *Fall Meeting of the APS Division of Nuclear Physics, Vancouver, British Columbia, Canada, 2016* (unpublished), p. JJ.003.
Robertson, R. G. H., P. Dyer, T. J. Bowles, R. E. Brown, N. Jarmie, C. J. Maggiore, and S. M. Austin, 1983, Phys. Rev. C **27**, 11.
Rochau, G. A., J. E. Bailey, R. E. Falcon, G. P. Loisel, T. Nagayama, R. C. Mancini, I. Hall, D. E. Winget, M. H. Montgomery, and D. A. Liedahl, 2014, Phys. Plasmas **21**, 056308.
Roger, T., *et al.*, 2012, Phys. Rev. Lett. **108**, 162502.

Rogers, F. J., and C. A. Iglesias, 1992, Astrophys. J. Suppl. Ser. **79**, 507.
Rolfs, C., 1973, Nucl. Phys. **A217**, 29.
Rolfs, C., 2001, Prog. Part. Nucl. Phys. **46**, 23.
Rolfs, C., and W. S. Rodney, 1974, Nucl. Phys. **A235**, 450.
Rolfs, C., W. S. Rodney, M. H. Shapiro, and H. Winkler, 1975, Nucl. Phys. **A241**, 460.
Rolfs, C., and E. Somorjai, 1995, Nucl. Instrum. Methods Phys. Res., Sect. B **99**, 297.
Rolfs, C. E., and W. S. Rodney, 1988, *Cauldrons in the Cosmos: Nuclear Astrophysics* (University of Chicago Press, Chicago).
Rowland, C., C. Iliadis, A. E. Champagne, C. Fox, J. José, and R. Runkle, 2004, Astrophys. J. **615**, L37.
Rowland, C., C. Iliadis, A. E. Champagne, and J. Mosher, 2002, Phys. Rev. C **65**, 064609.
Roxburgh, I. W., 1985, Sol. Phys. **100**, 21.
Runkle, R. C., A. E. Champagne, C. Angulo, C. Fox, C. Iliadis, R. Longland, and J. Pollanen, 2005, Phys. Rev. Lett. **94**, 082503.
Rupak, G., and P. Ravi, 2015, Phys. Lett. B **741**, 301.
Sahoo, L. K., and C. Basu, 2021, Int. J. Mod. Phys. E **30**, 2150102.
Salpeter, E. E., 1954, Aust. J. Phys. **7**, 373.
Salpeter, E. E., and H. M. van Horn, 1969, Astrophys. J. **155**, 183.
Salvat, D., 2017, talk, *Fall Meeting of the APS Division of Nuclear Physics, Pittsburgh, 2017* (unpublished), p. CG.007.
Sampson, D. H., H. L. Zhang, and C. J. Fontes, 2009, Phys. Rep. **477**, 111.
Santra, R., S. Chakraborty, and S. Roy, 2020, Phys. Rev. C **101**, 025802.
Sargsyan, G. H., *et al.*, 2022, Phys. Rev. Lett. **128**, 202503.
Savage, M. J., P. E. Shanahan, B. C. Tiburzi, M. L. Wagman, F. Winter, S. R. Beane, E. Chang, Z. Davoudi, W. Detmold, and K. Orginos (NPLQCD Collaboration), 2017, Phys. Rev. Lett. **119**, 062002.
Schaeuble, M. A., T. Nagayama, J. E. Bailey, B. H. Dunlap, and S. Patel, 2021, Phys. Plasmas **28**, 062902.
Schaeuble, M. A., T. Nagayama, J. E. Bailey, T. A. Gomez, M. H. Montgomery, and D. E. Winget, 2019, Astrophys. J. **885**, 86.
Schatzman, E., A. Maeder, F. Angrand, and R. Glowinski, 1981, Astron. Astrophys. **96**, 1, https://ui.adsabs.harvard.edu/abs/1981A%26A....96....1S/abstract.
Schiavilla, R., R. B. Wiringa, V. R. Pandharipande, and J. Carlson, 1992, Phys. Rev. C **45**, 2628.
Schiavilla, R., *et al.*, 1998, Phys. Rev. C **58**, 1263.
Schmid, G. J., B. J. Rice, R. M. Chasteler, M. A. Godwin, G. C. Kiang, L. L. Kiang, C. M. Laymon, R. M. Prior, D. R. Tilley, and H. R. Weller, 1997, Phys. Rev. C **56**, 2565.
Schröder, U., H. W. Becker, G. Bogaert, J. Görres, C. Rolfs, H. P. Trautvetter, R. E. Azuma, C. Campbell, J. D. King, and J. Vise, 1987, Nucl. Phys. **A467**, 240.
Schümann, F., *et al.*, 2003, Phys. Rev. Lett. **90**, 232501.
Schümann, F., *et al.*, 2006, Phys. Rev. C **73**, 015806.
Schürmann, D., R. Kunz, I. Lingner, C. Rolfs, F. Schümann, F. Strieder, and H. P. Trautvetter, 2008, Phys. Rev. C **77**, 055803.
Schury, D., *et al.*, 2020, J. Phys. Conf. Ser., **1412**, 162011.
Scott, D. A., *et al.*, 2012, Phys. Rev. Lett. **109**, 202501.
Seaton, M. J., 1987, J. Phys. B **20**, 8.
Sen, A., G. Domínguez-Cañizares, N. C. Podaru, D. J. W. Mous, M. Junker, G. Imbriani, and V. Rigato, 2019, Nucl. Instrum. Methods Phys. Res., Sect. B **450**, 390.
Serenelli, A. M., S. Basu, J. W. Ferguson, and M. Asplund, 2009, Astrophys. J. **705**, L123.
Serenelli, A. M., W. C. Haxton, and C. Peña-Garay, 2011, Astrophys. J. **743**, 24.
Sergi, M. L., *et al.*, 2015, Phys. Rev. C **91**, 065803.
Sharma, S., A. Gupta, M. R. Chowdhury, A. Mandal, A. Bisoi, V. Nanal, L. C. Tribedi, and M. S. Sarkar, 2020, Phys. Rev. C **102**, 024308.
Shoppa, T. D., M. Jeng, S. E. Koonin, K. Langanke, and R. Seki, 1996, Nucl. Phys. **A605**, 387.
Shoppa, T. D., S. E. Koonin, K. Langanke, and R. Seki, 1993, Phys. Rev. C **48**, 837.
Shornikov, A., A. E. Champagne, R. C. Walet, and D. J. W. Mous, 2023, Rev. Sci. Instrum. **94**, 073303.
Simon, N. R., 1982, Astrophys. J. **260**, L87.
Simonucci, S., S. Taioli, S. Palmerini, and M. Busso, 2013, Astrophys. J. **764**, 118.
Sinars, D. B., *et al.*, 2020, Phys. Plasmas **27**, 070501.
Singh, B. S., M. Hass, Y. Nir-El, and G. Haquin, 2004, Phys. Rev. Lett. **93**, 262503.
Skilling, J., 2006, Bayesian Anal. **1**, 833.
Skowronski, J., *et al.* (LUNA Collaboration), 2023a, Phys. Rev. Lett. **131**, 162701.
Skowronski, J., *et al.*, 2023b, Phys. Rev. C **107**, L062801.
Solovyev, A. S., and S. Y. Igashov, 2017, Phys. Rev. C **96**, 064605.
Solovyev, A. S., and S. Y. Igashov, 2019, Phys. Rev. C **99**, 054618.
Spergel, D. N., and W. H. Press, 1985, Astrophys. J. **294**, 663.
Spitaleri, C., C. A. Bertulani, L. Fortunato, and A. Vitturi, 2016, Phys. Lett. B **755**, 275.
Spitaleri, C., *et al.*, 2017, Phys. Rev. C **95**, 035801.
Springer, P. T., *et al.*, 1992, Phys. Rev. Lett. **69**, 3735.
Spyrou, K., C. Chronidou, S. Harissopulos, S. Kossionides, T. Paradellis, C. Rolfs, W. H. Schulte, and L. Borucki, 2000, Eur. Phys. J. A **7**, 79.
Stahler, S. W., 1988, Astrophys. J. **332**, 804.
Stambulchik, E., A. Calisti, H.-K. Chung, and M. Á. González, 2019, Atoms **7**, 20.
Steck, M., and Y. A. Litvinov, 2020, Prog. Part. Nucl. Phys. **115**, 103811.
Stöckel, K., *et al.*, 2024, Phys. Rev. C **110**, L032801.
Stonehill, L. C., J. A. Formaggio, and R. G. Robertson, 2004, Phys. Rev. C **69**, 015801.
Strieder, F., *et al.*, 2001, Nucl. Phys. **A696**, 219.
Sumikama, T., *et al.*, 2011, Phys. Rev. C **83**, 065501.
Switkowski, Z. E., R. O'Brien, A. K. Smith, and D. G. Sargood, 1975, Aust. J. Phys. **28**, 141.
Szücs, T., D. Bemmerer, D. Degering, A. Domula, M. Grieger, F. Ludwig, K. Schmidt, J. Steckling, S. Turkat, and K. Zuber, 2019, Eur. Phys. J. A **55**, 174.
Szücs, T., G. G. Kiss, G. Gyürky, Z. Halász, T. N. Szegedi, and Z. Fülöp, 2019, Phys. Rev. C **99**, 055804.
Tabacaru, G., *et al.*, 2006, Phys. Rev. C **73**, 025808.
Tews, I., *et al.*, 2022, Few-Body Syst. **63**, 67.
Thompson, I. J., 2022, Front. Phys. **10**.
Tilley, D. R., C. M. Cheves, J. L. Godwin, G. M. Hale, H. M. Hofmann, J. H. Kelley, C. G. Sheu, and H. R. Weller, 2002, Nucl. Phys. **A708**, 3.
Tilley, D. R., H. R. Weller, and C. M. Cheves, 1993, Nucl. Phys. **A564**, 1.
Tišma, I., M. Lipoglavšek, M. Mihovilovič, S. Markelj, M. Vencelj, and J. Vesić, 2019, Eur. Phys. J. A **55**, 137.
Tombrello, T. A., and P. D. Parker, 1963, Phys. Rev. **131**, 2582.
Tóth, Á., T. Szücs, T. N. Szegedi, G. Gyürky, Z. Halász, G. G. Kiss, and Z. Fülöp, 2023, Phys. Rev. C **108**, 025802.
Trache, L., A. Azhari, F. Carstoiu, H. L. Clark, C. A. Gagliardi, Y. W. Lui, A. M. Mukhamedzhanov, X. Tang, N. Timofeyuk, and R. E. Tribble, 2003, Phys. Rev. C **67**, 062801.

Tribble, R., C. Bertulani, M. La Cognata, A. Mukhamedzhanov, and C. Spitaleri, 2014, Rep. Prog. Phys. **77**, 106901.
Trippella, O., and M. L. Cognata, 2017, Astrophys. J. **837**, 41.
Tumino, A., C. A. Bertulani, M. L. Cognata, L. Lamia, R. G. Pizzone, S. Romano, and S. Typel, 2021, Annu. Rev. Nucl. Part. Sci. **71**, 345.
Tumino, A., *et al.*, 2014, Astrophys. J. **785**, 96.
Tumino, A., *et al.*, 2018, Nature (London) **557**, 687.
Turkat, S., 2023, Ph.D. thesis (Technische Universität Dresden).
Turkat, S., D. Bemmerer, A. Boeltzig, A. R. Domula, J. Koch, T. Lossin, M. Osswald, K. Schmidt, and K. Zuber, 2023, Astropart. Phys. **148**, 102816.
Turkat, S., *et al.*, 2021, Phys. Rev. C **103**, 045805.
Tursunov, E. M., S. A. Turakulov, and A. S. Kadyrov, 2018, Phys. Rev. C **97**, 035802.
Tursunov, E. M., S. A. Turakulov, and A. S. Kadyrov, 2021, Nucl. Phys. **A1006**, 122108.
Uberseder, E., and R. J. deBoer, 2015, AZURE2 user manual.
Vescovi, D., C. Mascaretti, F. Vissani, L. Piersanti, and O. Straniero, 2021, J. Phys. G **48**, 015201.
Vescovi, D., L. Piersanti, S. Cristallo, M. Busso, F. Vissani, S. Palmerini, S. Simonucci, and S. Taioli, 2019, Astron. Astrophys. **623**, A126.
Villante, F. L., 2010, Astrophys. J. **724**, 98.
Villante, F. L., 2015, Phys. Lett. B **742**, 279.
Vinyoles, N., A. M. Serenelli, F. L. Villante, S. Basu, J. Bergström, M. C. Gonzalez-Garcia, M. Maltoni, C. Peña-Garay, and N. Song, 2017, Astrophys. J. **835**, 202.
Viviani, M., E. Filandri, L. Girlanda, C. Gustavino, A. Kievsky, L. E. Marcucci, and R. Schiavilla, 2022, Phys. Rev. C **105**, 014001.
Viviani, M., A. Kievsky, and S. Rosati, 1995, Few-Body Syst. **18**, 25.
Viviani, M., S. Rosati, and A. Kievsky, 1998, Phys. Rev. Lett. **81**, 1580.
Vogelaar, R. B., T. R. Wang, S. E. Kellogg, and R. W. Kavanagh, 1990, Phys. Rev. C **42**, 753.
Volk, H., H. Kräwinkel, R. Santo, and L. Wallek, 1983, Z. Phys. A **310**, 91.
Vorabbi, M., P. Navrátil, S. Quaglioni, and G. Hupin, 2019, Phys. Rev. C **100**, 024304.
Wagner, L., *et al.*, 2018, Phys. Rev. C **97**, 015801.
Warren, J. B., K. L. Erdman, L. P. Robertson, D. A. Axen, and J. R. Macdonald, 1963, Phys. Rev. **132**, 1691.
Wiescher, M., H. W. Becker, J. Görres, K. U. Kettner, H. P. Trautvetter, W. E. Kieser, C. Rolfs, R. E. Azuma, K. P. Jackson, and J. W. Hammer, 1980, Nucl. Phys. **A349**, 165.
Wiescher, M., R. J. deBoer, and J. Görres, 2022, Front. Phys. **10**.
Wiescher, M., R. J. deBoer, and R. Reifarth, 2023, *Experimental Nuclear Astrophysics* (Springer Nature, Singapore), pp. 3491–3535.
Williams, M., P. Adsley, B. Davids, U. Greife, D. Hutcheon, J. Karpesky, A. Lennarz, M. Lovely, and C. Ruiz, 2021, Phys. Rev. C **103**, 055805.
Williams, M., *et al.*, 2020, Phys. Rev. C **102**, 035801.
Winhart, G., K. Eidmann, C. A. Iglesias, and A. Bar-Shalom, 1996, Phys. Rev. E **53**, R1332.
Winter, W., 2007, Ph.D. thesis (University of California, Berkeley).
Winter, W. T., S. J. Freedman, K. E. Rehm, and J. P. Schiffer, 2006, Phys. Rev. C **73**, 025503.
Winter, W. T., *et al.*, 2003, Phys. Rev. Lett. **91**, 252501.
Wiringa, R. B., V. G. J. Stoks, and R. Schiavilla, 1995, Phys. Rev. C **51**, 38.
Wolfenstein, L., 1978, Phys. Rev. D **17**, 2369.
Wonterghem, B. M. V., S. J. Brereton, R. F. Burr, P. Folta, D. L. Hardy, N. N. Jize, T. R. Kohut, T. A. Land, and B. T. Merritt, 2016, Fusion Sci. Technol. **69**, 452.
Wood, M. H., C. R. Brune, B. M. Fisher, H. J. Karwowski, D. S. Leonard, E. J. Ludwig, A. Kievsky, S. Rosati, and M. Viviani, 2002, Phys. Rev. C **65**, 034002.
Wood, S. R., K. Mussack, and J. A. Guzik, 2018, Sol. Phys. **293**, 111.
Workman, R. L., *et al.*, 2022, Prog. Theor. Exp. Phys. 083C01.
Xu, Y., K. Takahashi, S. Goriely, M. Arnould, M. Ohta, and H. Utsunomiya, 2013, Nucl. Phys. **A918**, 61.
Yeh, T.-H., K. A. Olive, and B. D. Fields, 2021, J. Cosmol. Astropart. Phys. 03, 046.
Young, P. R., 2018, Astrophys. J. **855**, 15.
Zeng, J., C. Gao, P. Liu, Y. Li, C. Meng, Y. Hou, D. Kang, and J. Yuan, 2022, Sci. China Phys. Mech. Astron. **65**, 233011.
Zhang, L., S. Xu, J. He, S. Wang, H. Chen, J. Hu, S. Ma, N. Zhang, S. Hou, and W. Liu, 2019, Nucl. Instrum. Methods Phys. Res., Sect. B **438**, 48.
Zhang, L., *et al.*, 2022, Nature (London) **610**7933, 656.
Zhang, L. Y., A. Y. López, M. Lugaro, J. J. He, and A. I. Karakas, 2021, Astrophys. J. **913**, 51.
Zhang, L. Y., *et al.*, 2021, Phys. Rev. Lett. **127**, 152702.
Zhang, X., K. M. Nollett, and D. R. Phillips, 2015, Phys. Lett. B **751**, 535.
Zhang, X., K. M. Nollett, and D. R. Phillips, 2018, Phys. Rev. C **98**, 034616.
Zhang, X., K. M. Nollett, and D. R. Phillips, 2020, J. Phys. G **47**, 054002.
Ziegler, J. F., M. D. Ziegler, and J. P. Biersack, 2010, Nucl. Instrum. Methods Phys. Res., Sect. B **268**, 1818.
Zinner, N. T., 2007, Nucl. Phys. **A781**, 81.
Zylstra, A. B., H. W. Herrmann, Y. H. Kim, A. McEvoy, K. Meaney, V. Y. Glebov, C. Forrest, and M. Rubery, 2019, Rev. Sci. Instrum. **90**, 123504.
Zylstra, A. B., *et al.*, 2016, Phys. Rev. Lett. **117**, 035002.
Zylstra, A. B., *et al.*, 2017, Phys. Rev. Lett. **119**, 222701.
Zylstra, A. B., *et al.*, 2020, Phys. Rev. C **101**, 042802.
See the Supplemental Material at http://link.aps.org/supplemental/10.1103/8lm7-gs18 for additional information on the S factor for the $^{7}\mathrm{Be}(p,\gamma)^{8}\mathrm{B}$ reaction, S_{17}.